



UNIVERSITÀ
DEGLI STUDI
DI PALERMO



MEDIZINISCHE
UNIVERSITÄT WIEN

Design, synthesis and biological evaluation of new anticancer drugs: FGFR inhibitors

Doctoral thesis in Molecular and Biomolecular Sciences - XXXIII CYCLE

Department of Biological, Chemical and Pharmaceutical Sciences and Technologies
University of Palermo

Institute of Cancer Research Department of Medicine I
Medical University of Vienna

CANDIDATE

Mery La Franca

SUPERVISORS

Prof. Giampaolo Barone

Prof. Walter Berger

COORDINATOR

Prof. Patrizia Diana

Firmato digitalmente da: Patrizia Diana
Organizzazione: UNIVERSITA' DEGLI STUDI DI PALERMO/80023730825
Data: 08/02/2021 16:20:38

Academic Year 2019/2021

TABLE OF CONTENTS

DECLARATION.....	VII
SUMMARY	VIII
LIST OF FIGURES.....	X
LIST OF TABLES	XVII
CHAPTER ONE, INTRODUCTION.....	1
1.1 Cancer as a central challenge of modern medicine	1
1.2 Fibroblast growth factor receptors.....	5
1.2.1 The biology of FGFs and FGFRs.....	8
1.2.2 FGFRs and cancer.....	10
1.2.3 Therapeutic targeting of oncogenic FGFRs alterations	11
1.2.4 Classification of FGFRs inhibitors	12
1.3 Lung cancer.....	13
1.3.1 Classification and pathology.....	13
1.3.2 Lung cancer epidemiology.....	14
1.3.3 Molecular alterations associated with lung cancer	16
1.3.4 Lung cancer therapy.....	17
1.3.5 FGFRs-targeted therapies for lung cancer	17
1.4 Brain Tumors	20
1.4.1 Classification and pathology.....	21
1.4.2 Brain Tumor epidemiology	24
1.4.3 Glioblastoma multiforme (GBM)	26
1.4.4 Molecular alterations associated with GBM.....	27
1.4.5 GBM and FGFRs	28
1.4.6 Therapy of GBM.....	29
1.4.7 FGFRs-targeted therapies for brain tumors and GBM	32
1.6 Metal drugs in cancer therapy	32
1.6.1 Copper complexes.....	35
1.7 Aims of the study	38
CHAPTER TWO, DRUG DESIGN.....	40
2.1 Drug design methods.....	40
2.2 Computer aided drug design of new FGFR inhibitors.....	41
2.3 Design of new FGFRs inhibitors	43
CHAPTER THREE, CHEMICAL SYNTHESIS	53
3.1 Chemical Synthesis.....	53
3.2 Synthesis of the molecules of group (I).....	54
3.3 Synthesis of the molecules of group (II).....	58
3.3.1 Purification of compounds.....	62

3.4 Synthesis of the molecules of group (III)	62
3.4.1 Compounds isolation and purification	70
CHAPTER FOUR, BIOLOGICAL EVALUATION	72
4.1 Screening of new drugs	72
4.2 Structure - Activity Relationship studies (SAR)	75
4.3 Copper (II) complexes	77
4.3.1 DCF-DA ROS formation assay	80
4.3.2 Hypoxic and normoxic environments	82
4.3.3 Apoptosis assay	83
4.3.4 Cell cycle analysis	86
4.3.5 Western Blot	88
4.3.6 Cell migration	92
4.3.7 Spheroids formation (3D)	95
4.3.8 Toxicity test in vivo	99
4.3.9 Summary of the biological activities of V49 and V49-Cu ...	100
4.4 V8 activity	101
4.4.1 Western Blot	103
4.4.2 Real-time PCR	108
4.4.3 Cell cycle	109
4.4.4 Apoptotic assay (Annexin V-FITC /PI)	110
4.4.5 Migration assay	111
4.4.6 Spheroids formation (3D)	112
4.4.7 Live cell (time-laps)	115
4.4.8 Toxicity test in vivo	117
4.4.9 Summary of V8	118
Conclusions and future prospects	120
MATERIALS AND METHODS	122
5.1 Chemistry	122
5.1.1 Synthesis of 2-methyl-7-nitro-4H-3,1-benzoxazin-4-one	122
5.1.2 Synthesis of 2-methyl-7-nitro-3- (pyridine-2-yl) quinazolin-4 (3H) -one	123
5.1.3 Synthesis of 7-amino-2-methyl-3- (pyridine-2-yl) quinazolin-4 (3H) -one	123
5.1.4 Synthesis of methyl 3-iodobenzoate	124
5.1.5 Synthesis of methyl 3-formylbenzoate	124
5.1.6 Synthesis of methyl 3-[(E)-2-(pyridine-2-yl)ethenyl]benzoate .. 125	
5.1.7 Synthesis of 3 - [(E) -2- (pirdin-2-yl) ethenyl] benzoic acid	126
5.1.8 Synthesis of 3-[(E)-2-(pyridine-2-yl)ethenyl]benzoyl chloride . 126	

5.1.9 Synthesis of (E) -N- (2-methyl-4-oxo-3- (pyridine-2-yl) -3,4-dihydroquinazolin-7-yl) -3- (2- (pyridine-2-yl) vinyl) benzamide	127
5.1.10 Synthesis of the (E) -N- (2-methyl-4-oxo-3- (pyridine-2-yl) -3,4-dihydroquinazolin-7-yl) -3- (2- (pyridin-2-) complex II) vinyl benzamide V49 (V49-Cu)	128
5.1.11 Synthesis of 2-methyl-7-nitro-4H-3,1-benzoxazin-4-one	128
5.1.12 Synthesis of 2-methyl-7-nitroquinazolin-4 (3H) -one	128
5.1.13 Synthesis of 7-amino-2-methylquinazolin-4 (3H) -one	129
5.1.14 Chlorination of substituted trans-cinnamic acids 6a-g	130
5.1.15 Synthesis of 2-methyl-7-nitro-4H-3,1-benzoxazin-4-one	130
5.1.16 Synthesis of 2-methyl-7-nitro-3- (pyridine-2-yl) quinazolin-4 (3H) -one	130
5.1.17 Synthesis of 7-amino-2-methyl-3- (pyridine-2-yl) quinazolin-4 (3H) -one	131
5.1.18 Chlorination of substituted trans-cinnamic acids 9a, c, d, e, g..	132
5.1.19 General synthesis of (2E) -3- (4-R-phenyl) -N- [2-methyl-4-oxo-3- (pyridine-2-yl) -3,4-dihydroquinazolin-7-yl] -3 -phenylprop-2-enamides 3a, c, d, e, g	132
5.1.20 General synthesis of the cupric complexes of (2E) -3- (4-R-phenyl) -N- [2methyl-4-oxo-3- (pyridin-2-yl) -3,4-dihydroquinazolin-7-yl] - 3-phenylprop-2-enamides 10a, e	134
5.1.21 General synthesis of (2E) -3- (4-R-phenyl) -N- (2-methyl-4-oxo-3,4-dihydro quinazolin-7-yl) prop-2-enamides 7a-g	135
5.1.22 General synthesis of (2E) -3- (4-R-phenyl) -N- {4-oxo-2 - [(E) -2-phenylethenyl] -3,4-dihydroquinazolin-7-yl} prop-2- 7h-n enamides	136
5.2 Biological	138
5.2.1 Cell colture	138
5.2.2 Cell-viability assay (MTT)	140
5.2.3 Clonogenic assay	140
5.2.4 Western Blotting	141
5.2.5 Cell cycle analysis	143
5.2.6 DCF-DA assay	144
5.2.7 Apoptosis assay	145
5.2.8 RNA-extraction, reverse transcription and RT-PCR	146
5.2.9 Filter migration assay	147
5.2.10 Would healing assay	147
5.2.11 Spheroids formation assay	148
3.3.12 ATP-assay	149
5.2.13 Live cell microscopy	149
5.2.14 Toxicity test in vivo	150

5.2.15 Statistical analyses	152
5.3 Computational	159
5.3.1 ADMET calculations	159
5.3.2 Molecular docking	165
ABBREVIATIONS	169
BIBLIOGRAPHY	174
Curriculum Vitae	206
Acknowledgements	211

DECLARATION

In the course of this thesis, the great majority of experiments was performed by myself in the lab of Prof. Walter Berger at the Institute of Cancer Research, Department of Medicine I, Medical University of Vienna, and in the labs of Prof. Giampaolo Barone and Dr. Maria Valeria Raimondi at the Department of Biological, Chemical and Pharmaceutical Sciences and Technologies, University of Palermo.

Some synthetic steps were performed also in the lab of Prof. Christian Kowol, at the Institute of Inorganic Chemistry of the University of Vienna.

The synthesis of the organic ligands was performed at the University of Palermo, with the contribution of the Master's students Roberto Spatola, Paolo Accardo, Maria Mallia, under the supervision of Dr. Maria Valeria Raimondi.

All *in vivo* experiments performed and herein presented were approved by the Ethics Committee of the Medical University of Vienna and the Austrian Ministry for Science, Research and Economy (Bundesministerium für Wissenschaft, Forschung und Wirtschaft, Verwaltungsbereich Wissenschaft und Forschung, WF/V/3b) (BMWWF-66.009/0081-WF/V/3b/2015 and BMWWF-66.009/0307-WF/V/3b/2015) and were conducted in accordance with the FELASA as well as the ARRIVE guidelines for animal handling and welfare.

SUMMARY

Fibroblast growth factor receptors (FGFRs) constitute a family of tyrosine kinases receptors (RTKs) that exert pivotal physiological functions in human embryonic and adult tissues.

Hyperactivated FGFR signaling drives tumorigenesis in multiple cancer types, including lung and brain cancers. Great effort has been laid on the development of new compounds that specifically target the FGFR axis. However, cancer cell-based and microenvironmental resistance mechanisms against FGFR inhibitors often arise and are currently poorly understood. Furthermore, FGFR-targeted therapy often presents different side effects, e due to the broad biological spectrum of the FGFR signaling axis as well as to its involvement in the homeostasis of many tissue types.

It is well known that metal complexes, e.g. of copper(II), zinc(II), nickel(II) and platinum(II) ions, may exhibit *in vitro* anti-proliferative activity against different human cancer cell lines. Usually, their cytotoxic activity has been related to their binding capabilities toward biological macromolecules.

In this thesis, the recently reported *in vitro* anticancer properties of copper(II) compounds, coupled to the known $\text{Cu}^{2+} \rightleftharpoons \text{Cu}^+$ redox activity, have been exploited to design and synthesize, new compounds as specific inhibitors of FGFR targets.

The ligands were designed on the basis of the crystal structures of FGFR1 and FGFR4 co-crystallized with their known inhibitor Ponatinib. It is worth mentioning that the onset of drug resistance to of Ponatinib has been associated to its low water solubility, which partially hinders cell membrane permeability and release to the cytosol and also increases its accumulations in lipid compartments like adiposomes. For this reason, in the following thesis work, an attempt has been taken to design, synthesize and test new ligands with structural similarity to Ponatinib, as well as their positively charged derivatives, as a consequence of their coordination to cationic metal ions such as Cu^{2+} .

The anti-proliferative activity of the most promising molecules was evaluated *in vitro* and *in vivo*, in order to understand their possible mechanism of action.

In details, 22 ligands and 3 copper(II) complexes have been synthesized as potential drugs against FGFR targets. In particular, the copper complexes were identified to act as pro-drugs that are spontaneously activated by hypoxia.

After a screening of several tumor cell lines to test the activity of the newly synthesized drug candidates, lung cancer and brain tumor turned out to be the most sensitive cancer types. This study shows that the most active drugs are able to inhibit the FGF/FGFR axis efficiently.

LIST OF FIGURES

Figure 1. Estimated number of new cases of cancer in 2019, worldwide, both sexes, all ages. Data from International Agency for Research of Cancer of World Health Organization

Figure 2. Eight essential hallmarks of Cancer.

Figure 3. Summary of the main roles of FGF/FGFR signaling in organ development, metabolism and disease (Yangli Xie et al, FGF/FGFR signaling in health and disease 2020).

Figure 4. FGFR structure and the classical downstream signaling Brady et al, 2013

Figure 5. Globocan 2018 estimated age-standardized incidence and mortality rates (World) in 2018, lung, all ages

Figure 6. World incidence and mortality rates of brain, nervous system tumors in 2018 according to the International Agency for Research on Cancer of World Health Organization.

Figure 7 . World Health Organization. 2018. Estimated age-standardized rates (World) in 2018, SNC cancer, both sexes, all ages

Figure 8. T 2-weighted image of a glioblastoma multiforme. *Aileen Quintana et al, 2017*

Figure 9. FGFR4^{high} subgroup tended to have a shorter overall survival (Gabler et al., 2020). Data are derived from the TCGA GBM dataset and were processed in R2.

Figure 10 . Evolution of the treatment of GMB from 1970 to 2020

Figure 11. Spontaneous reduction, in the tumor hypoxic environment, of the ligand-Cu (II) complex. The proposed mechanism is the release of the free ligand, after the spontaneous reduction of Cu (II) to Cu (I), due to the instability of the L-Cu (I) complex. The ligand can thus inhibit the target protein, the Cu (I) proteasomes.

Figure 12. Aim of the study: design (using computational tools), synthesis, characterization and biological evaluation of new FGFR inhibitors with anticancer properties.

Figure 13. PDB ID:4v04, Ponatinib complexed with FGFR1

Figure 14. PDB ID:4uxq, Ponatinib complexed with FGFR4

Figure 15. Crystal structure of Ponatinib complexed with FGFR4 (PDB ID: 4uxq) and the amino acids involved in the interaction.

Figure 16. Chemical structure of quinazolinone with the possible targets that give it anti-tumor characteristics: the DNA repair system, the epidermal growth factor receptor, thymidylate synthase and PARP-1.

Figure 17. ADMET properties of 22 new molecules and Ponatinib, calculated with QikProp v6.2

Figure 18. Docking with FGFR1 of V8 blue, Ponatinib brown, left hydrophobic surface, right ribbon

Figure 19. Docking with FGFR4 of V8 blue, Ponatinib brown, left hydrophobic surface, right ribbon

Figure 20. Docking with FGFR1 of V49 blue, Ponatinib brown, left hydrophobic surface, right ribbon

Figure 21. Docking with FGFR4 of V49 blue, Ponatinib brown, left hydrophobic surface, right ribbon

Figure 22. Condensation reaction of 7-amino-2-methylquinazolin-4 (3H) -one **4** with chlorides of the **6a-g** substituted trans-cinnamic acids in order to obtain **7a-g** compounds.

Figure 23. Proposed reaction mechanism for the synthesis of the compound **39**

Figure 24. Crystal violet with DMS114 cell line treated for 72 h with V49, V49-Cu, V50, V50-Cu, V55, V55-Cu and CuCl₂ control 1 μM, 10 μM, 25 μM and 50μM

Figure 25. Images with the fluorescence microscope with DMS114 cell line and V49 10 μM, on left in the phase-contrast (PC), in the center is DAPI, excited with ultraviolet light and detected through a blue/cyan filter and on the right picture PC

and DAPI merged. The blue spots are the small crystals of V49 in the cell medium.

Figure 26. Images with the fluorescence microscope with DMS114 cell line and V49 (left) and V49-Cu (right) both 10 μ M. Phase-contrast (PC) and green fluorescence. The crystals of V49 are fluorescent, while with V49-Cu no insoluble crystals are formed. The black things visible with PC and V49-Cu are apoptotic bodies from dead cells.

Figure 27. ROS formation assay, via DCF-DA. In the left flow cytometry elaboration results and in the right the quantification of ROS levels. The assay was performed for three times with V49 and V49-Cu 25 μ M. H₂O₂ was used like a positive control. The cells (DMS114 and K562) were treated for 1 h.

Figure 28. ROS formation assay, via DCF-DA cell free. The drugs V49 and V49-Cu and the positive control (H₂O₂) were incubated with DCF-DA for 1 h. The positive control is DCF-DA alone. The images were taken with the fluorescence microscope.

Figure 29. MTT results in normoxic (21% of oxygen) and hypoxic (1% of oxygen) environments. The experiments were performed with three cell lines: NCI H520, NCIH 1703 and DMS114 for three times in triplicates. The drugs were used in the same standard concentration of 10 μ M. Untreated control are set as 1.

Figure 30. Annexin-V-FITC / PI assay used to understand the mechanism of cell death induced by drugs V49 and V49-Cu 10 μ M, incubated with DMS114 for 24 h, with quantifications of the results on the right panel.

Figure 31. The phases of the cell cycle

Figure 32. Quantitation of cell cycle phases by propidium iodide and flow cytometry elaboration. DMS114 cells were exposed to 10 μ M of V49 and V49-Cu for 24 h. Statistically decrease in S phase and increase in G1 phase can be observed in the image below.

Figure 33. Western blot with NCI H1703 tumor cell line and 24 h exposure of V49 1 μ M, 10 μ M, 25 μ M and 50 μ M. Detected proteins: S6, phospho S6 (p-S6), AKT, phospho AKT (p-AKT), ERK, phospho ERK (p-ERK) and a control of β -actin.

Figure 34. Western blot with NCI H1703 tumor cell line and 24 h exposure of V49-Cu 1 μ M, 5 μ M, 10 μ M, 25 μ M and 50 μ M. Detected proteins and their phosphorylation: S6, phospho S6 (p-S6), AKT, phospho AKT (p-AKT), ERK, phospho ERK (p-ERK), phospho S6 kinase (p-S6K), phospho FGFR (pFGFR), β -catenin, 4EBP1, phospho GSK3B (pGSK3B), PARP and as loading control of β -actin.

Figure 35. Western blot with NCI H1703 and DMS 114 tumor cell lines and 24 h exposure of V49 and V49-Cu 1 μ M and 10 μ M. Detected proteins: phospho FGFR (pFGFR), phospho FRS2 (pFRS2), total FGFR1 (FGFR1), phospho ERK (ERK1/2), phospho AKT (pAKT), phospho S6 (pS6), total S6 (S6) and a control of β -actin.

Figure 36. Filter migration assay. Photographs depicting the amount of U251-MG cells able to migrate to the lower side of the trans-well chambers within 24h in absence (control) or presence of the indicated drugs V49 and V49-Cu at 5 μ M stained with crystal violet. The quantification of migrated cells is shown in the right panel.

Figure 37. Wound healing assay (scratch assay). U251-MG cells were left untreated or treated with 5 μ M of V49 and V49-Cu as indicated. Before treatment, the cell monolayer was wounded by a scratch with a pipette tip. Photomicrographs were taken at 24 and 48 h, with a fluorescent microscope to follow the ability of the cells to close the wound.

Figure 38. Western blot with glioblastoma (U251-MG) cell line with V49 and V49-Cu 1 μ M and 10 μ M, 24 h of exposure. The dose-dependent increase in vimentin is observed for both V49 and V49-Cu and the decrease in E-cadherin.

Figure 39. Spheroids formation assay, first part. In a non-adherent cell culture plates adherent cells can only survive by forming 3D-spheroids, a measure for stem-ness. Daoy cells, a human medulloblastoma model, were treated with V49 and V49-Cu at a concentration of 15 μ M. In the left panel photomicrographs taken at 24, 48 and 72 h under treatment are shown. In the right panel quantification of spheres areas is depicted.

Figure 40. Spheroids formation assay, second part. Retransfer of spheroids to cell culture plates allowing adherence is shown as a parameter to estimate the impact of the investigated drugs on the differentiation plasticity of the cancer cells and their adhesive capacity.

Figure 41. Spheroids formation assay, part three. Crystal violet stained wells depicting re-adhere spheroids (left) and quantification of integrated density (right) of drug-free controls, as well as V49 and V49-Cu 5 μ M, 10 μ M and 15 μ M-exposed cells.

Figure 42. Body weight (g) of four mice treated with 5 mg/kg and 10 mg/kg of V49 (left), and other four mice treated with 5 mg/kg and 10 mg/kg of V49-Cu (right).

Figure 43. Cell viability assay results, 72 h of co-incubation of V8 1 μ M, 5 μ M, 10 μ M, 15 μ M, 20 μ M and 25 μ M with DMS114 tumor cell line. IC₅₀ calculated from three independent experiments: 3.5 μ M.

Figure 44. Cell viability assay results, 72 h of co-incubation of V8 1 μ M, 5 μ M, 10 μ M, 15 μ M, 20 μ M and 25 μ M with NCI H1703 tumor cell line. IC₅₀ calculated from three independent experiments: 9.03 μ M.

Figure 45. Cell viability assay results, 72 h of co-incubation of V8 1 μ M, 5 μ M, 10 μ M, 15 μ M, 20 μ M and 25 μ M with U251-MG tumor cell line. IC₅₀ calculated from three independent experiments: 4.5 μ M.

Figure 46. Cell viability assay results, 72 h of co-incubation of V8 1 μ M, 5 μ M, 10 μ M, 15 μ M, 20 μ M and 25 μ M with BTL 1376/26 tumor cell line. IC₅₀ calculated from three independent experiments: 6.03 μ M.

Figure 47. Western blots (separated experiment) with U251-MG (Gly), U251-MG (GFP), UMUC14, DMS114, RKO wt and A431 tumor cell lines, 24 h of treatment with V8.

Figure 48. Western blots with NCI H1703 and NCI H520 (FGFR over-expressing tumor cell lines), 24 h of treatment with V8 1 μ M and 10 μ M. Proteins detected: total FGFR4, total FGFR1, phospo S6 (S6), total AKT, phospho AKT (pAKT) and β -actin control.

Figure 49. Western blots with DMS114, 24 h of treatment with V8 1 μ M, 2 μ M, 3 μ M, 4 μ M and 5 μ M.

Figure 50. Western blots with NCI H1703 and NCI H520, 24 h of treatment with V8 1 μ M and 10 μ M.

Figure 51. WB with A431 tumor cell line over-expressing EGFR. The experiment was performed with and without EGF stimulation for 10 min, with starved cells for 24 h and treated with V8 1 μ M and 10 μ M for 24 h with starved cells (Ctrl St.) and cells in normal conditions (Ctrl)

Figure 52. Ubiquitination processes. The first enzyme, E1, catalyzes ubiquitin “activation”, activated ubiquitin is transferred from E1 to a cysteinyl residue in a second protein called E2. Transfer of ubiquitin to substrate proteins typically requires a third activity called E3. The ubiquitinated proteins are recognized by the proteasomes that provide for their degradation.

Figure 53 . mRNA expression values of *FGFR1* (left) and *FGFR4* (right) are shown in response to V6 at two different concentrations and time points as indicated. Data are presented as mean +/- SD from triplicates. Statistical significance was tested by Student’s t-tests or 2-way ANOVA. *=p<0.05, **=p<0.01, ***=p<0.0001

Figure 54. Cell cycle analysis with DMS114 treated for 24 h with V8 10 μ M. The experiment was repeated three times. Statistically insignificant results were obtained.

Figure 55. Annexin-V-FITC / PI assay used to understand the mechanism of cell death induced by V8 incubated with DMS114 for 24 h, with quantifications of the results on the below panel.

Figure 56. Filter migration assay. The images of migration abilities in U251-MG cells in trans-well treated with V8 1 μ M and 2.5 μ M and the quantification of migrated cells in the right panel.

Figure 57. Wound healing assay or scratch assay. The cells were treated at time 0 with 2.5 μ M of V8 and the cells were scratched. The pictures were tacked at 24 h, 30 h and 48 h, with a fluorescent microscope.

Figure 58. Western blot with glioblastoma (U251-MG) cell line with V8 1 μ M, 2 μ M, 3 μ M, 4 μ M and 5 μ M, 24 h of exposure. The dose-dependent increase in vimentin and the decrease in E-cadherin can be observed.

Figure 59. Spheroids formation assay, first part. In non-adherent well-plate. Daoy cell line have been treated with V8 at different concentrations: 1 μ M, 5 μ M 10 μ M, 25 μ M and 50 μ M. The pictures were tacked after 24 h (**A**), 48 h (**B**) and 72 h (**C**). The spheroid surface was quantified (graphic below).

Figure 60. Spheroids formation assay, second part. In adherent well-plate. Estimation of the adhesive capacity of cells after 48 h.

Figure 61. Spheroids formation assay, part three. Crystal violet (left) and quantification of integrated density (below) of control and V8 at 1 μ M, 5 μ M, 10 μ M, 25 μ M and 50 μ M.

Figure 62. Live cell experiment. U251-MG GFP cells were treated with 3.5 μ M of V8 and pictures were taken every 15 minutes for each samples control (left) and V8 (right) for 64 h.

Figure 63. Body weight (g) of four mice treated with 5 mg/kg and 10 mg/kg of V8.

Figure 64. Mice treated with 5 mg/kg of V8, with “peritoneal loose bodies” (white formations).

Figure 65. Two tautomers **3a** and **3b** obtained obtained in the synthesis of Synthesis of 2-methyl-7-nitroquinazolin-4 (3H) -one **3**

LIST OF TABLES

Table 1. Classification of FGF family members.

Table 2. Brain tumors classification according World Health Organization 2020

Table 3. Chemical formula, molecular weight and R1, R2, R3 substituents of 25 synthesized molecules

Table 4. Docking scores, expressed in Kcal/mol, of 22 compounds against FGFR1 and FGFR4

Table 5. Cell lines and the corresponding tumor type used in all experiments

Table 6. IC₅₀ values of 22 synthesized molecules against DMS114, NCI-H1703, NCI-H520, U251-MG-Gly, U251-MG-GFP and PC9. Only some cell lines tested are shown in the table.

Table 7. IC₅₀ values of V51, V10, V8, V56, V33, V28, V49 against NCI-H1703 (NSCLC tumor cell line).

Table 8. IC₅₀ values of V8, V27, V11, V28, V51, V49, V56, V55 against DMS114 (SCLC tumor cell line).

Table 9. IC₅₀ values of V49, V49-Cu, V50, V50-Cu, V55, V55-Cu with DMS114 tumor cell line and 72 h of treatment.

Table 10. Cell viability assay results, 72 h of co-incubation of V8 1 μM, 5 μM, 10 μM, 15 μM, 20 μM and 25 μM. IC₅₀ calculated from three independent experiments.

Table 11. Taqman probes used for qRT-PCR (Thermo Fisher Scientific)

Table 12. Predicted ADMET properties, description and recommended values based on 95% of known drugs obtained with the software QikProp v6.2

Table 13. Grid boxes calculated for FGFR1 and FGFR4 based on Ponatinib coordinates at the receptors binding site.

CHAPTER ONE, INTRODUCTION

1.1 Cancer as a central challenge of modern medicine

According to data from the World Health Organization (WHO), cancer is the second leading cause of death globally, after cardiovascular diseases. It is considered responsible for about 9.6 million deaths in 2018, with a total of 18.1 million new cases of cancer estimated, of which 4.2 million occurred in Europe (Figure 1). Globally, about 1 in 6 deaths is due to cancer.

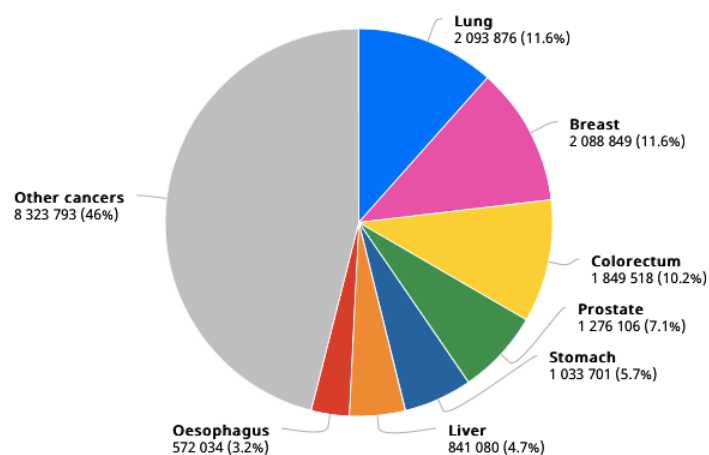


Figure 1. Estimated number of new cases of cancer in 2019, worldwide, both sexes, all ages. Data from International Agency for Research of Cancer of World Health Organization

The most common cancer types are: lung (2.09 million cases), breast (2.09 million cases), colorectal (1.80 million cases), prostate (1.28 million cases), skin (non-melanoma) (1.04 million cases) and stomach (1.03 million cases) cancers.

The most common causes of cancer death are due to cancers of the following organs: lung (1.76 million deaths), colorect (862 000 deaths), stomach (783 000 deaths), liver (782 000 deaths) and breast (627 000 deaths) (GLOBOCAN 2020).

Not only this constitutes a dramatic humanitarian burden, but the significant economic impact is still increasing, making cancer one of the critical issues causing health issue-based economic and financial trouble in the world today (World Health Organization, 2020).

There are more than one hundred distinct types of cancer known, which dramatically differ in behavior and response to different treatments (World Health Organization, 2020).

Cancer is characterized by the gradual loss of the regulatory mechanisms, that normally dominate every single cell to ensure the correct functionality of the multicellular organism within which it resides and survives (Chaffer and Weibner, 2015). In the multistep process of cancer development, sustained proliferation is observed which is constituted by the hyperactivation of mitogenic signaling pathways, such as growth factor receptors or downstream effectors, and the disruption of negative feedback control mechanisms (Lemmon and Schlessinger, 2010, Cheng J. et al., 2008, Wertz and Dixit, 2010). The acquired abilities responsible for tumor formation and its invasiveness can be summarized in eight essential hallmarks of cancer (Hanahan D. and Weinberg R.A., 2011): evading growth suppressors; enabling replicative immortality; resisting cell death; sustaining proliferative signaling; inducing angiogenesis; activating invasion and metastasis; reprogramming of energy metabolism; evading immune destruction (Figure 2).

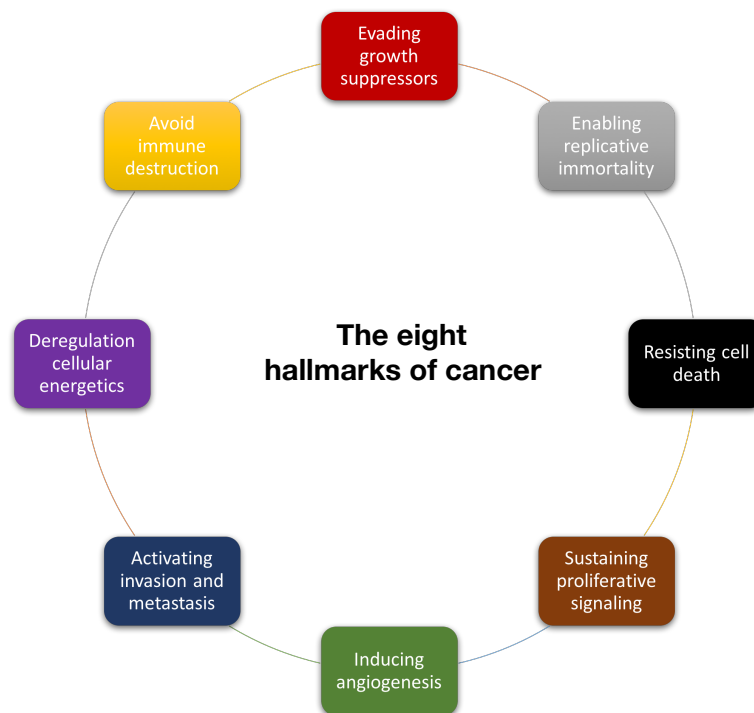


Figure 2. Eight essential hallmarks of Cancer.

Growth suppression is avoided by turning off negative regulatory factors that under normal conditions integrate internal or external stimuli to arrest cell cycle progression and induce apoptosis (Hanahan D. and Weinberg R.A., 2011, Burkhart and Sage, 2008). Malignant cells, in fact, become resistant to cell death by interrupting the cascades of intrinsic and extrinsic apoptosis. Furthermore, neoangiogenesis – the processes of vascularization of the malignant tissue by sprouting of existing vessels- allow for a greater supply of nutrients and oxygen (Baeriswyl and Christofori, 2009). The spread of cancer cells through the human body is allowed by alterations in cell shape and cell-cell adhesion, as well as by attachment to the extracellular matrix (ECM), which allows cells to invade other tissues and spread to various districts of the body. For epithelial cells, this program is called epithelial-mesenchymal transition (EMT) (Hanahan D. and Weinberg R.A., 2011).

The multiphase process of the metastasis includes the invasion of local tissues, intravasation into the blood and lymphatic vessels, the transit through the lymphatic or hematogenous system, as well as the extravasation and colonization of even distant tissues (Lambert et al., 2017, Talmadge and Fidler, 2010).

The chronically elevated expression of the different growth factor family members, including besides vascular endothelial growth factor (VEGF) also fibroblast growth factors (FGF), drives tumor neo-angiogenesis.

A hallmark of tumorigenic progression is genome instability characterized by random mutations and genome rearrangements (Hanahan D. and Weinberg R.A., 2011).

Another important hallmark is the evasion of immune destruction by cancer cells (Englinger B. et al, 2019). The correlation between alterations of the immune system and cancer regression or progression is not new, it was even known more than 150 years ago. In fact, it had already been noted that some tumors regressed spontaneously, when there was a general improvement in health (Messerschmidt JL et al.,2016). However, reported cases of spontaneous cancer regressions are rare, most commonly seen in neuroblastoma, lymphoma, leukemia, malignant

melanoma and renal cell carcinoma (Papac RJ. 1998). A possible hypothesis as to why these tumors can suddenly regrow and / or disappear is that the immune system can be activated, in an unexpected way, leading to the recognition of some altered proteins, inactive or poorly expressed under normal conditions, and to T-cell-mediated destruction of cancer cells (Messerschmidt JL et al.,2016). The reported cases of spontaneous regression open a new scenario in research and development of cancer treatments and can broaden the knowledge of the physio / pathology of the immune system itself (Papac RJ. 1996).

Tumors can be classified in different ways: by tissue, organ and system; by specific type; by level, according to WHO classifications; by spread, according to the Tumor Node Metastasis (TNM) system (Carbone A.,2020).

In the classifications of tumors organized by tissue or organ of origin, hematological tumors are distinguished from solid tumors. Hematological tumors originating from myeloid or lymphoid hematopoietic cells. Solid tumors are further classified as: 1) carcinomas, if they are of epithelial origin; 2) sarcomas, if they arise from connective tissue cells, such as blood vessels, muscles, joints, bones, nerves (Carbone A.,2020, Weinberg, 2014a).

Carcinomas are the most frequent form of cancer and the predominantly affected organs are prostate, lungs, breast, skin, gastrointestinal tract, larynx, kidney etc. Carcinomas are further distinguished by their origin from glandular or squamous cells, resulting in adenocarcinoma or squamous cell carcinoma, respectively (Weinberg, 2014a).

The classic therapeutic strategies of cancer are represented by surgery, chemotherapy and radiotherapy. New therapeutic approaches can be classified into immunotherapy (Stanculeanu DL, et al., 2016), hormone therapy (Burstein HJ, et al., 2019) and targeted therapy (Yan L, Rosen N, Arteaga C. 2011).

There are two main approaches for immunotherapy. One strategy is activating immunotherapy, which involves immunization against tumors via preventive or curative vaccination. The other approach is passive immunotherapy, which involves the administration of antibodies, which bind specifically to neo-antigens

present on the abnormal cell surface and by recruiting phagocytic or killer cells leading to the destruction of cancer cells (Zhang, H. and J. Chen, 2018). The novel therapy with immune checkpoint inhibitors, awarded by the Noble prize in 2018, is based on the antibody-mediated blockade of inhibitory immune checkpoint molecules (e.g. PD1/PD-L1 or CTLA4) either on regulatory immune cells or the cancer cells themselves (Zang X., 2018).

Hormone therapy is an approach primarily for steroid hormone-driven cancers, breast and prostate cancer. In breast cancer there is an over-expression of estrogen hormones, while in prostate cancer might grow in a androgen (testosterone)-dependent manner (Risbridger, G.P., et al, 2010).

Usually hormone therapy is used as an adjuvant therapy, it reduces the risk of cancer recurrence (NCI, 2020). Target-therapy is a precision medicinal approach (Health, N.C.I.a.t.N.I.o.2019). Unlike classic chemotherapeutics, which kill all rapidly dividing cells, targeted drugs act on proteins present only on cancer cells or on growth and cell survival promoters which are hyper-activated (NCI, 2020). Today's oncology landscape shows a wide range of new tools for early cancer diagnosis and treatment, resulting in lower mortality rates. However, people are still dying from cancer. For this reason, a strong intellectual investment is still needed to better understand the factors that drive tumorigenesis and mediate treatment evasion.

1.2 Fibroblast growth factor receptors

Members of the fibroblast growth factor (FGF) family act on a broad-spectrum of biological processes regulating embryonic development, metabolism and tissue homeostasis. In the course of evolution, the FGF ancestor has undergone several changes expanding into several members, thus acquiring different structural elements that also allow functional divergences (Li X, 2019).

FGFs are pleiotropic mitogens that are involved in the regulation of important cellular functions, such as migration, proliferation, differentiation, survival and neuronal signal transduction (**Figure 3**) (Ornitz DM and Itoh, 2001).

Anomalies of the signaling axis of the FGF receptor is observed in various diseases, such as congenital deformity (craniosynostosis) and dwarfism (achondroplasia), chronic kidney failure, insulin resistant diabetes, obesity and different cancers (Yangli Xie et al, 2020).

Although it was clear that the FGF / FGFR axis was being arrogated by malignant cells to drive tumorigenesis, it was for a long time not an extremely active research area of pharmaceutical science. This was likely due to the wide diversity of FGF ligands and their receptors, the complexity of ligand / receptor signaling,

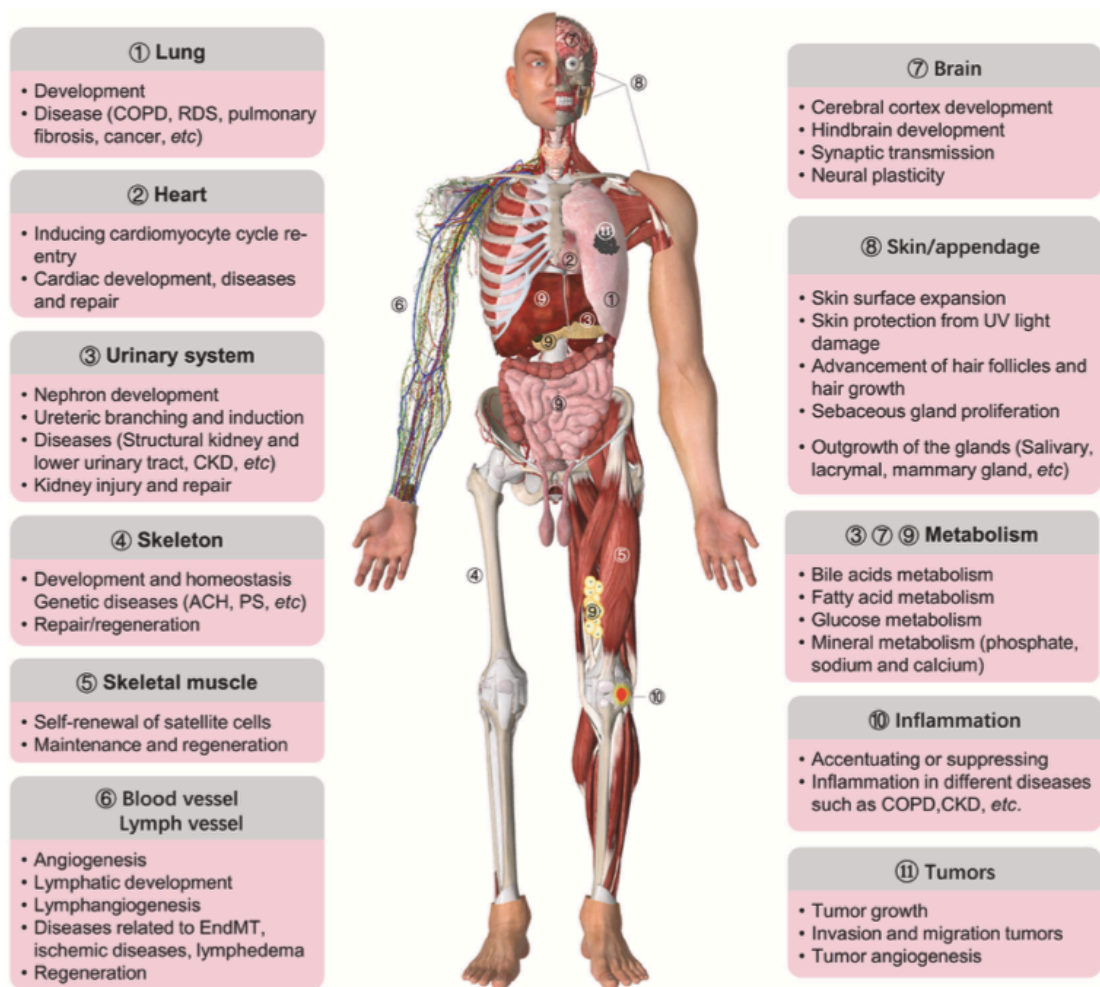


Figure 3. Summary of the main roles of FGF/FGFR signaling in organ development, metabolism and disease (Yangli Xie et al, FGF/FGFR signaling in health and disease 2020).

and the involvement of multiple downstream signaling pathways (Li X. et al., 2016, Feng et al., 2015).

More recent *in vitro* studies have suggested partial functional redundancy, attracting more research into this area.

As it is well known, one of the major clinical problems in cancer treatment is resistance to oncological therapy. Different studies have identified a critical role played by FGF signaling also in resistance to oncotherapy (Xie Y et al., 2020; Goyal L et al., 2020).

Furthermore, gene amplifications, point mutations and chromosomal translocations of the various FGFRs, which result in receptor overexpression and hyperactivation, have been identified in a wide range of cancer types (Touat M., et al, 2015).

Therefore, the FGF family represents a promising target for anticancer therapy.

The biological functions of FGFR signaling as well as its implications in the development and treatment of cancer will be discussed in the following chapters.

1.2.1 The biology of FGFs and FGFRs

The FGF family is among the largest and most diverse groups of growth factors in vertebrates. So far 22 FGF ligands have been identified, in mice and humans. The 18 FGFs identified in mammals are divided into 6 subfamilies, which in turn include 5 paracrine subfamilies and 1 endocrine subfamily. The paracrine subfamilies include the subfamilies FGF1, FGF4, FGF7, FGF8 and FGF9. Endocrine signals are attributable to the FGF19 subfamily (**Table 1**) (Ornitz, D. M. & Itoh, 2001).

	Subfamily	Members
Paracrine	FGF1	FGF1, FGF2
	FGF4	FGF4, FGF5, FGF6
	FGF7	FGF3, FGF7, FGF10, FGF22
	FGF8	FGF8, FGF17, FGF18
	FGF9	FGF9, FGF16, FGF20
Endocrine	FGF19	FGF19, FGF21, FGF23

Table 1. Classification of FGF family members.

FGFs exert their effects by binding and activating tyrosine kinase receptors encoded

by four genes (FGFR1, FGFR2, FGFR3 and FGFR4) and FGFR5 (known as FGFR1L), a FGFR without intracellular domain (Wiedemann, M. & Trueb, 2000).

FGFRs are transmembrane proteins. As classic tyrosine kinase (TK) receptors, they consist of three basic parts: extracellular domain, transmembrane domain and the

intracellular tyrosine kinase domain (Turner and Grose, 2010). The extracellular part, which is the ligand-binding region, consists of three immunoglobulin-like

domains (D1-D3). FGFs interact with the D2 and D3 domains and the interactions with D3 appear to be responsible for the specificity of the binding (Powers et al., 2000). Furthermore, FGFR5, variably referred to as FGFR-like 1 (FGFRL1), does not contain a tyrosine kinase domain and potentially acts as a decoy receptor (Wiedemann and Trueb, 2000). The real function of FGFR5 is under investigation.

The kinase domains of FGFR1, FGFR2, FGFR3 and FGFR4 show sequence homology of 80% (Li X. et al., 2016).

The transmembrane domain (TMD) maintains the receptors in the cell membrane and facilitates their dimerization. Binding of FGF induces dimerization of FGFR (**Figure 4**), leading to autophosphorylation of the intracellular tyrosine kinase domain (Farrell, B. & Breeze, 2018).

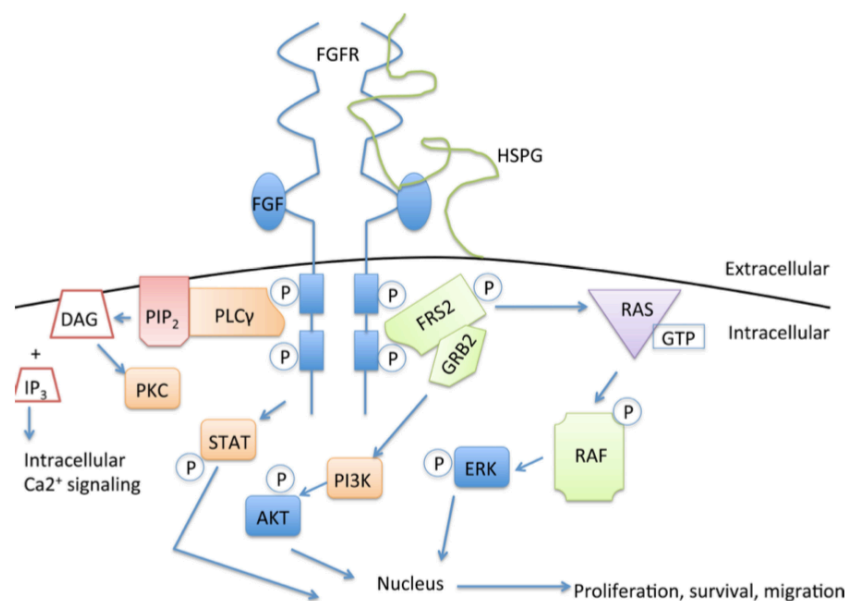


Figure 4. FGFR structure and the classical downstream signaling Brady et al, 2013.

Following dimerization and phosphorylation, adapter molecules, such as substrate FGFR 2 (FRS2), can in turn be phosphorylated and activated, subsequently transmitting the FGFR activation signal through a variety of downstream molecules to the cell nucleus (Nicholas Brady et al, 2013). This signaling cascade allows the activation of cellular processes including proliferation, survival,

migration and angiogenesis. Downstream of FGFR, a cascade of intracellular events and the following pathways are activated: Ras-Raf-MAPK, PI3-AKT, PLC γ and Jak-STAT (Li X. et al., 2016 and Babina, I.S. and N.C, 2017).

1.2.2 FGFRs and cancer

FGFR signaling is known to be altered in malignant cells and to contribute to various aspects of tumorigenesis (Tanner and Grose, 2016, Touat et al., 2015). A study conducted on more than 4800 different tumor samples shows that 7.1% of cancers have genetic alterations of the FGF / FGFR signaling axis (Porta et al., 2017). Among them, FGFR1 is the most affected, accounting for 49% of all FGFR abnormalities. This is followed by FGFR3, FGFR2, and FGFR4, which account for 23%, 19%, and 7% of FGFR-related changes in malignant tissues, respectively (Harding and Nechiporuk, 2012, Helsten et al., 2016). Interestingly, alterations in this signaling family are more common in women than men (17.6% versus 10%, respectively). Therefore, deregulations in the FGF / FGFR circuits are very important in cancer (Porta et al., 2017, Helsten et al., 2016).

Under pathological conditions, the enhancement of the FGF / FGFR axis is achieved by mutations, receptor amplification and chromosomal translocations. Furthermore, autocrine (from the tumor cell itself) and paracrine (from the stromal cells) signaling appear to play an important role (Babina, I.S. and N.C. 2017 and Turner, N. and Grose R., 2010). Genetic amplification accounts for approximately 66% of FGFR aberrations, especially for the FGFR1 gene (Helsten et al., 2016, Malchers et al., 2014).

Compared to mutation and translocation, amplification of the FGFR gene appears to be the most associated with poor prognosis, with low survival (Seo et al., 2014, Chang et al., 2014, Cihoric et al., 2014). Amplification of the FGFR1 and FGFR2 gene is commonly found in lung (16.9%), breast (13.4%), urethelium (7%), gastric (5.1%) and ovarial cancer (5%) (Weiss et al., 2010, Peifer et al., 2012, Chang J, Liu X, et al.,2014).

Instead, genetic amplifications of FGFR3 and FGFR4 appear to be comparable rare (Babina and Turner, 2017).

Somatic mutations in receptor genes account for 26% of FGFR alterations and are observed in various tumor types (Porta et al., 2017). Point mutations are common for FGFR2 (10-12% of the endometrium, 4% of the NSCLC) (Gao et al., 2013) and FGFR3 (75% in urothelial cancer) (Babina and Turner, 2017). For FGFR4, five mutations localized in the tyrosine kinase domain have been described (Sun X. et al., 2015). In a small percentage (8%) fusion events also occur (Wu Y.M. et al., 2013). These mainly concern FGFR2 and FGFR3 (Tanner and Grose, 2016). These mutations lead to a constitutive activation of the receptor (Wu Y.M. et al., 2013, Capelletti et al., 2014) and as a consequence the events already described in the previous chapters.

1.2.3 Therapeutic targeting of oncogenic FGFRs alterations

The increasing knowledge of the FGF / FGFR signaling axis and its identification as a key factor in the development and progression of various tumor types has led to great efforts in pharmaceutical science to develop novel targeted therapies (Hallinan et al., 2016, Greulich and Pollock, 2011).

Small molecule kinase inhibitors are, so far, the most widely used therapeutic approach for the inhibition of FGFR signaling (Touat M., et al., 2015). Other therapeutic modalities, such as RNA aptamers (Jurek PM, et al., 2017), antibody-based agents and FGF decoy receptors that target interactions between FGF and FGFR, small molecules that allosterically target the extracellular region of FGFR and a small molecule designed to induce post-translational changes of FGFR (Masaru Katoh, 2019). Experimental approaches are emerging such as monoclonal antibodies against FGFR.

1.2.4 Classification of FGFRs inhibitors

FGFR inhibitors can be classified in two different ways: (I) based on their target specificity; (II) based on their kinetic dissociation capacity.

Based on the classification according to specific targets, they can be distinguished into FGFR1/2/3 inhibitors (AZD4547, BGJ398, Debio-1347, dovitinib), FGFR4 inhibitors (BLU9931), pan-FGFR inhibitors (FIIN-2, JNJ-42756493, LY2874455, ponatinib, PRN1371) or multi-kinase FGFR inhibitors (nintedanib, pazopanib) (Cheng, W., et al.,2016).

Based on the dissociation kinetic these compounds are distinguished into reversible and irreversible inhibitors. Irreversible inhibitors (BLU9931, FIIN-2, H3B-6527, PRN1371) covalently bind specific cysteines or carbon atoms of the receptor site while reversible ones (AZD4547, BGJ398, BLU9931, Debio-1347, dovitinib, FIIN-2, JNJ-42756493, LY2874455, Ponatinib, BGJ398) bind to the ATP-binding pocket (Roskoski, R. Jr.,2018). Reversible inhibitors are further classified into type I (AZD4547), which bind with the ATP binding pockets of FGFR in the active DFG-in configuration (Gavine, P. R. et al.2014); type II (ponatinib), which bind with the ATP binding pockets of FGFR in the inactive DFG-out configuration (Tucker, J. A. et al. 2009).

The spectrum of FGFR inhibitors is greatly expanding thanks to the discovery of new compounds using chemical library screening and molecular modeling studies with computational prediction approaches (Cheng, W., et al.,2017).

Despite the efforts made in recent years in the search for new FGFR inhibitors, clinical studies indicate low response rates due to intrinsic resistance to FGFR-targeted therapies (Camidge, DR, Pao, W. & Sequist, LV 2016).

Therefore, a lot of scientific research is needed to overcome these problems.

1.3 Lung cancer

Worldwide, lung cancer is the most common cause of cancer-related death in men and second most common in women after breast cancer (World Cancer Report 2014). This cancer type is also the most preventable one, in fact is strongly associated with environmental and life-style factors, tobacco smoking being strongly linked to the epidemic of lung cancer (Brody, H., 2014; Giangreco, A., K.R. Groot, and S.M. 2007). The increase in incidence, so dramatically, is mainly attributable to the increase in cigarette smoking (Faraz Siddiqui and Abdul H. Siddiqui, 2020).

Lung cancer also occurs among non-smokers and this is attributable to air pollution and genetic factors are also powerful triggers (Brody, H., et al.,2014).

1.3.1 Classification and pathology

Lung cancer is classified according to the World Health Organization (WHO) and the International Association for the Study of Lung Cancer (IASLC) "2015 Classification of Tumors of the Lung, Pleura and Thymus" in (Travis et al., 2015, Bunn et al., 2016) non-small cell lung cancer (NSCLC) and small cell lung cancer (SCLC) (Chen, Z., et al.,2014; Lehman, JM, ME Gwin and P .P. Massion, 2017). SCLC comprises about 10% -15% of all lung cancers, it is the most aggressive and rapidly growing type. SCLC is strongly related to cigarette smoking. SCLCs rapidly metastasize to many distant sites within the body and most often the diagnosis occurs when metastases are already extensive (Kumar V, Abbas AK, Aster JC 2013).

NSCLC is the most common, accounting for about 85% of all lung cancers. NSCLC has three main types designated by the type of cells found in the tumor.

They are:

Adenocarcinomas are the most common type of NSCLC and constitute up to 40% of lung cancer cases.

Squamous cell carcinomas were previously more common than adenocarcinomas; today they account for about 25-30% of all lung cancer cases.

Large cell carcinomas, sometimes referred to as undifferentiated carcinomas, are the least common type of NSCLC, accounting for 10% -15% of all lung cancers (WHO, 2015).

NSCLC is sometimes treated with surgery, while SCLC usually responds better to chemotherapy and radiotherapy (Chapman S, et al., 2014).

1.3.2 Lung cancer epidemiology

Worldwide, lung cancer continues to be the leading cause of cancer-related death in both men and in recent years also in women (Fitzmaurice C, Dicker D, Pain A, et al. 2015).

A total of 2.09 million new cases of lung cancer and 1.76 million deaths in 2018 of both sexes worldwide, all ages were estimated by the International Agency for Research on Cancer (Globocan 2020).

Lung cancer incidence and mortality are closely linked to cigarette smoking patterns, but also to pollution and genetic factors (Barta JA, Powell CA, Wisnivesky JP, 2019). According to epidemiological studies, the incidence and geographic patterns, different for men and women, mainly reflect historical, cultural and regional differences in tobacco smoking (Ferlay J, Soerjomataram I, Ervik M, et al. 2013). Today, the number of women smokers start to exceeds that of men. There is a higher rate of lung cancer deaths among women in industrialized countries than in developing countries. Among women in developing countries, lung cancer deaths are lower than those from breast cancer (**Figure 5**) (Torre LA, et al., 2015).

In recent decades, lung cancer rates in women have been increasing around the world (Youlden DR, et al., 2008). For example, the incidence of female lung cancer in Europe increased for most of the 21st century and in 2017 and surpassed breast cancer death rates, 14.6 lung cancer deaths per 100,000 compared to 14 out of 100,000 for breast cancer (Malvezzi M, Carioli G, Bertuccio P, et al. 2017).

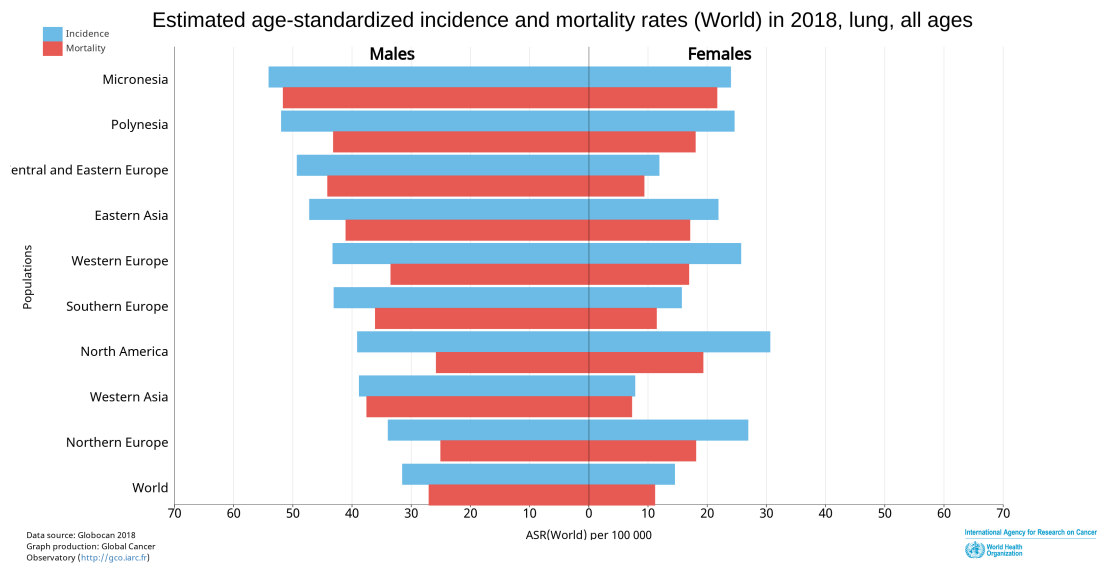


Figure 5. Globocan 2018 estimated age-standardized incidence and mortality rates (World) in 2018, lung, all ages.

One hypothesis is that women may be genetically more susceptible to the development of lung cancer (Kligerman S, White C, 2011). Indeed, there is a higher rate of lung cancer in non-smoking women than in non-smoking men (Patel JD, 2005). Accordingly, the estrogen receptor (ER) α , which is not present in normal lung tissue, is overexpressed in lung adenocarcinoma of women (Kligerman S, White C, 2011). However, more studies are needed to clarify the increased susceptibility of women to lung cancer.

Known risk factors for lung cancer include behavioral, environmental, and genetic parameters, all of which play a role in tumor development (De Groot PM et al., 2018). Additional factors contributing to the development of lung cancer are passive smoking, radiation therapy and exposure to asbestos or radon gas (Chen Z. et al., 2014), and prolonged exposure to various chemicals used in industry or laboratories. Lung damage caused by inflammation and infections are also implicated in lung cancer carcinogenesis (De Groot PM et al., 2018).

Furthermore, air pollution resulting from increased human mobility and industrial emissions is increasingly recognized as an additional risk factor (Raaschou-Nielsen et al., 2013, Loomis et al., 2013).

There is also a genetic susceptibility to pulmonary malignancy. Increases the risk of developing lung cancer 1.7 times if there is a family history (Lissowska J, Foretova L, Dabek J, et al. 2010).

Worldwide, it is estimated that 25% of lung cancer patients have never smoked (Pomerleau et al., 2004, Tsao et al., 2016, Okazaki I, Ishikawa S, Ando W, et al. 2016).

Despite extensive prevention and screening efforts, the overall lung cancer prognosis remains poor with 5-10% 5-year survival (Chen Z. et al., 2014, Sabari et al., 2017).

1.3.3 Molecular alterations associated with lung cancer

Recent advances in genomics, epigenomics and proteomics, allow the genome-wide analysis of molecular alterations that play a key role in the pathogenesis and progression of cancers, including lung cancer (Katarzyna Wadowska et al., 2020).

These molecular alterations discovered are used directly in precision medicine based approaches and translated into clinical lung cancer treatment.

Compared to many other types of cancer, lung cancer generally shows a high presence of mutations.

Eighteen significant genetic mutations have been identified in adenocarcinoma: TP53, KRAS, KEAP1, STK11, EGFR, NF1, BRAF, SETD2, RBM10, MGA, MET, ARID1A, PIK3CA, SMARCA4, RB1, CDKN2A, U2AF1 and RIT1.

In SCC 11 genetic mutations: TP53, CDKN2A, PTEN, PIK3CA, KEAP1, MLL2, HLA-A, NFE2L2, NOTCH1, RB1 and PDYN (Kentaro Inamura, 2017).

Several mutations, gene amplifications, and chromosomal translocations of FGFR have been found in both SCLC and NSCLC (ArpitaDesai and Alex A.Adjei, 2016).

For highly lethal SCLC, amplification of FGFR1 is observed in 6% of cases (Pietanza, MC and M. Ladanyi, 2012). SOX2 amplification and RLF-MYCL1 fusion were also detected in SCLC (George J, et al., 2015).

1.3.4 Lung cancer therapy

Much research progress has been made in recent years, both in lung cancer screening and personalized therapy (Fred R Hirsch et al, 2017).

Standard treatment of SCLC and NSCLC involves surgical resection and in the early stage of the disease platinum-based chemotherapy (Chen, Z., et al.,2014). For SCLC, therapy with cisplatin or carboplatin and etoposide is the standard therapy, at least for the early stages of the disease (Sabari, JK, et al., 2017). Indeed, a good response is almost always observed at the beginning of therapy, but SCLC rapidly becomes resistant to therapy, leading to high relapse rates (Lehman, JM, ME Gwin and PP Massion, 2017).

The advanced stages (III) of SCLC and NSCLC represent a heterogeneous disease, for this reason they are very difficult to treat with classic or standardized therapies, in fact surgery, chemotherapy and radiotherapy are followed by targeted agents or inhibitors of the immune checkpoint (Ruiz-Ceja and Chirino, 2017).

However, in recent years immune checkpoint inhibitory antibodies have developed into the first line therapy of NSCLC combined with platinum-based chemotherapeutic approaches (Onoi K. et al., 2020).

1.3.5 FGFRs-targeted therapies for lung cancer

Identification of FGFR1 as oncogenic driver in a subset of lung cancer patients has initiated extensive efforts to target this RTK by pharmacological inhibitors (Hashemi-Sadraei and Hanna, 2017, Tiseo et al., 2015, Desai and Adjei, 2016).

There are different selective FGFR inhibitors and broader multikinase inhibitors also targeting FGFR members in clinical trials for lung cancer treatment.

AZD4547 is a selective inhibitor of FGFR1, FGFR2, and FGFR3 tyrosine kinases that has shown potent antitumor activity (P.K. Paik, R. Shen, D. Ferry, et al., 2014).

AZD4547 is used with or without Docetaxel in treating patients with recurrent NSCLC (Phase 1,2; trial identifier: NCT01824901), in a second-line therapy in treating patients with recurrent stage IIIB–IV SCLC (Phase 2,3; trial identifier: NCT02154490); in patients with FGFR1 or FGFR2-amplified gastric cancer, esophageal cancer, breast cancer, and squamous cell carcinoma of the lung (Phase 2, trial identifier: NCT01795768). Other selective FGFR inhibitors in clinical trials are: BGJ398 (FGFR1-3), LY2874455(FGFR1-4), JNJ-42756493 (FGFR1-4), FP-1039 (FGF1, FGF2, FGF4).

(Arpita Desai and Alex A.Adjei, 2016).

FGFR multikinase inhibitors are non-selective and inhibit the tyrosine kinase domains present in a wider range of receptors. They are predominantly VEGFR inhibitors and are also capable of inhibiting mostly with a lower potency FGFR family members (Brooks A.N., et al., 2012).

The following multikinase inhibitors targeting FGFR are currently in clinical trials: Brivanib a VEGFR, FGFR inhibitor (phase 1; trial identifier: NCT00798252), Dovitinib a FGFR, PDGFR, VEGFR, FLT3, C-KIT inhibitor (phase 2, trial identifier: NCT01831726; phase 2, trial identifier: NCT01676714; phase 1, trial identifier: NCT01700270, phase 1, trial identifier: NCT01596647; phase 1, trial identifier: NCT01421004, phase 2, trial identifier: NCT01861197), Lenvatinib a FGFR, PDGFR, VEGFR inhibitor (Phase:1, trial identifier: NCT00121719; phase 2 , trial identifier: NCT01529112; phase 2 , trial identifier: NCT01877083), Nintedanib a FGFR,PDGFR,VEGFR inhibitor (Phase:2, trial identifier: NCT01948141; phase 1, trial identifier:NCT02225405; phase 1, trial identifier: NCT01346540; phase 1, trial identifier: NCT01684111; phase 1, trial identifier:NCT01683682; phase 1 trial identifier: NCT00876460; phase 1 trial identifier: NCT01349296; phase 3 trial identifier: NCT00805194; phase 3 trial identifier:NCT00806819; phase 1 trial identifier: NCT00979576; phase 3 trial identifier: NCT01441297); E-3810/Lucitanib a FGFR1, VEGFR inhibitor (phase 2, trial identifier: NCT02109016; phase 1, trial identifier: NCT01283945) (www.clinicaltrials.gov).

1.4 Brain Tumors

Despite modern surgical and adjuvant methods in cancer treatment, brain tumors represent the leading cause of cancer-related morbidity and mortality (**Figure 6**) in both adult and pediatric patients (Pandey et al., 2017).

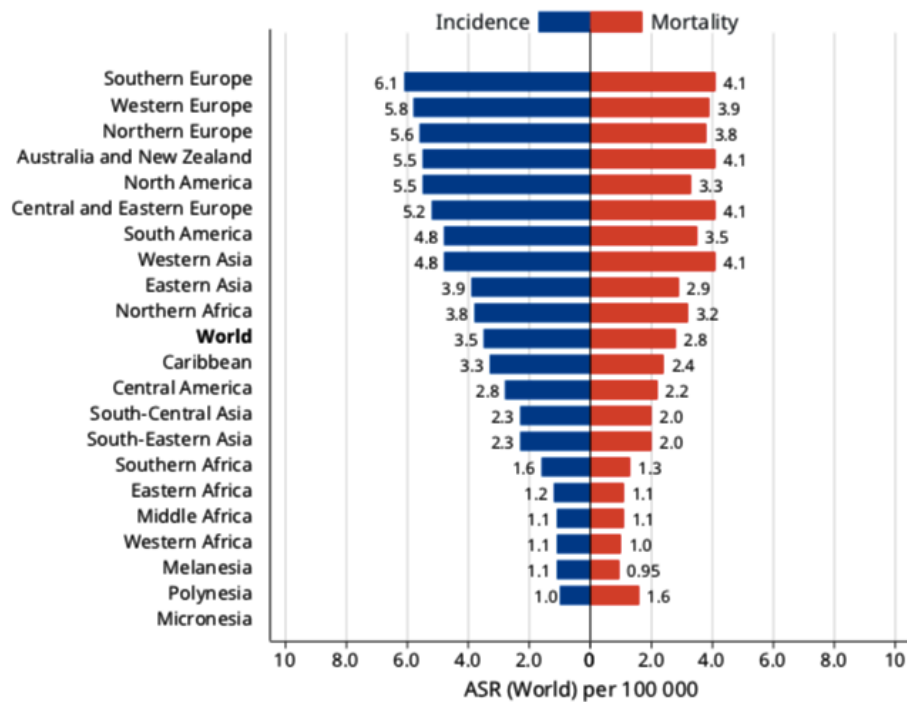


Figure 6. World incidence and mortality rates of brain, nervous system tumors in 2018 according to the International Agency for Research on Cancer of World Health Organization.

Brain neoplasia refers to a wide range of tumors that originate from brain cells, known as primary tumors, or from tumors that originate elsewhere but metastasize to the brain.

Primary brain tumors, which are the most frequent, are classified according to cell diversity according to the WHO. Primary brain tumors are characterized by histological, macroscopic and molecular differences (Butowski N.A., 2015).

The etiology of brain tumors is still unclear, although it is known that they can evolve from brain cells, meninges, nerves or glands.

Furthermore, various factors are known that can be attributed as a contributing cause to the development of cancer, including radiotherapy (Gilbert E.S., 2009), used as a cancer treatment but which at the same time represents a risk factor, additionally hereditary genetic conditions (Neurofibromatosis) (Cockey E. and Ullrich N.J., 2016) and probably viral infections (Epstein virus-Barr) (Zavala Vega S. et al., 2019).

1.4.1 Classification and pathology

According WHO more than 150 different brain tumors have been documented and can be classified as shown in the **Table 2**.

	Grade	Characteristics	Tumor Types
Low Grade	WHO Grade I	<ul style="list-style-type: none"> •Least malignant (benign) •Possibly curable via surgery alone •Non-infiltrative •Long-term survival •Slow growing 	<ul style="list-style-type: none"> •Pilocytic astrocytoma •Craniopharyngioma •Gangliocytoma •Ganglioglioma
	WHO Grade II	<ul style="list-style-type: none"> •Relatively slow growing •Somewhat infiltrative •May recur as higher grade 	<ul style="list-style-type: none"> •“Diffuse”Astrocytoma •Pineocytoma •Pure oligodendroglioma
High Grade	WHO Grade III	<ul style="list-style-type: none"> •Malignant •Infiltrative •Tend to recur as higher grade 	<ul style="list-style-type: none"> •Anaplastic astrocytoma •Anaplastic ependymoma •Anaplastic oligodendroglioma
	WHO Grade IV	<ul style="list-style-type: none"> •Most malignant •Raid growth, aggressive •Widely infiltrative •Rapid recurrence •Necrosis prone 	<ul style="list-style-type: none"> •Glioblastoma multiforme (GBM) •Pineoblastoma •Medulloblastoma •Ependymblastoma

Table 2. Brain tumors classification according World Health Organization 2020

Pilocytic astrocytoma (PA), also known as cystic cerebellar astrocytoma or juvenile pilocytic astrocytoma (Knight J. and De Jesus O., 2020), is the most frequent primary brain tumor in pediatric age, making up about 5.1% of all gliomas (Ohgaki et al. 2005, Collins et al 2015).

An incidence rate of 4.8 per 1 million per year is estimated (Burkhard et al., 2003).

PA is also commonly called optic glioma and infundibuloma, due to the distinct predilection of certain anatomical sites, including the cerebellum, optic pathways and third hypothalamic region (Louis D.N. et al., 2007). Although the causes of PA are thought to be due to non-hereditary but sporadic mutations, a strong association has been found between PA and type 1 neurofibromatosis (NF1).

In fact, 20% of patients with neurofibromatosis 1 develop pilocytic astrocytoma, most commonly in the optic pathway. A large number of patients with pilocytic astrocytoma are characterized by alterations in the MAPK signaling pathway and in the BRAF gene. The mutated BRAF proto-oncogene has been found in many types of tumors (Knight J. and De Jesus O., 2020).

Craniopharyngioma (CP) is a rare tumor that occurs in the pituitary, optic chiasm, and third ventricle. Clinical manifestations are related to the anatomical site of origin and can be disorders related to pituitary / hypothalamic hormones, visual problems and dangerous increase in intracranial pressure.

CP can have two subtypes CP adamantinomatous (ACP) and CP papillary (PCP). Point mutations in the gene encoding β -catenin (CTNNB1) have been identified in ACP (Buslei et al 2005). Due to this mutation, β -catenin is not degraded efficiently, accumulating inside the cell and activating different signaling pathways (Hölsken et al., 2010). PCP hosts somatic mutations of the oncogen BRAF-V600E (Brastianos et al., 2014, Hölsken et al., 2016). In PCP in adults with BRAF-V600E mutations, targeted therapy has provided promising new perspectives (Juratli T.A. et al., 2019).

Gangliocytomas and gangliogliomas are slow-growing neuroepithelial aberrations, represent 1.3% of all brain tumors and are the most frequent among glioneuronal tumors (38.5%). They can consist of neoplastic ganglion and / or

glial cells (Louis D.N. et al., 2007). Gangliogliomas comprise 37-46% of all tumors associated with surgically intractable epilepsy. The age of the patients varies greatly from 2 months to 70 years (Yazmin Oda, 2016).

Chromosomal imbalances have been identified in gangliomas, such as loss of chromosome 17p or gain of chromosome 7 (Hirose T. et al., 1998) and mutations in key cell cycle regulators, such as BRAF and ribosomal protein S6 (Boer K. et al., 2010).

“Diffuse” astrocytoma (AD) accounts for 11-15% of all astrocytic brain tumors. It occurs throughout the central nervous system with a preferential location in the frontal lobes of the cerebral hemispheres (Abdelzaher, 2020).

Frequently, patients with AD have mutations in the IDH genes: IDH1 or IDH2.

Pilocytic astrocytoma is a tumor of the epiphysis or pineal gland. It occurs in adults as a solid mass, although they are often confused with cysts due to the large spaces filled with fluid. After surgery, which is the first-line treatment, many relapses are often observed and the median survival is 7 years (Dahiya S. et al., 2010).

Oligodendrogliomas are gliomas of oligodendrocyte origin that occur mainly in adults (9.4% of all primary brain and CNS tumors) but can also occur in children (4% of all primary brain tumors) (Wesseling P., et al., 2015).

Anaplastic astrocytomas develop from astrocytes are quite rare, in fact they represent about 1-2% of all primary brain tumors (Ostrom et al, 2017). As in diffuse astrocytoma, mutations in the IDH1 or IDH2 genes have also been found in anaplastic astrocytomas.

Anaplastic ependymoma accounts for 5% of gliomas in adults and 10% of childhood cancers throughout the CNS (Gerstner ER et al., 2018; Hübner JM et al., 2018). It has a high tendency to infiltrate the surrounding brain and spread into the cerebrospinal fluid causing metastasis and poor prognosis (Armstrong et al., 2010). No genetic mutations have been highlighted in anaplastic ependymoma (Bruce et al, 2018) for this reason there is no specific therapy.

Almost all ependymomas show features of anaplasia with a high mitotic rate, cellular pleomorphism and intratumoral necrosis (Haaga et al., 2009).

Glioblastoma multiforme (GBM) is the most common and aggressive brain tumor in adults. The disease is characterized by a particularly invasive phenotype; therefore often only surgical removal is treatable. The prognosis of GBM patients is generally poor, as only a minority of cases benefit from the current standard therapy, with a five-year survival rate of 6.8% (Hegi M.E. et al, 2008).

Recently, fibroblast growth factor receptors (FGFR) have emerged as potential therapeutic targets in a GBM subgroup that exhibits gene translocations (Jimenez-Pascual A. et al., 2019)

Pineoblastoma is a tumor of the pineal gland and has a high incidence rate, mainly in children. Although the cause of pineoblastoma is unknown, redundant mutations in the RB1 and DICER1 genes have been identified (Parikh KA et al, 2017).

Medulloblastoma affects children between 2 and 7 years, very rare in adults, it is the most common type of primary brain cancer in children (Roussel MF et al., 2011). Males are more affected than females.

Many genetic mutations have been identified in patients with medulloblastoma, among the most common in the genes CTNNB1, PTCH1, MLL2, SMARCA4, DDX3X, CTDNEP1, KDM6A and TBR1 (Jones D.T. et al.,2012).

Ependymoblastoma is a primary, embryonic malignant neuroectodermal tumor that affects infants in early childhood and has a poor prognosis (Nowak J. et al., 2014; Amit S. et al., 2011). Ependymoblastoma is a very rare tumor showing rapid growth and diffuse infiltration through the leptomeningeal space (Wada C. et al., 1986). Only recently, the overexpression of the LIN28A protein has emerged as a potential player in the pathological phenotype (Lu J., et al., 2020).

1.4.2 Brain Tumor epidemiology

Brain cancer accounts for only 2% of all cancers (**Figure 7**) but, being very difficult to treat, it represents the 10th leading cause of cancer death. An estimated 18,020 adults (10,190 men and 7,830 women) will die from primary cancerous

tumors of the brain and CNS in 2020 (Statistics adapted from American Cancer Society, 2020).

Understanding the causes and underlying genetics can help address this devastating disease (Gould J., 2018).

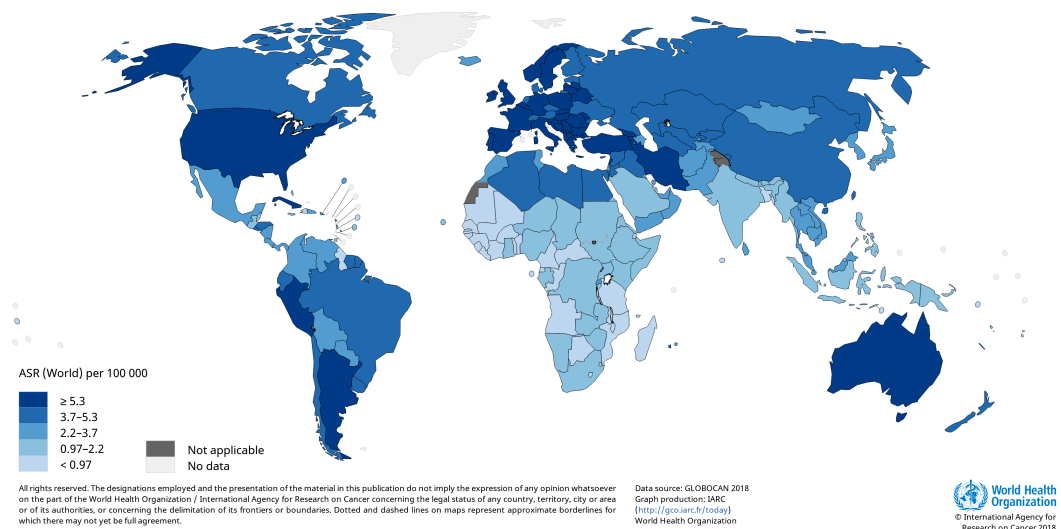


Figure 7 . World Health Organization. 2018. Estimated age-standardized rates (World) in 2018, SNC cancer, both sexes, all ages

GBM comprises 27% of all tumors and 80% of malignant tumors (Ostrom, Q. T. et al., 2015).

CNS cancer is responsible for substantial morbidity and mortality worldwide, and the incidence has increased over the past decade (Patel A.P. et al., 2019).

Most brain tumors occur in people with no known risk factors. But some factors can increase the risk of brain tumors, such as: radiation exposure, some inherited syndromes (such as neurofibromatosis, von Hippel-Lindau disease, Li-Fraumeni syndrome and tuberous sclerosis, have an increased risk growth of brain tumors), family history of brain tumors, weak immune system (AIDS or having undergone a related organ transplant), contact with chemicals such as vinyl chloride,

pesticides and petroleum products, ionization and non-ionizing radiation, infection with some viruses (Epstein-Barr virus) (Ostrom, Q. T. et al., 2015).

It is estimated that 25% of brain tumors are attributable to genetic factors of which 30% are currently identified and 70% not yet known (Melin B.S., et al., 2017).

1.4.3 Glioblastoma multiforme (GBM)

GBM is the deadliest, highly invasive and rapidly growing form of brain cancer (**Figure 8**). It accounts for 60% of all primary brain tumors (Ozdemir K.E. et al., 2018).

It develops from glial cells, rapidly invades surrounding tissue with degradation



Figure 8. T 2-weighted image of a glioblastoma multiforme. *Aileen Quintana et al, 2017.*

of the extracellular matrix, is mitotically very active and necrotic (Ozdemir K.E. et al., 2018).

It is classified by the World Health Organization as a highly malignant grade IV tumor (Tejaswi Kanderi and Vikas Gupta, 2020). GBM patients have a poor prognosis with a 1-year survival rate of 37.2% (Ostrom, Q. T. et al., 2015).

Primary glioblastoma multiforme is very rare in children, more common in the elderly. The secondary one, on the other hand, very often derives from oligodendroglioma or astrocytoma, they are also frequent in younger patients (Ostrom, Q. T. et al., 2015).

Usually the most recurring symptoms are due to the enhanced intracranial pressure that the tumor creates on the surrounding brain tissue. Diplopia, paralysis, amnesia, speech problems and recurrent headaches are observed.

Among the causes, still not well known, histories of radiotherapy (Tejaswi Kanderi and Vikas Gupta, 2020) and genetic mutations of isocitrate dehydrogenase (IDH1 and IDH2) have been identified. Three types of IDH mutations have been found: IDH-mutant, IDH-wild-type and NOS, but there are no targeted therapies yet (Taylor O.G..et al., 2019).

Some studies have shown a low risk of GBM with allergies and atopic diseases (Hanif F. et al., 2017). Additionally, the use of anti-inflammatory drugs was associated with a protective effect on glioblastoma, while no correlations with lifestyle factors have been identified (Tejaswi Kanderi and Vikas Gupta, 2020).

The correlation between reduced susceptibility to GBM and the use of anti-inflammatories could open new scenarios for understanding the etiological basis of the disease.

1.4.4 Molecular alterations associated with GBM

In GBM, recurrent genetic mutations have been identified in addition to IDH with the most frequent being EPHA3, EGFR, FGFR, MGMT, CDKN2, PTEN, PIK3CA, PDGFRA, MDM2, MET, SF / HGF, and VEGF (Le Rhun E., et al., 2019; Crespo I. et al., 2015). This mutation heterogeneity led to the revision of the World Health Organization classification as primary and secondary GBMs

according to the underlying genetic aberrations primarily in IDH genes (Montemurro N., 2020).

Recently, fibroblast growth factor receptors (FGFR) have emerged as potential therapeutic targets in the treatment of GBM. Chromosomal fusions in particular of FGFR1 or 3 with the Transforming Acid Coiled-Coil (TACC) gene have been identified in smaller subgroups of GBM (Touat M., et al., 2015; Turner N., et al., 2010).

1.4.5 GBM and FGFRs

As discussed extensively in previous chapters, fibroblast growth factors are key mitogens and survival factors regulating tissue homeostasis and promoting cancer. Recently, fibroblast growth factor receptors (FGFRs) have emerged as potential therapeutic targets in GBM (Jimenez P.A., et al., 2019).

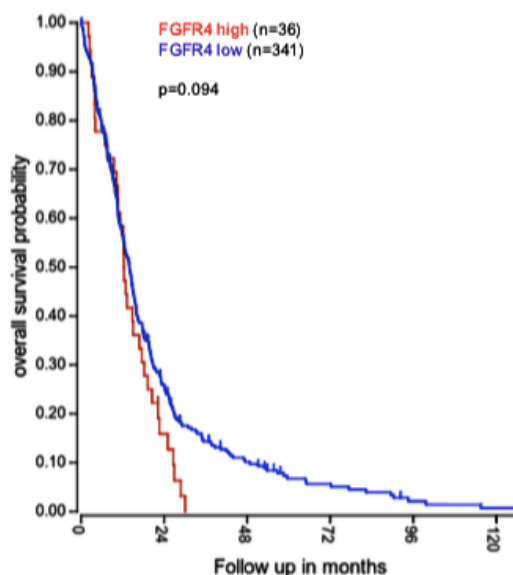


Figure 9. FGFR4high subgroup tended to have a shorter overall survival (Gabler et al., 2020). Data are derived from the TCGA GBM dataset and were processed in R2.

Concerning FGF ligands, FGF2 - which regulates the self-renewal of multiple stem cell types - has recently been implicated in the self-renewal of GBM stem cells (Ana Jimenez-Pascual, 2019).

Precision targeting of FGF / FGFR signaling could be a valid therapeutic approach for patients with GBM who harbor FGF / FGFR aberrations. There exists an extended body of literature about an oncogenic role of FGFR1 in human GBM. Overexpression of FGFR1 in GBM is associated with increased cell migration and invasiveness. The effect of promoting the malignancy of FGFR1, on the other hand, is attenuated with the use of specific inhibitory drugs (Jimenez P.A. et al., 2019). Unlike other members of the FGFR family (FGFR 1, 2 and 3), a potential role of FGFR4 in GBM has not yet been elucidated.

Recently, at the *Institute of Cancer Research* of Vienna, where I did my research work, generally low FGFR4 mRNA levels in healthy brain compared to other organs, elevated in GBM were found. Highly expressed FGFR4 in primary cell cultures established from surgical specimens and immortalized cell lines (approximately 10%) is associated with low overall survival (**Figure 9**). Furthermore, the expression levels of FGFR4 and associated ligand genes FGF19 and FGF23 increased markedly during GBM progression. Elevated levels of FGFR4 significantly promote the self-renewal and proliferation capacity of GBM *in vitro*. Conversely, FGFR4 blockade drastically alters these parameters and has also been associated with reduced migration capacity.

1.4.6 Therapy of GBM

The standard treatment of GBM is surgical removal followed by chemotherapy and radiotherapy (Tejaswi Kanderi and Vikas Gupta, 2020).

GBM is an often fatal disease due to very frequent relapses, and resistance to therapy is observed (Taylor O.G. et al., 2019). The survival rate varies from one to two years in most patients (Tejaswi Kanderi and Vikas Gupta, 2020).

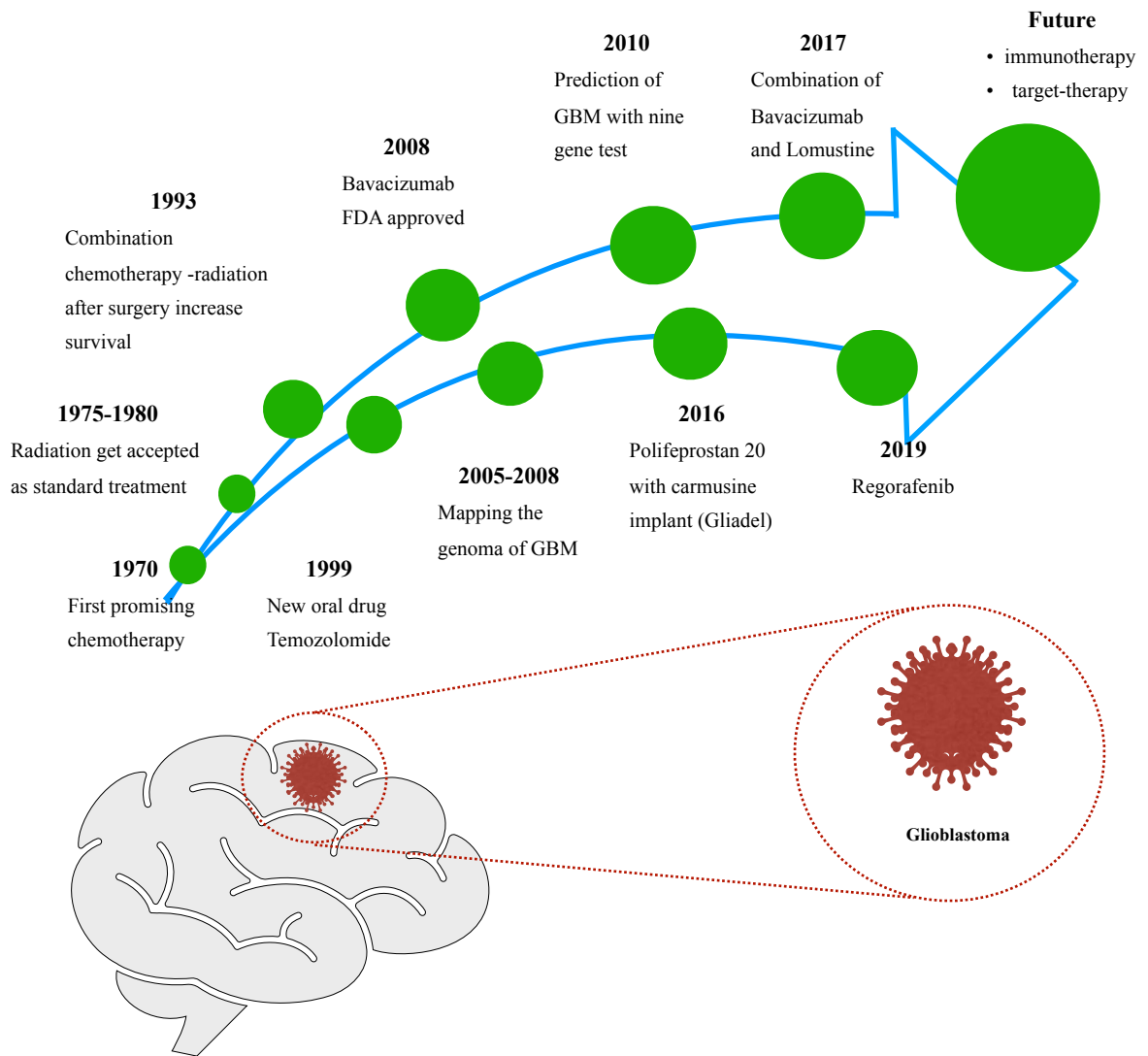


Figure 10 . Evolution of the treatment of GMB from 1970 to 2020

Until now, PI3K, AKT, mTOR, RB and EGFR have been used as specific therapeutic targets, but with comparably limited success, probably due to redundant compensatory mechanisms. Some GBM subgroups have been selected for specific therapies due to BRAF mutation, NTRK and fusion of the FGFR and MET gene (Le Rhun E., et al., 2019). The genetic profile of GBM biopsies revealed aberrant expression of several other potential therapeutic targets, including a number of RTKs (EphA3, EGFR, VEGF, PDGFR and MET), however, there has been varied and limited clinical success in the use of inhibitors of these targets as anti-cancer therapies (Taylor O.G..et al., 2019).

The standard treatment for glioblastoma remains surgery also with strong limitations, because its success depends on the infiltration of the tumor and on the involvement of the vascularization (Salcman M., 2003; Quigley and Maroon, 1991; Alifieris and Trafalis, 2015; Séhédic et al., 2015).

Conventional therapy for glioblastoma, typically the alkylating compound temozolomide (TMZ), has limited efficacy due to the resistance that develops to therapy and due to frequent devastating neurological deterioration (Kim et al., 2015; Jiapaer S., et al., 2018). In cases of TMZ therapy failure, lomustine is employed which results in marginally prolonged survival of only 8.6 to 9.8 months (Glas M. and Kebir S., 2019).

Other approved treatments are those with Polifeprosan 20 with carmustine polymer implant wafer (GLIADEL®). It is a biodegradable compound containing 3.85% carmustine. It is implanted in the brain during surgery to remove the tumor. The polymer slowly degrades allowing the release of the active ingredient in the tumor, thus bypassing the blood-brain barrier (Kleinberg L., 2016).

There is a growing body of evidence to suggest that a personalized therapeutic approach for stratifying GBM patients towards new treatment regimens is needed if improved survival rates for GBM patients are to be desired (Taylor O.G..et al., 2019).

Given its aggressive nature, even with maximal therapy, GBM has poor overall survival and a high relapse rate.

This highlights that a better understanding of the basic biology of GBM is needed so that additional targets can be identified.

Several drug candidates for GMB immunotherapy are in phase II and phase III clinical trials to date (e.g. Nivolumab, Pembrolizumab, Bevacizumab, Arelumab) (Weenink B. et al., 2020).

1.4.7 FGFRs-targeted therapies for brain tumors and GBM

The optimal use of targeted therapy in glioblastoma multiforme remains under investigation also due to still limited high quality clinical data. Emerging evidence has shown that some histological entities appear to be dominated by specific alterations of the FGF / FGFR signaling axis and represent an active area of investigation (Bale T.A. et al., 2020).

There are also differences between GBMs of adult and pediatric patients. Glioblastomas in adults most commonly harbor changes in IDH, while in children a heterogeneity of changes, including changes in FGFR, is observed. Recently, fibroblast growth factor receptors (FGFR) have emerged as potential therapeutic targets in some patients with GBM. However, significant heterogeneity remains between them even within tumors with FGFR alterations.

A recent *in vitro* study found that FGFR inhibitors, such as Ponatinib, AZ4547, Dovatinib, and PD173074, were more effective than TMZ in reducing the growth of pediatric diffuse intrinsic pontine glioma (Schramm K et al., 2019).

1.6 Metal drugs in cancer therapy

Nowadays, there is an important revival of metals in chemotherapy treatment due to novel discoveries on their specific model of action and their immunogenic mechanisms (Kaitlyn K. and Katarzyna R, 2019). The activity of cisplatin, (the first metal compound to be commercially available) against lymphoma and cancers of the head, neck and reproductive organs was first detected in the early 1970s (Dasai S. et al., 2014). Analogues of cisplatin, in both II and IV oxidation states, are currently in clinical trials, to try to bypass drug resistance and severe side effects that limit cisplatin use, such as ototoxicity, nephrotoxicity and hematotoxicity. For example satraplatin, a Pt(IV) drug intended to function as

cisplatin prodrug, is under advanced investigation for prostate cancer treatment (Choy H, Park C, Yao M., 2008).

Many other compounds containing a metal core have been synthesized and tested for their anticancer activity. In the last decades, ruthenium, gold and palladium-based complexes among others appear to be good alternatives to cisplatin, especially for the treatment of cisplatin-resistant cancers (Antonarakis ES et al., 2010; Lazarević T. et al., 2017; Abid M. et al., 2016 ; Bertrand B, et al., 2018 ; Vojtek M. et al., 2019).

Transition metal ions have unique properties which include:

- Change of charge: their charge strongly depends on the surrounding environment, ranging from positive to neutral to negative (Haas KL et al., 2010). In aqueous solutions they are usually positively charged and for this reason they electrostatically interact with anionic biological macromolecules (Frezza M. et al., 2010).
- Structure and bond: compared to organic molecules, metal complexes can assume more “sophisticated” coordination geometries. The nature of the metal ion and its oxidation state, coupled with designed bonding properties of selected ligands, confers them tunable thermodynamic and kinetic properties (Haas KL et al., 2010, Frezza M. et al., 2010, Yan Y.K., et al., 2005, Salga MS et al., 2012). These characteristics offer a wide range of advantages especially in both non-covalent and covalent binding with biological macromolecules (Frezza M. et al., 2010).
- Redox activity: all transition metals have a tendency to undergo redox reactions (Haas KL et al., 2010). When designing new coordination metal complexes, the oxidation state is one of the most important parameters to consider, since coordination properties drastically change with the metal oxidation state. This feature is exploited by nature, since many metalloproteins exert their biochemical properties by a reversible equilibrium between different oxidation states of the metal ions present in their active site.

The different coordination chemistry of metal ions in different oxidation states have recently been exploited for the design of new anticancer drugs with the following dual advantages:

1. Improved capacity to cross the cell membrane compared to organic ligands after their coordination to metal cations;
2. Ability to release the ligand in proximity of the biomolecular target after spontaneous reduction of the metal ion in a minor oxidation state, due to the hypoxic conditions which dominate cancer cells.

Copper(II) complexes, in addition to those of ruthenium (II), have been recently considered among the potential alternatives to cisplatin as anticancer agents (Santini C., et al., 2014 ; N.H. Campbell, et al., 2011).

1.6.1 Copper complexes

Copper coordination complexes have been developed in the last century as potential drugs with multiple pharmaceutical activities, such as antimicrobial (Geraghty, M., et al., 2000; Subramaniyam R. et al., 2014), for the treatment of neurodegenerative diseases, coronary heart disease and skin disease (Duncan C. and White A.R., 2012)

Cancer therapy is also considered as option for many copper-based drug candidates. In fact, copper has been correlated to a limitation the progression of tumors, inhibition of tumor growth, angiogenesis and metastasis (Benjamin Chibuzo Ejelonu, 2016). Copper complexes used in the past for the treatment of other diseases, such as tetratiomolybdate and clioquinol, have been recently re-evaluated for cancer therapy and have shown anticancer activity *in vitro* and *in vivo* (Delphine Denoyer et al, 2018).

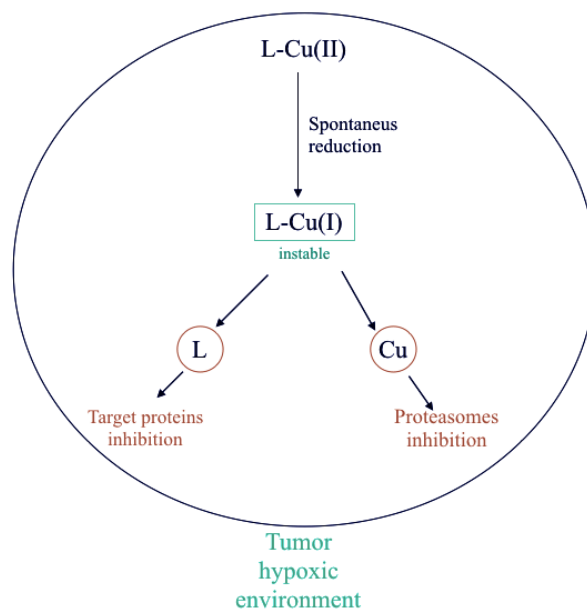


Figure 11. Spontaneous reduction, in the tumor hypoxic environment, of the ligand-Cu (II) complex. The proposed mechanism is the release of the free ligand, after the spontaneous reduction of Cu (II) to Cu (I), due to the instability of the L-Cu (I) complex. The ligand can thus inhibit the target protein, the Cu (I) proteasomes.

Remarkably, copper is a catalyst of redox reactions. During its biological activity, reactive oxygen species (ROS) originate, a process requiring a strict homeostatic regulation (Labbe, S. et al, 1999).

Copper complexes play important roles in biological systems, in particular in metalloproteins, usually being involved in a number of catalytic electron transfer reactions (Chakraborty A. et al., 2010).

The biological activity of metal complexes strongly depend on the type of ligand coordinated to the metal (Delphine Denoyer et al, 2015). For example, copper(II) complexes with bidentate chelating ligands with N, S, O donor atoms, have proven to be good anticancer candidates, thanks to their strong ability to bind DNA bases (Saadeh SM et al, 2013).

It has also been noted that some tumor cells resistant to conventional platinum-based drugs are on the other hand sensitive to copper-based drugs (Delphine Denoyer et al, 2015). Furthermore, it has been found that copper(I) inhibit proteasomes and tumor cells are more sensitive to proteasome inhibition than normal cells (Xiao Y. et al., 2010).

A large number of copper transition complexes have been synthesized with various sets of ligands that have shown cytotoxicity *in vitro* (Khan, RA et al, 2016; Tabassum, S. 2013; Usman, M et al 2017; Tisato, F et al , 2010). However, very few copper-based drug candidates have been tested *in vivo* (Khan, RA et al, 2017; Sarkar, A. et al, 2013; Santini, C. et al. 2014).

According to recent studies, metal-based anticancer drugs are not only capable to destroy cancer cells but are also capable to acting on the immune system in some way, probably by increasing the effect of immune checkpoint inhibitors (Englinger, B. et al., 2019). Cancer cells, also, differ from healthy cells in the microenvironment and the intracellular environment is often associated with hypoxia, increased redox metabolism and consequently with high ROS levels.

Taking advantage of these factors, the design of a redox active metal-based drug appears to be an attractive and promising approach for cancer therapy.

Considering copper, it is known that coordination of N,N' or N,O chelating ligands is weaker for Cu(I) compared to that of Cu(II). Consequently, the reduction of Cu(II) to Cu(I) (**Figure 11**), which could occur spontaneously in the hypoxic conditions of the intracellular environment, should allow the release of the ligand within the intracellular environment (Chen Y. et al., 2009). A similar strategy has recently been proposed by researchers at the Medical University of Vienna, for Co(III) complexes used as prodrugs of selective epidermal growth factor receptor (EGFR) inhibitors (Kowol C. et al., 2012). The free and active organic ligand will only be found in the tumor environment. Furthermore, free copper (I) in the cell, in addition to influencing redox activity, can also act as a proteasome inhibitor. In this way, a “smart drug” with triple action can in principle be obtained (Karnthaler-Benbakka C. , et al., 2014).

1.7 Aims of the study

The main aim of this thesis was to identify and synthesize new inhibitors of FGF1 and FGF4 receptors in order to treat tumors in which these receptors are over-expressed and/or hyperactivated (**Figure 12**).

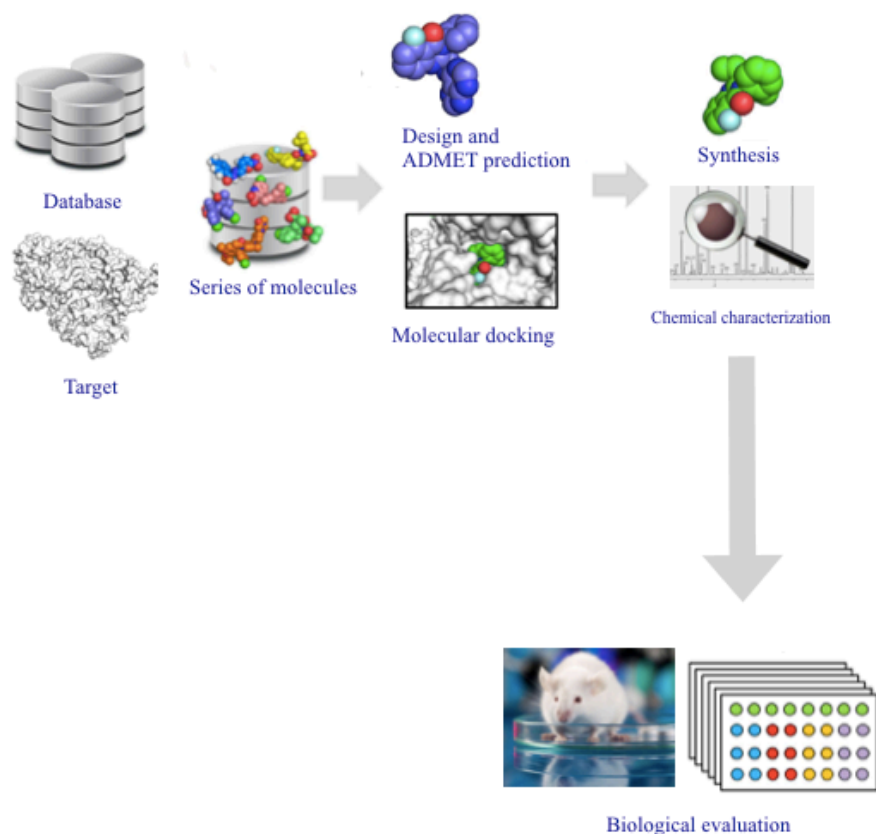


Figure 12. Aim of the study: design (using computational tools), synthesis, characterization and biological evaluation of new FGFR inhibitors with anticancer properties.

In particular, new Cu(II)-based prodrugs will be developed, which can release the organic inhibitor in the hypoxic environment present inside cancer cells.

For this purpose, this thesis work includes:

- the design by computational methods of new molecules capable of interacting with FGFR1 and FGFR4;
- the synthesis of 25 molecules, 22 organic ligands and 3 copper(II) metal complexes;

- the preliminary screening of the synthesized molecules against different cancer cell lines in order to select the most active molecules;
- *in vitro* studies on the selected molecules in order to identify their possible mechanism of action;
- *in vivo* studies on SCID mice to evaluate the toxicity and inhibition of tumor growth of the selected compounds.

CHAPTER TWO, DRUG DESIGN

2.1 Drug design methods

Drug design represents the process of finding new drugs based on the knowledge of a biological target or based on the chemical structure of existing drugs (Zhou SF, Zhong WZ. 2017). There are two main ways of drug design: rational drug design and computer aided drug design (CADD).

By rational design we mean the method that follows scientific tests and studies of structure-activity relationships with a specific biological target that leads to the creation of a set of new drug candidate molecules.

In contrast, the main objective in CADD is the prediction of the binding of a given molecule to a considered biological target, by using computational approaches such as molecular docking and molecular dynamics (Fosgerau, et al., 2015; Ciemny, Maciej et al., 2018), collectively called molecular modeling methods.

These approaches make use of specific algorithms and methods of molecular mechanics and of semi-empirical quantum chemistry. *Ab initio* or density functional theory methods are also used to provide optimized parameters for molecular mechanics calculations and to obtain the observables of electronic properties (Lewis RA, 2011).

Usually, the molecular modeling method are applied to predict receptor-ligand affinity before the ligand is synthesized, to virtually screen potential ligands and reduce costs and time employed for the synthesis of inefficient compounds (Singh J, et al., 2003).

2.2 Computer aided drug design of new FGFR inhibitors

Recently, the combination of molecular modeling and experimental approaches has greatly contributed to the identification and development of new promising compounds, both in academia and industry. Widely used in modern drug design, molecular docking is used to investigate the conformations of the ligand and its complementary shape with the binding pocket of biological targets. This procedure also roughly approximates the free energy of the interaction between the ligand and the biological macromolecule (Leonardo G Ferreira, et al., 2015).

Furthermore, besides the estimate of pharmacodynamic features (e.g., binding energy, affinity, efficacy, selectivity), also pharmacokinetic characteristics (ADMET: absorption, distribution, metabolism, elimination and toxicity) have been obtained by using molecular modeling methodologies.

The structure-based drug design (SBDD) approach starts with a known macromolecular biotarget and *in silico* approach are applied in order to estimate the quality of potential ligands. Molecular modeling studies are desirably followed by the synthesis of the most promising ligands (Wilson, G.L, et al., 2011; Meng, X.Y. et al., 2011; Torres PHM, et al 2019).

The search algorithms of molecular docking generate possible conformations and orientations of ligands inside the binding pocket of target proteins, sorted in order of the scoring values (Liu Y., et al., 2018).

An alternative possibility in drug design, especially in the absence of the structure of the receptor, is called “ligand-based” and relies on the knowledge of the structure of molecules that are known to bind to the considered biological target (Polamarasetty Aparoy et al., 2012).

All molecular docking calculations start with a target structure, typically obtained by X-ray crystallography or NMR spectroscopy (Gioia, D. et al., 2017). For example, in the following **Figures 13** and **Figure 14**, the crystal structure of Ponatinib complexed with FGFR1 (**Figure 13**) and FGFR4 (**Figure 14**) are reported.

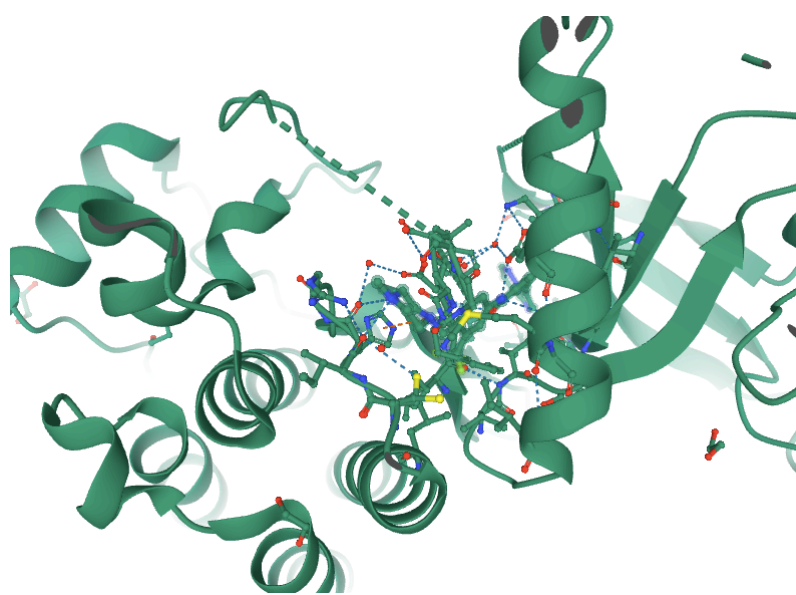


Figure 13. PDB ID: 4v04, Ponatinib complexed with FGFR1

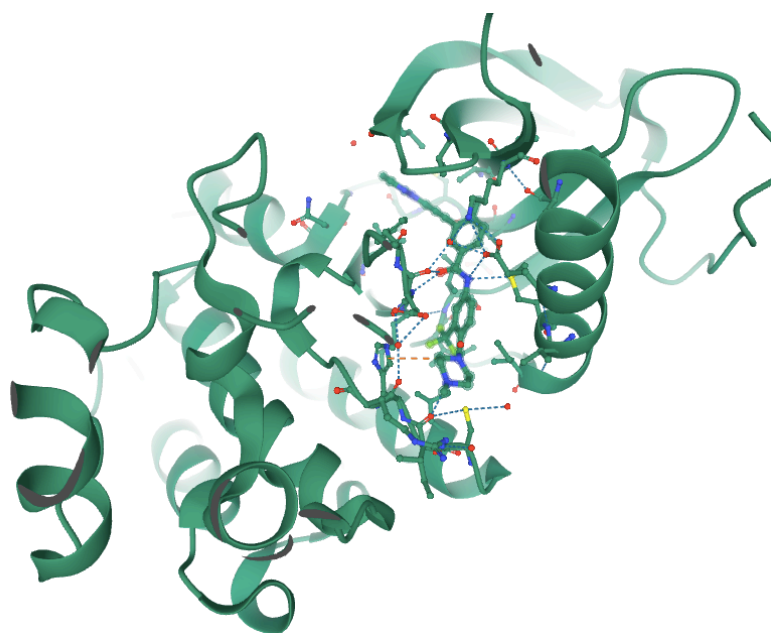


Figure 14. PDB ID: 4uxq, Ponatinib complexed with FGFR4

2.3 Design of new FGFRs inhibitors

On the basis of the considerations made in the introductory part of my thesis, my first goal was to design new inhibitors of FGFR receptors (in particular FGFR1 and FGFR4), using molecular docking methods. The receptors have been designed also taking into account the possibility to coordinate transition metal ions such as Cu^{2+} , by opportune chelating groups, in order to give them their prodrug properties and improve their pharmacokinetic characteristics, compared to the naked ligands.

The crystal structures of the FGFR1 and FGFR4 receptors, both co-crystallized with Ponatinib, were chosen as hosts for molecular docking. Ponatinib is a multi-targeted tyrosine-kinase inhibitor (Huang WS. et al., 2010), a drug approved by FDA for the treatment of chronic myeloid leukemia and under investigation for many therapeutic effects on several over-expressing FGFR tumors.

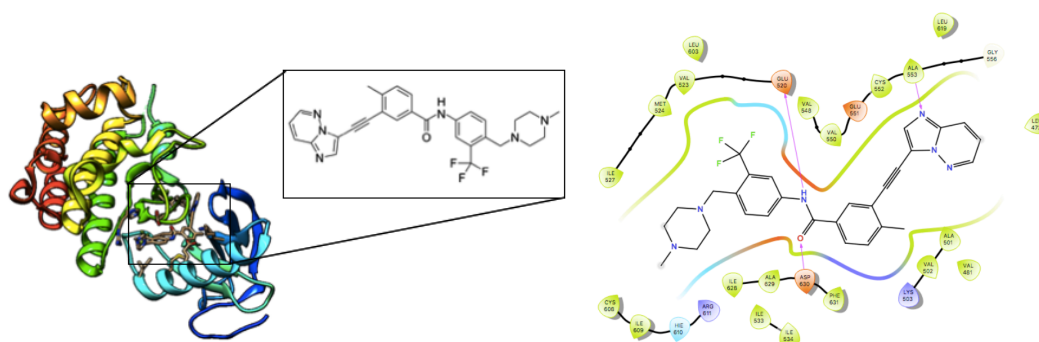


Figure 15. Crystal structure of Ponatinib complexed with FGFR4 (PDB ID: 4uxq) and the amino acids involved in the interaction.

For this reason, new ligands with similar structure to Ponatinib and good scoring in molecular docking with the Ponatinib binding site have been considered as new potential inhibitors of FGFR1 and FGFR4.

In the molecular design, a central bridge in the molecule is essential, consisting of a carbonyl and an amino group, which allow the interaction with the amino acids

residues Asp631 and Glu520, respectively. Moreover, at the two ends of the molecule presence of electron donor groups such as nitrogen seems to be also important., to establish interactions with Ala553 and Asp630 (**Figures 15**).

Finally, the correct intramolecular distances between the various groups of the molecules are critical, to establish a efficient interaction with the receptor. For this reason, it is necessary to introduce also a linker spacer, such as that present in Ponatinib.

One of the problems of Ponatinib is the very high lipophilicity that limits its use, as it accumulates in the adipose tissue, as well as causes central side effects. Hence, an attempt was made to replace the more lipophilic groups with reduced pharmacodynamic relevance.

The considerations above led to the choice of a quinazolinone core into the molecule, due to its known anticancer characteristics (**Figure 16**) (Al-Rashood ST, et ad., 2006).

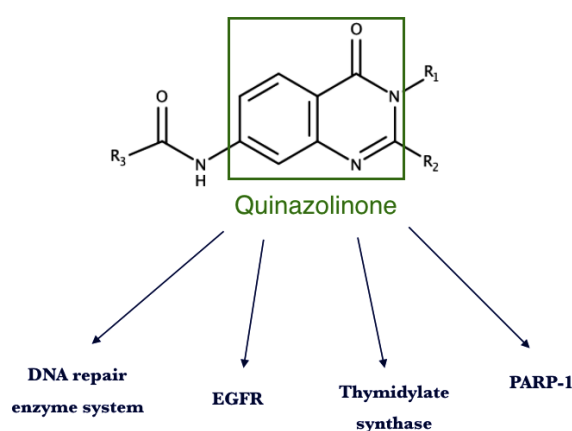


Figure 16. Chemical structure of quinazolinone with the possible targets that give it anti-tumor characteristics: the DNA repair system, the epidermal growth factor receptor, thymidylate synthase and PARP-1.

Drugs selective for a single biotarget often induce cancer cells to immediately develop resistance mechanisms. On the other hand, it has been shown that, in their anticancer activity, quinazolinones possess inhibitory properties for the following targets:

- inhibition of the DNA repair enzymatic system (Laddha SS, et al.,2012);
- inhibition of the epidermal growth factor receptor (EGFR) (a trans-membrane cellular receptor with tyrosine kinase activity that is overexpressed in a significant number of human cancers) (Devi KA, et al., 2012);
- inhibition of thymidylate synthase (Khalil AA, et al., 2003);
- inhibitory effects on tubulin polymerase (P. Skehan, et al., 1990) such as poly (ADP-ribose) polymerase-1 (PARP-1), an enzyme involved in many fundamental processes including DNA repair and transcriptional regulation.
- inhibitory effects on tubulin polymerase (P. Skehan, et al., 1990) such as poly (ADP-ribose) polymerase-1 (PARP-1), an enzyme involved in many fundamental processes including DNA repair and transcriptional regulation.

Based on these considerations, more than 160 quinazolinone derivatives, as possible FGFR1 and FGFR4 inhibitor molecules, have been designed.

In parallel to molecular docking investigations, the pharmacokinetic characteristics of all molecules were evaluated (**Figure 17**) using the QikProp v6.2 application of the Schrödinger's Maestro package, since nearly 40% of drug candidates are blocked in clinical trials due to their unfit ADMET features. In fact, QikProp allows one to quickly screen compound libraries and identify molecules with calculated properties that are outside the normal range of known drugs, hence making easy to filter out candidates with unsuitable ADMET properties.

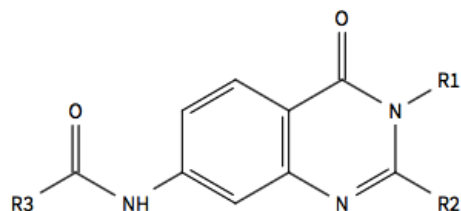
In order to identify new FGFR inhibitors, the starting structures of the designed molecules were created with the Avogadro software, version 1.2.0, and their geometry was optimized using the empirical Force Field GAFF (General AMBER Force Field).

All chemical features were studied using MarvinSketch version 20.7.

molecule	QLogPo/w	QLogS	CIQLogS	QLogHERG	QPPCaco	QLogBB	QPPMDCK	QLogKp	IP(eV)	EA(eV)	#metab	QLogKhsa	absorr	%HOAbsorption
V49	4.396	-6.813	-6.815	-8.033	493.504	-1.297	230.586	-1.561	9.085	957	3	568	1	100.000
V50	3.660	-5.689	-5.309	-7.408	978.038	-828	482.976	-1.332	8.872	805	2	276	3	100.000
V55	3.656	-5.714	-5.590	-6.681	646.555	-985	308.771	-2.045	9.090	956	3	386	3	100.000
V51	4.146	-6.422	-6.001	-7.301	959.986	-685	1165.067	-1.518	8.930	914	2	390	1	100.000
V53	3.955	-6.243	-5.590	-7.281	953.155	-869	469.708	-1.560	8.918	814	3	430	1	100.000
V56	3.634	-5.612	-6.001	-6.746	540.067	-964	390.985	-2.068	9.043	871	2	329	3	100.000
V8	2.364	-4.570	-4.003	-6.411	431.669	-1.175	199.522	-2.576	8.971	721	1	45	3	87.953
V9	2.741	-4.924	-4.665	-6.119	274.754	-1.227	301.405	-3.205	9.144	901	1	135	3	86.647
V10	2.747	-4.546	-4.271	-6.290	420.101	-1.226	193.749	-2.805	9.013	712	2	191	3	89.981
V11	2.772	-4.993	-4.665	-6.213	279.973	-1.233	307.052	-3.158	9.123	880	1	142	3	86.973
V12	2.607	-4.315	-4.271	-5.769	312.687	-1.259	140.807	-3.112	9.097	807	2	168	3	86.869
V14	2.886	-5.027	-4.665	-6.296	433.038	-1.040	440.858	-2.722	8.993	726	1	146	3	91.035
V15	2.597	-4.358	-4.271	-5.896	325.808	-1.267	147.204	-3.067	9.102	795	2	153	3	87.130
V26	4.427	-6.297	-6.361	-7.357	355.999	-1.498	162.001	-1.898	9.075	1.083	1	677	1	100.000
V27	4.288	-6.482	-6.081	-7.937	334.083	-1.624	151.249	-1.779	9.038	1.066	0	595	1	100.000
V28	4.972	-7.399	-6.770	-8.011	498.598	-1.299	573.908	-1.553	8.978	971	0	727	1	100.000
V32	4.560	-6.801	-6.361	-7.543	346.344	-1.593	157.258	-2.006	9.044	1.078	1	743	1	100.000
V33	4.695	-7.149	-6.770	-7.634	298.388	-1.528	329.035	-2.147	9.173	1.165	0	704	1	100.000
V30	4.518	-6.800	-6.361	-7.529	299.965	-1.665	134.625	-2.133	9.105	1.138	1	745	1	100.000
V31	4.937	-7.304	-6.770	-8.009	512.945	-1.297	528.130	-1.507	8.905	886	0	720	1	100.000
V69	3.670	-5.569	-5.590	-6.799	722.271	-917	348.034	-1.809	9.075	956	3	358	3	100.000
V71	3.891	-6.404	-6.001	-7.179	490.764	-1.024	563.424	-2.172	9.068	928	2	385	1	100.000
Ponatinib	4.529	-5.951	-5.471	-9.070	74.008	56	119.858	-5.446	9.036	900	6	806	2	73.961

Figure 17. ADMET properties of 22 new molecules and Ponatinib, calculated with QikProp v6.2

All molecules with non desirable ADMET features, compared to those of drugs on the market, were not considered. In conclusion, a list of 22 ligands was kept for further considerations: V49, V50, V55, V51, V53, V56, V8, V9, V10, V11, V12, V14, V15, V26, V27, V28, V32, V33, V31, V69, V71 (**Table 3**). V49, V50 and V55 possess also a N,O chelating unit and so their copper(II) complexes were also considered.



	R1	R2	R3	Chemical Formula	Molecular Weight (g/
V49	Pyridine	Methyl	2-[(1E)-2-phenylethenyl]pyrid	C ₂₈ H ₂₁ N ₅ O ₂	459.50
V50	Pyridine	Methyl	Ethenylbenzene	C ₂₃ H ₁₈ N ₄ O ₂	382.41
V55	Pyridine	Methyl	1-ethenyl-3-methylbenzene	C ₂₄ H ₂₀ N ₄ O ₂	396.44
V51	Pyridine	Methyl	4-chloro-1-ethenylbenzene	C ₂₃ H ₁₇ ClN ₄ O ₂	416.859
V53	Pyridine	Methyl	1-ethenyl-4-methylbenzene	C ₂₄ H ₂₀ N ₄ O ₂	396.441
V56	Pyridine	Methyl	2-chloro-1-ethenylbenzene	C ₂₃ H ₁₇ ClN ₄ O ₂	416.859
V8	H	Methyl	Ethenylbenzene	C ₁₈ H ₁₅ N ₃ O ₂	305.330
V9	H	Methyl	4-chloro-1-ethenylbenzene	C ₁₈ H ₁₄ ClN ₃ O ₂	339.775
V10	H	Methyl	1-ethenyl-4-methylbenzene	C ₁₉ H ₁₇ N ₃ O ₂	319.357
V11	H	Methyl	3-chloro-1-ethenylbenzene	C ₁₈ H ₁₄ ClN ₃ O ₂	339.775
V12	H	Methyl	1-ethenyl-3-methylbenzene	C ₁₉ H ₁₇ N ₃ O ₂	319.357
V14	H	Methyl	2-chloro-1-ethenylbenzene	C ₁₈ H ₁₄ ClN ₃ O ₂	339.775
V15	H	Methyl	1-ethenyl-2-methylbenzene	C ₁₉ H ₁₇ N ₃ O ₂	319.357
V26	H	Ethenylbenzene	1-ethenyl-2-methylbenzene	C ₂₆ H ₂₁ N ₃ O ₂	407.463
V27	H	Ethenylbenzene	Ethenylbenzene	C ₂₅ H ₁₉ N ₃ O ₂	393.882
V28	H	Ethenylbenzene	4-chloro-1-ethenylbenzene	C ₂₅ H ₁₈ ClN ₃ O ₂	427.882
V32	H	Ethenylbenzene	1-ethenyl-4-methylbenzene	C ₂₆ H ₂₁ N ₃ O ₂	407.463
V33	H	Ethenylbenzene	3-chloro-1-ethenylbenzene	C ₂₅ H ₁₈ ClN ₃ O ₂	427.882
V30	H	Ethenylbenzene	1-ethenyl-3-methylbenzene	C ₂₆ H ₂₁ N ₃ O ₂	407.463

V31	H	Ethenylbenzene	2-chloro-1-ethenylbenzene	C ₂₅ H ₁₈ ClN ₃ O ₂	427.882
V69	Pyridine	Methyl	1-ethenyl-2-methylbenzene	C ₁₉ H ₁₇ N ₃ O ₂	319.357
V71	Pyridine	Methyl	3-chloro-1-ethenylbenzene	C ₂₃ H ₁₇ ClN ₄ O ₂	416.859
V49-Cu	17-triaza-8-cupratetracyclo	Methyl	2-[(1E)-2-phenylethenyl]pyrid	C ₂₈ H ₂₄ N ₅ O ₄ CuCl ₄	699.887
V50-Cu	17-triaza-8-cupratetracyclo	Methyl	Ethenylbenzene	C ₂₃ H ₁₈ N ₄ O ₂ CuCl ₄	622-797
V55-Cu	17-triaza-8-cupratetracyclo	Methyl	1-ethenyl-3-methylbenzene	C ₂₄ H ₂₀ N ₄ O ₂ CuCl ₄	636.827

Table 3. Chemical formula, molecular weight and R1, R2, R3 substituents of 25 synthesized molecules

The Autodock Vina software, version 1.5, was used to perform the molecular docking study, by an automatic procedure that involves the treatment of both ligand and protein, in order to make them suitable for the calculation. The main changes made were the following: 1) elimination of water molecules around the protein; 2) addition of the possibly missing hydrogen atoms; 3) protonation of histidine residues; 4) conversion of selenomethionines into methionines.

At the end of the preparation, a short gradual reduction of the energy was performed, for the amino acid residues. In order to narrow the search field, no blind docking was carried out which would have affected the entire surface of the protein but, on the contrary, the positioning of the grid box was based on the coordinates of the Ponatinib, present inside the binding pocket.

The files with .pdbqt extension were created for all ligand candidates, as well as for Ponatinib, FGFR1 and FGFR4, by the following steps: 1) addition of hydrogen atoms to the molecule; 2) addition of partial charges; 3) deleting non-polar hydrogens and merging their charges with the carbon atoms; 4) assignment of atom types, definition of hydrogen bond acceptors and donors, and of aromatic and aliphatic carbon atoms; 5) choice of the torsion angles of the ligands allowed to rotate during the calculation of the docking scores.

The docking score is expressed in kcal/mol energy units and more negative scores are assigned to ligands with greater complementarity with the receptor binding pocket.

All compounds were re-docked for three times and the root mean square deviation (RMSD) values were calculated, which was always less than 1.5Å. RMSD is a common metric used to evaluate distance between the predicted pose and the native pose, given a superposition of their protein receptor structures (Eric W. Bell & Yang Zhang, 2019). The results obtained are summarized in **Table 4**.

(Kcal/mol)	FGFR1	FGFR4
V49	-26.5	-20.9
V50	-22.5	-22.19
V55	-23.4	-21.8
V51	-20.3	-20.27
V53	-8.3	-19.8
V56	-23.3	-21.46
V8	-20.1	-18.85
V9	-20.3	-18.56
V10	-19.2	-18.69
V11	-20.5	-19.42
V12	-20.4	-18.78
V14	-19.8	-18.99
V15	-20.6	-18.97
V26	-19.3	-23.86
V27	-22.4	-24.1
V28	-23.0	-23.03
V32	-22.3	-22.44
V33	-21.6	-23.41
V30	-20.3	-23.85
V31	-23.7	-23.40
V69	-22.4	-19.8
V71	-22.6	-22.8

Table 4. Docking scores, expressed in Kcal/mol, of 22 compounds against FGFR1 and FGFR4

All considered ligands show larger docking scores compared to Ponatinib, and better ADMET properties, compared to other drugs present on the market. For these reasons they all have been chemically synthesized. Pictures of the FGFR with the most promising ligands structures are reported in **Figures 18, 19, 20, 21**.

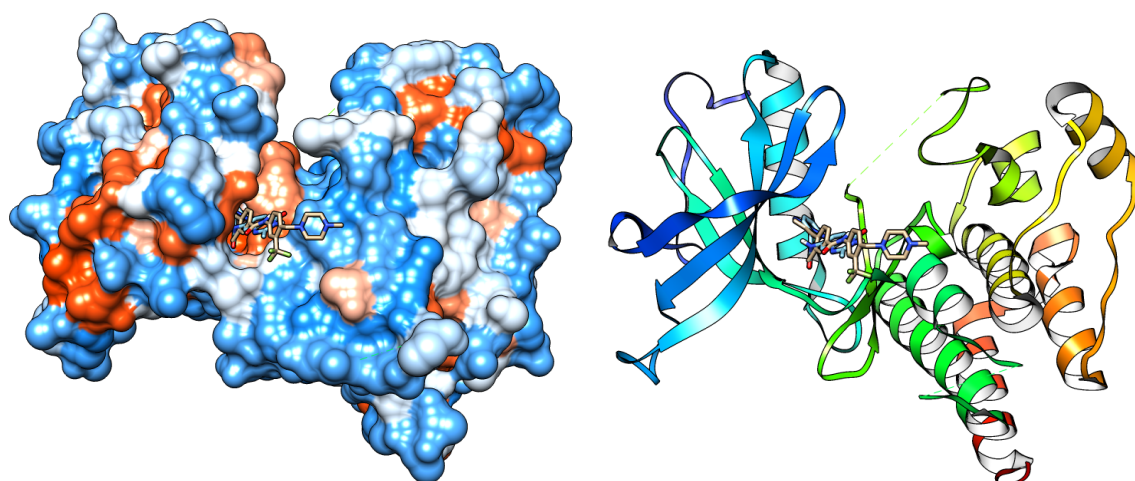


Figure 18. Docking with FGFR1 of V8 blue, Ponatinib brown, left hydrophobic surface, right ribbon

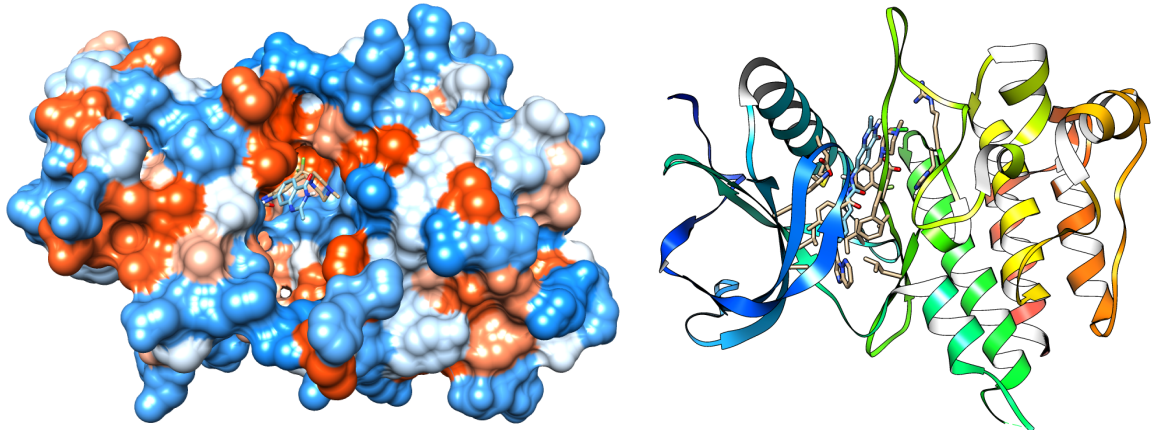


Figure 19. Docking with FGFR4 of V8 blue, Ponatinib brown, left hydrophobic surface, right ribbon

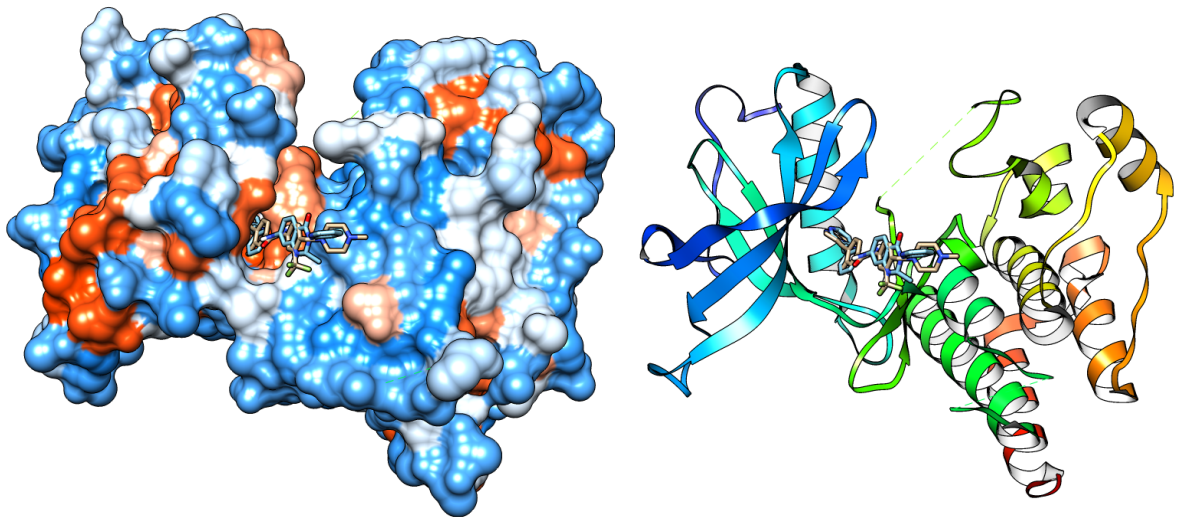


Figure 20. Docking with FGFR1 of V49 blue, Ponatinib brown, left hydrophobic surface, right ribbon

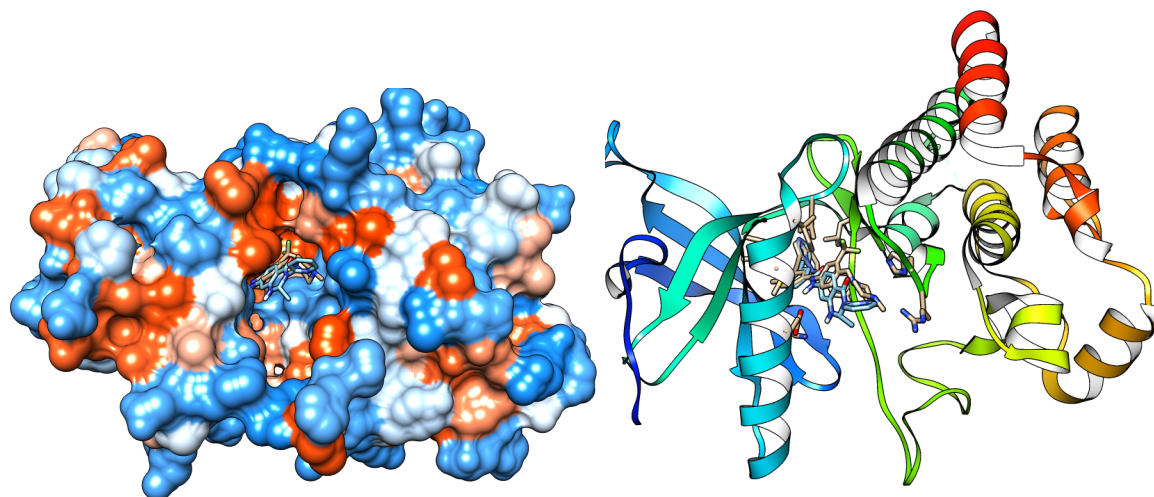


Figure 21. Docking with FGFR4 of V49 blue, Ponatinib brown, left hydrophobic surface, right ribbon

CHAPTER THREE, CHEMICAL SYNTHESIS

3.1 Chemical Synthesis

With the aim to build novel small-molecule libraries bearing diversity and complexity in their scaffolds and to fill the unknown chemical space with new potential bioactive molecules, 22 novel compounds, featuring a quinazolinone core and an amide linked to an α,β -unsaturated system, have been synthesized. Several substituents have been introduced into the scaffold in order to study the structure-activity relationship (SAR) with regard to the receptor system under consideration. On the basis of the substituents, we can group the new compounds into three series: (i) quinazolin-4(3H)ones with a substituted ethenylbenzene motif in R2 and/or R3 positions (compounds V8, V9, V10, V11, V12, V14, V15, V26, V27, V28, V31, V32, V33, V30); (ii) compounds with a 2-pyridinyl nucleus in R1, a methyl group in R2 and a substituted ethenylbenzene motif in R3 (V50, V55, V51, V53, V56; V69, V71); (iii) an analogue of V50 in which the α,β -unsaturated system was modified with the introduction of a 2-pyridinyl nucleus (V49). **Table 3** showed the chemical features of all compounds. Moreover, compounds V49, V50 and V55 were subjected to a complexation reaction with the metal cation Cu^{2+} , obtaining the new compounds V49-Cu and V50-Cu and V55-Cu respectively.

3.2 Synthesis of the molecules of group (I)

The project involved the synthesis of 7-amino-2-methylquinazolin-4(3H)-one **4** necessary for the condensation reaction with the chlorides of the **6a-g** substituted trans-cinnamic acids, to obtain the **7a-g** compounds.

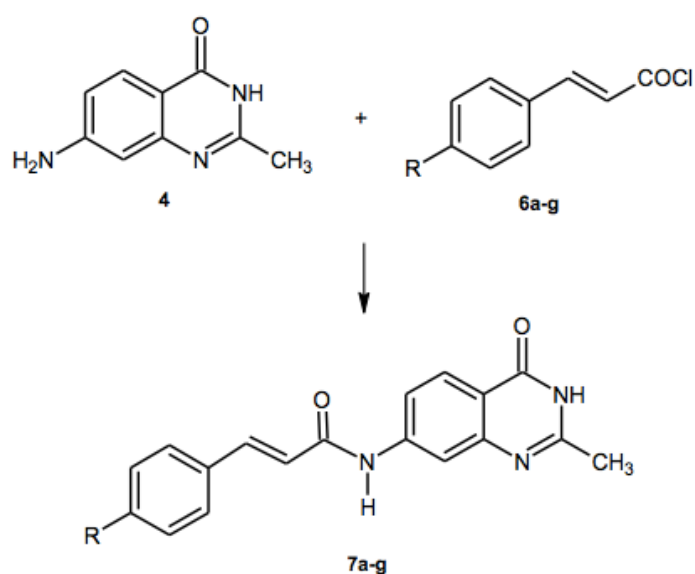
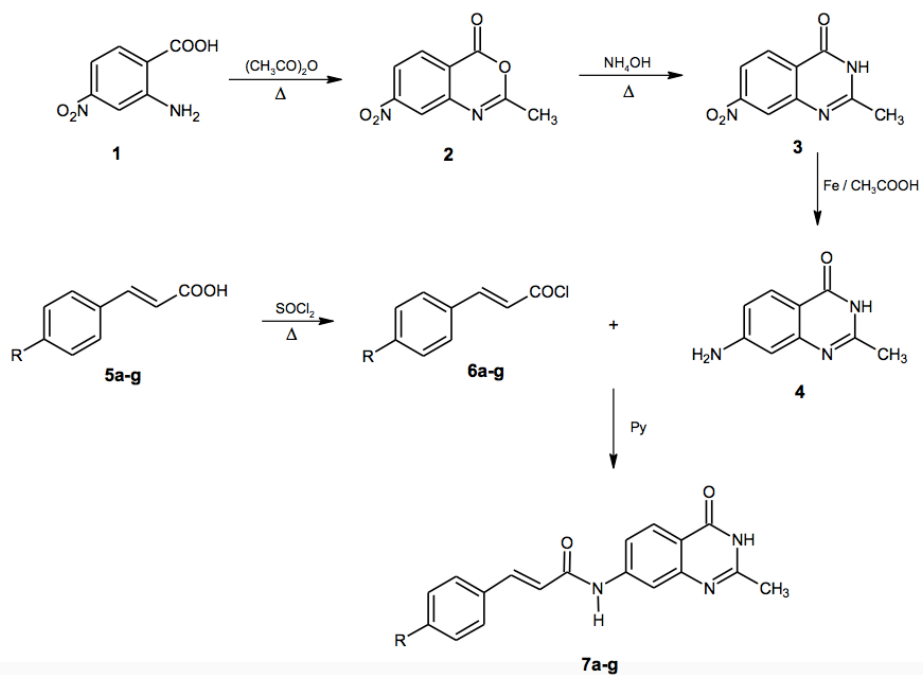


Figure 22. Condensation reaction of 7-amino-2-methylquinazolin-4(3H)-one **4** with chlorides of the **6a-g** substituted trans-cinnamic acids in order to obtain **7a-g** compounds.

The retro-synthesis studies led to the experimental protocol reported in **Scheme 1**.

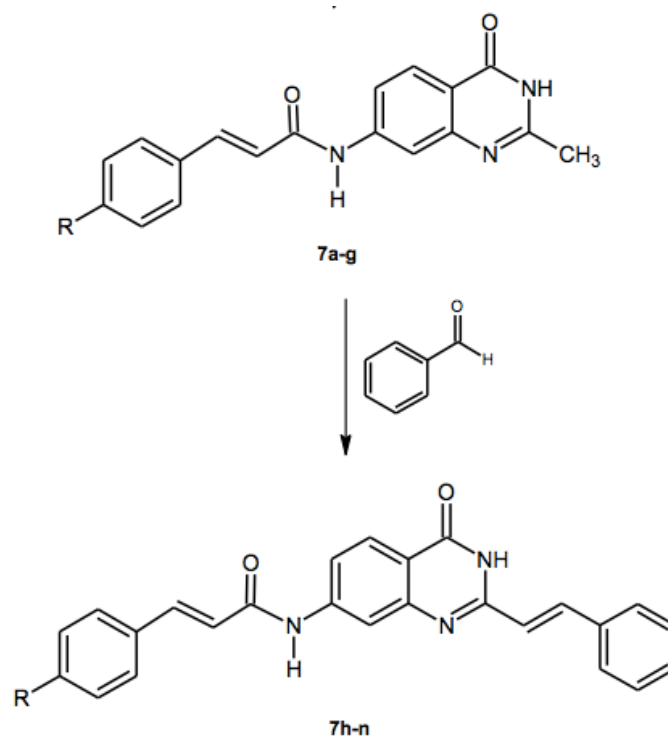
Scheme 1



	a	b	c	d	e	f	g
	V8	V15	V12	V10	V14	V11	V9
R	H	2-CH ₃	3-CH ₃	4-CH ₃	2-Cl	3-Cl	4-Cl

The 2-styrylquinazolinone compounds **7h-n** were obtained by reaction with the benzoic aldehyde of compounds **7a-g** (Scheme 2).

Scheme 2



	h	i	j	k	l	m	n
	V27	V26	V30	V32	V31	V33	V28
R	H	2-CH ₃	3-CH ₃	4-CH ₃	2-Cl	3-Cl	4-Cl

Specifically, the synthesis of the 4-quinazolinone nucleus involved the initial reaction between 2-amino-4-nitrobenzoic acid **1** and reflux acetic anhydride for 4 hours to obtain 2-methyl-7-nitro-4H -3,1-benzoxazin-4-one **2** which was subsequently transformed into 2-methyl-7-nitroquinazolin-4 (3H)-one **3** by reaction with ammonium hydroxide under reflux for 1 hour in dioxane. The reduction of the nitro group with the mixture of iron and acetic acid to 5% made it

possible to obtain 7-amino-2-methylquinazolin-4 (3H) -one **4**. Hence, the chlorides of the substituted trans-cinnamic acids **6a-g** were obtained by reaction of the respective **5a-g** acids with thionyl chloride under reflux for 5 hours. Finally, the condensation between 7-amino-2-methylquinazolin-4 (3H) -one **4** and the **6a-g** chlorides, carried out under magnetic stirring and at room temperature in pyridine for 96 h, allowed to obtain the (2E) - 3- (4-R-phenyl) -N- (2-methyl-4-oxo-3,4-dihydroquinazolin-7-yl) prop-2-enamides **7a-g**. The imine-enamine tautomerism of the 2-methylquinazolinone derivatives generates a methylene active as an electron-donor group in position 2, thus allowing the formation of an α , β -unsaturated bond by reaction with the protonated form of benzoic aldehyde in an acid environment. The derivatives (2E) -3- (4-R-phenyl) -N- {4-oxo-2 - [(E) -2-phenylethenyl] -3,4-dihydro quinazolin-7-yl} prop are thus obtained -2-enamide **7h-n** (Scheme 2).

All new compounds were identified on the basis of spectroscopic and elemental analysis data.

2-methyl-7-nitro-4H-3,1-benzoxazin-4-one **2** (Aschraf A. et al., 2003), 2-methyl-7-nitroquinazolin-4 (3H) -one **3** (Aschraf A. et al., 2003), and 7-amino- 2-methylquinazolin-4 (3H) -one **4** (Nagar A., et al., 2010) are known in the literature and therefore their spectroscopic data will not be discussed.

The ¹H-NMR spectra recorded in DMSO-d₆ of (2E)-3-(4-R-phenyl) -N- (2-methyl-4-oxo-3,4-dihydroquinazolin-7-yl) prop-2-enamides **7a-g** have the singlet that integrates at about 2.33 δ for the three protons of methyl in position 2 on the quinazolinone nucleus, the signals of the aromatic protons and the signals of the aliphatic CHs between 6.68-8.06 δ which have different multiplicities depending on substitution on the phenyl ring and the two exchangeable singlets with D₂O at about 10.64 and 12.10 δ for the NHs; for the tolyl derivatives **7b-d** we also find the singlet at about 2.34 δ which integrates for three protons. The ¹H-NMR spectra recorded in DMSO-d₆ of (2E) -3- (4-R-phenyl) -N- {4-oxo-2 - [(E) -2-phenylethenyl] -3,4-dihydroquinazolin- 7-yl} prop-2-enamides **7h-n** no longer have the singlet relative to methyl in position 2, confirming the occurrence of the

condensation reaction with the benzoic aldehyde. Instead, the area of integration of the peaks related to aromatic protons and aliphatic CHs has increased significantly in relation to the introduction of the phenylvinyl group in position 2 on the quinazolinone ring.

Also, the IR spectra recorded in KBr confirm the structures of the **7a-n** derivatives with the appearance of the bands at about 1616 and 1667 cm^{-1} relative to C = O and the bands at about 3322 and 3389 cm^{-1} relative to NH.

3.3 Synthesis of the molecules of group (II)

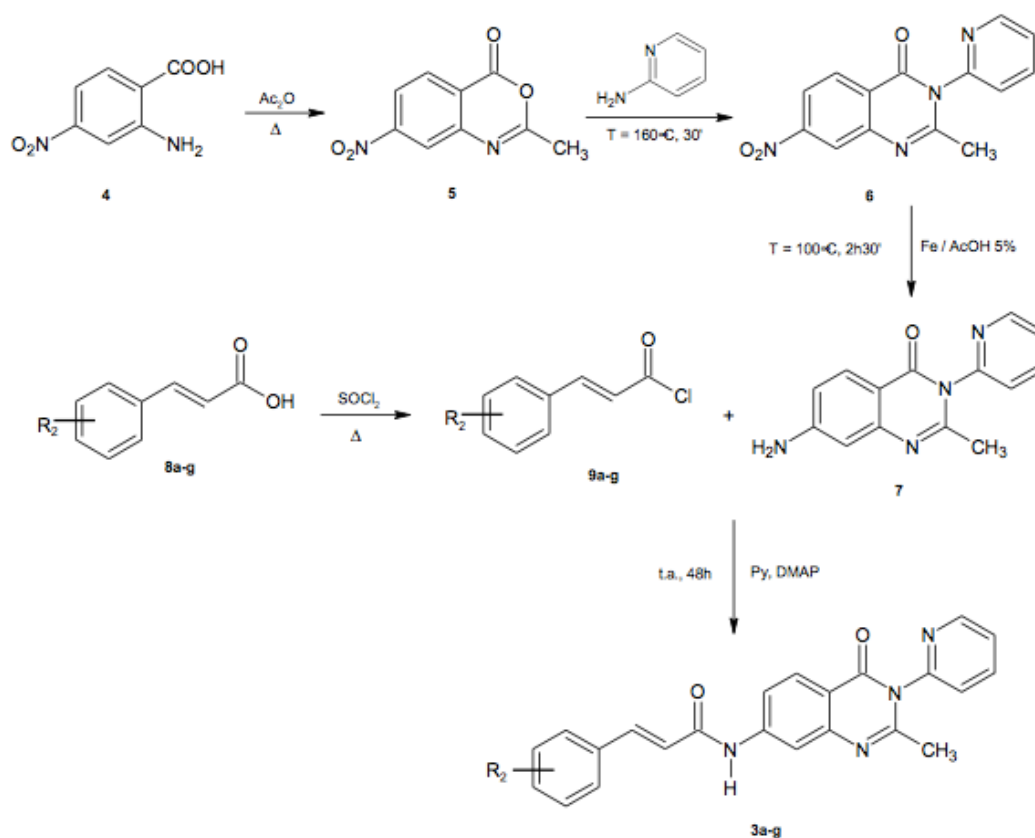
The synthetic protocol (**Scheme 3**) initially provided for the reaction between 2-amino-4-nitrobenzoic acid **4** and acetic anhydride, refluxing for 4 hours, to obtain 2-methyl-7-nitro-4H-3,1-benzoxazin-4-one **5**. The latter is very reactive to nucleophilic attack with consequent opening of the oxazinone ring. For this reason, compound **5** was used as crude for the subsequent reaction, after washing with cyclohexane.

The next step involved the formation of 2-methyl-7-nitro-3-(pyridin-2-yl)quinazolin-4(3H)-one **6**. In the literature it is reported that quinazolinones are obtained by melting at high temperatures of benzoxazinone with a primary amine. Then the reaction between compound **5** and aminopyridine was developed by fusion by varying the temperature and time parameters. After several attempts, 2-methyl-7-nitro-3-(pyridine-2-yl)quinazolin-4(3H)-one **6** was obtained by keeping the reaction mixture at 160 °C for 30 min. Purification by percolation on a column with 70-230 mesh silica gel as stationary phase and ethyl acetate as eluent, allowed to obtain compound **6** with a purity suitable for the subsequent reaction and with a yield of 50%.

The reduction of the nitro group with the suspension of iron and acetic acid to 5% allowed to obtain 7-amino-2-methyl-3-(pyridine-2-yl)quinazolin-4(3H)-one **7** in mixture with a by-product of reaction. For its purification the flash chromatography technique was applied using the CombiFlashRF200 automatic

chromatograph. This technique made it possible to isolate compound **7** with a yield of 41.4%.

Scheme 3



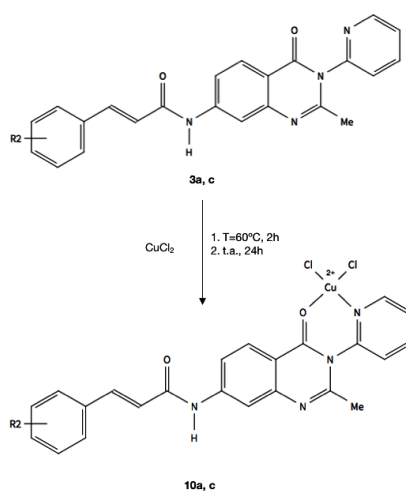
	a	b	c	d	e	f	g
	V50	V69	V55	V53	V56	V71	V51
R₂	H	2-CH ₃	3-CH ₃	4-CH ₃	2-Cl	3-Cl	4-Cl

The final reaction involves the condensation of aminoquinazolinone **7** with the chlorides of the substituted trans-cinnamic acids **9a-g**. The latter were in turn obtained by reaction of the respective acids **8a-g** with thionyl chloride, under reflux for 5 h. Finally, the condensation between 7-amino-2-methyl-3- (pyridin-2-yl) quinazolin-4 (3H) -one **7** and chlorides **9a-g**, carried out in pyridine under stirring magnetic and at room temperature, allowed to isolate the (2E) -3- (4-R-phenyl) -N- [2-methyl-4-oxo-3- (pyridin-2-yl) -3,4- dihydro quinazolin-7-yl] -3-phenylprop-2-enamides **3a-g**.

To obtain the final products with a purity greater than 95%, the amides **3a-g** were initially subjected to a crystallization with methanol to eliminate the insoluble residue, then they were chromatographed with CombiFlash RF200 using a mixture of acetate / acetone (1:1) as eluent, and finally they were crystallized from ethanol. The amides **3a-g** were isolated with a yield ranging from 17% to 66.6%.

Finally, the amides **3a-g**, and were subjected to a complexation reaction with cupric chloride in order to verify the biological potential of Cu^{2+} . The reactions were heated in ethanol at 60 °C, left under magnetic stirring for 24 h and kept at refrigeration temperature for another 24 h; the complexes **10a-g**, and were isolated by filtration and dried in an oven (**Scheme 4**).

Scheme 4



	a	c
	V50	V55
R ₂	H	3-CH ₃

All new compounds were identified on the basis of nuclear magnetic resonance spectroscopic data of proton and carbon, recorded in DMSO-d₆, and of infrared.

The ¹H-NMR spectrum of 2-methyl-7-nitro-3-(pyridin-2-yl)quinazolin-4(3H)-one **6** presents a singlet at 2.15 δ which integrates for the three protons of methyl in position 2 on the quinazolinone nucleus and a set of signals between 6.80-8.70 δ for the seven aromatic protons of the quinazolinone nucleus and of the pyridine ring. The IR spectrum confirms the presence of the carbonyl group with an intense stretching band at 1693 cm⁻¹.

The ¹H-NMR spectrum of 7-amino-2-methyl-3-(pyridin-2-yl)quinazolin-4(3H)-one **7** presents a singlet at 2.01 δ which integrates for the three protons of methyl in position 2 on the quinazolinone nucleus, a singlet exchangeable with D₂O at 6.19 δ which integrates for the two protons of the amino group and a set of signals between 6.61-8.65 δ for the seven aromatic protons of the quinazolinone nucleus and of the pyridine ring. The IR spectrum confirms the presence of the carbonyl group with an intense stretching band at 1656 cm⁻¹ and of the amino group at 3344-3415 cm⁻¹.

The ¹H-NMR spectra of (2E)-3-(4-R-phenyl)-N-[2-methyl-4-oxo-3-(pyridine-2-yl)-3,4-dihydroquinazolin-7-yl]-3-phenylprop-2-enamides **3a-g** have a singlet at about 2.10 δ which integrates for the three protons of methyl in position 2 on the quinazolinone nucleus, the signals of the aromatic Aliphatic CH between 6.88-8.69 δ which have different multiplicities according to the substitution on the phenyl ring and the singlet exchangeable with D₂O at about 10.73 δ for the amide NH; for the tolyl derivatives **3c,d** we also find the singlet at about 2.33 δ which integrates for three protons. The ¹³C-NMR spectra also confirm the presence of all the carbon atoms of the compounds **3a-g**.

Finally, the IR spectra confirm the presence of the two carbonyl groups with an intense stretching band at about 1611, 1697 cm⁻¹ and a stretching band at about 3333 cm⁻¹ relative to the NH.

The cupric complexes **10a, e** were confirmed by comparing their IR spectra with those of the ligands **3a, e**. In fact, we note the disappearance of the band relating to one of the two carbonyls, suggesting that oxygen is engaged in a coordination bond with the metal. Instead, the NH band remains and an intense band appears in the OH region at 3413 cm⁻¹ relative to the water molecules complexed by the metal.

3.3.1 Purification of compounds

Compound **6** was purified by column percolation (4.5 cm diameter) using 70-230 mesh silica gel as stationary phase and ethyl acetate as mobile phase.

Compound **7** was purified by flash chromatography using CombiFlash® RF200 automated chromatograph and 40g RediSep columns [stationary phase: silica gel: 230-400 mesh; mobile phase: mixture of ethyl acetate / acetone (1: 1)].

The final products **3a-g** were purified by methanol crystallization and flash chromatography with CombiFlash® RF200 and 40 g RediSep columns [stationary phase: silica gel: 230-400 mesh; mobile phase: mixture of ethyl acetate / acetone (8: 2)].

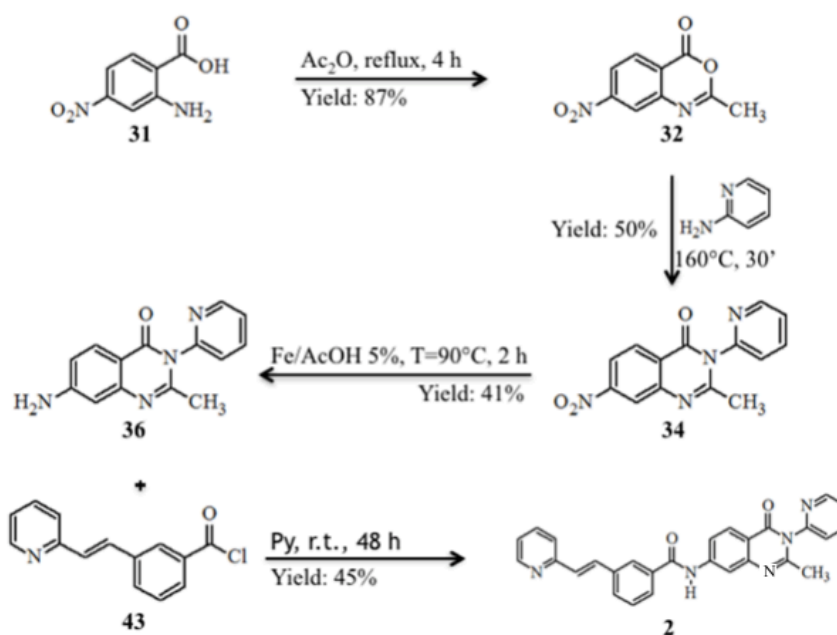
3.4 Synthesis of the molecules of group (III)

In order to obtain (*E*)-*N*-(2-methyl-4-oxo-3-(pyridin-2-yl)-3,4-dihydroquinazolin-7-yl)-3-(2-(pyridin-2-yl)vinyl)benzamide **V49**, the synthetic protocol initially envisaged the reaction between 2-amino-4-nitrobenzoic acid **31** and acetic anhydride, under reflux, for 4 hours, to obtain 2-methyl-7-nitro-4*H*-3,1-benzoxazin-4-one **32**. The latter is very reactive to the nucleophilic attack that involves opening the oxazinone ring. For this reason, compound **32** was used as crude for the subsequent reaction, after washing with cyclohexane.

2-Methyl-7-nitro-4*H*-3,1-benzoxazin-4-one **32**, after washing with cyclohexane, was subjected to a reaction with 2-aminopyridine, by melting at 160 °C, for 30 minutes, which led to obtaining a mixture, from which 2-methyl-7-nitro-3-(pyridin-2-yl)quinazolin-4(3*H*)-one **34** was isolated by washing with methanol and, subsequently, purified by column chromatography, with a yield of 50%.

Therefore, we proceeded with a reduction of the nitro group, in suspension of iron and acetic acid at 5%, for 2 h, which allowed to obtain 7-amino-2-methyl-3-(pyridine-2-yl)quinazolin-4(3*H*)-one **36**, isolated from the reaction mixture by flash chromatography, with a yield of 41%. Subsequently, compound **36** was reacted with compound **43**, in a condensation reaction, in a pyridine environment, under magnetic stirring, for 48 h, until a mixture was obtained, in turn subjected to washing in methanol, in order to eliminate insoluble impurities, and to purification with column chromatography which allowed to obtain compound **V49**. The latter was subsequently subjected to crystallization from ethanol, in order to obtain the crystalline product, with a yield of 45%. The reactions are showed in the **Scheme 5**.

Scheme 5



The synthesis of compound **40** was carried out starting from 3-iodobenzoic acid **37**, which was methylated with methyl iodide, under reflux, for 4 h. This reaction allowed to obtain methyl 3-iodobenzoate **38**, with a yield of 93%. The objective of this reaction is to mask the carboxyl group, in order to subsequently avoid obtaining an amphoteric molecule which would cause difficulties during the isolation and purification procedures of the reaction product.

Compound **38** was then subjected to a formylation reaction, in order to obtain methyl 3-formylbenzoate **39**. The reaction was carried out inside a sealed tube, kept in a water bath, at 80 °C and under magnetic stirring, for 8 h, exploiting the action of palladium chloride, iodine and triphenylphosphine which act as catalysts, triethylamine which acts as a base and formic acid which acts as a donor of a carbonaceous unit. The proposed reaction mechanism (**Figure 23**), based on experimental results, provides that, initially, iodine and triphenylphosphine generate the A complex that facilitates the release of CO from formic acid. Through a ligand exchange, the CO group is captured by the intermediate of aryl palladium B, generated by a rapid oxidative addition of palladium to aryl iodide. Following the addition of the CO group, the benzoylpalladium halide C is converted into a complex of arylpalladium and formic acid D and, simultaneously, releases HI. The final decarboxylation restores the palladium (II) which starts another catalytic cycle (P. R. Marsham, J. M. et al., 1999).

At the end of the reaction, a mixture was obtained which, following purification by column chromatography, made it possible to obtain compound **39**, with a yield of 54%. Subsequently, for the synthesis of methyl 3-[(*E*)-2-(pyridine-2-yl)ethenyl] benzoate **41**, the imine-enamine tautomerism of 2-methylpyridine was exploited which makes possible a nucleophilic attack on the formyl group of compound **39**. In particular, compound **39** was solubilized in glacial acetic acid and reacted with 2-methylpyridine, under reflux, for 130 h. The reaction mixture obtained was subjected to a purification, by column chromatography, in order to obtain the

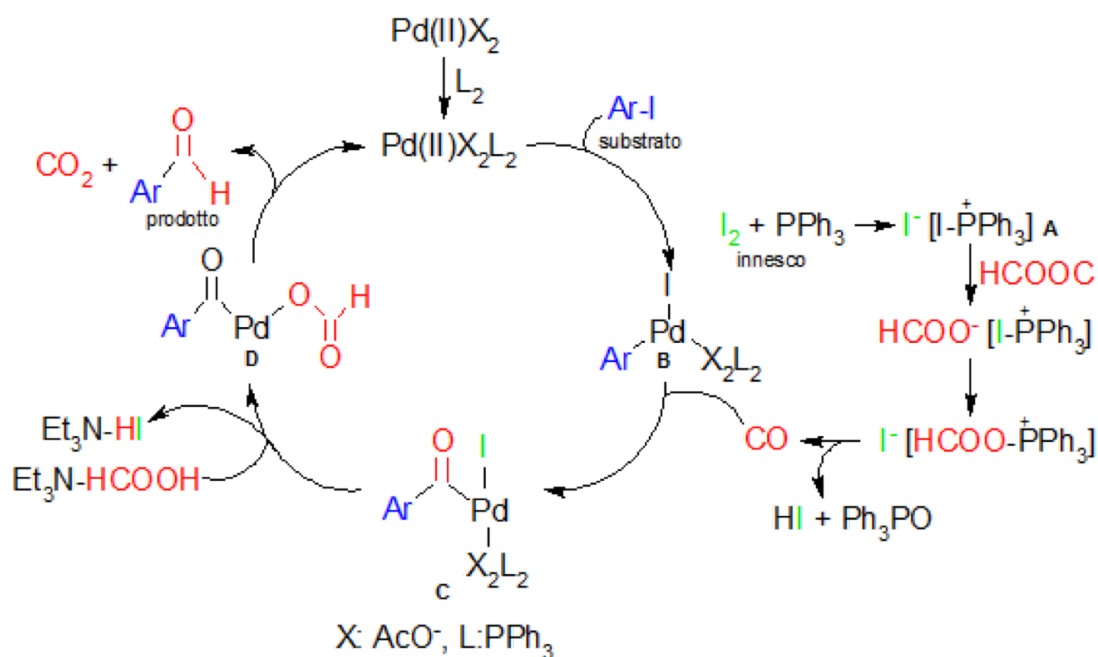


Figure 23. Proposed reaction mechanism for the synthesis of the compound **39**

compound **41**, with a yield of 51%. The configuration *E* was assigned on the basis of the calculation of the coupling *J* of the doublet at 7.24 δ relative to the vicinal protons of the CH=CH group, in the ¹H-NMR spectrum, which showed a value of 16.2 Hz. In fact, in the literature is reported that the *Z* configuration involves a coupling *J* with a value between 6 and 14 Hz, while the *E* configuration involves values between 11 and 18 Hz.

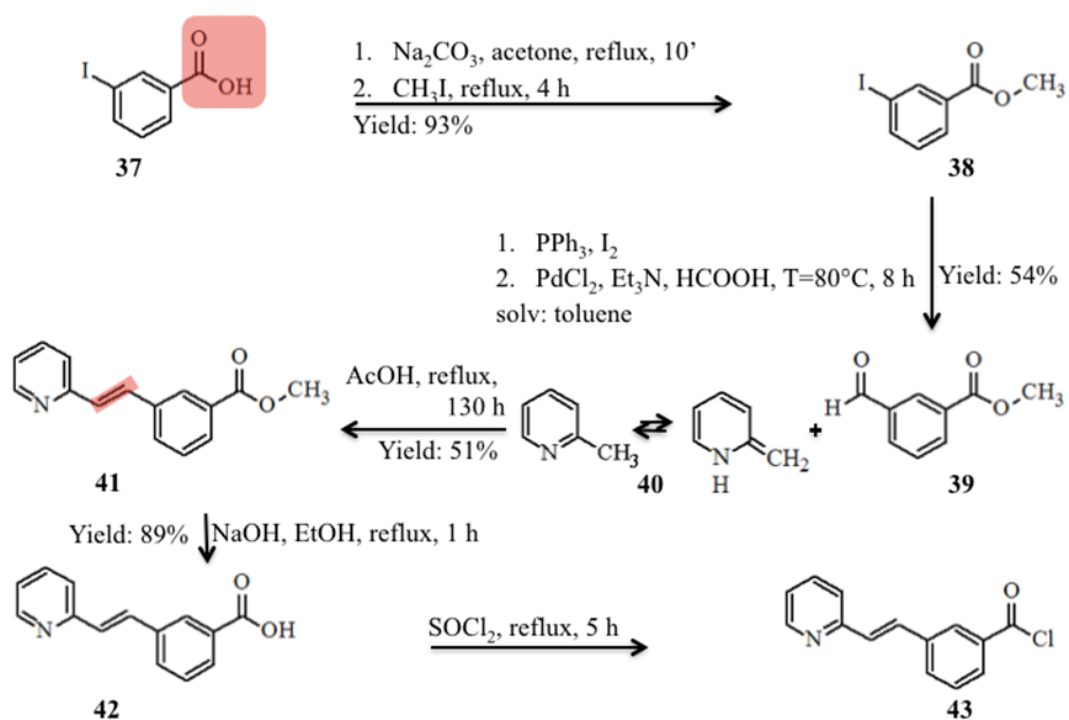
At this point it was necessary to subject the ester group of compound **41** to a basic hydrolysis that allowed the carboxylic group to be released. Therefore, compound **41** was solubilized in ethanol and, in the presence of sodium hydroxide, it was refluxed, under magnetic stirring, for 1 h. Subsequently, once the pH was brought to a value between 5 and 7, by adding 6M hydrochloric acid solution, the 3-[(*E*)-2-(pirdin-2-yl)ethenyl]benzoic acid **42** was isolated by filtration, with a yield of 89%. Finally, compound **42** was subjected to a chlorination, so as to obtain an acyl chloride which increased the reactivity in a subsequent condensation reaction. Therefore, compound **42** was subjected to the action of thionyl chloride,

at reflux, for 5 h, so as to obtain 3-[(E)-2-(pyridin-2-yl)ethenyl] benzoyl chloride **43**.

In order to obtain (E) -N- (2-methyl-4-oxo-3- (pyridin-2-yl) -3,4-dihydroquinazolin-7-yl) -3- (2- (pyridin-2 -yl) vinyl) benzamide **2**, on the other hand, 2-methyl-7-nitro-4H-3,1-benzoxazin-4-one **32**, after washing with cyclohexane, was subjected to a reaction with 2-aminopyridine, by fusion at 160 °C, for 30 minutes, which led to obtaining a mixture, from which 2-methyl-7-nitro-3- (pyridin-2-yl) quinazolin-4 (3H) -one **34**, was isolated by washing with methanol and, subsequently, purified by column chromatography, with a yield of 50%.

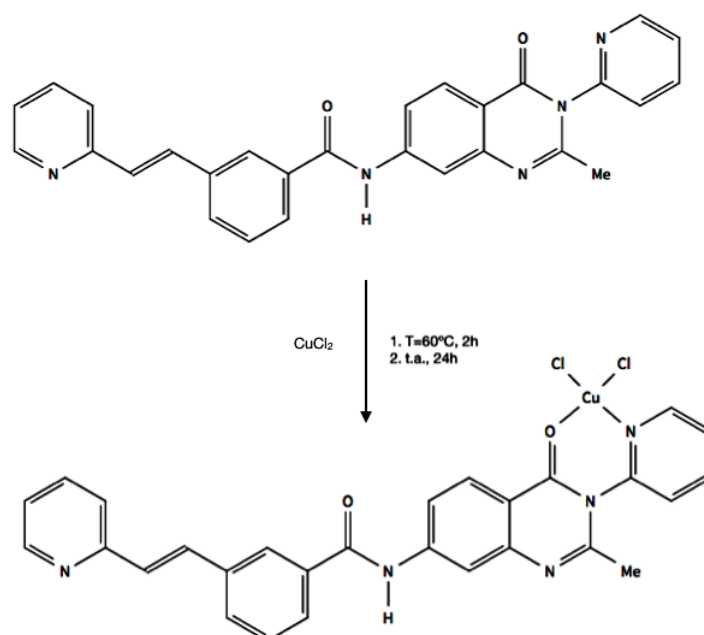
Therefore, we proceeded with a reduction of the nitro group, in suspension of iron and acetic acid at 5%, for 2 h, which allowed to obtain 7-amino-2-methyl-3-(pyridine-2-yl) quinazolin-4 (3H) -one **36**, isolated from the reaction mixture by flash chromatography, with a yield of 41%. Subsequently, compound **36** was reacted with compound **43**, in a condensation reaction, in a pyridine environment, under magnetic stirring, for 48 h, until a mixture was obtained, in turn subjected to washing in methanol, in order to eliminate insoluble impurities, and to purification with column chromatography which allowed to obtain compound **V49**. The latter was subsequently subjected to crystallization from ethanol, in order to obtain the crystalline product, with a yield of 45%. The reactions are shown in the **Scheme 6**.

Scheme 6



Compound **V49** was used for the complexation reaction with the copper (II) cation (**V49-Cu**), carried out according to **Scheme 7**.

Scheme 7



In particular, 50 mg (0.109 mmol) of compound **V49** were reacted with 14.66 mg (0.109) of CuCl₂, at 60 °C, under magnetic stirring, for 2 h. Thereafter, the reaction mixture was cooled to room temperature and kept under magnetic stirring for 24 h. Finally, the mixture was kept at 4 °C for 24 h. Finally, the **V49-Cu** complex was isolated by filtration, with a yield of 50%.

All new compounds were identified on the basis of nuclear magnetic resonance spectroscopic data of proton and carbon, recorded in DMSO-d₆, and of infrared analysis.

The ¹H-NMR spectrum of 2-methyl-7-nitro-3-(pyrimidin-2-yl)quinazolin-4(3*H*)-one **33** presents a singlet at 2.18 δ which integrates for the three protons of methyl in position 2 on the quinazolinone nucleus and a set of signals between 7.81-9.15 δ for the six aromatic protons of the quinazolinone nucleus and of the pyrimidine ring. The IR spectrum confirms the presence of the carbonyl group with an intense stretching band at 1695 cm⁻¹.

The ¹H-NMR spectrum of 2-methyl-7-nitro-3-(pyridin-2-yl)quinazolin-4(3*H*)-one **34** presents a singlet at 2.15 δ which integrates for the three protons of methyl in position 2 on the quinazolinone nucleus and a set of signals between 6.80-8.70 δ for the seven aromatic protons of the quinazolinone nucleus and of the pyridine ring. The IR spectrum confirms the presence of the carbonyl group with an intense stretching band at 1693 cm⁻¹.

The ¹H-NMR spectrum of 7-amino-2-methyl-3-(pyrimidin-2-yl)quinazolin-4(3*H*)-one **35** presents a singlet at 2.02 δ which integrates for the three protons of methyl in position 2 on the quinazolinone nucleus, a singlet exchangeable with D₂O at 6.27 δ which integrates for the two protons of the amino group and a set of signals between 6.63-9.07 δ for the six aromatic protons of the quinazolinone nucleus and of the pyrimidine ring. The IR spectrum confirms the presence of the carbonyl group with an intense stretching band at 1670 cm⁻¹ and of the amino group at 3344-3423 cm⁻¹.

The $^1\text{H-NMR}$ spectrum of 7-amino-2-methyl-3-(pyridin-2-yl)quinazolin-4(3*H*)-one **36** presents a singlet at 2.01 δ which integrates for the three protons of methyl in position 2 on the quinazolinone nucleus, a singlet exchangeable with D_2O at 6.19 δ which integrates for the two protons of the amino group and a set of signals between 6.61-8.65 δ for the seven aromatic protons of the quinazolinone nucleus and of the pyridine ring. The IR spectrum confirms the presence of the carbonyl group with an intense stretching band at 1656 cm^{-1} and of the amino group at 3344-3415 cm^{-1} .

The $^1\text{H-NMR}$ spectrum of methyl 3-iodobenzoate **38** shows a deshielded singlet at 3.92 δ which integrates for the three protons of methoxyl and a set of signals between 7.18-8.38 δ for the four aromatic protons of phenyl. The IR spectrum confirms the presence of the carbonyl group with an intense stretching band at 1705 cm^{-1} .

The $^1\text{H-NMR}$ spectrum of methyl 3-formylbenzoate **39** shows a singlet deshielded at 3.88 δ which integrates for the three protons of methoxyl, a set of signals between 7.70-8.40 δ for the four aromatic protons of phenyl and a singlet at 10.07 δ which integrates for a proton of the aldehyde CH. The IR spectrum confirms the presence of the two carbonyl groups at 1688, 1730 cm^{-1} .

The $^1\text{H-NMR}$ spectrum of methyl 3-[(*E*)-2-(pyridine-2-yl)ethenyl]benzoate **41** shows a deshielded singlet at 3.94 δ which integrates for the three protons of methoxyl, a set of signals ranging from 7.13-8.62 δ for the eight aromatic protons of phenyl and pyridine and for the two aliphatic CHs ($J = 16.2$ Hz). The IR spectrum confirms the presence of the carbonyl group with an intense stretching band at 1708 cm^{-1} .

The $^1\text{H-NMR}$ spectrum of 3-[(*E*)-2-(pyridin-2-yl)ethenyl]benzoic acid **42** shows a signal set between 7.25-8.59 δ for the eight aromatic protons of phenyl and pyridine and for the two aliphatic CHs and the singlet enlarged to 13.15 δ of OH, exchangeable with D_2O . The IR spectrum confirms the presence of the carbonyl group with an intense stretching band at 1700 cm^{-1} and a band at 3464 cm^{-1} for OH.

The $^1\text{H-NMR}$ spectra of (*E*)-*N*-(2-methyl-4-oxo-3-(Het-2-yl)-3,4-dihydroquinazolin-7-yl)-3-(2-(pyridin-2-yl)vinyl)benzamides **1,2** have a singlet at about 2.11 δ which integrates for the three methyl protons in position 2 on the quinazolinone nucleus, the signals of the aromatic protons and the signals of the aliphatic CHs between 7.32-8.70 δ and the singlet exchangeable with D_2O at about 10.78 δ for the amide NH. The IR spectrum confirms the presence of the two carbonyl groups at about 1668, 1679 cm^{-1} and the band at about 3300 for the amide NH.

The formation of the cupric **49-Cu** complex was confirmed by comparing its IR spectrum with that of ligand **V49**. In fact, the disappearance of the band relating to one of the two carbonyls is noted, suggesting that oxygen is engaged in a coordination bond with the metal. Instead, the NH band remains and an intense band appears in the OH region at 3445 cm^{-1} relative to the water molecules complexed by the metal. The elementary analysis of the complex was performed in order to confirm the structure.

3.4.1 Compounds isolation and purification

Compound **34** was isolated from the reaction mixture, by washing with methanol, and purified by column chromatography, using Merck silica gel, 70-230 mesh ASTM, (170 g) and ethyl acetate, as mobile phase.

Compound **36** was isolated from the reaction mixture, by CombiFlash® RF200 automated flash chromatography, using RediSep columns, Merck silica gel, 230-400 mesh ASTM (60 g), as stationary phase, and an ethyl acetate /acetone (1:1) mixture, as the mobile phase.

Compounds **39** and **41** were purified by column chromatography, using Merck silica gel, 70-230 mesh ASTM (250 g), as stationary phase, and a cyclohexane/ethyl acetate (7:3) mixture, as mobile phase .

Compound **V49** was isolated from the reaction mixture by washing with methanol. It was then purified by column chromatography, using Merck silica gel, 70-230 mesh ASTM (150 g), as the stationary phase, and an ethyl acetate /

acetone (1:1) mixture, as the mobile phase. Subsequently, compound **2** was subjected to crystallization from ethanol, in order to obtain a crystalline product. The **V49-Cu** complex was isolated from the reaction mixture by filtration.

CHAPTER FOUR, BIOLOGICAL EVALUATION

4.1 Screening of new drugs

The biological activity of the 25 new drug candidates toward 23 cancer cell lines (Table 5) was investigated, initially by screening cell viability through MTT assay.

Tumor Cell lines	Type
DMS114	human carcinoma, small cell lung cancer
NCIH-1703	human lung squamous, non-small cell lung cancer
NCI-H520	human squamous cell carcinoma
U251-MG-Ctr /GFP /Arg /Gly /KA /KD	human glioblastoma multiforme
BTL1528-GFP/Gly	human glioblastoma
Daoy	desmoplastic cerebellar medulloblastoma
Siwa	human glioblastoma multiforme
UMUC 14 and UMUC 14 Ponatinib resistance	human transitional cell carcinoma of the renal pelvis
VMCUB1	bladder carcinoma
RKO/wt	human colon carcinoma
A431	human epidermoid carcinoma
PC9	lung adenocarcinoma from Lymph node
BTL1376/26	human glioblastoma multiforme
HCT116 p53/wt	colon carcinoma
HCT116 p53/KO	colon carcinoma
K562	chronic myelogenous leukemia (CML)

Table 5. Cell lines and the corresponding tumor type used in all experiments

Some of the IC₅₀ values obtained are shown in **Table 6**.

IC ₅₀ (μM)	DMS114	NCI-H1703	NCI-H520	U251-MG-Gly	U251-MG-GFP	PC9
V49	16.46	26.46	>50	28.4	29.31	24.01
V50	>50	>50	>50	>50	>50	>50
V55	40.97	>50	>50	>50	>50	>50
V51	15.39	5.514	>50	—	—	—
V53	>25	>25	>25	>25	>25	>25
V56	17.04	15.43	—	>25	>25	>25
V8	3.5	13.5	24.4	7.18	7.84	>25
V9	>25	>25	>25	>25	>25	>25
V10	>25	13.05	>25	>25	>25	>25
V11	9.5	>25	>25	>25	>25	>25
V12	>25	>25	>25	>25	>25	>25
V14	>25	>25	>25	>25	>25	>25
V15	>25	>25	>25	>25	>25	>25
V26	>25	>25	—	—	—	>25
V27	6.23	>25	—	—	—	>25
V28	13	24.9	—	—	—	>25
V32	>25	46.5	—	>25	>25	—
V33	>25	19.7	—	—	—	>25
V30	>25	>25	—	—	—	—
V31	>25	>25	—	—	—	—
V69	>25	>25	40.28	—	—	—
V71	>25	>25	—	—	—	—

Table 6. IC₅₀ values of 22 synthesized molecules against DMS114, NCI-H1703, NCI-H520, U251-MG-Gly, U251-MG-GFP and PC9. Only some cell lines tested are shown in the table.

Results not shown are non-significant, since the activity of the corresponding molecules was observed at concentration higher than 50 μ M. The less active molecules have not been tested on all cell lines to reduce times and costs.

According to the MTT assay, V49, V49-Cu and V8 were the molecules with the more promising biological activity. These three compounds were found to be particularly selective for both lung and glioblastoma cancer cell lines, while they did not show significant activity at low doses in other cancer cell lines. Other molecules with moderate anti-proliferative activity were V55, V55-Cu, V51, V56, V11, V27, V28, which showed activity towards lung cancer, but not against glioblastoma.

For this reason, more in-depth studies have been made with V49, V49-Cu and V8 to deepen their possible mechanism of action.

4.2 Structure - Activity Relationship studies (SAR)

The structure-activity relationship (SAR) is the relationship between the chemical structure of a molecule and its biological activity. SAR analysis allows to determine the chemical group responsible for the biological effect in the organism (Guha R., 2013).

SAR analysis of all compounds were conducted on SCLC (DMS114) (**Table 7**) and NSCLC (NCI H1703) (**Table 8**) cell lines.

The introduction of a chlorine atom into the ethenylbenzene motif (R3) improved the activity towards both tumors, SCLC and NSCLC cell lines. In fact, among the six compounds able to inhibit the cell growth of both tumors, three of them (V51, V56, V28) bear a chlorine atom in the ethenylbenzene motif. Also, compounds V51, V49, V56 bear a pyridine nucleus in R₁ position and a methyl group in R₂. Replacing *para*-Cl atom of ethenylbenzene with a *meta*-methyl group causes loss of activity towards both tumors. Furthermore, the activity is maintained on both cell lines when R₂ = CH₃ and R₁ and R₃ are not substituted.

NSCLC (NCI-H1703)	μM
V51	5.51
V10	13.05
V8	13.5
V56	15.43
V33	19.7
V28	24.9
V49	26.46

Table 7. IC₅₀ values of V51, V10, V8, V56, V33, V28, V49 against NCI-H1703 (NSCLC tumor cell line).

SCLC (DMS114)	μM
V8	3.5
V27	6.23
V11	9.5
V28	13
V51	15.39
V49	16.46
V56	17.04
V55	40.97

Table 8. IC₅₀ values of V8, V27, V11, V28, V51, V49, V56, V55 against DMS114 (SCLC tumor cell line).

Interesting, compounds not substituted in R1 showed a selectivity against SCLC cell line, like compounds V8, V27 and V11 with IC₅₀ values of 3.5, 6.23 and 9.5 μM , respectively, while compound V51, bearing a pyridine nucleus in R1, showed the better activity against a NSCLS cell line with an IC₅₀ of 5.51 μM .

Within the group of molecules substituted in R1 with pyridine and in R2 with a methyl group (V49, V50, V55, V51, V53, V56; V69, V71) we noticed a loss of activity with the introduction of a methyl in the ethenylbenzene motif (R3) and of a *meta*-chlorine in the ethenylbenzene (R3), acquiring strong activity when there is a *para*-chlorine, and a lower activity when the chlorine is in *ortho*-position in the ethenylbenzene (R3). Furthermore, the *para*-chlorine favored the activity towards NSCLC.

Within the group of molecules substituted in R1 = H and R2 = methyl (V8, V9, V10, V11, V12, V14, V15) we noticed a loss of activity when the ethenylbenzene motif (R3) is replaced with a methyl group in positions 2 and 3 or with a chlorine

atom in positions 2 and 4. Interesting, the activity is increased when chlorine is in position 4 or a methyl group is in *meta*-position.

Within the group of molecules substituted in R1 = H and R2 = ethenylbenzene (V26, V27, V28, V31, V32, V33, V30, V31) we noticed a loss of activity when chlorine is present in the ethenylbenzene motif (R3), and when a *meta*-methyl is present. Notable, there is an increase in activity when the methyl is in *para*-position or when the ethenylbenzene is not substituted.

Finally, when phenylethenyl pyridine is present in R3, the activity remains similar in both SCLC and NSCLC.

4.3 Copper (II) complexes

Among the three copper (II) complexes synthesized (V49-Cu, V50-Cu and V55-Cu), V49-Cu appeared to have a better activity (7.04 μ M with DMS114), especially on the DMS114 cell line, as well as its V49 ligand (16.46 μ M with DMS114). The IC₅₀ values with DMS114 of three ligands (V49, V50, V55) and the three metal complexes (V49-Cu, V50-Cu, V55-Cu) are shown in the **Table 9** and the crystal violet staining for cell survival with the same compounds and the same cell line is show in the **Figure 24**.

IC ₅₀ (μ M)	V49	V49-Cu	V50	V50-Cu	V55	V55-Cu
DMS114	16.46	7.04	> 50	> 50	40.9	13.5

Table 9. IC₅₀ values of V49, V49-Cu, V50, V50-Cu, V55, V55-Cu with DMS114 tumor cell line and 72 h of treatment.

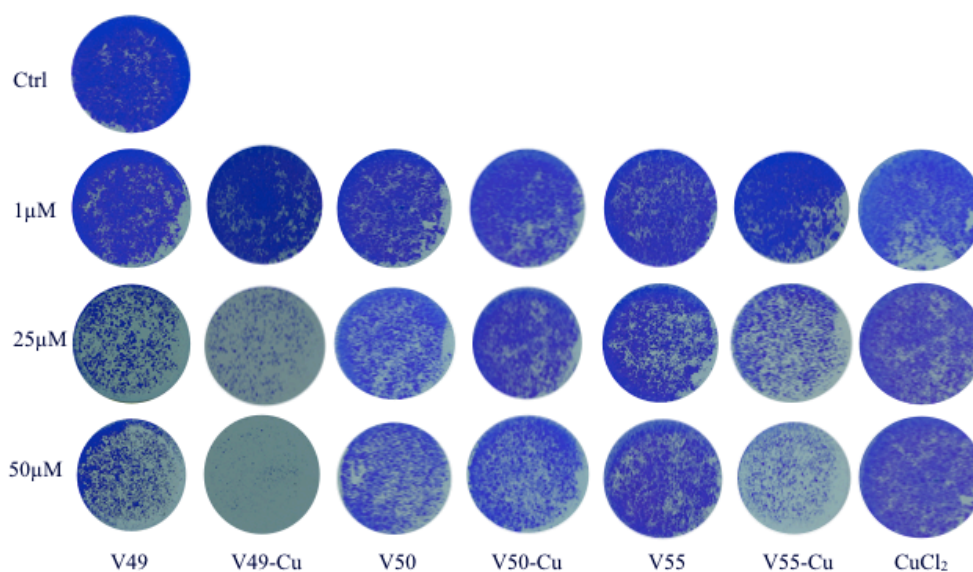


Figure 24. Crystal violet with DMS114 cell line treated for 72 h with V49, V49-Cu, V50, V50-Cu, V55, V55-Cu and CuCl₂ control 1 μ M, 10 μ M, 25 μ M and 50 μ M

The reason of the weaker activity of the V49 ligand was attributed to its lower solubility in biologically compatible media. In fact, as obvious from **Figure 25**, the compound forms crystals visible under the microscope. Interestingly, as expected, the solubility of V49 is greatly improved by the coordination of V49 with copper (**Figure 26**). To improve the solubility of V49 in the cell medium, it was diluted from a 10 mM DMSO stock solution to a medium enriched with 20% FBS. In this way, the IC₅₀ value of V49 against NCI-H1703 decreased from 42.825 μ M to 26.46 μ M.

However, its copper complex, V49-Cu, always showed a remarkably higher activity. The explanation of the improved solubility in aqueous media can be found on the positive charge of the metal complex, that in addition favors cell membrane crossing.

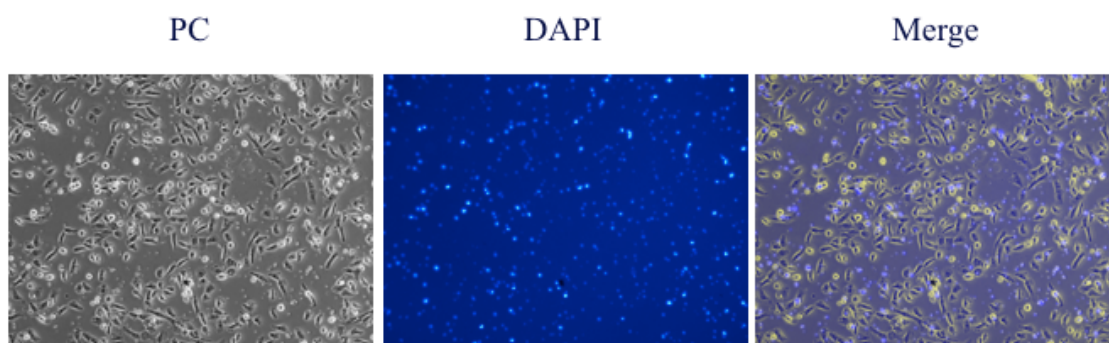


Figure 25. Images with the fluorescence microscope with DMS114 cell line and V49 10 μ M, on left in the phase-contrast (PC), in the center is DAPI, excited with ultraviolet light and detected through a blue/cyan filter and on the right picture PC and DAPI merged. The blue spots are the small crystals of V49 in the cell medium.

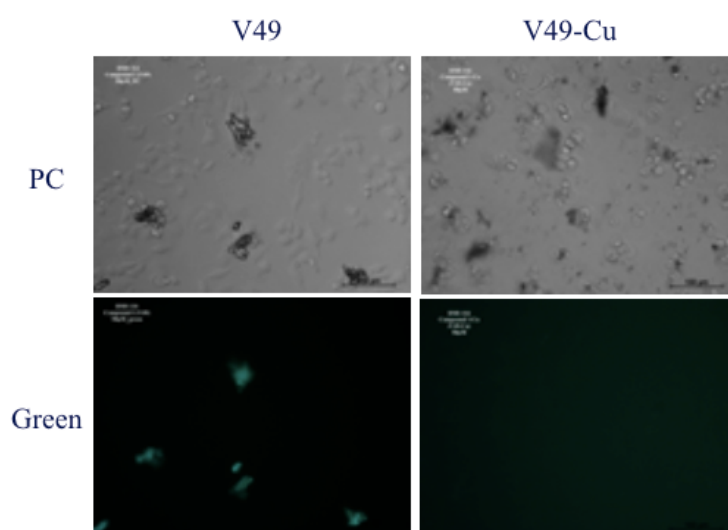


Figure 26. Images with the fluorescence microscope with DMS114 cell line and V49 (left) and V49-Cu (right) both 10 μ M. Phase-contrast (PC) and green fluorescence. The crystals of V49 are fluorescent, while with V49-Cu no insoluble crystals are formed. The black things visible with PC and V49-Cu are apoptotic bodies from dead cells.

4.3.1 DCF-DA ROS formation assay

To understand if the activity of the V49-Cu copper complex was derived from generation of ROS inside the cell under normoxic conditions, the DCF-DA assay was performed using H_2O_2 as a positive control (**Figure 27**). Interestingly, ROS dynamically affect the cancer microenvironment and are known to initiate cancer angiogenesis, metastasis, and survival at varying concentrations. At moderate concentrations, ROS activate the tumor cell survival signaling cascade. At high concentrations, ROS can cause apoptosis of cancer cells (Aggarwal V, et al., 2019). The goal was to obtain a metal compound stable under normoxic conditions and therefore unable to generate ROS.

The result obtained was encouraging, since the fluorescence intensity corresponding to the ROS levels inside the cells in a normoxic environment was comparable for V49 and V49-Cu. This result confirms that the presence of copper improves the cytotoxic properties of its free ligand and that its activity is not attributable only to the known $2^+/1^+$ redox equilibrium of the copper atom, inducing the formation of ROS by a Fenton-like activity. The interpretation of this

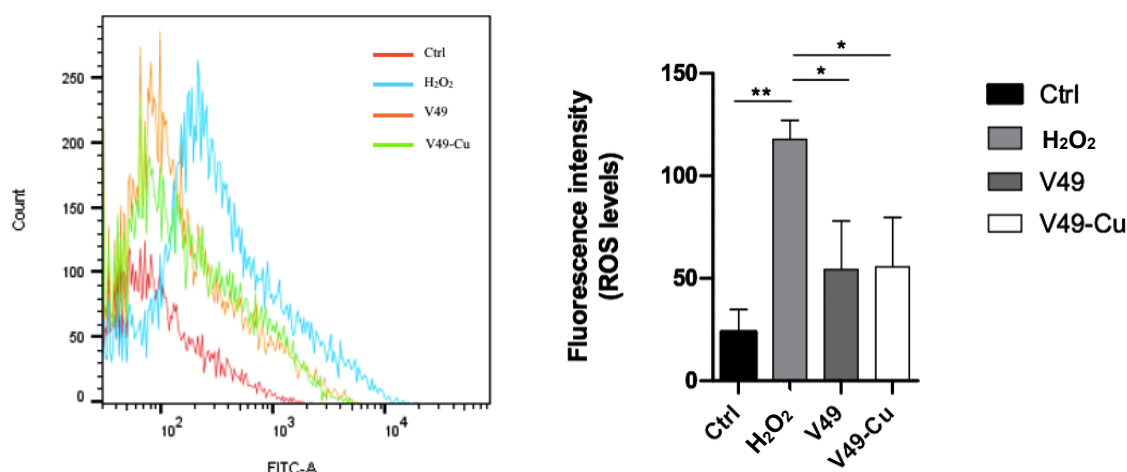


Figure 27. ROS formation assay, via DCF-DA. In the left flow cytometry elaboration results and in the right the quantification of ROS levels. The assay was performed for three times with V49 and V49-Cu 25 μ M. H_2O_2 was used like a positive control. The cells (DMS114 and K562) were treated for 1 h.

result can be given in terms of the coordination chemistry of copper complexes. It is in fact known that the reduction of Cu(II) to Cu(I) in hypoxic conditions weakens the coordination bonds with the ligand. As a consequence, under such conditions, the ligand can be detached from the metal ion and, being inside the cytoplasm, the ligand can reach the biotarget and inhibit its biological activity. Besides, the Cu-V49 complex, in the higher oxidation state of the Cu(II) ion, being positively charged, can cross the cell membrane more easily than the V49 isolated and neutral ligand. In conclusion, Cu-V49 can be considered as a prodrug which is activated by the hypoxic conditions, characteristic for most cancers. The experiment was also performed cell free, always was obtaining the same result observable with the fluorescence microscope (**Figure 28**).

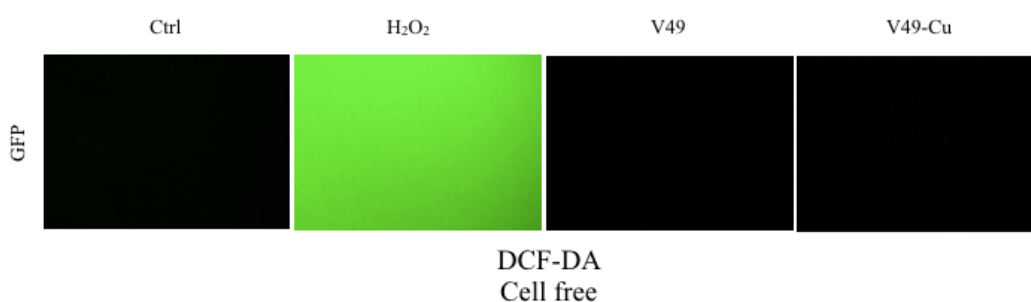


Figure 28. ROS formation assay, via DCF-DA cell free. The drugs V49 and V49-Cu and the positive control (H₂O₂) were incubated with DCF-DA for 1 h. The positive control is DCF-DA alone. The images were taken with the fluorescence microscope.

The experiments were conducted only in common incubators under normoxic conditions, as such an experiment technically cannot be conducted in incubators which maintain hypoxic conditions.

4.3.2 Hypoxic and normoxic environments

Hypoxia is a known characteristic of the cancer microenvironment and resistance to chemotherapy is often caused by several factors related to hypoxia (Spiegelberg L, et al., 2019). Therefore, targeting cancer hypoxia is a research hotspot for cancer therapy.

To investigate the ability of the copper complex to behave as a prodrug possibly activated in a hypoxic environment, viability assays of cells treated in normoxic (21% of oxygen) and hypoxic conditions (1% of oxygen) were performed using DMS114, NCI H520 and NCI H1703 FGF-driven lung cancer cell lines (**Figure 29**).

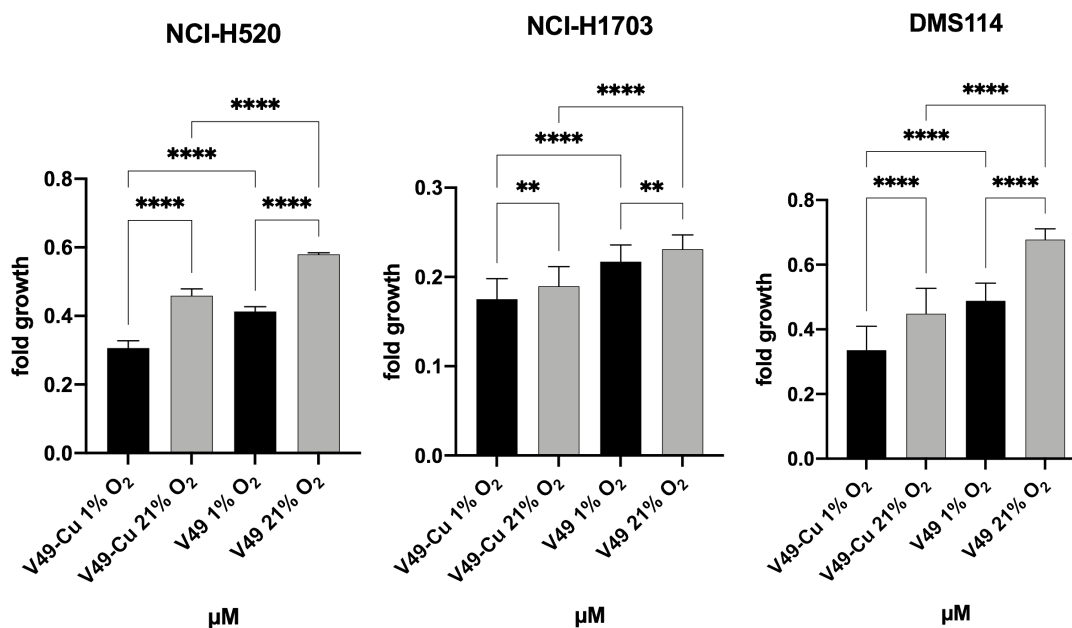


Figure 29. MTT results in normoxic (21% of oxygen) and hypoxic (1% of oxygen) environments. The experiments were performed with three cell lines: NCI H520, NCIH 1703 and DMS114 for three times in triplicates. The drugs were used in the same standard concentration of 10 μM. Untreated control are set as 1.

The difference in activity between V49 and V49-Cu is always statistically significant even in a hypoxic environment. V49-Cu shows an increasingly higher activity particular in hypoxic environment. An unusual finding was that V49 also exhibits improved activity in hypoxic conditions. This is not a feature of many anticancer agents, even those clinically approved, where it is in fact known that almost all drugs dramatically lose their activity.

This could open new perspectives on the use of 2-methyl-quinazolinon -4 (3H) ones as prodrugs that can be activated in a hypoxic environment. In fact, this mechanism, in the absence of metals, is known for several molecules such as: quinones, nitroaromatics / nitroimidazole, N-oxides (Zeng Y, et al., 2018), but studies on quinazolinones and hypoxia are missing.

4.3.3 Apoptosis assay

Cell apoptosis assays have been significantly improved by the introduction of methods based on flow cytometry. Propidium iodide (PI) is widely used in combination with annexin V to determine whether cells are viable, apoptotic or necrotic, based on differences in plasma membrane integrity and permeability (Rieger AM, et al 2011).

Generally, two modes of cell death can be distinguished: apoptosis, or programmed cell death, and necrosis, a form of traumatic cell death.

Apoptosis plays a regulatory function during the development and homeostasis of tissues. The “suicide” of cells is activated and controlled by a precise program of intracellular cell death execution mechanisms. It results in characteristic morphological changes such as membrane blebbing, cell shrinkage, nuclear fragmentation, and chromatin condensation. Phosphatidylserine (PS) is found on the cytoplasmic side of the cell membrane in healthy cells. In apoptotic cells PS appears on the extracellular surface of the membranes. A fluorescein

isothiocyanate (FITC) conjugated form of annexin V is used to detect PS-exposing cells thereby marking apoptotic cells. However, due to membrane disintegration during necrosis, annexin V will also bind to intracellularly located PS in dead, necrotic cells. Therefore, the cell impermeable dye PI is added to distinguish among apoptotic and necrotic cells. The ability of PI to enter a cell depends on the permeability of the membrane. PI does not stain live cells because the plasma membrane is intact. In late apoptotic and necrotic cells, the integrity of plasma and nuclear membranes decreases thus allowing PI to pass through membranes, intercalate in nucleic acids and display a red fluorescence.

In this way the early apoptotic cell will be sensitive only to annexin V staining, while the late apoptotic cell will be marked by both annexin V and PI. Necrotic cells, on the other hand, will only be positive for PI.

Subsequently, to discern between apoptotic or necrotic activity mechanism, of the two drug candidates V49 and V49-Cu, an annexin-V-FITC and PI were used to detect apoptotic cells from intermediate to advanced stages (**Figure 30**).

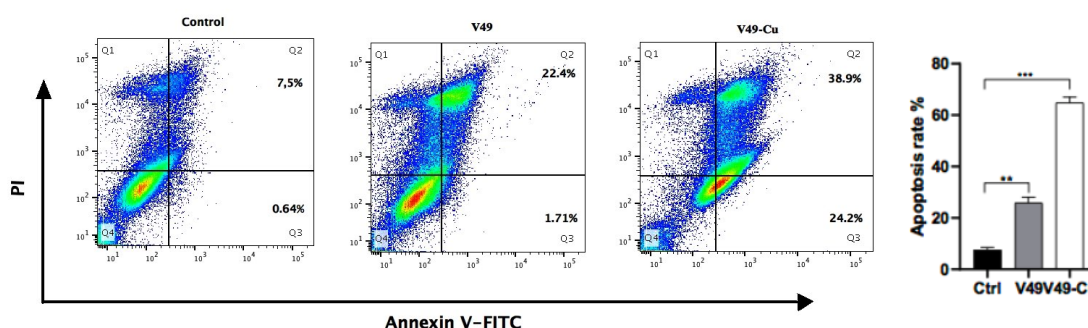


Figure 30. Annexin-V-FITC / PI assay used to understand the mechanism of cell death induced by drugs V49 and V49-Cu 10 μ M, incubated with DMS114 for 24 h, with quantifications of the results on the right panel.

The results of the apoptosis assay also provided encouraging data, confirming that treatment with 10 μ M of V49 and V49-Cu induces apoptosis in 24.11% and 63.1% of cells, respectively. The results are statistically significant.

In the upper quadrant Q1, necrotic cells are present (positive only to the PI), in Q2 the cells in late apoptosis (positive both to PI and annexin V), in lower Q3 in early

apoptosis (positive only for annexin V) and in Q4 the living cells (negative to both PI and annexin V). A small percentage of cells, even in the untreated control, undergoes necrosis due to the stress experienced by the experiment.

4.3.4 Cell cycle analysis

Cell cycle can be determined by staining the DNA with a fluorescent dye, such as IPI. The dye stains DNA stoichiometrically, allowing to differentiate cells regarding their position in the cell cycle into G₀ / G₁, S and G₂ / M phases.

G₁ and G₂ are phases of protein translation, growth and monitoring of the internal and external environment. S is the DNA synthesis phase, and M is the division phase (Christopher C. Mills, EA. et al., 2017).

G₁ has variable length, depending on external conditions and on the signals coming from other cells; if the external conditions are not favorable, the cell does not progress in the cycle and can even enter a specialized condition of rest (G₀). If growth and division signals arrive, the cell in initial G₁ or in G₀ phases proceeds in G₁ to the start point (or restriction point) after which the cell is commissioned in S even if the growth signals are removed (**Figure 31**) (Bai J, Li Y, Zhang G. 2017).

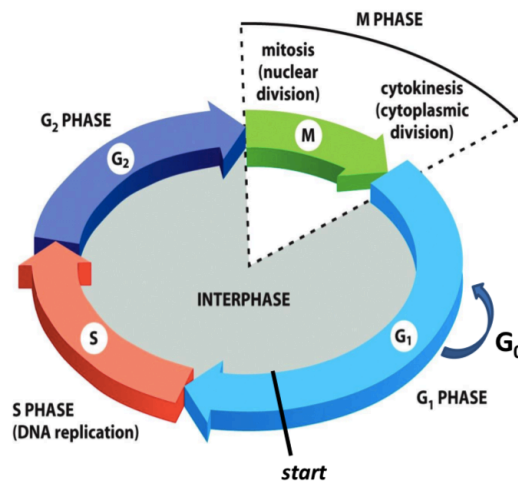


Figure 31. The phases of the cell cycle

Cell cycle progression is controlled by specific molecular mechanisms (checkpoints) that primarily operate at the level of phase transitions (G₁ / S, G₂ / M) but in some cases also during the respective cell cycle phase (e.g. spindle checkpoint during mitosis). Molecular signals converge on these mechanisms that

allow the completion of the processes relating to the specific phases of the cycle, as well as environmental signals. In the presence of anomalies, the cell can interrupt the progression of the cycle at the level of the checkpoints (Jackson Robert C. , et al., 2017).

In order to control whether V49 and V49-Cu influenced cell cycle progression and how, we performed a cell cycle assay through FACS analysis, using 10 μ M of the drug candidates and PI as DNA staining agent.

The results obtained (**Figure 32**), show that both V49 and V49-Cu block the cells in the G1 phase, where the cells increase their metabolic capacities. In phase G1, several factors are increased, such as growth factors. Compared to control cells, the S phase of cells treated with V49 and V49-Cu decreases. This means that both V49 and V49-Cu can act on some factor of the G1 phase of the cell cycle,

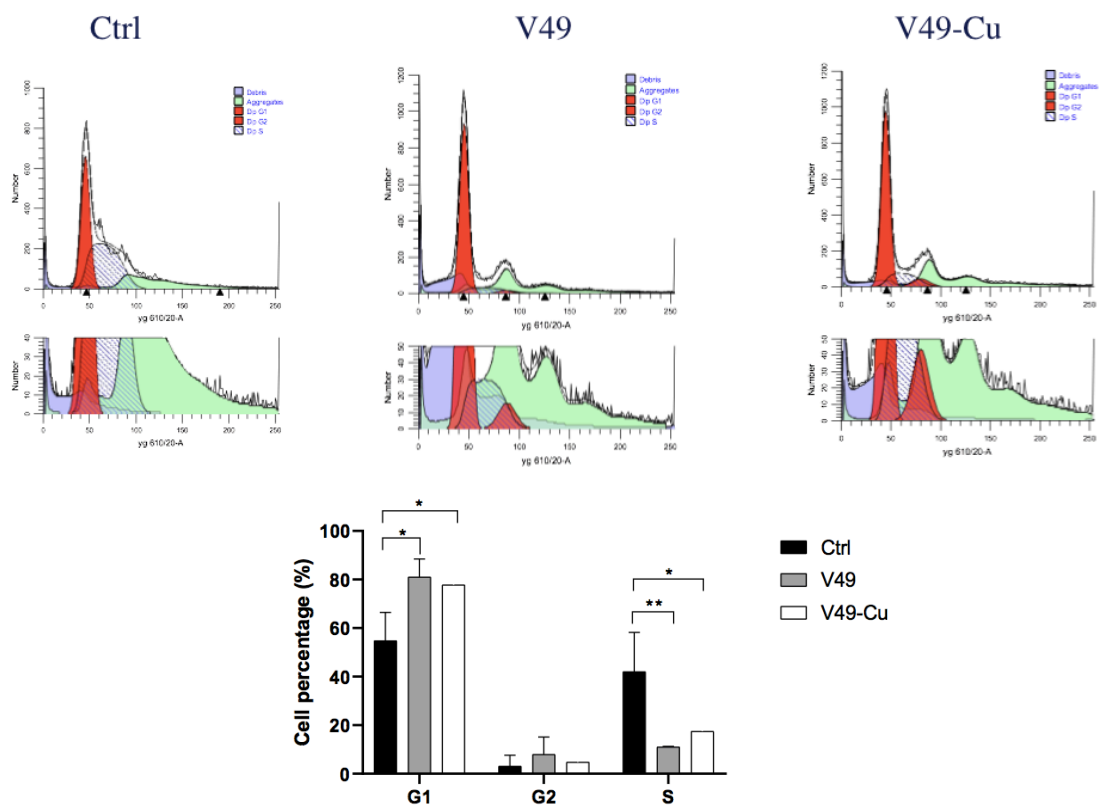


Figure 32. Quantitation of cell cycle phases by propidium iodide and flow cytometry elaboration. DMS114 cells were exposed to 10 μ M of V49 and V49-Cu for 24 h. Statistically decrease in S phase and increase in G1 phase can be observed in the image below.

blocking the progression of the cycle towards the S phase. Additionally, a major checkpoint for DNA damage detection based on p53/Rb1 (retinoblastoma 1) signaling is residing at the G1/S position of the cell cycle. Accordingly, cells in S phase are diminished significantly. However, it needs to be considered that DMS114 cell harbor a p53 mutation, thus making activation of this checkpoint rather unlikely. Numerous anticancer drugs in the clinic are able to block cells in the G1 phase of the cell cycle, such as methotrexate (Uzbekov R. E., 2004), mitomycin (Sognier MA, Hittelman WN. 1986), asparaginase (Ueno, K et al., 1997).

Cell cycle regulation in the G1 phase in recent years represents a promising target for the development of new anticancer chemotherapy agents (Owa T, et al., 2001).

4.3.5 Western Blot

The next step was to investigate further which proteins were the targets of the two drugs, via Western blot analysis. In particular, attention was paid to the FGFR pathway. Western blot analysis was performed with V49 and V49-Cu using the DMS114 and NCI-H1703 cancer cell lines and several primary/secondary antibodies to cell proliferation and viability pathway proteins and their phosphorylated forms. With the treatment of V49 at 1 μ M, 10 μ M, 25 μ M and 50 μ M for 24 h with NCI-H1703 an unusual result was observed, which nonetheless confirmed the hypotheses previously formulated about the solubility problems of the ligand (**Figure 33**).

In fact, at lower doses V49 (10 μ M and 25 μ M) inhibited expression of total S6, and consequently the phosphorylation of this translation-related protein, as well as phosphorylation of AKT and ERK. At higher doses (50 μ M) this effect was diminished due to its insolubility of the drugs and tendency to precipitate in crystals, finally leading to reduced concentrations of the active drug concentrations..

The same experiment was done with V49-Cu at increasing concentrations 1 μ M, 5 μ M, 10 μ M, 15 μ M, 25 μ M and 50 μ M (**Figure 34**).

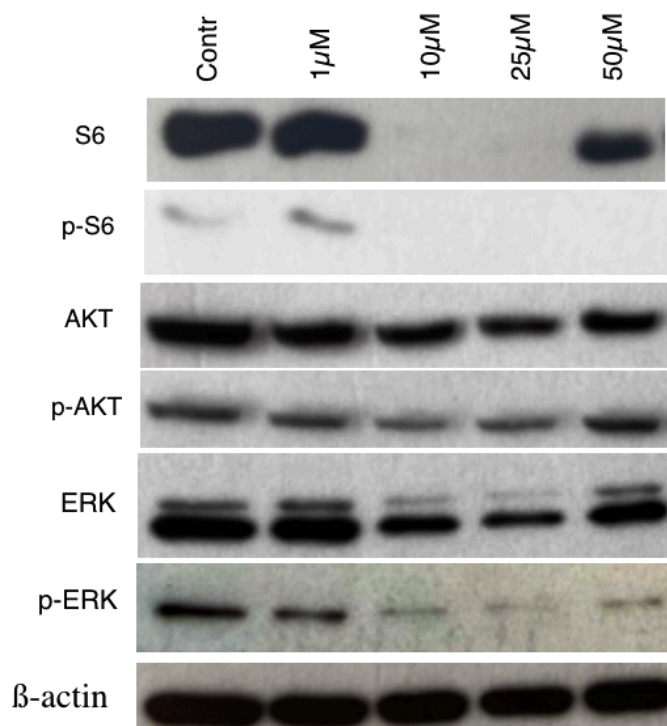


Figure 33. Western blot with NCI H1703 tumor cell line and 24 h exposure of V49 1 μM, 10 μM, 25 μM and 50 μM. Detected proteins: S6, phospho S6 (p-S6), AKT, phospho AKT (p-AKT), ERK, phospho ERK (p-ERK) and a control of β-actin.

First, the inhibitory capacity of V49-Cu of the signaling pathway does not decrease with increasing concentration but exactly the opposite. At higher doses, a stronger effect is observed. This confirms that the V49-Cu has improved chemical-physical properties as compared to V49, in particular solubility. Furthermore, V49-Cu and V49 are able to inhibit total and consequently phospho S6, phospho AKT and phospho ERK, like V49, but also phospho S6K, phospho FGFR, beta Catenin, 4EBP1, pGSK3B and PARP. PARP is a DNA repair protein cleaved during apoptosis thus confirming programmed cell death induction by this compound.

The same experiment was repeated with NCI-H1703 and DMS114, again with 24 h of exposure with V49 1 μM and 10 μM and V49-Cu 1 μM and 10 μM (**Figure 35**).

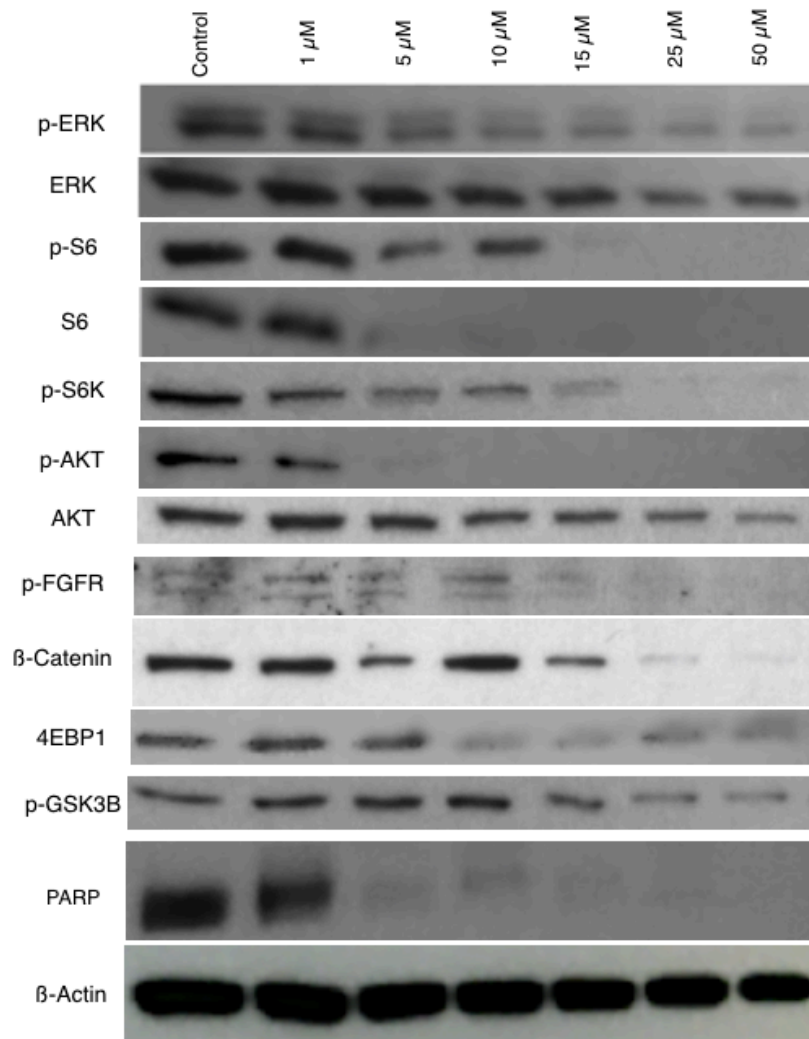


Figure 34. Western blot with NCI H1703 tumor cell line and 24 h exposure of V49-Cu 1 μ M, 5 μ M, 10 μ M, 25 μ M and 50 μ M. Detected proteins and their phosphorylation: S6, phospho S6 (p-S6), AKT, phospho AKT (p-AKT), ERK, phospho ERK (p-ERK), phospho S6 kinase (p-S6K), phospho FGFR (pFGFR), β -catenin, 4EBP1, phospho GSK3B (pGSK3B), PARP and as loading control of β -actin.

Again, the inhibition of total S6 is strong, even at comparably low doses. The inhibition of phospho FGFR is also observed, while total total FGFR1 even tends to be upregulated. This is a classical feature of FGFR inhibition, which in case of activation, is internalized and degraded (Auciello G. et al., 2013). Phosphorylation of FRS2 is inhibited (more visible in DMS114) as well as phosphor of the downstream PI3K molecule AKT and and the MAPK signal mediator ERK. S6 and S6K recently have been identified as direct targets for nuclear FGFR1 and appears to play a key role in FGFR1 signaling (Yafang Hu et al., 2004).

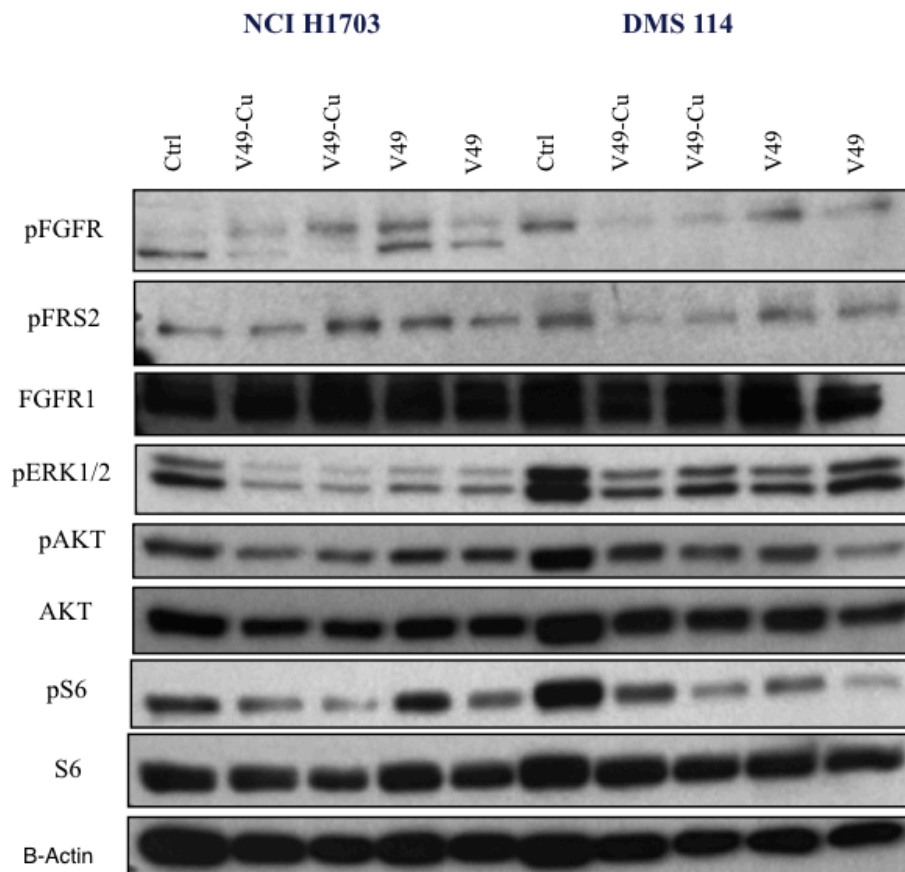


Figure 35. Western blot with NCI H1703 and DMS 114 tumor cell lines and 24 h exposure of V49 and V49-Cu 1 μ M and 10 μ M. Detected proteins: phospho FGFR (pFGFR), phospho FRS2 (pFRS2), total FGFR1 (FGFR1), phospho ERK (ERK1/2), phospho AKT (pAKT), phospho S6 (pS6), total S6 (S6) and a control of β -actin.

A strong connection was also found between the ERK / AKT-p70S6K-S6 signal and the FGF19 / FGFR4 axis in a recent study, associated with a poorer overall survival (Lang L, Teng Y. 2019).

The data obtained confirm that the two drugs V49 and V49-Cu inhibit the signaling pathway related to the FGF receptor, based a tyrosine kinase inhibition mechanism as anticipated by the original drug design strategy.

4.3.6 Cell migration

FGF/FGFR-mediated signals are key in regulation of cell migration and invasion in many cell types and especially in diverse cancer types (Turner N. and Grose R., 2010). Moreover, there is a strong correlation between FGFR inhibition and blockade of epithelial mesenchymal transition (EMT). EMT plays a key role in tumor invasion and metastasis. Numerous studies have shown that the migration capacity of many malignant tumor cells is initiated by EMT processes (Zhou J, et al., 2015).

Loss of E-cadherin and acquisition of vimentin are two critical steps in EMT. E-cadherin is a calcium-dependent transmembrane glycoprotein located in epithelial tissue. It is a cell-cell adhesion protein and an important signal transduction factor. E-cadherin is involved in the main cell-cell adhesion structures including tight junctions. Moreover, E-cadherin is interacting with the oncogenic transcription

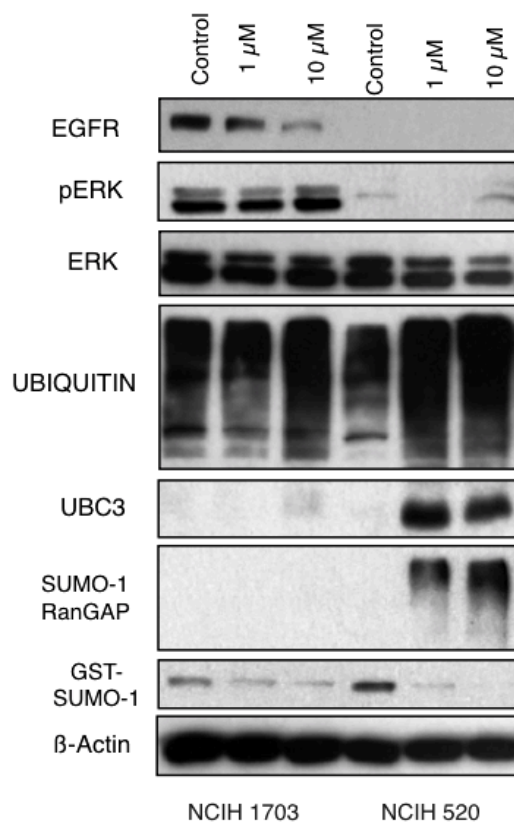


Figure 50. Western blots with NCI H1703 and NCI H520, 24 h of treatment with V8 1 μM and 10 μM.

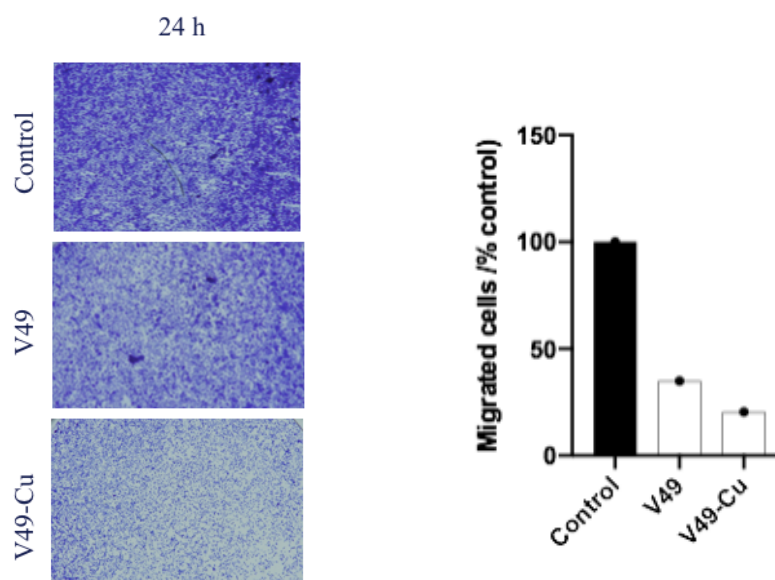


Figure 36. Filter migration assay. Photographs depicting the amount of U251-MG cells able to migrate to the lower side of the trans-well chambers within 24h in absence (control) or presence of the indicated drugs V49 and V49-Cu at 5 μ M stained with crystal violet. The quantification of migrated cells is shown in the right panel.

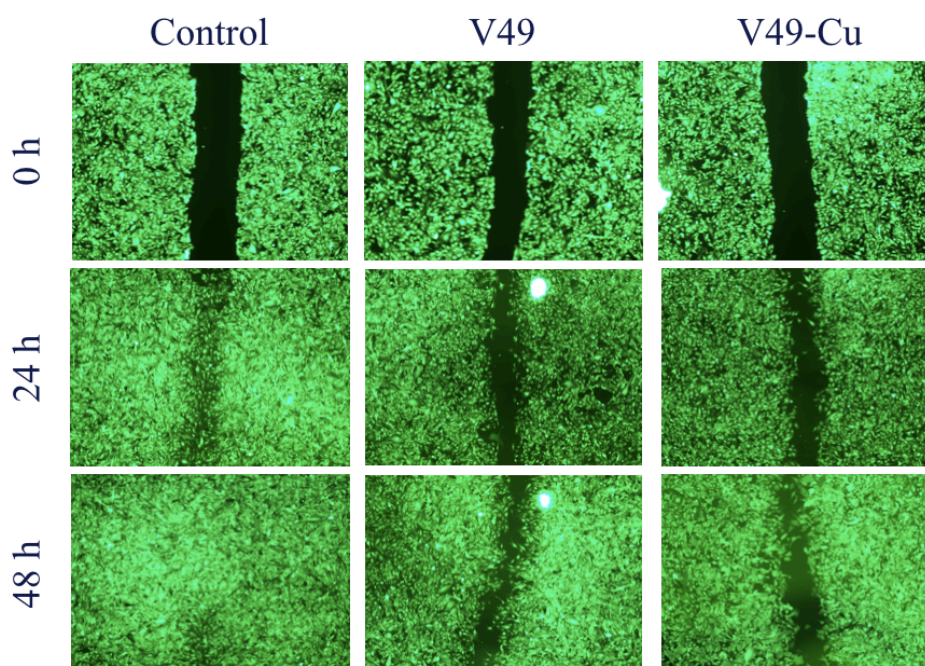


Figure 37. Wound healing assay (scratch assay). U251-MG cells were left untreated or treated with 5 μ M of V49 and V49-Cu as indicated. Before treatment, the cell monolayer was wounded by a scratch with a pipette tip. Photomicrographs were taken at 24 and 48 h, with a fluorescent microscope to follow the ability of the cells to close the wound.

factor beta-catenin on the inner side of the plasma membrane thus inhibiting its translocation to the nucleus. E-cadherin represents an important factor preventing

EMT and consequently tumor cell invasion and metastasis. Therefore, drugs capable of increasing E-cadherin levels represent possible therapeutic, antimetastatic perspectives. Vimentin is a cytoskeletal protein, not expressed in normal epithelial cells, but widely distributed in fibroblasts, endothelial cells and lymphocytes in interstitial cells. Several studies have found that the abnormal over-expression of vimentin is strongly present in a variety of epithelial tumors and is closely related to tumor cell differentiation, invasion and metastasis (Myong NH, 2012).

In particular, it was reported recently that targeting FGFR overcomes EMT-mediated resistance different non-small cell lung cancer (Sana Raouf et al, 2019). For these reasons, we wanted to investigated a possible inhibition of cell migration by V49 and V49-Cu.

The choice regarding the cell line to use fell on the FGFR4 over-expressing glioblastoma cell line (U251-MG) which has strong FGFR4-dependent migratory capacities.

Three separate experiments were performed to evaluate the inhibition of migration capacity of glioblastoma cell line under the impact of our novel FGFR inhibitors: filter migration assay (trans-well Boyden Chambers) (**Figure 36**), wound healing assay (**Figure 37**) and - to elucidate important EMT and cell adhesion related proteins E-cadherin and vimentin - Western blot (**Figure 38**).

Low, non-toxic, concentrations of V49 (5 μ M) and V49-Cu (5 μ M) were used in the selected cell line for 24 h for the filter migration assay. The migratory capacity is strongly inhibited by the copper complex V49-Cu and weaker but still highly significant by the free ligand V49 (**Figure 36**).

A similar ability of V49 and V49-Cu to inhibit migration is observed when a scratch is generated on a confluent cell monolayer (wound healing assay) (**Figure 37**).

Well in agreement with the blocked migratory ability of cells treated with our drugs, a in vimentin and an increase in E-cadherin was detected by Western blot analysis (**Figure 38**).

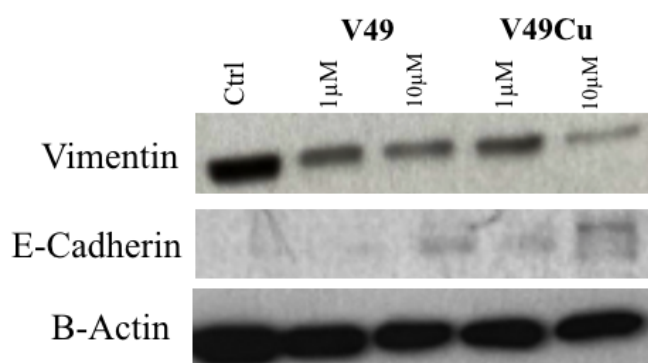


Figure 38. Western blot with glioblastoma (U251-MG) cell line with V49 and V49-Cu 1 µM and 10 µM, 24 h of exposure. The dose-dependent increase in vimentin is observed for both V49 and V49-Cu and the decrease in E-cadherin.

Therefore, the results obtained allow us to affirm that compounds V49 and V49-Cu are able to inhibit cell migration of over-expressing FGFR4 glioblastoma cell line (U251-MG). Together these data suggest that V49 and to a higher extent its copper complex are able to block EMT processes and, consequently, cell migration of FGFR-driven cancer cell models.

4.3.7 Spheroids formation (3D)

3D cellular models like organoids and spheroids offer an opportunity to better understand complex biology in a physiologically relevant context where 2D models have not proven as successful. Moreover, 3D spheroid formation from a single cell solution under non-adherent conditions is considered as a parameter to estimate stem-cell properties of a cancer cell model.

For this reason, cell proliferation inhibition capabilities of 10 μM of V49 and V49-Cu have also been studied in 3D cell models, with spheroids from formed by Daoy cells, human desmoplastic cerebellar medulloblastoma cells with strong stem-cell like properties.

The experiment was performed in two main phases. Initially, cells are placed in a non-adherent cell culture plate. The formation of spheroids under these stressful conditions is then monitored and the ability of the drug to inhibit their formation is evaluated (**Figure 39**).

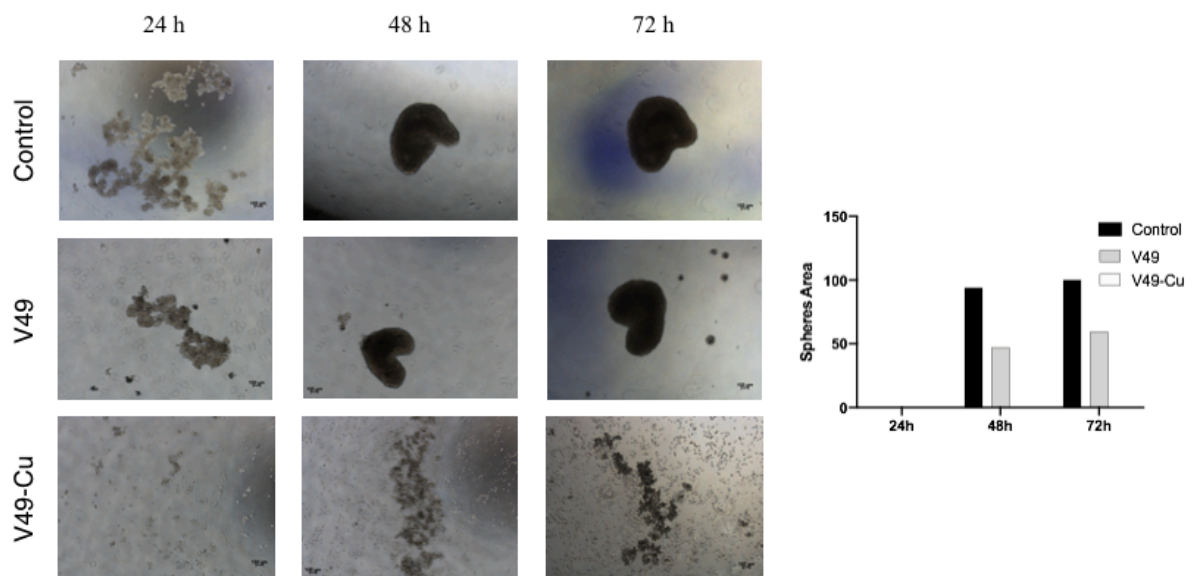


Figure 39. Spheroids formation assay, first part. In a non-adherent cell culture plates adherent cells can only survive by forming 3D-spheroides, a measure for stem-ness. Daoy cells, a human medulloblastoma model, were treated with V49 and V49-Cu at a concentration of 15 μM . In the left panel photomicrographs taken at 24, 48 and 72 h under treatment are shown. In the right panel quantification of spheres areas is depicted.

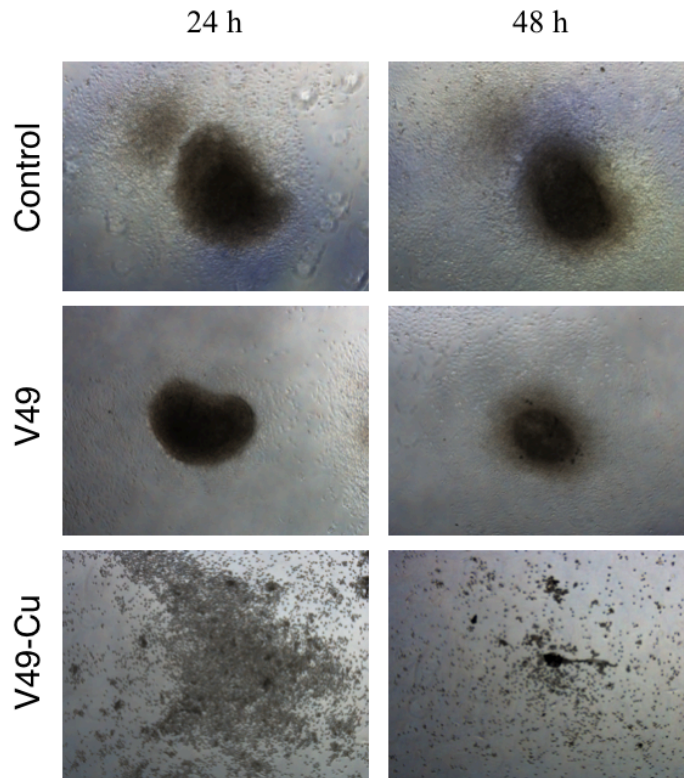


Figure 40. Spheroids formation assay, second part. Retransfer of spheroids to cell culture plates allowing adherence is shown as a parameter to estimate the impact of the investigated drugs on the differentiation plasticity of the cancer cells and their adhesive capacity.

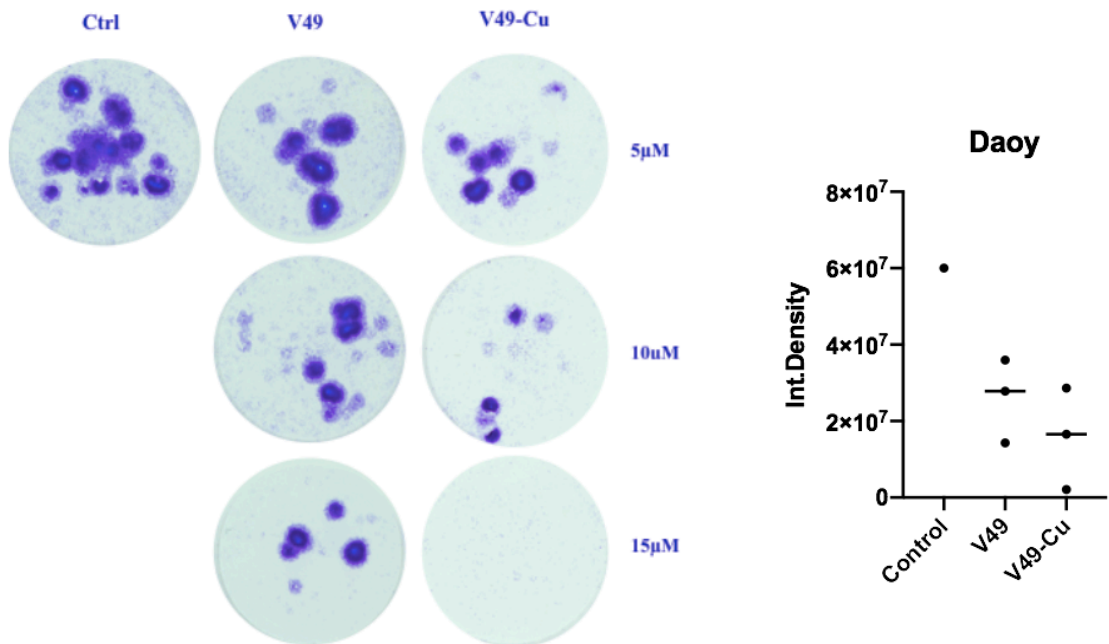


Figure 41. Spheroids formation assay, part three. Crystal violet stained wells depicting re-adhere spheroids (left) and quantification of integrated density (right) of drug-free controls, as well as V49 and V49-Cu 5 μM, 10 μM and 15 μM-exposed cells.

In the second phase, the cells are moved to a plate that allows the cells to adhere, therefore the ability of the cells treated with the drugs to re-adhere to the cell culture plastic and create cell-cell contacts is evaluated as a parameter indicating differentiation plasticity of these cell models (**Figure 40**).

The first phase of the experiment involved the growth of Daoy cells together with the drugs V49 and V49-Cu at 5 μ M, 10 μ M and 15 μ M, in a non-adherent well plates. Only cells with stem cell properties are believed to survive and form floating 3D-spheroides under these conditions. Pictures were taken every 24 hours for 74 hours (**Figure 39**) and spheroids area was measured after 24 h, 48 h and 74 h. V49-Cu, at the same concentration as its V49 ligand, completely prevents the formation of spheroids. This indicates that this drug is massively targeting cancer stem cells. With V49, spheroids still formed but with dimensions reduced by about 50% compared to the control. Then, both the spheroids and the separated suspended cells were re-transferred to a 24-well plate which allows cell adhesion. The ability of the cells to re-adhere to the wells was observed for 48 h (**Figure 40**). After this time, cells were fixed, treated with Crystal Violet and integrated density was measured for each sample (**Figure 41**).

With V49-Cu, cells lose not only the ability to form 3D models but also to re-adhere to the wells. With V49, the cells that retain the ability to adhere to the wells are always about 50% compared to the control.

4.3.8 Toxicity test *in vivo*

In vivo toxicity experiments on SCID mice were performed with the aim of determine the impact of intraperitoneal injection (IP) of V49 and V49-Cu drugs (5 mg/kg and 10 mg/kg) on mice survival and welfare. The primary purpose was to determine possible toxic impacts and to estimate the tolerability of the compound with an endpoint of overall survival.

The toxicology test (**Figure 42**) confirmed that V49 and V49-Cu are non-toxic in mice, as no mice died, and they all maintained a stable body weight throughout the test.

In fact, body weight is one of the most used parameters in toxicological assessments to indicate the appearance of toxic effects of a certain substance in the animal organism. The absence of signals, such as: reduced water consumption and feed intake, behavioral changes and apathy, all suggest that a new drug does not exhibit toxicity at the used concentrations and conditions (Luzia Leiros Sena Fernandes Ribeiro Dantas et al, 2018).

In addition, vital organs were analyzed 30 days after starting treatment and no changes or abnormalities were observed.

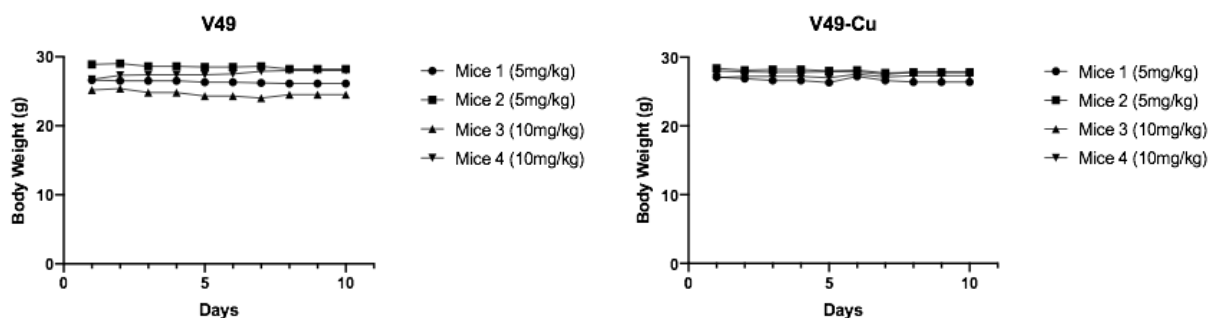


Figure 42. Body weight (g) of four mice treated with 5 mg/kg and 10 mg/kg of V49 (left), and other four mice treated with 5 mg/kg and 10 mg/kg of V49-Cu (right).

4.3.9 Summary of the biological activities of V49 and V49-Cu

This part of my work, concerning the investigated biological properties of both V49 and V49-Cu, can be summarized as follows. Both V49 and V49-Cu:

- inhibit the FGFR pathway;
- increase the apoptotic rate of different cancer cell lines;
- block the cells in G1 and G2 phases;
- inhibit the migration of cells over-expressing FGFR;
- act as hypoxic activatable drugs;
- are not toxic *in vivo* in SCID mice.

Furthermore, V49-Cu does not kill cancer cells via ROS generation and shows both increased water solubility and cytotoxicity compared to V49.

Currently, at the *Institute of Cancer Research in Vienna*, other *in vivo* studies are underway on V49 and V49-Cu to evaluate their ability to decrease tumor volume (subcutaneous tumor induced with DMS114 cells) in SCID mice.

4.4 V8 activity

Compound V8 has shown to have strong anticancer capacities in the order of 3.5 μM in SCLC (DMS114) (**Figure 43**), 9 μM in NSCLC (NCI H1703) (**Figure 44**) and 4.5 μM in glioblastoma multiforme (U251-MG) (**Figure 45**), 6.03 μM against glioblastoma multiforme (BTL1376/26) (**Figure 46**).

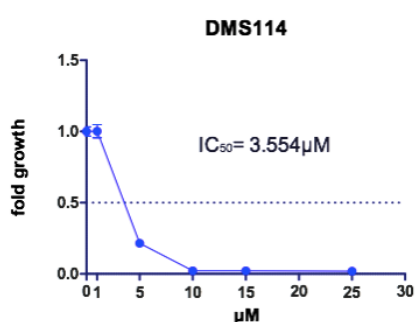


Figure 43. Cell viability assay results, 72 h of co-incubation of V8 1 μM , 5 μM , 10 μM , 15 μM , 20 μM and 25 μM with DMS114 tumor cell line. IC_{50} calculated from three independent experiments: 3.5 μM .

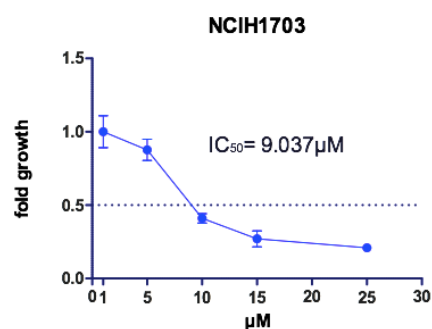


Figure 44. Cell viability assay results, 72 h of co-incubation of V8 1 μM , 5 μM , 10 μM , 15 μM , 20 μM and 25 μM with NCI H1703 tumor cell line. IC_{50} calculated from three independent experiments: 9.03 μM .

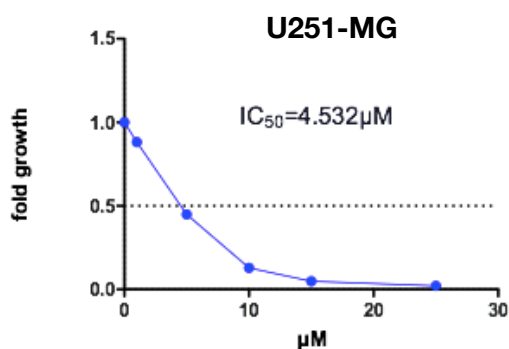


Figure 45. Cell viability assay results, 72 h of co-incubation of V8 1 μM , 5 μM , 10 μM , 15 μM , 20 μM and 25 μM with U251-MG tumor cell line. IC_{50} calculated from three independent experiments: 4.5 μM .

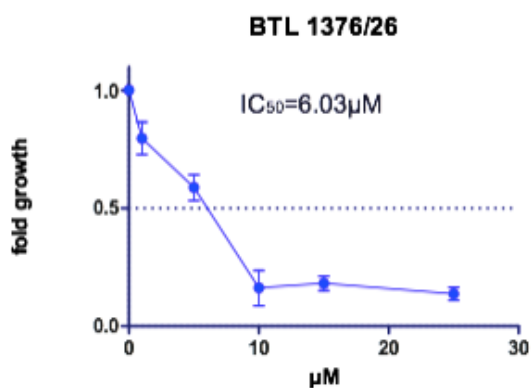


Figure 46. Cell viability assay results, 72 h of co-incubation of V8 1 μM , 5 μM , 10 μM , 15 μM , 20 μM and 25 μM with BTL 1376/26 tumor cell line. IC_{50} calculated from three independent experiments: 6.03 μM .

The **Table 10** shows the IC₅₀ values on other cell lines.

Cell lines	IC ₅₀ (μM)
DMS114	3.54
DMS 114 Ponatinib res.	> 25
NCI H1703	9.04
NCI H520	25.4
SIWA	6.37
RKO wt	11.9
Daoy	9.406
U251-MG Ctrl	5.26
U251-MG GFP	7.84
U251-MG KD	4.1
U251-MG KA	4.5
U251-MG Gly	7.18
U251-MG Arg	4.25
PC9	> 25
A431	> 25
UMUC 14	10
UMUC 14 Ponatinib res.	> 25
VMCUB1	> 25
BTL 1376/26	6.03
HCT116 p53 wt	> 25
HCT116 p53 KO	> 25

Table 10. Cell viability assay results, 72 h of co-incubation of V8 1 μM, 5 μM, 10 μM, 15 μM, 20 μM and 25 μM. IC₅₀ calculated from three independent experiments.

4.4.1 Western Blot

To observe which protein was inhibited by V8 several Western blots were performed (**Figure 47**) using different cell lines.

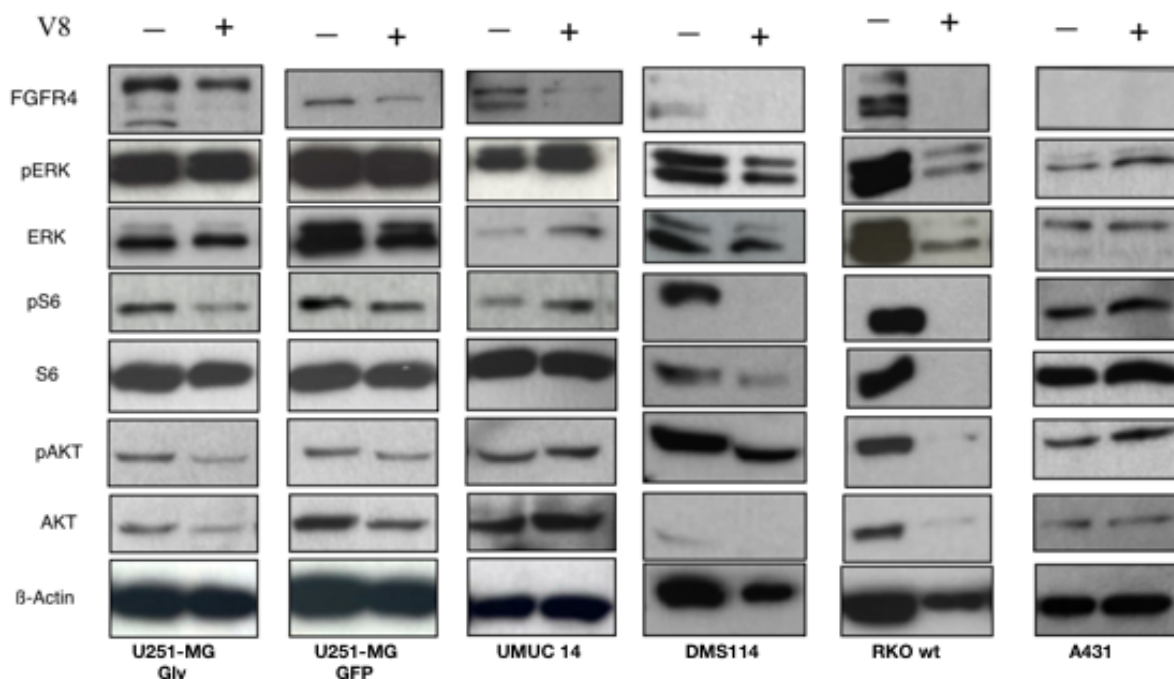


Figure 47. Western blots (separated experiment) with U251-MG (Gly), U251-MG (GFP), UMUC14, DMS114, RKO wt and A431 tumor cell lines, 24 h of treatment with V8.

We observed that, in FGFR4 over-expressing cells (U251-MG Gly, U251-MG GFP, UMUC14, DMS114, RKO wt), the compound has the ability to inhibit several proteins of the tyrosine-kinase pathway. In the FGFR4 deficient cell line (A431), V8 showed no activity. Not all proteins, in different cell lines, were inhibited equally. But the most interesting thing was that the compound was able to inhibit total FGFR4, a feature not found in drugs that affect tyrosine kinase activity. For this reason, other experiments were necessary to investigate the possible mechanism of action of V8.

The most significant results were obtained with NCI H520 and NCI H1703 treated with V8 at 1 μ M and 10 μ M (**Figure 48**). The data obtained were, indeed,

unexpected. The new small molecule V8 was capable of inhibiting total FGFR1

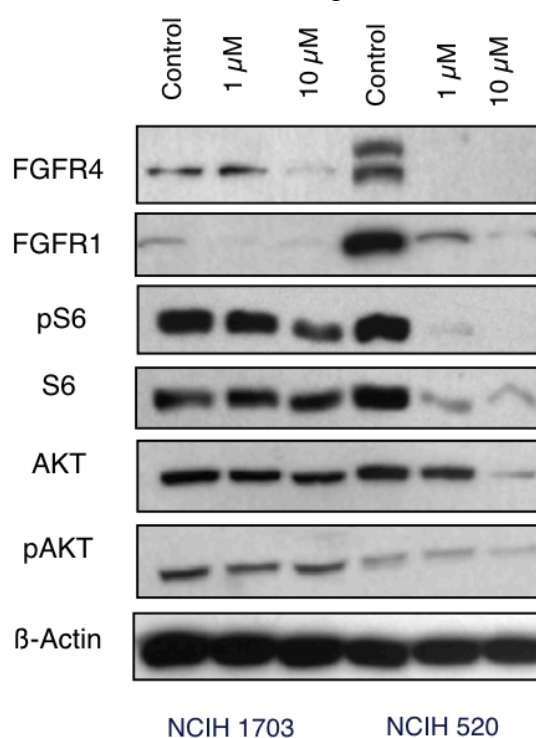


Figure 48. Western blots with NCI H1703 and NCI H520 (FGFR over-expressing tumor cell lines), 24 h of treatment with V8 1 μM and 10 μM. Proteins detected: total FGFR4, total FGFR1, phospho S6 (S6), total AKT, phospho AKT (pAKT) and β-actin control.

and FGFR4, in addition to S6 phospho S6, AKT and phospho AKT.

Therefore, it was clear that it was not a classic tyrosine kinase inhibitor. To understand by what mechanism it could carry out its cytotoxic activity, we investigated further what other proteins might be affected.

Another Western blot was performed with DMS114 cell line (**Figure 49**) after 24 h of exposure of V8. The obtained results were similar to the one observed in the first western blot: V8 is able to inhibit total FGFR1, total FGFR4, phospho S6, phospho S6 kinase, phospho FGFR, beta catenin. But AKT/phospho AKT, ERK/phospho ERK were not involved in the mechanism of action.

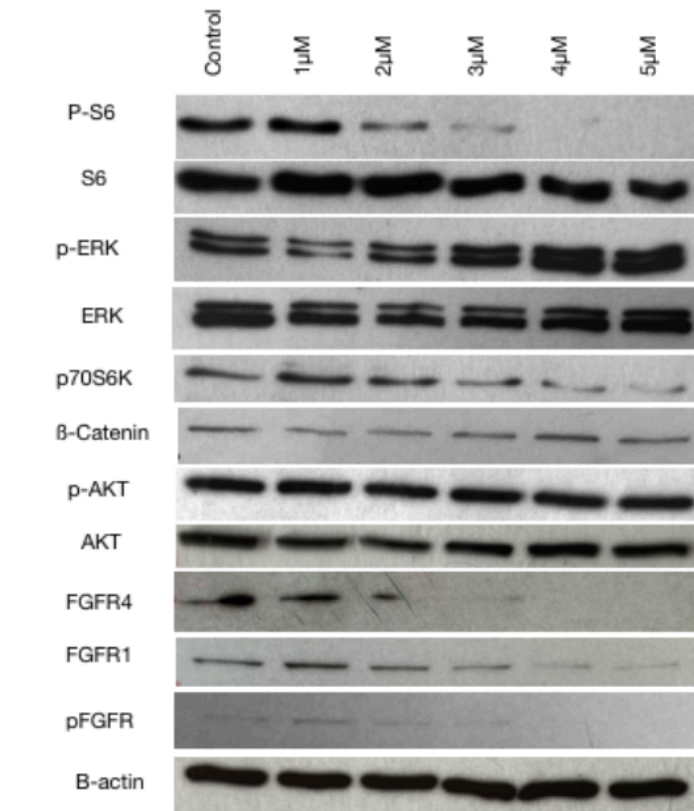


Figure 49. Western blots with DMS114, 24 h of treatment with V8 1 μ M, 2 μ M, 3 μ M, 4 μ M and 5 μ M.

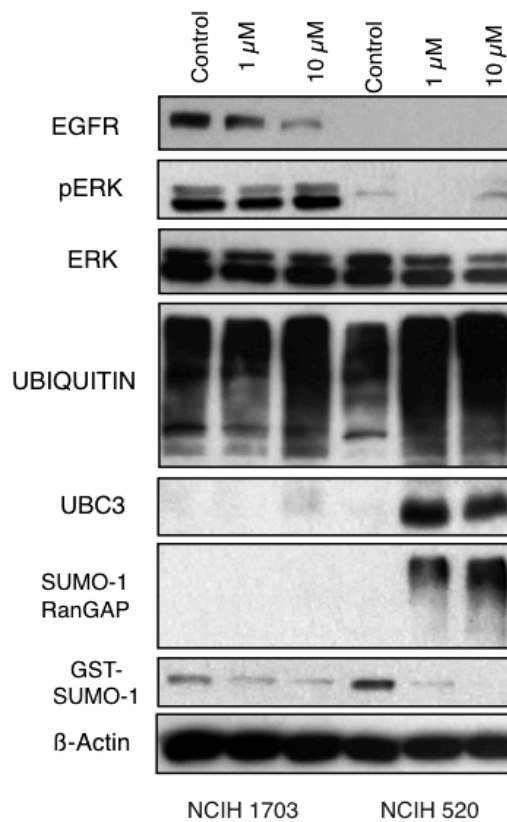


Figure 50. Western blots with NCI H1703 and NCI H520, 24 h of treatment with V8 1 μ M and 10 μ M.

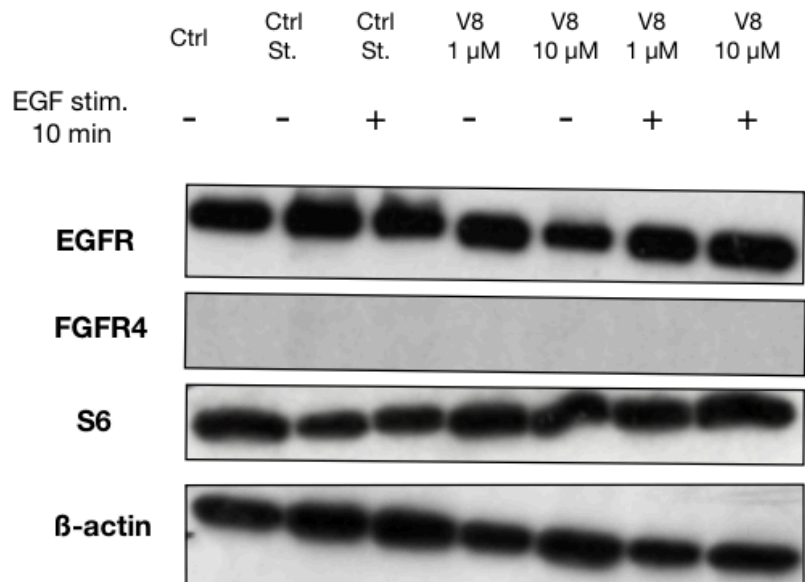


Figure 51. WB with A431 tumor cell line over-expressing EGFR. The experiment was performed with and without EGF stimulation for 10 min, with starved cells for 24 h and treated with V8 1 μ M and 10 μ M for 24 h with starved cells (Ctrl St.) and cells in normal conditions (Ctrl)

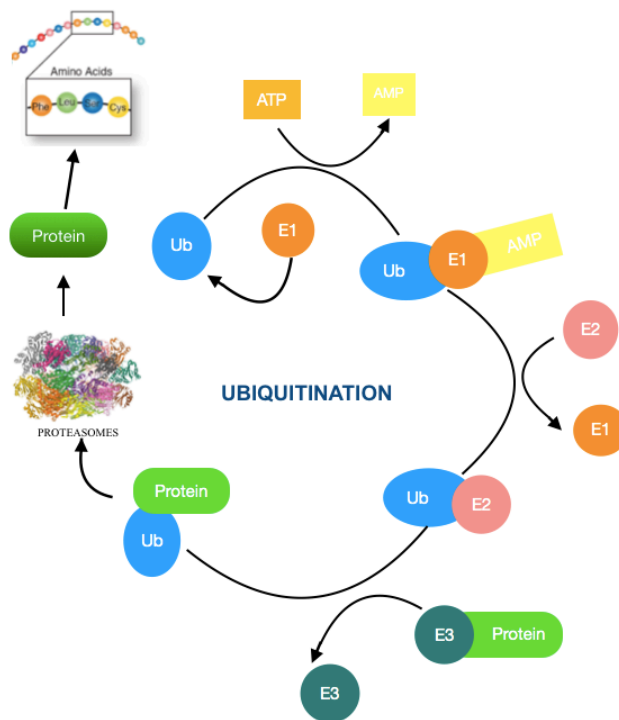


Figure 52. Ubiquitination processes. The first enzyme, E1, catalyzes ubiquitin “activation”, activated ubiquitin is transferred from E1 to a cysteinyl residue in a second protein called E2. Transfer of ubiquitin to substrate proteins typically requires a third activity called E3. The ubiquitinated proteins are recognized by the proteasomes that provide for their degradation.

Therefore, another western blot was performed under the same conditions with NCI H1703 and NCI H520 (**Figure 50**). V8 is also capable of inhibiting total EGFR, in NCIH 1703 and NCI H520. Western blot was also performed with different EGFR over-expressing cell lines (A431: human epidermal carcinoma of the vulva) (**Figure 51**) but with these. V8 showed no activity and no ability to inhibit EGFR and S6.

The observed inhibition was given by a mechanism in which FGFR is certainly involved. The ability to inhibit total receptors is usually associated with drugs that activate ubiquitination processes (**Figure 52**). The subsequent investigation fell, then, on ubiquitin and UBC3.

Three main types of enzyme groups are involved in the mechanism of ubiquitination, including ubiquitin-activating enzymes (E1), ubiquitin-conjugating enzymes (E2) and ubiquitin ligases (E3). Each of these types of enzyme has an important role to play in the ubiquitination and presentation of proteins that will be degraded by the proteasome (Deol, Kirandeep K. et al., 2019).

V8 at 1 μ M and 10 μ M concentration strongly increased the levels of ubiquitin and UBC3, corresponding to a strong inhibition of FGFR1, FGFR4, EGFR, S6.

SUMOylation also appears to be a mechanism of action of V8 against fibroblast growth factor receptors (**Figure 50**). SUMOylation is a post-translational process. It is similar to ubiquitylation in terms of the reaction pattern and enzymatic classes used, but rather than conjugating proteins via ubiquitin, SUMOylation involves the addition of SUMO (small ubiquitin-like modifiers) (Hay RT, 2005).

It represents an unusual mechanism of action for a small molecule since usually these types of mechanisms of action are possible with Aa proteolysis targeting chimera (PROTAC) (Cermakova K and Hodges HC, 2018) drugs with a linker with specific antibodies to recognize the factors involved in ubiquitination and activate it.

4.4.2 Real-time PCR

The mechanism of action of V8 is much more complex than a simple tyrosine kinase inhibitor. To further understand the mechanism by which V8 acted, real time PCR was performed with DMS114 to both assess the amount of FGFR1 and FGFR4 mRNA (**Figure 53**).

Real time PCRs were performed at 6 h and 24 h starting from the coincubation of the cells with V8. After 6 h, both FGFR1 and FGFR4 mRNA levels gradually increased. The latter can be explained by the fact that the drug V8 certainly induces a strong stress that leads the cell to rapidly express growth factors to counteract external stress and survive. Regarding FGFR4, even after 6 h and 4.5 μ M of V8 the mRNA levels decrease. But it is still not statistically relevant.

What is, certainly, statistically significant is the increase in both FGFR1 and FGFR4 mRNA levels after 24 h of V8 treatment. This could mean that V8 is able to act on the transcription of FGFR1 and FGFR4 as well.

Messenger RNA (mRNA) is the intermediate molecule between genes and

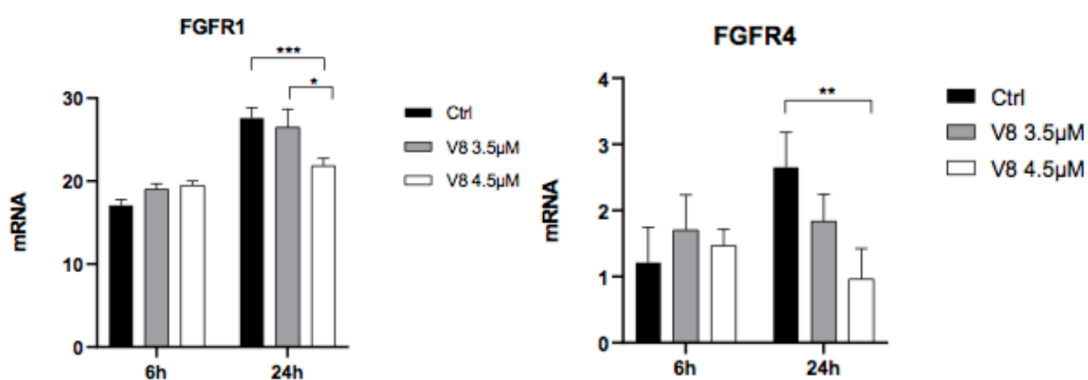


Figure 53 . mRNA expression values of *FGFR1* (left) and *FGFR4* (right) are shown in response to V6 at two different concentrations and time points as indicated. Data are presented as mean \pm SD from triplicates. Statistical significance was tested by Student's t-tests or 2-way ANOVA. *= $p < 0.05$, **= $p < 0.01$, ***= $p < 0.0001$

proteins. mRNA encodes the information / instructions that are used to synthesize proteins. It has emerged as a promising drug target in recent years. Indeed, mRNA

inhibition could offer another avenue to control protein production, rather than targeting proteins directly (Malina A, et al., 2012).

4.4.3 Cell cycle

Cell cycle analysis via FACS was performed in order to understand if 10 μ M of V8 was capable to block the cells in some phases of cell cycle (**Figure 54**). But after 24 hours of treatment he showed no significant changes in the cell cycle,

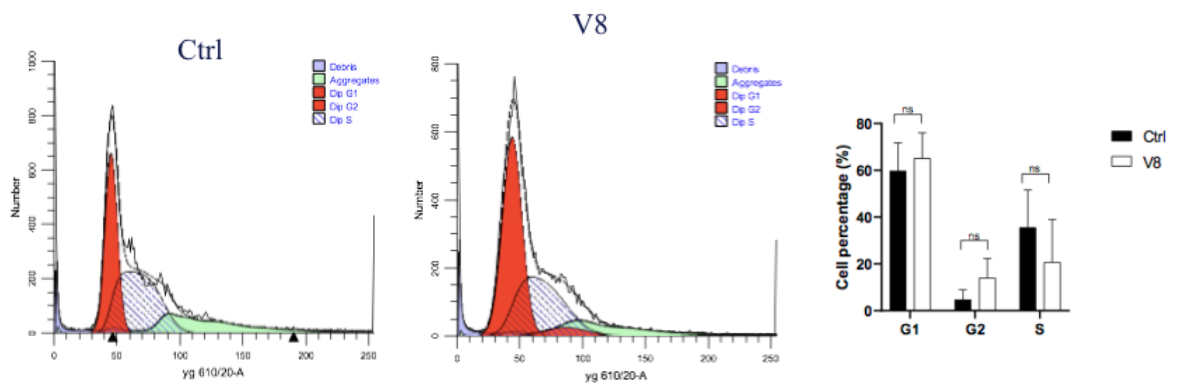


Figure 54. Cell cycle analysis with DMS114 treated for 24 h with V8 10 μ M. The experiment was repeated three times. Statistically insignificant results were obtained.

compared to the control. The experiment was repeated three times, only small, statistically insignificant variations were obtained.

In conclusion, V8 has no ability to block cells at any stage of the cell cycle.

4.4.4 Apoptotic assay (Annexin V-FITC /PI)

It was important to understand whether the cell death mechanism induced by V8 was apoptotic or necrotic. For this reason, the apoptosis assay was performed with Annexin V-FITC and PI.

A very significant result was obtained (**Figure 55**). In fact, there was an increase in apoptotic cells directly proportional to the concentration of V8. With V8 3.5 μM 10% of cells were in early and late apoptosis, with 4.5 μM 26% and 5.5 μM 50.2%. The obtained data, in three independent experiment, were always statistically significant.

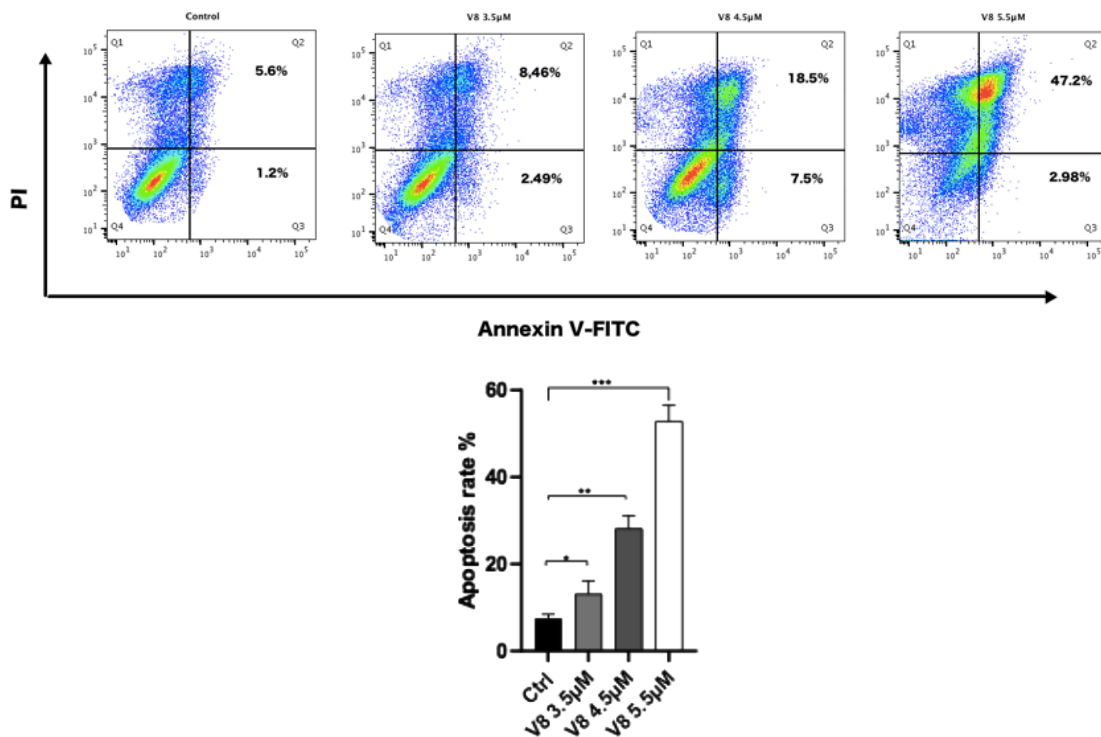


Figure 55. Annexin-V-FITC / PI assay used to understand the mechanism of cell death induced by V8 incubated with DMS114 for 24 h, with quantifications of the results on the below panel.

4.4.5 Migration assay

Also for V8, three separate experiments were performed to evaluate the inhibition of migration capacity of glioblastoma cell line (U251-MG GFP): filter migration assay (**Figure 56**), wound healing assay (**Figure 57**) and Western blot (**Figure 58**).

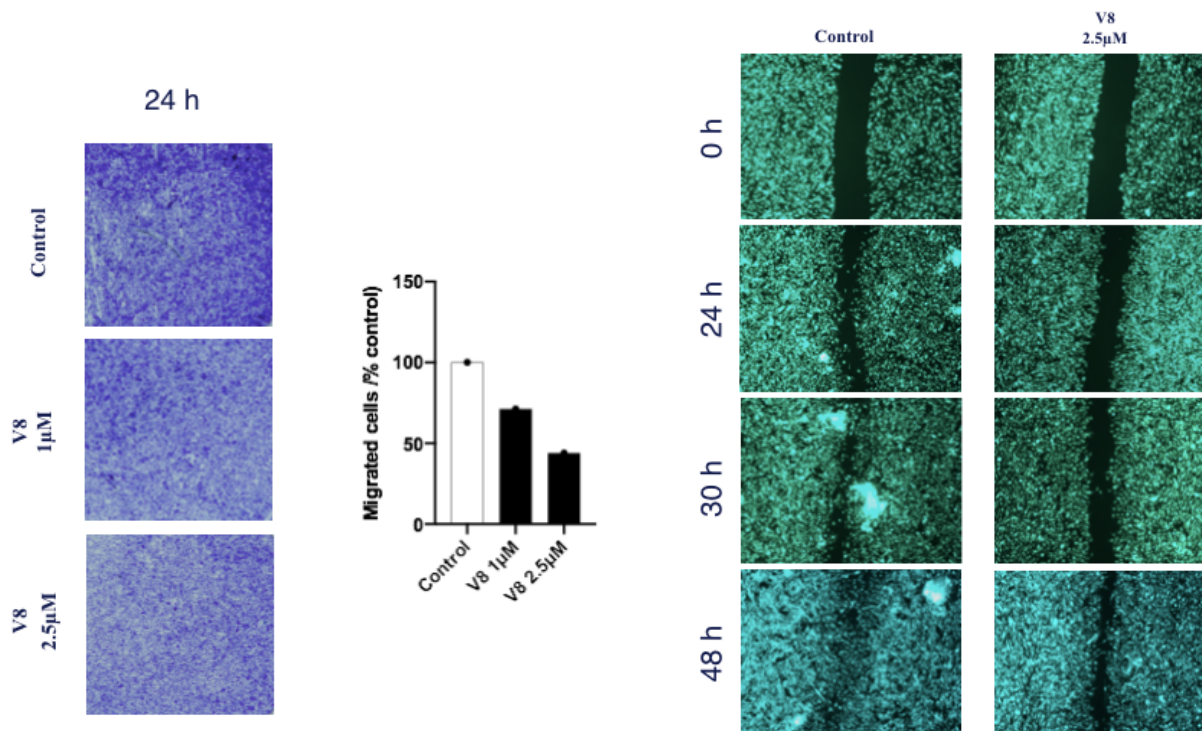


Figure 56. Filter migration assay. The images of migration abilities in U251-MG cells in trans-well treated with V8 1 μ M and 2.5 μ M and the quantification of migrated cells in the right panel.

Figure 57. Wound healing assay or scratch assay. The cells were treated at time 0 with 2.5 μ M of V8 and the cells were scratched. The pictures were tacked at 24 h, 30 h and 48 h, with a fluorescent microscope.

Compound V8 has a strong ability to inhibit cell migration of human glioblastoma multiforme, also confirmed by the inhibition of vimentin and increase of E-Cadherin observed in the western blot analysis (**Figure 58**).

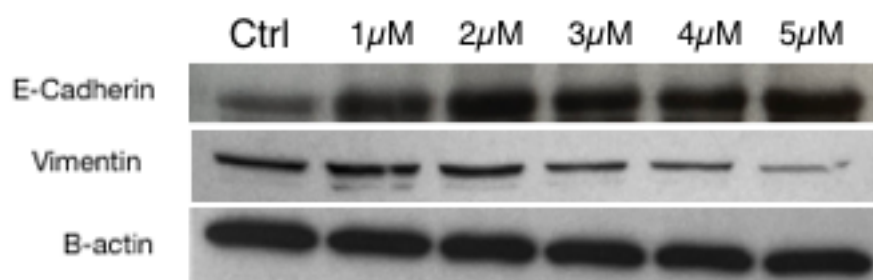


Figure 58. Western blot with glioblastoma (U251-MG) cell line with V8 1 μ M, 2 μ M, 3 μ M, 4 μ M and 5 μ M, 24 h of exposure. The dose-dependent increase in vimentin and the decrease in E-cadherin can be observed.

4.4.6 Spheroids formation (3D)

Cell proliferation inhibition capabilities of V8 have also been observed in 3D cell models, with spheroids from Daoy, human desmoplastic cerebellar medulloblastoma, in the same modalities used for V49 and V49-Cu.

The experiment was performed in two main phases. The first, in which the cells are placed in a non-adherent plate and then the formation of spheroids is induced and the ability of the drug to inhibit their formation is evaluated (**Figure 59 A, B, C**). In the second phase, the cells are moved to a plate that allows the cells to adhere, therefore the ability of the cells treated with the drugs to adhere and create interconnections between them is evaluated (**Figure 60**).

After this time, cells were fixed and treated with crystal violet and Int Density was calculated for each sample (**Figure 61**).

The results show a very high capacity of V8 to inhibit spheroids formation. In fact, already in the first 24 h V8 at 10 μ M prevents the formation of spheroids (**Figure 59A**). After 48 h this ability is strongly visible (**Figure 59B**), since perfect spheres are visible in the control and at low concentrations (1 and 5 μ M). Furthermore, many cells treated with V8 lose the ability to re-adhere to the wells when they are transferred to the well-plate that allows adhesion (**Figure 60**), easily observable even with crystal violet (**Figure 61**).

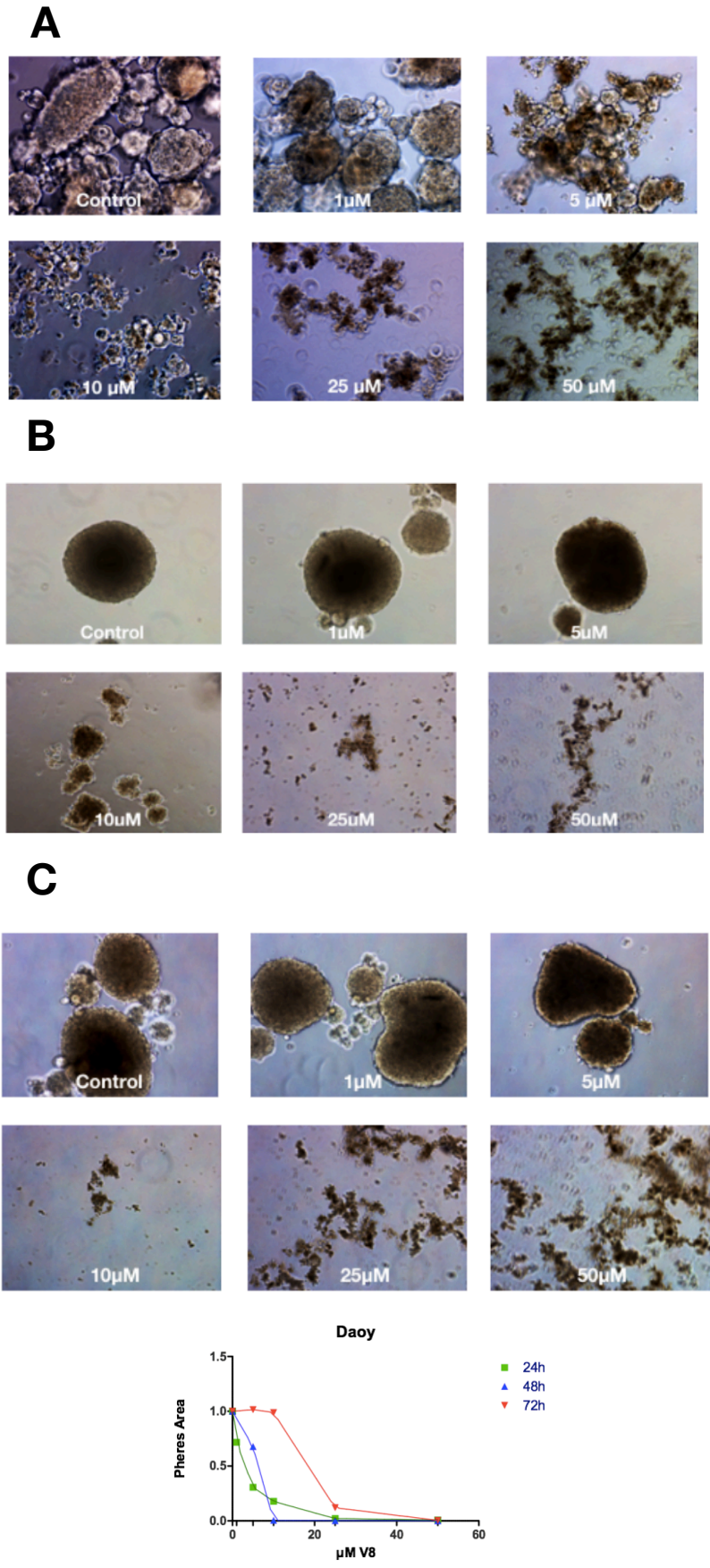


Figure 59. Spheroids formation assay, first part. In non-adherent well-plate. Daoy cell line have been treated with V8 at different concentrations: 1μM, 5 μM 10 μM, 25 μM and 50 μM. The pictures were tacked after 24 h (A), 48 h (B) and 72 h (C). The spheroid surface was quantified (graphic below).

After 48h of incubation in the new (adherent) plate

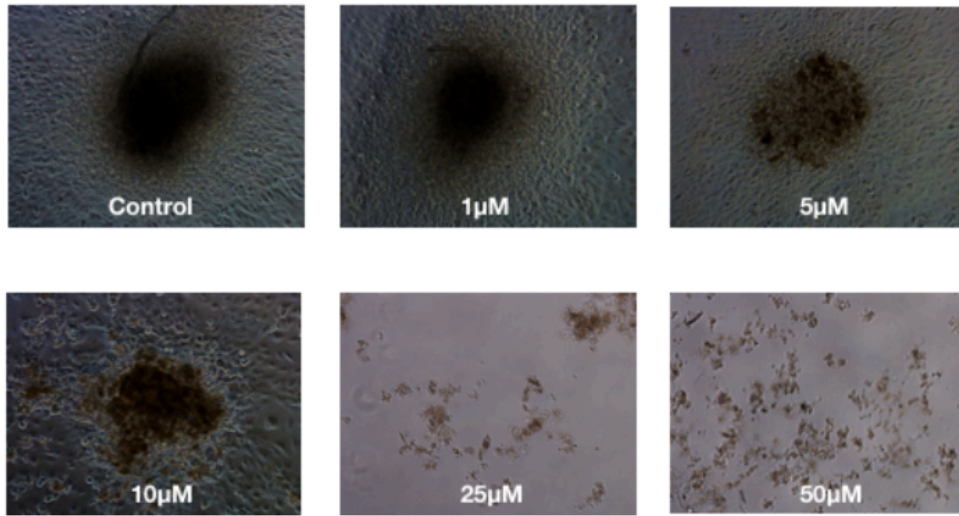


Figure 60. Spheroids formation assay, second part. In adherent well-plate. Estimation of the adhesive capacity of cells after 48 h.

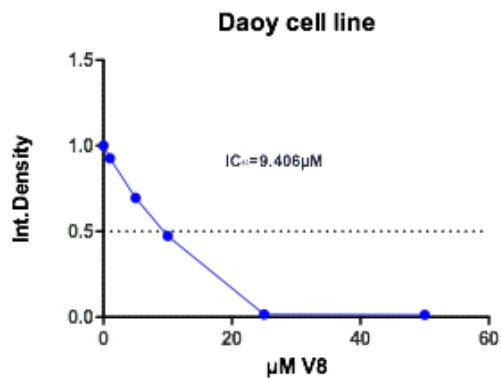
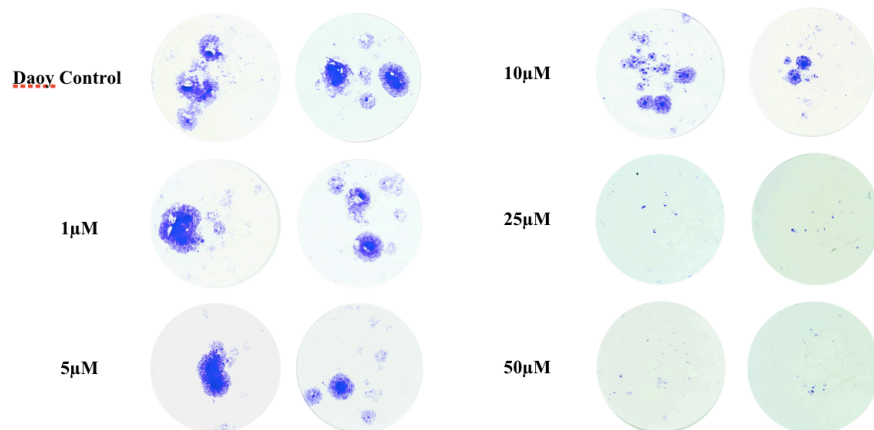


Figure 61. Spheroids formation assay, part three. Crystal violet (left) and quantification of integrated density (below) of control and V8 at 1 µM, 5 µM, 10 µM, 25 µM and 50 µM.

4.4.7 Live cell (time-laps)

A live cell experiment was also performed, using the GFP cell line of glioblastoma multiforme and V8 at 3.5 μ M, images were taken every 5 min for 64 h (**Figure 62**). What can be confirmed is that V8 certainly acts with an apoptotic mechanism. Comparing it with the control, V8 is able to degenerate the cells that are more able to make mitosis already a couple of hours after the treatment and go into apoptosis.

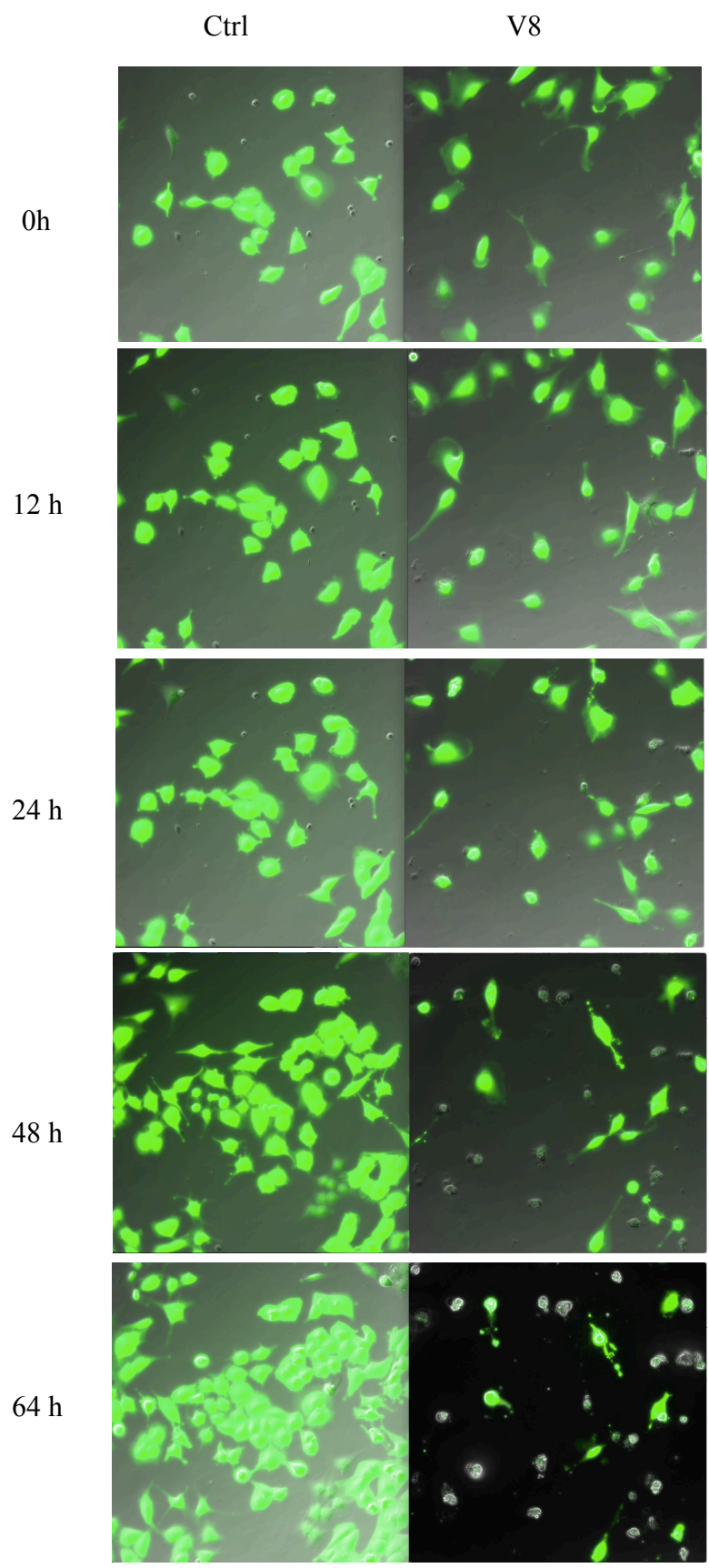


Figure 62. Live cell experiment. U251-MG GFP cells were treated with 3.5 μ M of V8 and pictures were taken every 15 minutes for each samples control (left) and V8 (right) for 64 h.

4.4.8 Toxicity test in vivo

In vivo toxicity study on SCID mice was performed with aim of determination of the impact of V8 mice survival and welfare. V8 was administered at 5 and 10 mg/kg three-times a week every other day, and four were used for the experiment.

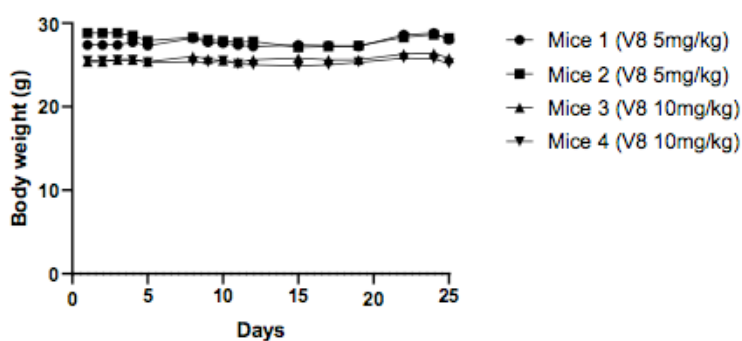


Figure 63. Body weight (g) of four mice treated with 5 mg/kg and 10 mg/kg of V8.

All mice maintained a stable body weight (**Figure 63**). All were then sacrificed to assess organ toxicity. Only one of these mice showed strange white formations at the peritoneal level (mice 1 that received 5 mg/kg of V8 (**Figure 64**)).



Figure 64. Mice treated with 5 mg/kg of V8, with “peritoneal loose bodies” (white formations).

These solid formations are translucent when removed after a couple of hours. Having the doubt that it was perhaps the precipitated drug, we tried to solubilize it in solvents in which V8 is soluble (DMSO, Methanol), but without success.

Furthermore, the other mice showed no abnormalities, not even those that received double the dose (10 mg/kg). After a detailed literature search, we came to the conclusion that it could be a very rare pathological situation: unattached infarcted appendages are known as "peritoneal loose bodies" or "peritoneal mice" (Gonzalez R, 2020).

4.4.9 Summary of V8

Therefore, this second part of my biological work can be summarized by concluding that a small drug has been found with anticancer activity against several glioblastoma and lung cell lines that over-express FGFR. V8 is capable of:

- inhibit total FGFR4, FGFR1, S6, EGFR in cell line over-expressing FGFR
- increase Ubiquitin levels and E2 levels
- increase the apoptotic rate of tumor cells
- not interfere with the cell cycle
- inhibit tumor spheroids formation
- inhibit the migration of cells over-expressing FGFR
- is not toxic *in vivo* in SCID mice

Currently, at the *Institute of Cancer Research in Vienna*, other *in vivo* studies are underway on V8 to evaluate its ability to decrease tumor volume (subcutaneous tumor induced with DMS114 cells) in SCID mice.

Conclusions and future prospects

The aim of this thesis was to identify the genetic alterations of FGFR present in lung and brain tumors. This made it possible to select some cellular models for the study of new specific target drugs. In this regard, more than 160 molecules have been designed, using computational tools, of which 22 have been synthesized. In addition to the 22 organic molecules, three Cu (II) complexes were synthesized with the aim of obtaining pro-drugs that can be activated in the hypoxic tumor environment. Of all the new drugs the most promising were **V49** and its metal complex **V49-Cu** and the small molecule **V8**. The latter three, in fact, have been investigated in more detail to better understand the mechanism of action.

V49 and **V49-Cu** are capable of inhibiting the FGFR pathway; increase the rate of apoptosis of several cancer cell lines; blocking the cells in phases G1 and G2; inhibit the migration of cells that overexpress FGFR; act as hypoxic activatable drugs; they are not toxic *in vivo* in SCID mice. The mechanism of action of these drugs seems very promising, for this reason at the *Institute of Cancer Research of Vienna* they are still under investigation to analyze their activity on tumors *in vivo*.

V8 is capable to inhibit total FGFR4, FGFR1, S6, EGFR in cell line over-expressing FGFR; increase Ubiquitin levels and E2 levels; increase the apoptotic rate of tumor cells; not interfere with the cell cycle; inhibit tumor spheroids formation; inhibit the migration of cells over-expressing FGFR; is not toxic *in vivo* in SCID mice. The mechanism of action of this small molecule is very interesting and particular, it needs further studies to be really well understood. At the *Institute of Cancer Research of Vienna* **V8** is still under investigation to analyze the activity on tumors *in vivo*.

MATERIALS AND METHODS

5.1 Chemistry

The progress of the reactions was monitored by TLC on silica gel (Merck 60, F254, 0.2 mm). The purification of the products was performed by crystallization or by chromatographic techniques, using Merck silica gel, 230-400 mesh ASTM or 70-230 mesh ASTM, as the stationary phase. The automatic chromatography was performed with a CombiFlash® RF200 (Teledyne Isco) RediSep cartridge (35-70 μm) (40 g) device.

The yields as a percentage refer to purified products. The melting points were determined with a Mel-Temp II device, Laboratory Devices (USA) and are not correct. The $^1\text{H-NMR}$ spectra were recorded in DMSO- d_6 , using a Bruker AC 300 (300 MHz) and TMS apparatus, as internal standard. The $^{13}\text{C-NMR}$ spectra were recorded at 75 MHz. The IR spectra were recorded with a Perkin Elmer Spectrum RXI FT-IR System Two spectrophotometer, in KBr.

5.1.1 Synthesis of 2-methyl-7-nitro-4H-3,1-benzoxazin-4-one

1 g (5.49 mmol) of 2-amino-4-nitrobenzoic acid **31** is solubilized in 16.6 mL of acetic anhydride and the reaction mixture is refluxed, under magnetic stirring, for 4 h. The excess acetic anhydride is removed in the rotavapor and the solid residue is washed with cyclohexane and filtered. 984.7 mg (4.78 mmol) of 2-methyl-7-nitro-4H-3,1-benzoxazin-4-one **32** are obtained, unitary on TLC, which is used as crude, for the subsequent reaction.

Yield: 87%. M.p .: 134-5 $^{\circ}\text{C}$ (Lit. 138 $^{\circ}\text{C}$).

5.1.2 Synthesis of 2-methyl-7-nitro-3- (pyridine-2-yl) quinazolin-4 (3H) -one

2-methyl-7-nitro-4H-3,1-benzoxazin-4-one **32** crude (4.78 mmol) is added with 450 mg (4.78 mmol) of 2-aminopyridine and a reaction is carried out by fusion, in a bath of sand, at 160 °C, for 30 minutes. The desired product is isolated by washing the yellow-brown solid, under heat, with methanol and by filtration of the mother liquors, after concentration by evaporation. 1 g of impure compound **34** is obtained which is purified by column chromatography. The chromatography is performed on a sample of 500 mg: 170 g of Merck silica gel, 70-230 mesh ASTM; eluent: ethyl acetate; column diameter: 4.5 cm; collected fractions: 1-100, 15 mL each; fractions joined: 47-85.

Yield: 50%. M.p .: 148-153 °C. ¹H-NMR (δ): 2.15 (3H, S, CH₃); 6.80-8.70 (7H, one set of signals, C₆H₃, C₅H₄N). ¹³C-NMR (δ): 24.41 (CH₃); 120.61 (CH); 122.57 (CH); 124.25 (CH); 125.22 (C); 125.60 (CH); 128.00 (CH); 140.00 (CH); 141.50 (C); 148.12 (C); 150.37 (C); 150.65 (C); 156.58 (C); 169.60 (CO). IR^(cm⁻¹): 1693 (CO).

5.1.3 Synthesis of 7-amino-2-methyl-3- (pyridine-2-yl) quinazolin-4 (3H) -one

350 mg (1.30 mmol) of 2-methyl-7-nitro-3- (pyridine-2-yl) quinazolin-4 (3H) -one **34** are added to a suspension of 1.05 g of iron and 1.31 mL of acetic acid at the 5%, in the period of 2 h, in a water bath and under stirring. After 2 h of stirring at 100 °C, the acidity of the reaction mixture is reduced to pH = 8, with a saturated solution of NaOH and filtered. The dry solid residue is extracted with hot methanol. From the yellow solid (280 mg) thus obtained, compound **36** is isolated by CombiFlash® RF200 automatic chromatography: 60 g of Merck silica gel, 230-400 mesh ASTM; eluent: ethyl acetate / acetone mixture (1:1); collected fractions: 1-50, 10 mL each; fractions joined: 26-45.

Yield: 41%. M.p .: 190-210 °C. ¹H-NMR (δ): 2.01 (3H, S, CH₃); 6.19 (2H, S, NH₂, exchangeable with D₂O); 6.61-8.65 (7H, one set of signals, C₆H₃, C₅H₄N).

^{13}C -NMR (δ): 24.41 (CH₃); 120.61 (CH); 122.57 (CH); 124.25 (CH); 125.22 (C); 125.60 (CH); 128.00 (CH); 140.00 (CH); 141.50 (C); 148.12 (C); 150.37 (CH); 150.65 (C); 156.58 (C); 169.60 (CO). IR (cm^{-1}): 1656 (CO); 3344-3415 (NH₂).

5.1.4 Synthesis of methyl 3-iodobenzoate

3 grams (12.1 mmol) of 3-iodobenzoic acid **37** are solubilized, under heat, in 42 mL of RPE acetone. 2.51 g (18.16 mmol) of anhydrous K₂CO₃ are added and the reaction mixture is refluxed and under magnetic stirring for 10 minutes. The reaction mixture is carried out at rt. and proceed with the addition of 1.14 mL of CH₃I (> 99%). The resulting mixture is then refluxed and under magnetic stirring for 5 h. After filtration, the acetone is removed to the rotavapor, under reduced pressure. 10 mL of saturated solution of NaHCO₃, 15 mL of ethyl acetate are added and proceed with a liquid-liquid extraction. Excess water is eliminated with anhydrous sodium sulphate and the solvent is removed in the rotavapor, under reduced pressure. 2.95 g (11.26 mmol) of methyl 3-iodobenzoate **38**, unitary on TLC, are obtained.

Yield: 93%. M.p. : 50-52 °C (Lit. 54.5 °C). ^1H -NMR (CDCl₃) (δ): 3.92 (3H, s, OCH₃); 7.18-8.38 (4H, one set of signals, C₆H₄). ^{13}C -NMR (CDCl₃) (δ): 52.5 (OCH₃); 93.9 (C); 128.9 (CH); 130.2 (CH); 132.1 (C); 138.6 (CH); 141.9 (CH); 165.7 (CO). IR (cm^{-1}): 1705 (CO).

5.1.5 Synthesis of methyl 3-formylbenzoate

380 mg (1.45 mmol) of PPh₃ and 320 mg (1.26 mmol) of I₂ are solubilized in 2.5 mL of toluene, at RT, inside a sealed tube and everything is kept under magnetic stirring for 15 minutes. To the reaction mixture are added 250 mg (0.95 mmol) of methyl 3-iodobenzoate **38**, solubilized in 5 mL of toluene, 8.7 mg (0.05 mmol) of PdCl₂, 1.32 ml of Et₃N (99.5%) and 0.3 mL of HCOOH (99%).

The reaction proceeds in a water bath, at 80 °C, under magnetic stirring, for 8 hours, until the deep purple color disappears. Finally, the palladium chloride is removed by filtration and the toluene is removed in the rota vapor, under reduced pressure.

From each reaction, about 570 mg of mixture are obtained, from which methyl 3-formylbenzoate **39** is purified by column chromatography, carried out on a sample of 3.4 g:

250 g Merck silica gel, 230-400 mesh ASTM; eluent: cyclohexane / ethyl acetate mixture (7: 3); column diameter: 4.5 cm; collected fractions: 1-115, 10 mL each; united fractions: 89-114.

Yield: 54%. M.p .: 100-5 °C. ¹H-NMR (δ): 3.88 (3H, S, OCH₃); 7.70-8.40 (4H, a set of signals, C₆H₄); 10.07 (1H, S, CHO). ¹³C-NMR (CDC13): 52.4 (CH₃); 129.2 (C); 131.2 (C); 131.4 (CH); 133.0 (CH); 135.1 (CH); 136.7 (CH); 165.9 (CO); 191.1 (CHO). IR (cm⁻¹): 1688, 1730 (2xCO).

5.1.6 Synthesis of methyl 3-[(E)-2-(pyridine-2-yl)ethenyl]benzoate

580 mg (3.53 mmol) of methyl 3-formylbenzoate **39** are solubilized in 5 mL of glacial acetic acid and 1.1 mL of 2-methylpyridine **40** (> 98%) are added.

The reaction mixture is refluxed for 130 h. Finally, the acetic acid is removed in the rotavapor, under reduced pressure, the oily residue is taken up with 10 mL distilled water and a liquid-liquid extraction is carried out, with three 10 mL aliquots of ethyl acetate. Excess water is eliminated with anhydrous sodium sulphate and the solvent is removed in the rotavapor, under reduced pressure. 820 mg of the desired, impure product are obtained. Methyl 3 - [(E) -2- (pyridine-2-yl) ethenyl] benzoate **41** is then purified by means of column chromatography:

250 g of Merck silica gel, 230-400 mesh ASTM; eluent: cyclohexane / ethyl acetate mixture (7:3); column diameter: 4.5 cm; fractions collected: 1-149; fractions joined: 81-144.

Yield: 51%. M.p .: 82-4 °C. ¹H-NMR (δ): 3.94 (3H, S, OCH₃); 7.13-8.62 (10H, one set of signals, C₆H₄, C₅H₄N, CH = CH). ¹³C-NMR (δ): 52.16 (OCH₃); 122.31 (2xCH); 127.88 (CH); 129.11 (CH); 129.15 (CH); 130.66 (C); 131.50 (CH);

131.56 (CH); 136.56 (CH); 137.01 (C); 149.72 (CH); 155.19 (C); 166.87 (CO).
IR (cm⁻¹): 1708 (CO).

5.1.7 Synthesis of 3 - [(E) -2- (pyridin-2-yl) ethenyl] benzoic acid

370 mg (1.55 mmol) of methyl 3 - [(E) -2- (pyridine-2-yl) ethenyl] benzoate **41** are solubilized in 2.04 mL of EtOH and 6.18 mL of 1M NaOH are added. The reaction mixture is then refluxed, under magnetic stirring, for 1 h. The ethanol is removed by the rotavapor, under reduced pressure. 6M HCl is added until complete precipitation (pH = 5-7).

A white solid is obtained, from which the 3 - [(E) -2- (pyridin-2-yl) ethenyl] benzoic acid **42** is isolated by filtration.

Yield: 89%. M.p: 180-2 °C. ¹H-NMR (δ): 7.25-8.59 (10H, one set of signals, C₆H₄, C₅H₄N, CH = CH); 13.15 (1H, s widened, OH, exchangeable with D₂O). ¹³C-NMR (δ): 123.06 (CH); 123.12 (CH); 127.97 (CH); 129.42 (CH); 129.55 (CH); 129.65 (CH); 131.48 (CH); 131.65 (CH); 132.00 (C); 137.22 (C); 137.30 (CH); 149.97 (CH); 155.15 (C); 167.63 (CO). IR (cm⁻¹): 1700 (CO); 3464 (OH).

5.1.8 Synthesis of 3-[(E)-2-(pyridine-2-yl)ethenyl]benzoyl chloride

446 mg (1.98 mmol) of 3 - [(E) -2- (pyridin-2-yl) ethenyl] benzoic acid **42** are solubilized in 5 mL of SOCl₂ (99.7%) and the solution is refluxed for 5 h . Thereafter, the thionyl chloride is removed in the rotavapor, under reduced pressure. Compound **43** is used as crude, for the next reaction.

5.1.9 Synthesis of (E) -N- (2-methyl-4-oxo-3- (pyridine-2-yl) -3,4-dihydroquinazolin-7-yl) -3- (2- (pyridine-2-yl) vinyl) benzamide

482.53 mg (1.98 mmol) of 3 - [(E) -2- (pyridine-2-yl) ethenyl] benzoyl chloride **33** are added to 500 mg (1.98 mmol) of 7-amino-2-methyl-3- (pyridine -2-yl) quinazolin-4 (3H) -one **36** and the mixture is solubilized in 3 mL of pyridine (99.7%)

The whole is kept under magnetic stirring, at RT, for 48 h. The reaction mixture is poured on ice and the aqueous solution is kept at 4 °C, for 24 h.

Following filtration, the residue collected on the filter (800 mg) is washed with methanol, in order to eliminate insoluble impurities. The solvent is removed in the rotavapor, under reduced pressure and from the solid obtained (480 mg), the compound **2** is purified by column chromatography:

150 g of Merck silica gel, 230-400 mesh ASTM; eluent: ethyl acetate / acetone mixture (1: 1); column diameter: 4.5 cm; fractions collected: 1-109; combined fractions: 38-104.

The obtained compound **2** is subjected to crystallization from ethanol, in order to obtain the crystalline product.

Yield: 45%. P.f.:210-5°C. ¹H-NMR (δ): 2.11 (3H, S, CH₃); 7.32-8.70 (17H, one set of signals, C₆H₄, C₆H₃, 2xC₅H₄N, CH = CH); 10.78 (1H, S, NH, exchangeable with D₂O). ¹³C-NMR (δ): 23.71 (CH₃); 116.24 (CH); 119.64 (CH); 123.12 (2xCH); 124.61 (CH); 125.22 (CH); 126.57 (CH); 127.55 (CH); 128.23 (CH); 129.52 (2xCH); 131.01 (CH); 131.83 (CH); 135.66 (C); 137.10 (2xC); 137.63 (CH); 139.80 (CH); 145.40 (C); 148.79 (C); 149.85 (CH); 150.22 (CH); 151.30 (C); 154.40 (C); 155.04 (C); 161.16 (CO); 166.58 (CO). IR (cm⁻¹): 1668, 1679 (2xCO); 3300 (NH).

5.1.10 Synthesis of the (E) -N- (2-methyl-4-oxo-3- (pyridine-2-yl) -3,4-dihydroquinazolin-7-yl) -3- (2- (pyridin-2-) complex II) vinyl) benzamide V49 (V49-Cu)

50 mg (0.109 mmol) of compound **2** are dissolved in 10 mL of EtOH, at 60 °C and under magnetic stirring. 14.66 mg (0.109 mmol) of CuCl₂ are dissolved in 1 mL of EtOH and the resulting solution is added to the reaction environment. The mixture is kept at 60 °C under magnetic stirring for 2 h. Thereafter, the reaction mixture is cooled to rt. and kept under magnetic stirring for 24 h. Finally, the reaction mixture is kept at 4 °C for 24 h. A solid, the 2-Cu complex, is isolated by filtration.

Yield: 50%. M.p.: 140-150 °C. IR (cm⁻¹): 1671 (CO); 3300 (NH); 3445 (OH).

Elemental analysis: w-%C 48.18 +/-0.07, w-%H 3.31 +/-0.01, w-%N 10.04 +/-0.01, w-%S 0.133 +/-0.008, w%O 8.96 +/- 0.18, w%Cu 9.1 w%Cl 20.3 C:N 5.60, C:O 7.16.

5.1.11 Synthesis of 2-methyl-7-nitro-4H-3,1-benzoxazin-4-one

300 mg of 2-amino-4-nitrobenzoic acid **1** were solubilized in 5 mL of acetic anhydride and the reaction mixture was refluxed and under magnetic stirring for 4 h. Then, the excess acetic anhydride was removed with the rotavapor and the solid residue was washed with cyclohexane and filtered. The solid thus obtained, unitary on TLC, was used as crude for the subsequent reaction.

M.p. : 134-135 °C , Lit. 138 °C (Ashraf A. et al., 2003).

5.1.12 Synthesis of 2-methyl-7-nitroquinazolin-4 (3H) -one

The crude 2-methyl-7-nitro-4H-3,1-benzoxazin-4-one **2** obtained from the previous reaction was solubilized in 2.5 mL of dioxane and was refluxed and under magnetic stirring for 1 h with 2.5 mL of NH₄OH at 32%. The reaction

mixture was evaporated in a rotavapor and the solid was filtered and crystallized from ethanol.

M.p .: 285-290 °C, Lit. 287-290 °C (Ashraf A. et al., 2003).

The ¹H-NMR spectrum showed the signals of the two tautomers **3a** and **3b** (Figure 65):

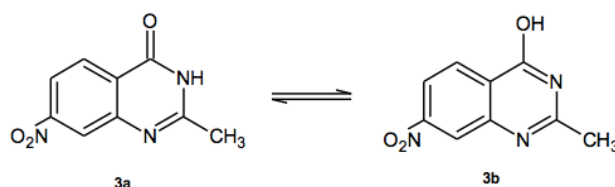


Figure 65. Two tautomers **3a** and **3b** obtained in the synthesis of Synthesis of 2-methyl-7-nitroquinazolin-4 (3H) -one **3**

3a (δ): 2.15 (3H, singlet, CH₃); 7.92-8.53 (3H, one set of signals, C₆H₃); 11.46 (1H, singlet, NH, exchangeable with D₂O).

3b (δ): 2.39 (3H, singlet, CH₃); 7.92-9.24 (3H, one set of signals, C₆H₃); 12.68 (1H, enlarged singlet, OH, exchangeable with D₂O).

5.1.13 Synthesis of 7-amino-2-methylquinazolin-4 (3H) -one

500 mg of 2-methyl-7-nitroquinazolin-4 (3H) -one **3** was added to a suspension of 1.5 g of iron and 1.87 mL of 5% acetic acid over a period of 1 h, in a water bath and under stirring. After 2 h 30' of stirring at 100 °C, the reaction mixture was alkalized up to pH = 8 with the minimum amount of an aqueous solution of 2M NaOH and the suspension was filtered. The solid residue was then extracted with hot methanol, obtaining almost unitary 7-amino-2-methylquinazolin-4 (3H) -one **4**. Finally, crystallization from methanol made it possible to obtain pure compound **4**.

M.p .: 305-307 °C (Lit. 311 °C). ¹H-NMR (δ): 2.24 (3H, singlet, CH₃); 6.02 (2H, singlet, NH₂, exchangeable with D₂O); 6.53-7.72 (3H, one set of signals, C₆H₃); 11.61 (1H, singlet, NH, exchangeable with D₂O).

5.1.14 Chlorination of substituted trans-cinnamic acids 6a-g

An equimolar quantity of **5a-g** substituted trans-cinnamic acid to be used for the subsequent condensation reaction was chlorinated by refluxing it and under magnetic stirring in 3 mL of thionyl chloride for 5 h. The excess of thionyl chloride was then removed in the rotavapor and the product thus obtained was used as crude for the subsequent reaction.

5.1.15 Synthesis of 2-methyl-7-nitro-4H-3,1-benzoxazin-4-one

1 g of 2-amino-4-nitrobenzoic acid **4** was solubilized in 16.6 mL of acetic anhydride and the reaction mixture was refluxed for 4 h. Then, the excess acetic anhydride was removed with the rotavapor and the solid residue was washed with cyclohexane and filtered. The solid thus obtained, unitary on TLC, was used as crude for the subsequent reaction.

M.p .: 134-135 °C (Lit. 138 °C).

5.1.16 Synthesis of 2-methyl-7-nitro-3- (pyridine-2-yl) quinazolin-4 (3H) -one

To the crude 2-methyl-7-nitro-4H-3,1-benzoxazin-4-one **5** obtained from the previous reaction, 460 mg of 2-aminopyridine was added and it was subjected to the fusion reaction for 30 min., Reaching the temperature of 160 °C. After cooling to room temperature, a hot wash with methanol was carried out on the reaction mixture and the yellow solid was filtered. The desired product was isolated both from the filtration mother liquors after concentration by evaporation, and by extraction of the yellow solid with hot methanol.

1 g of impure compound **6** was obtained, subsequently purified by column chromatography. Chromatography was carried out on a sample of 500 mg: 170 g of Merck silica gel, 70-230 mesh ASTM; eluent: ethyl acetate; column diameter: 4.5 cm; collected fractions: 1-90, 15 mL each; fractions joined: 47-85.

Yield: 50%. M.p. : 148-53 °C. ¹H-NMR (δ): 2.15 (3H, s, CH₃); 6.80-8.70 (7H, one set of signals, C₆H₃, C₅H₄N). ¹³C-NMR (δ): 24.41 (CH₃); 120.61 (CH); 122.57 (CH); 124.25 (CH); 125.22 (C); 125.60 (CH); 128.00 (CH); 140.00 (CH); 141.50 (C); 148.12 (C); 150.37 (CH); 150.65 (C); 156.58 (C); 169.60 (CO). IR (cm⁻¹): 1693 (CO).

5.1.17 Synthesis of 7-amino-2-methyl-3- (pyridine-2-yl) quinazolin-4 (3H) -one

350 mg of 2-methyl-7-nitro-3- (pyridine-2-yl) quinazolin-4 (3H) -one **6** was added to a suspension of 1.05 g of iron and 1.31 mL of 5% acetic acid in the period of 2 h and 30 min., in a water bath and under stirring. After 2 h of stirring at 100 °C, the reaction mixture was basified up to pH = 8 with a saturated solution of NaOH, then filtered and the dry solid residue was extracted with hot methanol. The yellow solid (290 mg) thus obtained was purified by CombiFlash® RF200 automatic chromatography: 60 g of Merck silica gel, 230-400 mesh ASTM; eluent: mixture of ethyl acetate / acetone (1: 1); collected fractions: 1-55, 15 mL each; fractions joined: 28-47.

Yield: 41.4%. M.p.: 190-210 °C. ¹H-NMR (δ): 2.01 (3H, s, CH₃); 6.19 (2H, s, NH₂, exchangeable with D₂O); 6.61-8.65 (7H, one set of signals, C₆H₃, C₅H₄N). ¹³C-NMR (δ): 22.56 (CH₃); 107.05 (CH); 109.21 (C); 115.14 (CH); 124.74 (CH); 124.88 (CH); 128.09 (CH); 138.52 (CH); 149.84 (C); 150.01 (CH); 151.70 (C); 153.40 (C); 155.34 (C); 161.11 (CO). IR: 1656 (CO); 3344-3415 (NH₂).

5.1.18 Chlorination of substituted trans-cinnamic acids **9a, c, d, e, g**

An equimolar amount of substituted trans-cinnamic acid **8a, c, d, e, g** to be used for the subsequent condensation reaction was chlorinated by refluxing it in 3 mL of thionyl chloride (99.7%) for 5 h. The excess of thionyl chloride was then removed in the rotavapor and the product thus obtained was used as crude for the subsequent reaction.

5.1.19 General synthesis of (2E) -3- (4-R-phenyl) -N- [2-methyl-4-oxo-3-(pyridine-2-yl) -3,4-dihydroquinazolin-7-yl] -3 -phenylprop-2-enamides **3a, c, d, e, g**

Equimolar amounts of 7-amino-2-methyl-3- (pyridine-2-yl) quinazolin-4 (3H) -one **7** and substituted trans-cinnamic acid chloride **9a, c, d, e, g** were made to react in 3 mL of pyridine (99.7%) under magnetic stirring and at room temperature for 48 h. The product solidified by adding crushed ice. Finally, the solid formed was isolated by filtration.

Compounds **3a, c, d, e, g** were purified by crystallization or automatic chromatography CombiFlash® RF200: 60 g of Merck silica gel, 230-400 mesh ASTM; eluent: mixture of ethyl acetate / acetone (8: 2).

3a. Yield: 66.6%; m.p .: 228-30 °C. Crystallized from ethanol. ¹H-NMR (δ): 2.10 (3H, s, CH₃); 6.88-8.69 (14H, one set of signals, C₆H₅, C₆H₃, C₅H₄N, CH = CH); 10.73 (1H, s, NH, exchangeable with D₂O). ¹³C-NMR (δ): 23.68 (CH₃); 115.24 (CH); 115.96 (C); 118.74 (CH); 122.18 (CH); 124.60 (CH); 125.21 (CH); 127.79 (CH); 128.37 (2xCH); 129.54 (2xCH); 130.54 (CH); 134.98 (C); 139.80 (CH); 141.77 (CH); 145.39 (C); 148.91 (C); 150.20 (CH); 151.29 (C); 154.43 (C); 161.10 (CO); 164.69 (CO). IR (cm⁻¹): 1668, 1678 (2xCO); 3333 (NH).

3b: Yield: 57%; m.p .: 235-237 °C. Crystallizes from ethanol. ¹H-NMR (δ): 2.13 (3H, s, CH₃); 2.47 (3H, s, CH₃); 6.86-8.71 (13H, one set of signals, C₆H₅, C₆H₃, C₅H₄N, CH = CH); 10.76 (1H, s, NH, exchangeable with D₂O). ¹³C-NMR (δ): 19.95 (CH₃); 23.69 (CH₃); 115.28 (CH); 115.99 (C); 118.77 (CH); 123.38 (CH);

124.61 (CH); 125.22 (CH); 125.67 (CH); 126.98 (CH); 127.79 (CH); 130.26 (CH); 131.32 (CH); 133.81 (C); 137.69 (C); 139.22 (CH); 139.81 (CH); 145.39 (C); 148.95 (C); 150.84 (CH); 151.55 (C); 154.45 (C); 161.46 (CO); 164.70 (CO). IR (cm⁻¹): 1668, 1688 (2xCO); 3304 (NH).

3c. Yield: 38.5%; m.p.: 260 °C. CombiFlash® RF200 automatic chromatography: 60 g of Merck silica gel, 230-400 mesh ASTM; eluent: ethyl acetate / acetone mixture (8: 2). Collected fractions: 1-50, 15 mL each; fractions joined: 17-23. Crystallized from ethanol. ¹H-NMR (δ): 2.10 (3H, s, CH₃); 6.87-8.69 (13H, one set of signals, C₆H₅, C₆H₃, C₅H₄N, CH = CH); 10.74 (1H, s, NH, exchangeable with D₂O). ¹³C-NMR (δ): 23.67 (CH₃); 115.27 (CH); 116.01 (C); 118.74 (CH); 123.00 (CH); 124.59 (CH); 125.21 (CH); 127.80 (CH); 129.58 (2xCH); 130.05 (2xCH); 133.96 (C); 134.95 (C); 139.80 (CH); 140.36 (CH); 145.30 (C); 148.90 (C); 150.20 (CH); 151.27 (C); 154.45 (C); 161.09 (CO); 164.49 (CO). IR (cm⁻¹): 1659, 1693 (2xCO); 3333 (NH).

3d. Yield: 21.7%; m.p.: 270 °C. CombiFlash® RF automatic chromatography 200 60 g Merck silica gel, 230-400 mesh ASTM; eluent: mixture of ethyl acetate / acetone (8: 2). Collected fractions: 1-50, 15 mL each; fractions joined: 15-27. Crystallized from ethanol. ¹H-NMR (δ): 2.10 (3H, s, CH₃); 2.35 (3H, s, CH₃); 6.82-8.69 (13H, one set of signals, C₆H₅, C₆H₃, C₅H₄N, CH = CH); 10.70 (1H, s, NH, exchangeable with D₂O). ¹³C-NMR (δ): 21.48 (CH₃); 23.68 (CH₃); 115.19 (CH); 115.89 (C); 118.72 (CH); 121.13 (CH); 124.60 (CH); 125.21 (CH); 127.77 (CH); 128.36 (2xCH); 130.13 (2xCH); 132.25 (C); 139.80 (CH); 140.44 (C); 141.74 (CH); 145.47 (C); 148.91 (C); 150.20 (CH); 151.29 (C); 154.41 (C); 161.10 (CO); 164.85 (CO). IR (cm⁻¹): 1668, 1684 (2xCO); 3333 (NH).

3e. Yield: 36%; m.p. : 220 °C. CombiFlash® RF200 automatic chromatography: 60 g of Merck silica gel, 230-400 mesh ASTM; eluent: mixture of ethyl acetate / acetone (8: 2). Collected fractions: 1-50, 15 mL each; fractions joined: 16-20. Crystallized from ethanol. ¹H-NMR (δ): 2.10 (3H, s, CH₃); 2.36 (3H, s, CH₃); 6.86-8.69 (13H, one set of signals, C₆H₅, C₆H₃, C₅H₄N, CH = CH); 10.70 (1H, s, NH, exchangeable with D₂O). ¹³C-NMR (δ): 21.39 (CH₃); 23.68 (CH₃); 115.20 (CH); 115.94 (C); 118.72 (CH); 122.04 (CH); 124.60 (CH); 125.21 (CH); 125.62

(CH); 127.79 (CH); 128.82 (CH); 129.43 (CH); 131.24 (CH); 134.92 (C); 138.70 (C); 139.80 (CH); 141.82 (CH); 145.40 (C); 148.91 (C); 150.20 (CH); 151.29 (C); 154.42 (C); 161.10 (CO); 164.72 (CO). IR (cm⁻¹): 1666, 1687 (2xCO); 3300 (NH).

3f. Yield: 64%; m.p. : 224 °C. Crystallizes from ethanol. ¹H-NMR (δ): 2.10 (3H, s, CH₃); 6.91-8.69 (13H, one set of signals, C₆H₄, C₆H₃, C₅H₄N, CH = CH); 10.72 (1H, s, NH, exchangeable with D₂O). ¹³C-NMR (δ): 23.68 (CH₃); 115.30 (CH); 116.06 (C); 118.74 (CH); 123.93 (CH); 124.59 (CH); 125.22 (CH); 126.75 (CH); 127.82 (CH); 128.05 (CH); 130.09 (CH); 131.34 (CH); 134.22 (C); 137.28 (C); 139.80 (CH); 140.07 (CH); 145.23 (C); 148.90 (C); 150.21 (CH); 151.27 (C); 154.46 (C); 161.09 (CO); 164.34 (CO). IR (cm⁻¹): 1661, 1697 (2xCO); 3334 (NH).

3g. Yield: 17%; m.p. : 220 °C. CombiFlash® RF200 automatic chromatography: 60 g of silica gel; eluent: mixture of ethyl acetate / acetone (8: 2). Collected fractions: 1-50, 15 mL each; fractions joined: 17-20. Crystallized from ethanol. ¹H-NMR (δ): 3.07 (3H, s, CH₃); 6.93-8.69 (13H, a set of signals C₆H₄, C₆H₃, C₅H₃, C₅H₄N); 10.82 (1H, s, NH, exchangeable with D₂O). ¹³C-NMR (δ): 23.69 (CH₃); 115.40 (CH); 116.14 (C); 118.79 (CH); 124.59 (CH); 125.22 (CH); 125.31 (CH); 127.83 (CH); 128.28 (CH); 128.38 (CH); 130.60 (CH); 131.95 (CH); 132.75 (C); 134.06 (C); 136.78 (CH); 139.81 (CH); 145.17 (C); 148.90 (C); 150.21 (CH); 151.27 (C); 154.48 (C); 161.09 (CO); 164.16 (CO). IR (cm⁻¹): 1611, 1661 (2xCO); 3336 (NH).

5.1.20 General synthesis of the cupric complexes of (2E) -3- (4-R-phenyl) -N- [2methyl-4-oxo-3- (pyridin-2-yl) -3,4-dihydroquinazolin-7-yl] - 3- phenylprop-2-enamides 10a, e

Equimolar amounts of (2E) -3- (4-R-phenyl) -N- [2-methyl-4-oxo-3- (pyridine-2-yl) -3,4-dihydroquinazolin-7-yl] -3 -phenylprop-2-enamides **3a**, and were complexed with cupric (II) chloride in ethanol (12 mL) and the solution was heated to 60 °C [Cupric (II) chloride in 2 mL of ethanol was added slowly].

The reaction mixture was left under magnetic stirring and at rt. for 24 h and, thereafter, it was kept at refrigeration temperature for 24 h. The greenish solid formed was isolated by filtration and dried in an oven.

10a: Yield: 5.25%. M.p.: 270° C. IR (cm⁻¹): 16; Elementar analysis: w-%C 48.18 +/-0.07, w-%H 3.31 +/-0.01, w-%N 10.04 +/-0.01, w-%S 0.133 +/-0.008, w%O 8.96 +/- 0.18, w%Cu 9.1 w%Cl 20.3 C:N 5.60, C:O 7.16.

5.1.21 General synthesis of (2E) -3- (4-R-phenyl) -N- (2-methyl-4-oxo-3,4-dihydro quinazolin-7-yl) prop-2-enamides 7a-g

Equimolar amounts of 7-amino-2-methylquinazolin-4 (3H) -one **4** and of the **6a-g** substituted trans-cinnamic acid chloride were reacted in 3 mL of pyridine under magnetic stirring and at room temperature for 96 h. Then, the reaction mixture was poured into crushed ice and the solid formed was filtered and crystallized from methanol.

7a. M.p.: 290-293 °C. Yield: 40%; ¹H-NMR (δ): 2.34 (3H, singlet, CH₃); 6.86-8.06 (10H, a set of signals, C₆H₃, C₆H₅, 2xCH); 10.64 (1H, singlet, NH, exchangeable with D₂O); 12.10 (1H, singlet, NH, exchangeable with D₂O). IR (cm⁻¹): 1682 (2xCO, broadband); 3330 (2xNH, broadband).

7b. M.p.: 297-299 °C. Yield: 38%; ¹H-NMR (δ): 2.34 (3H, singlet, CH₃); 2.43 (3H, singlet, CH₃); 6.76-8.06 (9H, a set of signals, C₆H₃, C₆H₄, 2xCH); 10.65 (1H, singlet, NH, exchangeable with D₂O); 12.09 (1H, singlet, NH, exchangeable with D₂O). IR (cm⁻¹): 1668, 1694 (2xCO); 3294 (2xNH, broadband).

7c. M.p.: 268-270 °C. Yield: 62%; ¹H-NMR (δ): 2.33 (3H, singlet, CH₃); 2.35 (3H, singlet, CH₃); 6.84-8.06 (9H, a set of signals, C₆H₃, C₆H₄, 2xCH); 10.63 (1H, singlet, NH, exchangeable with D₂O); 12.10 (1H, singlet, NH, exchangeable with D₂O). IR (cm⁻¹): 1627, 1669 (2xCO); 3237, 3304 (2xNH).

7d. M.p.: 290-293 °C. Yield: 58%; ¹H-NMR (δ): 2.33 (3H, singlet, CH₃); 2.34 (3H, singlet, CH₃); 6.79-8.05 (9H, a set of signals, C₆H₃, C₆H₄, 2xCH); 10.58

(1H, singlet, NH, exchangeable with D₂O); 12.09 (1H, singlet, NH, exchangeable with D₂O). IR (cm⁻¹): 1618, 1682 (2xCO); 3285, 3314 (2xNH).

7e. M.p.: 284-290 °C. Yield: 57%; ¹H-NMR (δ): 2.34 (3H, singlet, CH₃); 6.91-8.04 (9H, one set of signals, C₆H₃, C₆H₄, 2xCH); 10.71 (1H, singlet, NH, exchangeable with D₂O); 12.09 (1H, singlet, NH, exchangeable with D₂O). IR (cm⁻¹): 1668, 1683 (2xCO); 3303, 3387 (2xNH).

7f. M.p.: 282-284 °C. Yield: 51%; ¹H-NMR (δ): 2.33 (3H, singlet, CH₃); 6.88-8.05 (9H, a set of signals, C₆H₃, C₆H₄, 2xCH); 10.62 (1H, singlet, NH, exchangeable with D₂O); 12.10 (1H, singlet, NH, exchangeable with D₂O). IR (cm⁻¹): 1619, 1675 (2xCO); 3285 (2xNH, broadband).

7g. M.p.: 306-310 °C. Yield: 57%; ¹H-NMR (δ): 2.33 (3H, singlet, CH₃); 6.85-8.06 (9H, a set of signals, C₆H₃, C₆H₄, 2xCH); 10.66 (1H, singlet, NH, exchangeable with D₂O); 12.10 (1H, singlet, NH, exchangeable with D₂O). IR (cm⁻¹): 1615, 1668 (2xCO); 3322, 3389 (2xNH).

5.1.22 General synthesis of (2E) -3- (4-R-phenyl) -N- {4-oxo-2 - [(E) -2-phenylethenyl] -3,4-dihydroquinazolin-7-yl} prop-2- 7h-n enamides

At a 0.4 mmol solution of (2E) -3- (4-R-phenyl) -N- (2-methyl-4-oxo-3,4-dihydroquinazolin-7-yl) prop-2-enamides **7a-g** 0.4 mmoles of benzoic aldehyde were added to 6 mL of glacial acetic acid, and the reaction mixture was refluxed and under magnetic stirring. The reaction of derivative **7k** was completed after 12h of reflux. For derivatives **7h-j**, l-n it was necessary to add an additional aliquot of benzoic aldehyde (equimolar) every 24 h of reflux until the completion of the reaction (about 64 h). The reaction mixture was dried in the rotavapor and the solid residue was washed with ethyl acetate and filtered. Compounds **7h-n** were obtained unitary after crystallization from methanol.

7h: 64 h total reflux. m.p.: 286-288 °C. Yield: 41%. ¹H-NMR (δ): 6.87-8.24 (17H, one set of signals, C₆H₃, 2xC₆H₅, 4xCH); 10.62 (1H, singlet, NH, exchangeable with D₂O); 12.21 (1H, singlet, NH, exchangeable with D₂O). IR (cm⁻¹): 1661 (2xCO, broadband); 3314 (2xNH, broadband).

7i: total 64 h of reflux. m.p.: 325 °C. Yield: 51%. ¹H-NMR (δ): 2.35 (3H, singlet, CH₃); 6.80-8.23 (16H, a set of signals, C₆H₃, C₆H₄, C₆H₅, 4xCH); 10.58 (1H, singlet, NH, exchangeable with D₂O); 12.21 (1H, singlet, NH, exchangeable with D₂O). IR (cm⁻¹): 1667 (2xCO, broadband); 3279 (2xNH, broadband).

7j: 64 h total reflux. m.p.: 327 °C. Yield: 49%. ¹H-NMR (δ): 2.35 (3H, singlet, CH₃); 6.80-8.23 (16H, a set of signals, C₆H₃, C₆H₄, C₆H₅, 4xCH); 10.58 (1H, singlet, NH, exchangeable with D₂O); 12.21 (1H, singlet, NH, exchangeable with D₂O). IR (cm⁻¹): 1667 (2xCO, broadband); 3279 (2xNH, broadband).

7k: 12 hours of total reflux. m.p.: 320 °C. Yield: 47.4%. ¹H-NMR (δ): 2.35 (3H, singlet, CH₃); 6.80-8.23 (16H, a set of signals, C₆H₃, C₆H₄, C₆H₅, 4xCH); 10.58 (1H, singlet, NH, exchangeable with D₂O); 12.21 (1H, singlet, NH, exchangeable with D₂O). IR (cm⁻¹): 1667 (2xCO, broadband); 3279 (2xNH, broadband).

7l: 64 h total reflux. m.p.: 328-330 °C. Yield: 53%. ¹H-NMR (δ): 6.86-8.23 (16H, one set of signals, C₆H₃, C₆H₄, C₆H₅, 4xCH); 10.62 (1H, singlet, NH); 12.20 (1H, singlet, NH). IR (cm⁻¹): 1667 (2xCO, broadband); 3325 (2xNH, broadband).

7m: 64 hours of total reflux. m.p.: 330 °C. Yield: 56%. ¹H-NMR (δ): 6.86-8.23 (16H, one set of signals, C₆H₃, C₆H₄, C₆H₅, 4xCH); 10.62 (1H, singlet, NH); 12.20 (1H, singlet, NH). IR (cm⁻¹): 1667 (2xCO, broadband); 3325 (2xNH, broadband).

7n: total 64 h of reflux. m.p.: 326-328 °C. Yield: 50.3%. ¹H-NMR (δ): 6.86-8.23 (16H, one set of signals, C₆H₃, C₆H₄, C₆H₅, 4xCH); 10.62 (1H, singlet, NH); 12.20 (1H, singlet, NH). IR (cm⁻¹): 1667 (2xCO, broadband); 3325 (2xNH, broadband).

5.2 Biological

5.2.1 Cell culture

All cells were grown in sterile T25 cell culture flasks and were cultured under humidified conditions at 37°C and 5% CO₂ and regularly checked for *Mycoplasma* contamination. They were all passaged using Trypsin - EDTA (0.1% Trypsin, 0.01% EDTA) every 3-4 days and fresh medium recommended for the respective cell lines was added. The extent of reduction was determined according to the confluence of the cell monolayer. All cells were freshly thawed from liquid nitrogen every six weeks to avoid additional genomic changes during cell culture propagation.

Cell lines and medium used:

Cell line	Medium + additives
DMS 114	RPMI-1640, supplemented with 10% fetal calf serum (FCS,PAA, Linz, Austria)
NCI H1703	RPMI-1640, supplemented with 10% fetal calf serum (FCS,PAA, Linz, Austria)
NCI H520	RPMI-1640, supplemented with 10% fetal calf serum (FCS,PAA, Linz, Austria)
U251-MG/Gly/GFP/Arg/KD/KA	RPMI- 1640 medium (Sigma-Aldrich, Missouri, USA) supplemented with 10% fetal calf serum (FCS, Gibco, Thermo Fisher Scientific, MA, USA)
BTL1529 GFP/Gly	RPMI- 1640 medium (Sigma-Aldrich, Missouri, USA) supplemented with 10% fetal calf serum (FCS, Gibco, Thermo Fisher Scientific, MA, USA)
DAOY	RPMI- 1640 medium (Sigma-Aldrich, Missouri, USA) supplemented with 10% fetal calf serum (FCS, Gibco, Thermo Fisher Scientific, MA, USA)
SIWA	RPMI- 1640 medium (Sigma-Aldrich, Missouri, USA) supplemented with 10% fetal calf serum (FCS, Gibco, Thermo Fisher Scientific, MA, USA)
UMUC14	RPMI- 1640 medium (Sigma-Aldrich, Missouri, USA) supplemented with 10% fetal calf serum (FCS, Gibco, Thermo Fisher Scientific, MA, USA)
UMUC14 Ponatinib res.	RPMI- 1640 medium (Sigma-Aldrich, Missouri, USA) supplemented with 10% fetal calf serum (FCS, Gibco, Thermo Fisher Scientific, MA, USA)
VMCUB1	RPMI- 1640 medium (Sigma-Aldrich, Missouri, USA) supplemented with 10% fetal calf serum (FCS, Gibco, Thermo Fisher Scientific, MA, USA)
RKO/wt	McCoy's 5A Modified Medium + 2mM glutamine + 10%FBS

Cell line	Medium + additives
A431	RPMI- 1640 medium (Sigma-Aldrich, Missouri, USA) supplemented with 10% fetal calf serum (FCS, Gibco, Thermo Fisher Scientific, MA, USA)
PC9	RPMI- 1640 medium (Sigma-Aldrich, Missouri, USA) supplemented with 10% fetal calf serum (FCS, Gibco, Thermo Fisher Scientific, MA, USA)
BTL 1376/26	RPMI- 1640 medium (Sigma-Aldrich, Missouri, USA) supplemented with 10% fetal calf serum (FCS, Gibco, Thermo Fisher Scientific, MA, USA)
HCT116 p53/wt	McCoy's 5A Modified Medium + 2mM glutamine + 10%FBS
HCT116 p53/KO	McCoy's 5A Modified Medium + 2mM glutamine + 10%FBS

The human lung cancer cell lines NCI-H1703, NCI-H520 (non-small cell lung cancer, NSCLC) and DMS114 (small cell lung cancer, SCLC) were purchased from American Type Culture Collection (Manassas, VA, USA) and grown in RPMI-1640 supplemented with 10% fetal calf serum (FCS, PAA, Linz, Austria) at 37 °C and 5% CO₂. U251-MG is a human glioblastoma multiforme cell line, purchased from American Type Culture Collection (ATCC, Manassas, VA, USA). BTL1528 is a primary cell model, established from surgical specimens of a glioblastoma multiforme patient, treated in our clinics. All drugs used in this study were dissolved in DMSO and stored as 10mM Stocks at - 20 °C. Most compounds were stable under these conditions. Metal complexes V49-Cu, V50-Cu and V55-Cu, showed a decrease in anti-proliferative activity after a few cycles of freezing and thawing. Thus, in order to obtain reproducible results, these three compounds were dissolved newly every time before use.

5.2.2 Cell-viability assay (MTT)

The MTT assay was performed using the protocol of the Institute of Cancer Research of Vienna.

2×10^4 cells/mL, were seeded in 100 μ l of medium on a 96-well plate and left for 24h incubation at 37°C and 5% CO₂. The next day, the drugs were then added at particular concentration 2x concentrated in 100 μ M and incubated for 72h. Evaluation was performed using 3-(4,5-dimethylthiazol-2-yl)-2,5-diphenyltetrazolium bromide (MTT)-vitality assay (EZ4U, Biomedica, Vienna, Austria). One glass bottle of EZ4U powder was dissolved in 2.5 ml activator solution and diluted 1:10 in medium. The medium was removed from the 96-well plate and 100 μ l of developer solution were added to each well. After 2-5h of incubation, depending on the change of color in the wells, measurement of the values was performed using the TECAN Infinite M200 Pro plate reader at 450 nm wavelength with a reference wavelength of 620 nm. Analysis of the results was carried out using the software Microsoft Excel® and GraphPad Prism. The blank values were subtracted from the results following normalization to the control group with no drug added. IC₅₀ values (half maximal inhibitory concentration) were determined using GraphPad Prism by calculating the interpolated X values. Similarly, t-test and p-value calculation were performed with GraphPad Prism. Results are given as mean \pm SD and were normalized to untreated control cells.

5.2.3 Clonogenic assay

In order to perform this assay 2×10^3 cells/ml were seeded in 500 μ l on a 6 - or 24-well plates and left for 24 h incubation at 37°C and 5% CO₂. The drug of interest was added at differing concentrations and 6x concentrated in 100 μ l and left for 7d and then removed the medium to dry the wells overnight. The following day the wells were washed with PBS and left in methanol (VWR, Austria) for 20 min at 4°C. Then were washed with PBS again and Crystal violet (Merck, Germany) -

PBS was added. It was left on for a few minutes before removing the Crystal violet-PBS solution and left for drying. Pictures of wells were taken using a Nikon camera. Clone counting was performed using the software ImageJ and analyzed using Microsoft Excel®. The clone counts were normalized to the control group. The results were visualized using GraphPad Prism and Adobe® Photoshop. PBS was obtained using: 95 g Na₂HPO₄ X 2H₂O, 32 g NaHPO₄, 44 g NaCl diluted in 1 L ddH₂O. Na₂HPO₄, NaHPO₄, NaCl by Sigma-Aldrich, USA.

5.2.4 Western Blotting

Western Blotting is a method using polyacrylamide gel electrophoresis in order to separate proteins by size. After installing an electric current on the gel, negatively charged proteins move towards to anode. As not all proteins are negatively charged a priori, SDS is used as detergent in order to add a negative charge to otherwise lipophilic proteins. As the polyacrylamide gel is structured by multiple pores of the same size, smaller proteins move more rapid further towards the anode along the electric current. After separation the protein are blotted onto a polyvinylidenfluorid (PDV) membrane and can be detected by specific primary antibodies against epitopes characteristic for the protein of interest.

Western blotting was performed according the protocol of the Institute of Cancer Research of Vienna.

<i>List of primary antibodies used for Western blot analysis</i>				
Antigen	A n t i b o d y source	Dilution	Size (KDa)	Company
β-actin	M o u s e monoclonal	1:1000	42	Cell signaling
S6	Rabbit	1:1000	32	Cell signaling
Phospho-S6 (Ser235/236)	Rabbit	1:1000	32	Cell signaling
Phospho-S6K (Thr421/Ser424)	Rabbit	1:1000	70, 85	Cell signaling
AKT	Rabbit	1:1000	60	Cell signaling
Phospho-AKT (Ser473, D9E)	Rabbit	1:1000	60	Cell signaling

<i>List of primary antibodies used for Western blot analysis</i>				
ERK1/2 (p44/42 MAPK)	Rabbit	1:1000	42, 44	Cell signaling
Phospho-ERK1/2 (p44/42 MAPK, Thr202/Tyr204)	Rabbit	1:1000	42, 44	Cell signaling
Phospho-FGFR (Tyr653/654)	Rabbit	1:500	120, 145	Santa Cruz
β-catenin	Rabbit	1:1000	92	Cell signaling
4EBP1 (53H11)	Rabbit	1:1000	15-20	Cell signaling
Phospho-GSK-3β (Ser9)	Rabbit	1:1000	46	Cell signaling
PARP	Rabbit	1:1000	89	Cell signaling
Phospho-FRS2-α (Tyr196)	Rabbit	1:1000	85	Santa Cruz
FGFR1 (sc-121) Flg(C-15)	Rabbit	1:500	75-160	Santa Cruz
FGFR4 (sc-124) (C-16)	Rabbit	1:500	95	Santa Cruz
UBIQUITIN	Rabbit	1:1000	————	Cell signaling
UBC3	Rabbit	1:1000	32	Cell signaling
SUMO-1	Rabbit	1:1000	11.5	Cell signaling
E-Cadherin	Rabbit	1:1000	97	Cell signaling
Vimentin	Rabbit	1:1000	54	Cell signaling

4×10^5 - 6×10^5 cells/well were seeded in 2 ml of growth medium in 6-well plates and left under normal cell culture conditions for recovery. On the next day when 80 – 90% confluence was reached, cells were treated with drugs of interest for 6 or 24 h. Upon scraping and washing the cells in PBS, cells were mechanically (ultrasound for 5 min) and chemically lysed (lysis buffer: 50 mM Tris/HCl (pH 7.6), 300mM NaCl, 0.5% Triton X-100, supplemented with protease inhibitors

PMSF and complete and phosphatase inhibitor PhosSTOP; all supplements from Roche, Rotkeuz, Switzerland). The suspension was left for incubation for 30-45 min on ice.

Total protein concentrations were determined following manufacturer's instructions ("Pierce™ BCA Protein Assay Kit", Rockford, IL, USA). 15µg of proteins were loaded onto 10% polyacrylamide-gels and polyacrylamide gel electrophoresis was run at 90 V. Proteins were blotted onto polyvinylidene difluoride membranes via semidry blotting. Blotting efficiency was checked with Ponceau (from Sigma-Aldrich Austria) protein staining. The blots were afterwards washed in 1xTBST (1xTBST: 100 ml 10x TBS, 900 ml ddH₂O, 1 ml Tween20 from Biorad Laboratories Austria; 10xTBS: 120 g Tris (Tris-hydroxymethyl-aminomethane, from VWR Austria), 90 g NaCl from VWR Austria, 1 l ddH₂O, pH 7.4) and then placed in milk solution for 1 h at r.t. The primary antibody was added and incubated overnight at 4 °C. Antibodies detecting target proteins were diluted 1:1000 in 3% BSA in Tris-buffered saline with 0.1% Tween20. The primary antibody was removed and washed in TBST. The secondary antibody was added (in 1% BSA) and left for 1 h incubation at r.t. The luminol was then used to detect the peroxidase signal. It was visualized using X-ray to develop the films.

5.2.5 Cell cycle analysis

Cell cycle analysis using PI (propidium iodide) staining is a method used to assess the percentage of the cells in a certain stage of cell cycle. PI binds to DNA and is thus utilized as a fluorescent dye to quantify the amount of DNA in a single cell. In order to ensure that the cell's DNA is not altered by enzymatic action or apoptotic processes and to stabilize it for analysis, they are fixed using ethanol. Additionally, ethanol affects cell permeability and allows the staining dye to enter all cells. RNase is used to digest proteins and ensure analysis of DNA only. FACS is utilized for measurement of the fluorescence emitted by PI. With the help of FACS it is therefore possible to evaluate the relative amount of DNA per cell and subsequently divide the cells into subgroups correlating to their quantity of

genetic material. As a result, it is possible to sub-divide them into the subgroups in G0-G1, G2-M and S phase of the cell cycle at the respective analysis point.

All cell cycle analysis was performed using the protocol from Institute of Cancer Research of Vienna.

5×10^5 cell/well were seeded in 2 ml of growth medium in 6-well plates and incubated at 37°C and incubated overnight.

They were treated with the specific drug at different concentrations and left 24 h. The cells were trypsinized and centrifuged at 1200 rpm for 8 min. They were resuspended in 100µl 0.9% NaCl. Afterwards they were slowly dropped in 1.8 ml 70% ice cold ethanol and stored at 4 °C for at least 1 h. They were again centrifuged at 8000 rpm for 1 min and the pellet was diluted in 1 ml PBS. 2µl RNase were added and left for 30 min incubation at 37 °C. 5µl PI were added and left for 30 min incubation at 4 °C. Analysis was performed using FACS.

5.2.6 DCF-DA assay

DCFH-DA (2',7'-Dichlorofluorescein diacetate) is a cell-permeable non-fluorescent probe. 2',7'-Dichlorofluorescein diacetate is de-esterified intracellularly and turns to highly fluorescent DCF (2',7'-dichlorofluorescein) upon oxidation. Applications include sensitive and rapid quantitation of oxygen-reactive species in response to oxidative metabolism, microplate assay for detecting oxidative products in phagocytic cells, and quantitative multiwell myeloid differentiation assays.

The DCF-DA assay was performed according the protocol of the Institute of Cancer Research of Vienna. Due to the light-sensitive DCFH-DA, the work was performed in the dark.

5×10^5 cells/per sample were suspended in 400µl of phenol free HBSS (H6648 from Sigma Aldrich) + 10µl DCFH-DA (ab113851) in 5 ml FACS tubes. DCFH-DA was mixed using 10µl DCF-DA stock + 668µl HBSS. The cells were incubated for 30 min at 37 °C and 5% CO₂. 50µl of the 10x concentrated drug solution were added to a total of 500µl. H₂O₂ was used as a positive control. 100µl were taken of this solution and mixed again with 780µl HBSS. 50µl of this

solution were then used as the H₂O₂ positive control in the previously prepared suspension (5 x 10⁵ cells in 440 μl HBSS + 10 μl DCFH-DA). The results were measured using FACS. The DCF-DA assay was performed also cell free, using the same method.

5.2.7 Apoptosis assay

Apoptosis is the cellular process of programmed cell death. This process involves many ordered steps including membrane blebbing, condensation of the cytoplasm and nucleus and cleavage of DNA. Notably, the plasma membrane lipids are re-ordered during apoptosis. Phosphatidylserine, phosphatidylethanolamine and phosphatidylinositol are located at the inner side (intracellular) of the membrane, whereas phosphatidylcholine and sphingomyelin are on the outer membrane (extracellular). During apoptosis, phosphatidylserine is flipped to the outer side of the membrane and exposed to the extracellular space. Biologically, this flipping process helps macrophages to detect dying cells for phagocytosis.

Annexin V is able to bind to the phosphatidylserine for identification of early apoptotic cells. A co-staining with PI is used to detect also the late apoptotic cells already dead. It is worth mentioning that PI can only enter into late apoptotic cells where the membranes are already permeable. Thus, cells without Annexin V or PI staining are considered as viable cells. Annexin V-positive, PI-negative cells are in the early stage of apoptosis whereas Annexin V and propidium iodide positive ones are in late apoptosis or already dead.

Apoptosis assay was performed using Annexin -V-FITC/PI Staining via FACS.

2x10⁵ cells/sample were seeded in 6-well plates and left for 24 h incubation at 37 °C and 5% CO₂.

The next day, the drugs were then added in a toxic concentration and incubate for 24 h. Then cell monolayers were trypsinized and centrifuge with 1200 rpm for 5 min and washed with PBS for one time. The cells re-suspended in 100 μl ABB and

were transferred into FACS tube, where 2 μ l PI (from 50 μ g/ml stock) + 2 μ l Annexin V-FITC were added at all samples including control. Due to the light-sensitive PI and Annexin V-FITC, the work was performed in the dark. After 10-15min incubation at r.t. in the dark 200 μ l ABB was added and immediately measure cells with FACS.

Apoptosis Assay, Annexin V:

Annexin V Binding Buffer (ABB)

2.38g (10mM) HEPES

8.18g (140mM) NaCl

367mg (2.5mM) CaCl₂

Fill up to a final volume of 1000ml with ddH₂O

5.2.8 RNA-extraction, reverse transcription and RT-PCR

4 \times 10⁵⁻⁶ \times 10⁵ cells/well were seeded in 6-well plates in 2 ml of the respective growth medium. After 24 hours, cells were exposed to 3.5 and 4.5 μ M of the V8 inhibitor for 16 hours. RNA isolation and qRT-PCR using TaqMan probes were performed as published previously (Sevelde F. et al., 2015). In short, total RNA was isolated using TRIzol reagent (Thermo Fisher Scientific, Waltham, MS, USA) and chloroform isolation according to standard protocols. Purity (260/280 ratio > 1.8) and concentration (100-500 ng / μ l) were checked using Nanodrop 1000 (Thermo Fisher Scientific). 1 μ g of RNA was reverse transcribed into cDNA using Revert aid reverse transcriptase (Thermo Fisher Scientific). cDNA was diluted 1:25 and mixed with FAM/ROX qPCR Mastermix (Thermo Fisher Scientific) and the according TaqMan probes (Thermo Fisher Scientific, **Table 11**) following the manufacturer's instructions. PCR was run on a CFX Connect Real-Time PCR Detection System and data were analyzed using the analysis software (BioRad, Hercules, CA, USA). Data were normalized to ACTB serving as housekeeping gene (Δ CT) and converted to a linear form using 2- Δ CT. In treatment

experiments, expression values were additionally normalized to untreated controls, set to 1 ($2^{-\Delta\Delta CT}$).

Taqman probe	number
FGFR1	HS00915137_m1
FGFR4	HS01106913_g1
ACTB	HS99999903_m1

Table 11. Taqman probes used for qRT-PCR (Thermo Fisher Scientific)

5.2.9 Filter migration assay

The trans-well migration assay is a commonly used test to study the migratory response of different cell types including e.g. endothelial cells to (angiogenic) inducers or inhibitors. Thus it is possible to measure the capacity of cell motility and invasiveness toward a chemo-attractant gradient. During this assay, cancer cells are placed on the upper layer of a cell culture insert with permeable membrane and a solution containing the test agent is placed below the cell permeable membrane. Following an incubation period (3–18 hours), the cells that have migrated through the membrane are stained and counted. Cells were serum starved for 24h after transfection and harvested and re-suspended in serum-free medium in a Trans-well chamber (CORNING, 3422). After incubation, cells were fixed and then stained with 0.1% crystal violet dye. The stained cells were counted at three randomly selected views for subsequent calculations.

5.2.10 Wound healing assay

Wound healing assay allows to study directional cell migration *in vitro*. The steps involve creating a “wound” in a cell monolayer, capturing the images at the

beginning and at regular intervals during cell migration to close the wound, and comparing the images to quantify the migration rate of the cells.

5×10^4 U373-GFP cells were seeded in 8-well chamber slides (Ibidi, Martinsried, Germany) in 300 μ l medium and the cells were grown to a density of 90%, the drug was added the next day and immediately were scratched and cultured with fresh medium. Photomicrographs were taken after scratching. Analysis of the results was carried out using the software Microsoft Excel® and GraphPad Prism.

5.2.11 Spheroids formation assay

Cultures of cancer cells and especially GMB cells in form of non-adherent spheroids is considered to reflect the presence of cancer stem cells in the cancer cell models. Substances successfully targeting spheroids are considered to have anticancer stem cell activity (Erhart F., et al., 2019)..

To generate spheroids from adherent cells, adherent cells Daoy (medulloblastoma brain tumor cells) 5×10^4 c/ml were harvested and cultured in sphere-inducing medium (MB+) and non-adherent plate (Costar® 24 Well Plate, With Lid, Flat Bottom, Ultra-Low Attachment Surface, Polystyrene). Spheroids started to form after ~24 h.

In the experiment with the drug V8 the following concentrations were used: 1 μ M, 5 μ M, 10 μ M, 25 μ M and 50 μ M, from 10mM stock in DMSO.

In the experiment with the drugs V49 and V49-Cu the following concentrations were used: 5 μ M, 10 μ M and 15 μ M.

The cells were incubated with drugs for 72 h and pictures were taken every day.

Spheroid size was evaluated by measuring spheroid perimeter using Image J software.

After 72 h, the cells were removed from the wells, centrifuged, the supernatant was removed and the cells, redispersed in fresh medium (MNP10), were placed in a 24-well normal cell culture plate which allowed for adhesion. The cells were incubated for 48 h and crystal violet staining and quantification was performed.

3.3.12 ATP-assay

ATP assay was performed using ATP- ViaLight® Plus Kit. 2×10^4 cells/mL, were seeded in 100 μ l of medium on a 96-well plate and left for 24h incubation at 37°C and 5% CO₂. The next day, the drugs were then added at particular concentration 2x concentrated in 100 μ M and incubated for 72h. Before analysis, the AMR PLUS was reconstituted in Assay Buffer and left for 15 minutes at room temperature to ensure complete rehydration. The culture plate was removed from the incubator allowing to room temperature for at least 5 minutes. 50 μ l of Cell Lysis Reagent was added to each well and left at least 10 minutes. 100 μ l of cell lysate was transferred to a white walled luminometer plate. 100 μ l of AMR PLUS was added to each appropriate well and incubate the plate for 2 minutes at room temperature. Cell viability was analyzed based on the cellular ATP content following manufacturer's instructions ("CellTiter-Glo® Luminescent Cell Viability Assay", Promega, Madison, WI, USA). Luminescence was measured at 1000 nm at the Tecan infinite 200Pro. Raw data were analyzed using GraphPad Prism software 5.0. Results are given as mean \pm SD and were normalized to untreated control cells.

5.2.13 Live cell microscopy

5×10^4 U373-GFP cells were seeded in 8-well chamber slides (Ibidi, Martinsried, Germany) in 300 μ l medium. After 24 h, cells were treated with V8 and intracellular drug accumulation was imaged at the indicated time-points on a live cell microscope (Visitron Systems, Puchheim, Germany) using a 40 \times oil

immersion DIC objective and VisiView® software. LEDs were used for widefield DIC and fluorescence (395/25 nm excitation and 460/50 nm bandpass filter for blue (DAPI) fluorescence and 475/34 nm excitation and 525/50 nm bandpass filter for green (FITC) fluorescence) illumination (Visitron Systems). Images were taken with a sCMOS 4.2MPx1 digital camera. The fluorescence intensity over time was quantified using ImageJ software.

Pictures were taken every 15 minutes for each sample for 64 h

5.2.14 Toxicity test *in vivo*

All animal experiments were carried out in agreement with the ethical animal license protocol in accordance with the current laws of Austria, approved by the Bundesministerium für Wissenschaft und Forschung, Austria (Permit number BMFWF 66.015/0010-WF/ v/3b/2017).

The toxicity tests on SCID mice was performed using V49 and V49-Cu 5mg/kg and 10mg/kg i.p. injection and was observed body weight and overall survival. The drug solutions will be administered i.p.

V49 and V49-Cu powders was dissolved in DMSO and diluted with PEG 400 (35%) and serum-free RPMI (65%) to 5% DMSO.

Animals (4 groups a 2 animals) was dosed intra-peritoneal (i.p.) using 30 gauge needles. V49 and V49-Cu was administered at 5 and 10mg/kg three-times a week every other day. Body weight was measured every working day (Monday to Friday).

Species	<i>Mus musculus</i>
Strain	CB17/SCID
Number and sex	8 males
Supplier	Bread in-house (originally Harlan)
Health status	healthy, tumor-free
Expected weight range at 1st drug administration	~25-30g

Age	~4months
Acclimatization	Not necessary because bred in the same room

Powder of V8 (stocks stored at 4°C) was dissolved freshly before use in serum-free RPMI (60%) and PEG 400 (35%) with 5% DMSO. The drug solutions was administered i.p.

V8 was dissolved in DMSO and diluted with PEG 400 (35%) and serum-free RPMI (60%) to 5% DMSO.

Animals (2 groups a 2 animals) was dosed i.p. using 30 gauge needles. V8 was administered at 5 and 10mg/kg three-times a week every other day. Body weight was measured every working day (Monday to Friday).

Species	<i>Mus musculus</i>
Strain	CB17/SCID
Number and sex	4 males
Supplier	Bread in-house (originally Harlan)
Health status	healthy, tumor-free
Expected weight range at 1st drug administration	~25-30g
Age	~4months
Acclimatization	Not necessary because bred in the same room

5.2.15 Statistical analyses

GraphPad Prism was used to calculate statistics. Two-tailed student's t-test, two-tailed Mann Whitney U test, and one-way ANOVA were performed as indicated in the figure legends. In this study, a p-value of < 0.05 was considered statistically significant. All values are represented as mean \pm SD unless otherwise indicated.

Description of the solutions used during the biological evaluation

Chemical	Supplier	additional Information
10x TBS	Medical University Vienna, Austria	120 g Tris 90 g NaCl Dissolved in 1 L ddH2O pH 7.6
4x loading dye	Medical University Vienna, Austria	4 ml 99,5 % Glycerine 2 ml 2-Mercaptoethanol 0.92 g SDS 0.2 mg Bromophenol blue 2.5 ml 1 M Tris-HCl (pH 6.8) Filled up to 10 ml with A.bidest
Bjerrum buffer with Methanol	Medical University Vienna, Austria	5.82 g Tris 2.93 g Glycine 200 ml Methanol Filled up to 1 L with ddH2O
Bjerrum Buffer with SDS	Medical University Vienna, Austria	5.82 g Tris 2.93 g Glycine 0.375 g SDS dissolve in 1 L ddH2O

Chemoluminescence substrate	Medical University Vienna, Austria	5 mL 1.5 M Tris 200 µL Luminol 250 µL Cumaric Acid filled up to 50 mL with ddH ₂ O
EZ4U solution	Biomedica GmbH & Co KG, Austria	Produced with EZ4U solution kit Catalog-number: BI-5000
FACS-PBS	Medical University Vienna, Austria	11.5 g Na ₂ HPO ₄ x 2H ₂ O 2 g KH ₂ PO ₄ 2 g KCl 80 g NaCl pH 7.4 Diluted in 1 L ddH ₂ O
Lämmli electrophoresis buffer	Medical University Vienna, Austria	30 g Tris 144 g Glycine 10 g SDS dissolved in 1 L ddH ₂ O
Lysis buffer	Medical University Vienna, Austria	50 mM Tris 300 mM NaCl 0.5 % TritonX-100
Micro BCA solution	Thermo Fisher Scientific, USA	Created using the Micro BCA Protein Assay Reagent Kit
PBS	Medical University Vienna, Austria	95 g Na ₂ HPO ₄ x 2H ₂ O 32 g NaH ₂ PO ₄ x H ₂ O 44 g NaCl Diluted in 1 L ddH ₂ O
Ponceau stain for Western Blot	Medical University Vienna, Austria	0.5 g Ponceau S 2.5 ml Acetic acid 475 ml ddH ₂ O
RPMI-Medium	Sigma Aldrich, USA	bought as powder fetal bovine serum added
TBST	Medical University Vienna, Austria	100 ml 10xTBS 900 ml ddH ₂ O 1 ml Tween

Tris HCL 1.5M	Medical University Vienna, Austria	18.2 g Tris 80 mL HCL pH 8.8 filled up to 100 mL with ddH2O
Tris HCL 0.5M	Medical University Vienna, Austria	3 g Tris 35 mL HCL pH 6.8 filled up to 50 mL with ddH2O
Trypan blue solution	Sigma Aldrich, USA	Concentration: 0.4 % CAS-number: 72-57-1
Trypsin	Sigma Aldrich, USA	CAS-number: 9002-07-7

Chemical	Supplier	Additional information
2-Mercaptoethanol	Merck KGaA, Germany	CAS-number: 60-24-2
Acetic acid	Merck KGaA, Germany	Purity = 100% CAS-number: 64-19-7
Acrylamid	Biorad Laboratories; Austria	40% CAS-number: 1610144
Ammonium persulfate (APS)	Sigma Aldrich, USA	Purity ≥98% CAS-number: 7727-54-0
Bodipy 493/503	Thermo Fisher Scientific, USA	Lipid stain 3.8mM, dissolved in DMSO Cat-number: D3922
Bromphenol blue	Merck KGaA, Germany	CAS-number: 115-39-9
BSA (Albumin fraction V)	Roth-Lactan, Austria	Purity ≥98% CAS-number: T844.2

Coumaric acid	Sigma Aldrich, USA	Purity ≥ 98% CAS-number: 501-98-4
Doubledistilled water (A.bidest)	Medical University Vienna, Austria	Distilled water autoclaved at 121 °C and 1.5 bar for 15 minutes
Ethanol	VWR International, USA	Purity ≥ 99.8% CAS-number: 64-17-5
Glycerin	Sigma Aldrich, USA	Purity ≥ 99% CAS-number: 56-81-5
Glycine	Sigma Aldrich, USA	Purity ≥ 99.5% CAS-number: 56-81-5
H ₂ O ₂	Sigma Aldrich, USA	30%(w/w) in H ₂ O CAS-number: 7722-84-1
HCl	Sigma Aldrich, USA	37% CAS-number: 7647-01-0
KCl	Merck KGaA, Germany	Purity ≥ 99.5% CAS-number: 7447-407
KH ₂ PO ₄	Merck KGaA, Germany	Purity ≥ 99.5% CAS-number: 7778-770
Luminol	Sigma Aldrich, USA	Purity ≥ 97% CAS-number: 521-31-3
Methanol	VWR International, USA	Purity ≥ 99% CAS-number: 67-56-1
N,N,N',N'- Tetramethylethylenediamine (TEMED)	Sigma Aldrich, USA	Purity ~ 99% CAS-number: 110-18-9
Na ₂ HPO ₄ x 2H ₂ O	Merck KGaA, Germany	Purity ≥ 99.5% CAS-number: 10028-247
NaCl	VWR International, USA	purity ≥ 99% CAS-number: 7647-14-5
Ethanol	VWR International, USA	Purity ≥ 99.8% CAS-number: 64-17-5
Glycerin	Sigma Aldrich, USA	Purity ≥ 99% CAS-number: 56-81-5

Glycine	Sigma Aldrich, USA	Purity \geq 99.5% CAS-number: 56-81-5
H ₂ O ₂	Sigma Aldrich, USA	30%(w/w) in H ₂ O CAS-number: 7722-84-1
HCl	Sigma Aldrich, USA	37% CAS-number: 7647-01-0
KCl	Merck KGaA, Germany	Purity \geq 99.5% CAS-number: 7447-407
KH ₂ PO ₄	Merck KGaA, Germany	Purity \geq 99.5% CAS-number: 7778-770
Luminol	Sigma Aldrich, USA	Purity \geq 97% CAS-number: 521-31-3
Methanol	VWR International, USA	Purity \geq 99% CAS-number: 67-56-1
N,N,N',N'- Tetramethylethylenediamine (TEMED)	Sigma Aldrich, USA	Purity \sim 99% CAS-number: 110-18-9
Na ₂ HPO ₄ x 2H ₂ O	Merck KGaA, Germany	Purity \geq 99.5% CAS-number: 10028-247
NaCl	VWR International, USA	purity \geq 99% CAS-number: 7647-14-5

Information about the machines used to gather data

machine	Producer	additional Information
colorimeter	Biochrom, UK	ASYS Expert Plus serial number: 28366

Flow cytometer	BD Bioscience; Austria	LSRFortessa serial-number: H649225R7014
gel electrophoresis chamber	Biorad Laboratories; Austria	Mini-Protean Tetra System Product-number: 1658004EDU
Laboratory centrifuge	Eppendorf AG, Austria	5417R CAT-number: 5409000012 serial-number: 0023977
Live cell microscope	Visitron Systems GmbH, Germany	serial number:637482
MTT photometer	Tecan GmbH, Austria	TECAN Infinite M200 Pro serial number: 1007006129
Protein transfer system	Biorad Laboratories, Austria	Trans Blot Turbo CAT-number: 1704150 serial number:690BR008612
X-ray developer machine	Protec GmbH & Co.KG, Germany	OPTIMAX serial number:

Product	Supplier	Additional Information
50 mL tube	VWR International, USA	CAS-number: 10025-712
8 well slide	Ibidi, Germany	CAS-number: 80827
beaker	Rasotherm	5 mL; 10 mL; 100 mL
Counting chamber	A.Hartenstein gmbH; Germany	CAT-number: ZK06
CytoOne 6 well plate	STARLAB, United Kingdom	Cat.-number: CC7682-7506
CytoOne 96 well plate	STARLAB, United Kingdom	Cat.-number: CC7682-7596
CytoOne T-25 flask	STARLAB, United Kingdom	25 cm ² growing area CAS-number: CC7682-4325
Eppendorf tubes	Eppendorf, Austria	1.5 mL; 2 mL
FALCON 15mL centrifuge tube	STARLAB, United Kingdom	CAS-number: 14-959-53A
FALCON FACS tube	Thermo Fisher Scientific, USA	CAS-number: 60819-295
Filter paper for Western Blot	Biorad Laboratories; Austria	CAT-number:1703969

Measuring cylinder	VWR International, USA	50 mL; 100 mL; 200 mL
Micro BCA Protein Assay Reagent Kit	Thermo Fisher Scientific, USA	CAS-number: 23235
pipette	Eppendorf, Austria	10 μ L; 20 μ L; 200 μ L; 1000 μ L
PVDF-Membrane for Western Blot	Biorad Laboratories; Austria	CAT-number: 162-0177

5.3 Computational

5.3.1 ADMET calculations

QikProp v6.2 package (Schrödinger, LLC, New York, NY, 2020) was used in order to evaluate ADMET properties of all compounds.

Accurate prediction of ADMET properties prior to expensive experimental procedures, can eliminate unnecessary testing on compounds that will ultimately fail; ADMET prediction can also be used to focus lead optimization efforts to enhance the desired properties of a given compound. Finally, incorporating ADMET predictions as a part of the development process can generate lead compounds that are more likely to exhibit satisfactory ADMET performances during clinical trials.

QikProp rapidly screens compound libraries for hits. QikProp identifies molecules with computed properties that fall outside the normal range of known drugs, making it simple to filter out candidates with unsuitable ADMET properties.

The 3D structures were created and optimized with Avogadro version 1.2.0 software, using Force Field GAFF (General AMBER Force Field) and MOL2 files were used for calculations.

The calculated properties are shown in the **Table 12**.

Property or Descriptor	Description	Range or recommended values (For 95% of know drugs)
#stars	Number of property or descriptor values that fall outside the 95% range of similar values for known drugs. Outlying descriptors and predicted properties are denoted with asterisks (*) in the .out file. A large number of stars suggests that a molecule is less drug-like than molecules with few stars. The following properties and descriptors are included in the determination of #stars: MW, dipole, IP, EA, SASA, FOSA, FISA, PISA, WPSA, PSA, volume, #rotor, donorHB, accptHB, glob, QPpolrz, QPlogPC16, QPlogPoct, QPlogPw, QPlogPo/w, logS, QPlogKhsa, QPlogBB, #metabol	0 – 5
#amine	Number of non-conjugated amine groups.	0 – 1
#amidine	Number of amidine and guanidine groups.	0
#acid	Number of carboxylic acid groups.	0 – 1
#amide	Number of non-conjugated amide groups.	0 – 1
#rotor	Number of non-trivial (not CX3), non-hindered (not alkene, amide, small ring) rotatable bonds.	0 – 15
#rtvFG	Number of reactive functional groups; the specific groups are listed in the <i>jobname</i> .out file. The presence of these groups can lead to false positives in HTS assays and to decomposition, reactivity, or toxicity problems <i>in vivo</i> .	0 – 2
CNS	Predicted central nervous system activity on a –2 (inactive) to +2 (active) scale.	–2 (inactive), +2 (active)
mol_MW	Molecular weight of the molecule.	130.0 – 725.0
dipole†	Computed dipole moment of the molecule.	1.0 – 12.5
SASA	Total solvent accessible surface area (SASA) in square angstroms using a probe with a 1.4 Å radius.	300.0 – 1000.0

Property or Descriptor	Description	Range or recommended values (For 95% of know drugs)
FOSA	Hydrophobic component of the SASA (saturated carbon and attached hydrogen).	0.0 – 750.0
FISA	Hydrophilic component of the SASA (SASA on N, O, H on heteroatoms, carbonyl C).	7.0 – 330.0
PISA	π (carbon and attached hydrogen) component of the SASA.	0.0 – 450.0
WPSA	Weakly polar component of the SASA (halogens, P, and S).	0.0 – 175.0
volume	Total solvent-accessible volume in cubic angstroms using a probe with a 1.4 Å radius.	500.0 – 2000.0
donorHB	Estimated number of hydrogen bonds that would be donated by the solute to water molecules in an aqueous solution. Values are averages taken over a number of configurations, so they can be non-integer.	0.0 – 6.0
acceptHB	Estimated number of hydrogen bonds that would be accepted by the solute from water molecules in an aqueous solution. Values are averages taken over a number of configurations, so they can be non-integer.	2.0 – 20.0
dip²/V[†]	Square of the dipole moment divided by the molecular volume. This is the key term in the Kirkwood-Onsager equation for the free energy of solvation of a dipole with volume V.	0.0 – 0.13
ACxDN^{0.5}/SA	Index of cohesive interaction in solids. This term represents the relationship (acceptHB(donorHB))/(SA)	0.0 – 0.05
glob	Globularity descriptor, $(4\pi r^2)/(SASA)$, where r is the radius of a sphere with a volume equal to the molecular volume. Globularity is 1.0 for a spherical molecule.	0.75 – 0.95

Property or Descriptor	Description	Range or recommended values (For 95% of know drugs)
QPpolrz	Predicted polarizability in cubic angstroms.	13.0 – 70.0
QPlogPC16	Predicted hexadecane/gas partition coefficient.	4.0 – 18.0
QPlogPoct‡	Predicted octanol/gas partition coefficient.	8.0 – 35.0
QPlogPw	Predicted water/gas partition coefficient.	4.0 – 45.0
QPlogPo/w	Predicted octanol/water partition coefficient.	-2.0 – 6.5
QPlogS	Predicted aqueous solubility, log S. S in mol dm ⁻³ is the concentration of the solute in a saturated solution that is in equilibrium with the crystalline solid. Conformation-independent predicted aqueous solubility,	-6.5 – 0.5
CIQPlogS	log S. S in mol dm ⁻³ is the concentration of the solute in a saturated solution that is in equilibrium with the crystalline solid.	-6.5 – 0.5
QPlogHERG	Predicted IC ₅₀ value for blockage of HERG K ⁺ channels.	concern below -5
QPPCaco	Predicted apparent Caco-2 cell permeability in nm/sec. Caco-2 cells are a model for the gut-blood barrier. QikProp predictions are for non-active transport.	<25 poor, >500 great
QPlogBB	Predicted brain/blood partition coefficient. Note: QikProp predictions are for orally delivered drugs so, for example, dopamine and serotonin are CNS negative because they are too polar to cross the blood-brain barrier	-3.0 – 1.2
QPPMDCK	Predicted apparent MDCK cell permeability in nm/sec. MDCK cells are considered to be a good mimic for the blood-brain barrier	<25 poor, >500 great
QPlogKp	Predicted skin permeability, log K _p	-8.0 – -1.0
IP(ev)†	PM3 calculated ionization potential (negative of HOMO energy)	7.9 – 10.5

Property or Descriptor	Description	Range or recommended values (For 95% of know drugs)
EA(eV)†	PM3 calculated electron affinity (negative of LUMO energy)	-0.9 – 1.7
#metab‡	Number of likely metabolic reactions	1 – 8
QPlogKhsa	Prediction of binding to human serum albumin.	-1.5 – 1.5
HumanOralAbsorption	Predicted qualitative human oral absorption: 1, 2, or 3 for low, medium, or high. The text version is reported in the output. The assessment uses a knowledge-based set of rules, including checking for suitable values of PercentHumanOralAbsorption, number of metabolites, number of rotatable bonds, logP, solubility and cell permeability	
PercentHumanOralAbsorption	Predicted human oral absorption on 0 to 100% scale. The prediction is based on a quantitative multiple linear regression model. This property usually correlates well with HumanOralAbsorption, as both measure the same property.	>80% is high <25% is poor
SAFluorine	Solvent-accessible surface area of fluorine atoms	0.0 – 100.0
SAamideO	Solvent-accessible surface area of amide oxygen atoms.	0.0 – 35.0
PSA	Van der Waals surface area of polar nitrogen and oxygen atoms and carbonyl carbon atoms.	7.0 – 200.0
#NandO	Number of nitrogen and oxygen atoms.	2 – 15
RuleOfFive	Number of violations of Lipinski's rule of five [3]. The rules are: mol_MW < 500, QPlogPo/w < 5, donorHB ≤ 5, accptHB ≤ 10. Compounds that satisfy these rules are considered drug-like. (The "five" refers to the limits, which are multiples of 5.)	maximum is 4

Property or Descriptor	Description	Range or recommended values (For 95% of know drugs)
RuleOfThree	Number of violations of Jorgensen's rule of three. The three rules are: QPlogS > -5.7, QP PCaco > 22 nm/s, # Primary Metabolites < 7. Compounds with fewer (and preferably no) violations of these rules are more likely to be orally available.	maximum is 3
#ringatoms	Number of atoms in a ring	
#in34	Number of atoms in 3- or 4-membered rings	
#in56	Number of atoms in 5- or 6-membered rings	
#noncon	number of ring atoms not able to form conjugated aromatic systems (e.g. sp ³ C).	
#nonHatm	Number of heavy atoms (nonhydrogen atoms)	
Jm	Predicted maximum transdermal transport rate, $K_p \times MW \times S$ ($\mu\text{g cm}^{-2} \text{hr}^{-1}$). K_p and S are obtained from the aqueous solubility and skin permeability, QPlogKp and QPlogS. This property is only written to the output file: it is not used in any other calculations.	

Table 12. Predicted ADMET properties, description and recommended values based on 95% of known drugs obtained with the software QikProp v6.2

On the basis of all these calculated properties, all molecules that had properties outside the reference range were excluded. Only molecules with the number of stars equal to zero were considered.

5.3.2 Molecular docking

The 2D structures have been drawn with MarvinSketch version 20.7.0 (<http://www.chemaxon.com>), which also allowed the study of chemical characteristics, such as: H bond donor/acceptor, possible structural frameworks, pka, isoelectric point, logP, logD, aqueous solubility, charge polarizability, orbital electronegativity and dipole moment.

The 3D structures of the designed molecules were created and optimized with Avogadro version 1.2.0 software, using Force Field GAFF (General AMBER Force Field) PDB files (.pdb) were used for calculations.

PDB files of proteins were obtained from the Protein Data Bank (PDB; <http://www.rcsb.org/pdb/>), worldwide archive of structural data of biological macromolecules.

The following PDB protein files have been downloaded and used: FGFR1 (PDB ID: [4v04](#)), FGFR4 (PDB ID: [4uxq](#)).

Before carrying out the molecular docking, the study, carried out with Autodock Vina version 1.5, initially envisaged the modification of the raw .pdb files, in order to make them suitable for the calculation.

The changes made were the following:

- elimination of residual water molecules;
- elimination of residual sulfur dioxide molecules;
- addition of the missing hydrogen atoms;
- protonation of histidine residues;
- conversion of selenomethionines into methionines;
- addition and optimization of the atoms of the side chains;
- pH setting at 7.0 ± 2.0 .

At the end of the preparation a short gradual reduction of the energy was performed, for the amino acids.

In order to narrow the search field, no blind docking was carried out which would have affected the entire surface of the protein but, on the contrary, the positioning

Grid Boxes	FGFR1	FGFR4
x-size	30	16
y-size	46	14
z-size	54	26
x-center	27.814	2.613
y-center	5.016	-3.005
z-center	16.789	14.858

Table 13. Grid boxes calculated for FGFR1 and FGFR4 based on Ponatinib coordinates at the receptors binding site.

of the grid box (**Table 13**) was based on the coordinates of the Ponatinib, present inside the binding pocket, so as to simplify the calculation.

Were created the .pdbqt files of all candidate compounds and ponatinib, FGFR1 and FGFR4.

Steps for create a .pdbqt file:

- 1) Addition of hydrogen atoms to the molecule;
- 2) Addition of partial charges;
- 3) Delete non-polar hydrogens and merging their charges with the carbon atoms
- 4) Assignment of atom types, definition hydrogen bond acceptors and donors and aromatic and aliphatic carbon atoms;
- 5) Choice of a root atom that will act as the root for the torsion tree description of flexibility;
- 6) Definition of rotatable bonds and build the torsion tree.

The docking score is expressed in terms of kcal / mol and the software provides that molecules with greater complementarity with the receptor pocket are assigned a more negative score.

All compounds were re-docked for three times and the root mean square deviation (RMSD) values were calculated, which was always less than 1.5Å. RMSD is a common metric used to evaluate distance between the predicted pose and the native pose, given a superposition of their protein receptor structures.

The results and images of the calculations were visualized with UCSF Chimera production version 1.11.2.

ABBREVIATIONS

WHO - World Health Organization

4EBP1 – Eukaryotic translation initiation factor 4E-binding protein 1

ACP – Adamantinomatous

AD - “Diffuse” astrocyroma

ADMET – absorption, distribution, metabolism, and excretion - toxicity in pharmacokinetics

ADP-ribose – Adenosine diphosphate ribose

AIDS - acquired immune deficiency syndrome

AKT/ p-AKT - Protein kinase B and phosphorylated Protein kinase B

Ala553 – Alanine in position 553

ARID1A - AT-rich interactive domain-containing protein 1A

Asp630 – Aspartic acid in position 630

Asp631 - Aspartic acid in position 631

ATP – Adenosine triphosphate

BRAF - human gene that encodes a protein called B-Raf

BRAF-V600E - mutation of the BRAF gene in which valine (V) is substituted by glutamic acid (E) at amino acid 600

BSA – Bovine Serum Albumin solution

CADD - Computer Aided Drug Design

CDKN2A - Cyclin-dependent kinase inhibitor 2A

CNS – Central Nervous System

CP - Craniopharyngioma

CTDNEP1 - CTD nuclear envelope phosphatase 1

Cu - Copper

DCFH-DA - 2',7'-Dichlorofluorescein diacetate

DDX3X - ATP-dependent RNA helicase DDX3X

DFG - Asp-Phe-Gly motif

DICER - Endoribonuclease Dicer or helicase with RNase motif

DMSO – Dimethyl sulfoxide

ECM - extracellular matrix

EDTA – Ethylenediaminetetraacetic acid

EGFR - epidermal growth factor receptor

EMT - epithelial-mesenchymal transition

EPHA3 - EPH receptor A3 (ephrin type-A receptor 3)

ER - estrogen receptor

ERK/ p-ERK – Extracellular-signal-regulated kinase and phosphorylated extracellular-signal-regulated kinase

FDA – Food and Drug Administration

FGF/FGFR - fibroblast growth factor and fibroblast growth factor receptor

FGFRL1 - FGFR-like 1

FRS2 - FGFR substrate 2

GBM - Glioblastoma multiforme

Glu520 – Glutamic acid in position 520

GSK3B/ p- GSK3B – Glycogen synthase kinase 3 beta and phosphorylated Glycogen synthase kinase 3 beta

HLA - human leukocyte antigens

IASLC - International Association for the Study of Lung Cancer

IC₅₀ - Half Maximal Inhibitory Concentration

IDH – isocitrate dehydrogenase

I.P. - Intraperitoneal

IR - Infrared spectroscopy

KDM6A - Gene encoding Lysine-specific demethylase 6A

KEAP1 - Kelch-like ECH-associated protein 1

KRAS - Gene provides instructions for making a protein called K-Ras

LIN28A - Gene encoding Lin-28 homolog B

LogD - Logarithm of distribution coefficient

LogP - Logarithm of partition coefficient

MAPK - mitogen-activated protein kinase

MDM2 - Mouse double minute 2 homolog or E3 ubiquitin-protein ligase Mdm2

MET - Proto-Oncogene, Receptor Tyrosine Kinase

MGA - DNA-binding protein

MLL2 - Histone-lysine N-methyltransferase 2

mRNA - messenger RNA

mTOR - mammalian target of rapamycin

NF1- Neurofibromatosis type 1

NFE2L2 - Nuclear factor erythroid 2-related factor 2

NMR - Nuclear magnetic resonance

NOS - Nitrous Oxide Systems

NOTCH1 - genes encoding the NOTCH family of proteins

NSCLC - Non-small cell lung cancer

p-70S6K – Phosphorilated Ribosomal protein S6 kinase beta-1

PA - Pilocytic astrocytoma

PARP – poly(ADP-ribose) polymerase

PBS – Phosphate-buffered saline

PCP - Papillary Craniopharyngioma

PCR - Polymerase Chain Reaction

PDB - Protein Data Bank

PDGFRA - Platelet-derived growth factor receptor A

PDYN - Prodynorphin

PI - Propidium Iodide

PI3K - phosphatidylinositol-4,5-bisphosphate 3-kinase

PIK3CA - phosphatidylinositol-4,5-bisphosphate 3-kinase catalytic subunit alpha

Pka

PLCY - Phospholipase C Gamma

PS – Phosphatidylserine

Pt – Protein

PTEN - Phosphatase and tensin homolog

RAF - proto-oncogene serine/threonine-**protein** kinase

RAS - guanosine-nucleotide-binding **protein**

RB - Retinoblastoma protein

RB1 - RB Transcriptional Corepressor 1

RBM10 - RNA Binding Motif Protein 10
RIT1 - Ras Like Without CAAX 1
RMSD - Root Mean Square Deviation
RNA - Ribonucleic acid
ROS - Reactive Oxygen Species
RT - Room Temperature
RT-PCR – real-time polymerase chain reaction
RTK- Receptor Tyrosine Kinase
S6/p-S6 – Ribosomal **protein S6** and phosphorilated Ribosomal **protein S6**
SAR - Structure-Activity Relationship
SBBD - Structure-Based Drug Design
SCID - Severe Combined Immunodeficient
SCLC - small cell lung cancer
SETD2 - SET Domain Containing 2, Histone Lysine Methyltransferase
SMARCA4 - SWI/SNF Related, Matrix Associated, Actin Dependent Regulator
Of Chromatin, Subfamily A, Member 4
SOX2 - sex determining region Y-box 2
STK11 - Serine/Threonine Kinase 11
SUMO - Small Ubiquitin-like Modifier protein
TACC - Transforming Acid Coiled-Coil
TBR1 - T-Box Brain Transcription Factor 1
TBST – mixture of tris-buffered saline (TBS) and Polysorbate 20
TK - tyrosine kinase
TLC – Thin-layer chromatography
TMD - transmembrane domain
TMZ – Temozolomide
TNM - Tumor, Node, Metastasis
U2AF1 - U2 Small Nuclear RNA Auxiliary Factor 1
UBC3 - Ubiquitin-conjugating enzyme E2 3
VEGF - vascular endothelial growth factor

BIBLIOGRAPHY

- ABID M., SHAMSI F., AZAM A. Ruthenium Complexes: An Emerging Ground to the Development of Metallopharmaceuticals for Cancer Therapy. *Mini Rev Med Chem.* **2016**;16(10):772-86.
- ACHARYA, C.; COOP A.; POLLI, J.E.; MACKERELL, A.D. JR. Recent advances in ligand-based drug design: relevance and utility of the conformationally sampled pharmacophore approach. *Curr. Comput. Aided Drug Des.* **2011**, 7(1), 10-22
- AGGARWAL V, TULI HS, VAROL A, THAKRAL F, YERER MB, SAK K, VAROL M, JAIN A, KHAN MA, SETHI G. Role of Reactive Oxygen Species in Cancer Progression: Molecular Mechanisms and Recent Advancements. *Biomolecules.* **2019** Nov 13;9(11):735.
- AL-RASHOOD ST, ABOLDAHAB IA, NAGI MN, ABOUZEID LA, ABDEL-AZIZ AAM, ABDEL-HAMIDE SG, ET AL., *Bioorg,Med Chem.* **2006**;14:8608-8621.
- ALIFIERIS C, TRAFALIS DT. Glioblastoma multiforme: Pathogenesis and treatment. *Pharmacol Ther.* **2015** Aug;152:63-82.
- AMIT S, CHAND P, PANTOLA C, AGARWAL A. Ependymoblastoma in an adult: a diagnostic challenge on cytology. *BMJ Case Rep.* 2011 Nov 8; **2011**.
- AMUNDSEN, A.R.; WHELAN, J.; Bonich, B.; *J. Am. Chem. Soc.* **1977**, 99, 6730.
- A. JIMENEZ-PASCUAL *ET AL.*, "ADAMDEC1 maintains a growth factor signaling loop in cancer stem cells," *Cancer Discov.*, **2019**.
- ANTONARAKIS ES, EMADI A. Ruthenium-based chemotherapeutics: are they ready for prime time? *Cancer Chemother Pharmacol.* **2010** May;66(1): 1-9.

- ARMSTRONG TS, VERA-BOLANOS E, BEKELE BN, ALDAPE K, GILBERT MR. Adult ependymal tumors: prognosis and the M. D. Anderson Cancer Center experience. *Neuro Oncol.* **2010** Aug;12(8):862-70.
- ARPITADESAI AND ALEX A.ADJEI, FGFR Signaling as a Target for Lung Cancer Therapy, *Journal of Thoracic oncology*, **2016**, 11, 1 (9-20).
- AUCIELLO G, CUNNINGHAM DL, TATAR T, HEATH JK, RAPPOPORT JZ. Regulation of fibroblast growth factor receptor signalling and trafficking by Src and Eps8. *J Cell Sci.* **2013** Jan 15;126(Pt 2):613-24.
- ASHRAF A. KHALIL SAMI G. ABDEL HAMIDE ABDULRAHMAN M. AL-OBAID HUSSEIN I. EL-SUBBAGH. Substituted Quinazolines, Part 2. Synthesis and In-Vitro Anticancer Evaluation of New 2-Substituted Mercapto-3H-quinazoline Analogs. *Arch Pharm Pharm Med Chem.* **2003**, 336: 95-103.
- BABINA, I. S. & TURNER, N. C. Advances and challenges in targeting FGFR signalling in cancer. *Nat. Rev. Cancer* 17, 318–332 (**2017**)
- BAERISWYL, V. & CHRISTOFORI, G. **2009**. The angiogenic switch in carcinogenesis. *Semin Cancer Biol*, 19, 329-37.
- BAI J, LI Y, ZHANG G. Cell cycle regulation and anticancer drug discovery. *Cancer Biol Med.* **2017**;14(4):348-362.
- BALE TA. FGFR- gene family alterations in low-grade neuroepithelial tumors. *Acta Neuropathol Commun.* 2020 Feb 21;8(1):21.
- BARTA JA, POWELL CA, WISNIVESKY JP. Global Epidemiology of Lung Cancer. *Ann Glob Health.* **2019**;85(1):8.
- BENJAMIN CHIBUZO EJELONU, Potential of Copper and its Complexes as Therapeutic Agents, *World Journal of Research and Review*, Volume-3, Issue-3, September 2016 Pages 47-52.
- BERTRAND B, WILLIAMS MRM, BOCHMANN M. Gold(III) Complexes for Antitumor Applications: An Overview. *Chemistry.* **2018** Aug 14;24(46): 11840-11851.

- BOER K, TROOST D, TIMMERMANS W, VAN RIJEN PC, SPLIET WGM, ARONICA E. Pi3K-mTOR Signaling and AMOG expression in epilepsy-associated glioneuronal tumors. *Brain pathol.* **2010**; 20: 234-244.
- BRASTIANOS PK, TAYLOR-WEINER A, MANLEY PE, JONES RT, DIAS-SANTAGATA D, THORNER AR, LAWRENCE MS, RODRIGUEZ FJ, BERNARDO LA, SCHUBERT L, SUNKAVALLI A, SHILLINGFORD N, CALICCHIO ML, LIDOV HG, TAHA H, MARTINEZ-LAGE M, SANTI M, STORM PB, LEE JY, PALMER JN, ADAPPA ND, SCOTT RM, DUNN IF, LAWS ER JR, STEWART C, LIGON KL, HOANG MP, VAN HUMMELEN P, HAHN WC, LOUIS DN, RESNICK AC, KIERAN MW, GETZ G, SANTAGATA S. Exome sequencing identifies BRAF mutations in papillary craniopharyngiomas. *Nat Genet.* **2014** Feb;46(2):161-5.
- BRODY, H., *Lung cancer*. Nature, 2014. **513**(7517): p. S1. Giangreco, A., K.R. Groot, and S.M. Janes, *Lung cancer and lung stem cells: strange bedfellows?*
- BROOKS A.N., E. KILGOUR, P.D. SMITH Molecular pathways: fibroblast growth factor signaling: a new therapeutic opportunity in cancer. *Clin Cancer Res*, 18 (2012), pp. 1855-1862
- BRUCE JN, FUSCO DJ, FELDSTEIN NA, AND KENNEDY B. Ependymoma. *Medscape*. February 2, **2018**.
- BUNN, P. A., JR., MINNA, J. D., AUGUSTYN, A., GAZDAR, A. F., OUADAH, Y., KRASNOW, M. A., BERNS, A., BRAMBILLA, E., REKHTMAN, N., MASSION, P. P., NIEDERST, M., PEIFER, M., YOKOTA, J., GOVINDAN, R., POIRIER, J. T., BYERS, L. A., WYNES, M. W., MCFADDEN, D. G., MACPHERSON, D., HANN, C. L., FARAGO, A. F., DIVE, C., TEICHER, B. A., PEACOCK, C. D., JOHNSON, J. E., COBB, M. H., WENDEL, H. G., SPIGEL, D., SAGE, J., YANG, P., PIETANZA, M. C., KRUG, L. M., HEYMACH, J., UJHAZY, P., ZHOU, C., GOTO, K., DOWLATI, A., CHRISTENSEN, C. L., PARK, K., EINHORN, L. H., EDELMAN, M. J., GIACCONE, G., GERBER, D. E., SALGIA, R., OWONIKOKO, T., MALIK, S., KARACHALIOU, N., GANDARA, D. R., SLOTMAN, B. J., BLACKHALL, F., GOSS, G., THOMAS, R., RUDIN, C.

M. & HIRSCH, F. R. **2016**. Small Cell Lung Cancer: Can Recent Advances in Biology and Molecular Biology Be Translated into Improved Outcomes? *J Thorac Oncol*, 11, 453-74.

- BURKHARD C, DI PATRE PL, SCHÜLER D, SCHÜLER G, YAŞARGIL MG, YONEKAWA Y, LÜTOLF UM, KLEIHUES P, OHGAKI H. A population-based study of the incidence and survival rates in patients with pilocytic astrocytoma. *J Neurosurg*. **2003** Jun;98(6):1170-4.
- BURKHART DL, SAGE J. Cellular mechanisms of tumour suppression by the retinoblastoma gene. *Nat Rev Cancer*. **2008**;8(9):671-682.
- BURSTEIN HJ, LACCHETTI C, ANDERSON H, BUCHHOLZ TA, DAVIDSON NE, GELMON KA ET AL. Adjuvant Endocrine Therapy for Women With Hormone Receptor-Positive Breast Cancer: ASCO Clinical Practice Guideline Focused Update. *J Clin Oncol*. **2019** Feb 10;37(5):423-438
- BUSLEI R, NOLDE M, HOFMANN B, MEISSNER S, EYUPOGLU IY, SIEBZEHRUBL F, HAHNEN E, KREUTZER J & FAHLBUSCH R **2005** Common mutations of b-catenin in adamantinomatous craniopharyngiomas but not in other tumours originating from the sellar region. *Acta Neuropathologica* 109 589–597.
- BUTOWSKI NICHOLAS A. Epidemiology and Diagnosis of Brain Tumors, MD, **2015**.
- CAMIDGE, D. R., PAO, W. & SEQUIST, L. V. Acquired resistance to TKIs in solid tumours: learning from lung cancer. *Nat. Rev. Clin. Oncol*. 11, 473–481 (**2014**).
- CARBONE A. Cancer Classification at the Crossroads. *Cancers (Basel)*. 2020;12(4):980. Published **2020** Apr 15.
- CAPELLETTI, M., DODGE, M. E., ERCAN, D., HAMMERMAN, P. S., PARK, S. I., KIM, J., SASAKI, H., JABLONS, D. M., LIPSON, D., YOUNG, L., STEPHENS, P. J., MILLER, V. A., LINDEMAN, N. I., MUNIR, K. J., RICHARDS, W. G. & JANNE, P. A. **2014**. Identification of

- recurrent FGFR3-TACC3 fusion oncogenes from lung adenocarcinoma. *Clin Cancer Res*, 20, 6551-8.
- CERMAKOVA K, HODGES HC. "Next-Generation Drugs and Probes for Chromatin Biology: From Targeted Protein Degradation to Phase Separation". *Molecules*. 23 (8): 1958 (August **2018**).
 - CHAFFER, C. L. & WEINBERG, R. A. **2015**. How does multistep tumorigenesis really proceed? *Cancer Discov*, 5, 22-4.
 - CHAKRABORTY A., KUMAR P., GHOSH K., AND ROY P., "Evaluation of a Schiff base copper complex compound as potent anticancer molecule with multiple targets of action. *European Journal of Pharmacology*. vol. 647, no. 1–3, pp. 1–12, **2010**.
 - Chang J, Liu X, Wang S, et al. Prognostic value of FGFR gene amplification in patients with different cancers: a review systematics and a meta-analysis. *PLoS One*. **2014**; 9 (8)
 - CHAPMAN S, ROBINSON G, STRADLING J, WEST S, WRIGHTSON J (**2014**). "Chapter 31". *Oxford Handbook of Respiratory Medicine* (3rd ed.). Oxford University Press. p. 284.
 - CHEN Y, HU L. Design of anticancer prodrugs for reductive activation. *Med Res Rev*. **2009**;29(1):29–64.
 - Chen, Z., et al., Non-small-cell lung cancers: a heterogeneous set of diseases. *Nat Rev Cancer*, **2014**. 14(8): p. 535-46.
 - CHENG, J., TÜRKEL, N., HEMATI, N., FULLER, M.T., HUNT, A.J., YAMASHITA, Y.M. (**2008**). Centrosome misorientation reduces stem cell division during ageing.
 - CHENG, W., WANG, M., TIAN, X. & ZHANG, X. An overview of the binding models of FGFR tyrosine kinases in complex with small molecule inhibitors. *Eur. J. Med. Chem.* **126**, 476–490 (2017)
 - CHOY H, PARK C, YAO M. Current status and future prospects for satraplatin, an oral platinum analogue. *Clin Cancer Res*. **2008** Mar 15;14(6): 1633-8

- CHRISTINE L. CHAFFER AND ROBERT A. WEINBER, in Focus, How Does Multistep Tumorigenesis Really Proceed? *In Focus, Cancer Discovery* **2015**;5:22-24
- CHRISTOPHER C. MILLS, EA. KOLB AND VALERIE B. SAMPSON, Recent Advances of Cell-Cycle Inhibitor Therapies for Pediatric Cancer, *Cancer Research*, **2017**.
- CIEMNY, MACIEJ; KURCINSKI, MATEUSZ; KAMEL, KAROL; KOLINSKI, ANDRZEJ; ALAM, NAWSAD; SCHUELER-FURMAN, ORA; KMIIECIK, SEBASTIAN (**2018**). "Protein–peptide docking: opportunities and challenges". *Drug Discovery Today*. 23 (8): 1530–1537
- CIHORIC, N., SAVIC, S., SCHNEIDER, S., ACKERMANN, I., BICHSEL-NAEF, M., SCHMID, R. A., LARDINOIS, D., GUGGER, M., BUBENDORF, L., ZLOBEC, I. & TAPIA, C. **2014**. Prognostic role of FGFR1 amplification in early-stage non-small cell lung cancer. *Br J Cancer*, 110, 2914-22.
- COCKEY EMILY and ULLRICH NICOLE J. Neurofibromatosis type 1-associated brain tumors. *Journal of Rare Disease Research & Treatment*. **2016**.
- COLLINS VP, JONES DT, GIANNINI C. Pilocytic astrocytoma: pathology, molecular mechanisms and markers. *Acta Neuropathol*. **2015** Jun;129(6): 775-88.
- CRESPO I, VITAL AL, GONZALEZ-TABLAS M, PATINO MDEL C, OTERO A, LOPES MC, DE OLIVEIRA C, DOMINGUES P, ORFAO A, TABERNERO MD. Molecular and Genomic Alterations in Glioblastoma Multiforme. *Am J Pathol*. **2015** Jul;185(7):1820-33.
- DAHIYA S, PERRY A. Pineal tumors. *Adv Anat Pathol*. **2010** Nov;17(6): 419-27.
- DE GROOT PM, WU CC, CARTER BW, MUNDEN RF. The epidemiology of lung cancer. *Transl Lung Cancer Res*. **2018**;7(3):220-233.

- DELPHINE DENOYER, SHASHANK MASALDAN, SHARON LA FONTAINE, MICHAEL A CATER, Targeting copper in cancer therapy: 'Copper That Cancer'. *Metallomics*. **2015** Nov;7(11):1459-76.
- DASARI S, TCHOUNWOU PB. Cisplatin in cancer therapy: molecular mechanisms of action. *Eur J Pharmacol*. **2014** Oct 5;740:364-78.
- DENARDO DG, ANDREU P, COUSSENS LM. Interactions between lymphocytes and myeloid cells regulate pro- versus anti-tumor immunity. *Cancer Metastasis Rev*. **2010**;29(2):309-316.
- DENOYER D, CLATWORTHY SAS, CATER MA. Copper Complexes in Cancer Therapy. *Met Ions Life Sci*. **2018** Feb 5;18
- DEOL, KIRANDEEP K. LORENZ, SONJA STRIETER, ERIC R, Enzymatic Logic of Ubiquitin Chain Assembly, *Front. Physiol.*, 05 July **2019**
- DESAI, A. & ADJEI, A. A. **2016**. FGFR Signaling as a Target for Lung Cancer Therapy. *J Thorac Oncol*, 11, 9-20.
- DEVI KA, SRIRAM MS, *Int J Drug*. (**2012**);4: 324-327
- DUNCAN CLARE AND WHITE ANTHONY R., Copper complexes as therapeutic agents, *Metallomics*, **2012**, 4, 127-138.
- ENGLINGER B., PIRKER C., PETRA HEFFETER, ALESSIO TERENCE, CHRISTIAN R. KOWOL, BERNHARD K. KEPPLER, AND WALTER BERGER, Metal Drugs and the Anticancer Immune Response, *Chem. Rev*. **2019**, 119, 2, 1519–1624.
- ENGLINGER, B., PIRKER, C., HEFFETER, P., TERENCE, A., KOWOL, C.R., KEPPLER, B.K., BERGER, W. Metal drugs and the anticancer immune response, *Chemical Reviews* Volume 119, Issue 2, 23 January **2019**, Pages 1519-1624.
- ERIC W. BELL & YANG ZHANG, DockRMSD: an open-source tool for atom mapping and RMSD calculation of symmetric molecules through graph isomorphism. *Journal of Cheminformatics*. volume **11**, Article number: 40 (**2019**)
- ERHART F. ET AL. Spheroid glioblastoma culture conditions as antigen source for dendritic cell-based immunotherapy: spheroid proteins are survival-

- relevant targets but can impair immunogenic interferon γ production. *Cytotherapy*, **2020**, 21, 6 (643-658).
- FARAZ SIDDIQUI AND ABDUL H. SIDDIQUI, Cancer, Lung, StatPearls, 2020
 - FARRELL, B.& BREEZE, A. L. Structure, activation and dysregulation of fibroblast growth factor receptor kinases: perspectives for clinical targeting. *Biochem. Soc. Trans.* 46, 1753–1770 (**2018**)
 - FENG, S., ZHOU, L., NICE, E. C. & HUANG, C. **2015**. Fibroblast growth factor receptors: multifactorial-contributors to tumor initiation and progression. *Histol Histopathol*, 30, 13-31.
 - FERLAY J, SOERJOMATARAM I, ERVIK M, ET AL. GLOBOCAN **2012** v1.0, Cancer Incidence and Mortality worldwide: IARC CancerBase No. 11 [Internet] Lyon, France: International Agency for Research on Cancer, 2013
 - FITZMAURICE C, DICKER D, PAIN A, ET AL. The Global Burden of Cancer 2013. *JAMA Oncology*. **2015**; 1(4): 505–527.
 - FOSGERAU, KELD; HOFFMANN, TORSTEN (**2015**). "Peptide therapeutics: current status and future directions". *Drug Discovery Today*. 20 (1): 122–128.
 - FRED R HIRSCH ET AL, Lung cancer: current therapies and new targeted treatments, *Lancet* 2017; 389: 299–311
 - FREZZA M, HINDO S, CHEN D, ET AL. Novel metals and metal complexes as platforms for cancer therapy. *Curr Pharm Des*. **2010**;16(16):1813–1825.
 - GAO, J., AKSOY, B. A., DOGRUSOZ, U., DRESDNER, G., GROSS, B., SUMER, S. O., SUN, Y., JACOBSEN, A., SINHA, R., LARSSON, E., CERAMI, E., SANDER, C. & SCHULTZ, N. **2013**. Integrative analysis of complex cancer genomics and clinical profiles using the cBioPortal. *Sci Signal*, 6, p11.
 - GAVINE, P. R. et al. AZD4547: an orally bioavailable, potent, and selective inhibitor of the fibroblast growth factor receptor tyrosine kinase family. *Cancer Res*. 72, 2045–2056 (**2012**).

- GEORGE J, LIM JS, JANG SJ, CUN Y, OZRETIC L, KONG G, ET AL. Complete genomic profiles of small cell lung cancer. *Nature*. (2015) 524 (7563): 47-53.
- GERAGHTY, M., CRONIN, J.F., DEVEREUX, M. *ET AL*. Synthesis and antimicrobial activity of copper(II) and manganese(II) α,ω -dicarboxylate complexes. *Biometals*. 13, 1–8 (2000).
- GERSTNER ER, PAJTLER KW. Ependymoma. *Semin Neurol*. 2018 Feb;38(1): 104-111.
- GIANGRECO, A., K.R. GROOT, AND S.M. JANES, Lung cancer and lung stem cells: strange bedfellows? *Am J Respir Crit Care Med*, 2007. 175(6): p. 547-53.
- GILBERT ETHEL S. Ionizing Radiation and Cancer Risks: What Have We Learned From Epidemiology? *International Journal of Radiation Biology*. 2009. 85(6):467-482.
- GIOIA, D.; BERTAZZO, M.; RECANATINI, M.; MASETTI, M.; CAVALLI, A. Dynamic docking: A paradigm shift in computational drug discovery. *Molecules*. 2017, 22, 2029
- GLAS M, KEBIR S. Regorafenib in glioblastoma recurrence: how to deal with conflicting ‘real-life’ experiences? *Therapeutic Advances in Medical Oncology*. January. 2019.
- GLOBOCAN 2020. <https://gco.iarc.fr>
- GONZALEZ R. Infarcted epiploic appendages. PathologyOutlines.com website. <https://www.pathologyoutlines.com/topic/coloninfarcted.html>. Accessed September 25th, 2020.
- GOULD JULIE. Breaking Down Brain Cancer. *Nature*. 2018, 561 (S41).
- GOYAL L, SAHA SK, LIU LY, SIRAVEGNA G, LESHCHINER I, AHRONIAN LG, LENNERZ JK, VU P, DESHPANDE V, KAMBADAKONE A, MUSSOLIN B, REYES S, HENDERSON L, SUN JE, VAN SEVENTER EE, GURSKI JM JR, BALTSCHUKAT S, SCHACHER-ENGSTLER B, BARYS L, STAMM C, FURET P, RYAN DP, STONE JR, IAFRATE AJ, GETZ G, PORTA DG, TIEDT R, BARDELLI A, JURIC D, CORCORAN RB,

- BARDEESY N, ZHU AX. Polyclonal Secondary *FGFR2* Mutations Drive Acquired Resistance to FGFR Inhibition in Patients with FGFR2 Fusion-Positive Cholangiocarcinoma. *Cancer Discov.* **2017** Mar;7(3):252-263.
- GREULICH, H. & POLLOCK, P. M. **2011**. Targeting mutant fibroblast growth factor receptors in cancer. *Trends Mol Med*, 17, 283-92.
 - GRIVENNIKOV SI, GRETEN FR, KARIN M. Immunity, inflammation, and cancer. *Cell.* **2010**;140(6):883-899.
 - GUHA R. On exploring structure-activity relationships. *Methods Mol Biol.* **2013**;993:81-94
 - HAAGA JR, BOLL D. CT and MRI of the whole body. Mosby. (2009) ISBN: 0323053750.
 - HAAS KL, FRANZ KJ. Application of metal coordination chemistry to explore and manipulate cell biology. *Chem Rev.* **2010**;109(10):4921–4960
 - Hegi Monika E, Lili Liu, James G Herman, Roger Stupp, Wolfgang Wick, Michael Weller, Minesh P Mehta, Mark R Gilbert. Correlation of O6-methylguanine methyltransferase (MGMT) promoter methylation with clinical outcomes in glioblastoma and clinical strategies to modulate MGMT activity. *Journal of clinical oncology*, **2008**, 26, 25, 4189-4199.
 - HALLINAN, N., FINN, S., CUFFE, S., RAFEE, S., O'BYRNE, K. & GATELY, K. **2016**. Targeting the fibroblast growth factor receptor family in cancer. *Cancer Treat Rev*, 46, 51-62.
 - HANAHAN, D. AND R.A. WEINBERG, Hallmarks of cancer: the next generation. *Cell*, **2011**. 144(5): p. 646-74
 - HANAHAN, D. AND R.A. Weinberg, The hallmarks of cancer. *Cell*, **2000**. 100(1): p. 57-70
 - HANIF F, MUZAFFAR K, PERVEEN K, MALHI SM, SIMJEE SHU. Glioblastoma Multiforme: A Review of its Epidemiology and Pathogenesis through Clinical Presentation and Treatment. *Asian Pac J Cancer Prev.* **2017** Jan 1;18(1):3-9.

- HARDING, M. J. & NECHIPORUK, A. V. Fgfr-Ras-MAPK signaling is required for apical constriction via apical positioning of Rho-associated kinase during mechanosensory organ formation. *Development*, **2012**,139, 3130-5.
- HASHEMI-SADRAEI, N. & HANNA, N. **2017**. Targeting FGFR in Squamous Cell Carcinoma of the Lung. *Target Oncol*.
- HAY RT "SUMO: a history of modification". *Molecular Cell*. **18** (1): 1–12 (April 2005)
- Health, N.C.I.a.t.N.I.o., Targeted Cancer Therapies Fact Sheet. **2019**.
- HELSTEN, T., ELKIN, S., ARTHUR, E., TOMSON, B. N., CARTER, J. & KURZROCK, R. The FGFR Landscape in Cancer: Analysis of 4,853 Tumors by Next- Generation Sequencing. *Clin Cancer Res*, **2016** 22, 259-67.
- HIROSE TAKANORI, BERND W. SCHEITHAUER, BEATRIZ S. LOPES, HEINZ A. GERBER, HANS J. ALTERMATT, SCOTT R. VANDENBERG, Ganglioglioma, An ultrastructural and immunohistochemical study, *Cancer*, Volume79, Issue5, 1 March **1997**, Pages 989-1003
- HÖLSKEN A, BUCHFELDER M, FAHLBUSCH R, BLÜMCKE I, BUSLEI R. Tumour cell migration in adamantinomatous craniopharyngiomas is promoted by activated Wnt-signalling. *Acta Neuropathol*. **2010** May;119(5): 631-9.
- HÖLSKEN A, SILL M, MERKLE J, SCHWEIZER L, BUCHFELDER M, FLITSCH J, FAHLBUSCH R, METZLER M, KOOL M, PFISTER SM, VON DEIMLING A, CAPPER D, JONES DT, BUSLEI R. Adamantinomatous and papillary craniopharyngiomas are characterized by distinct epigenomic as well as mutational and transcriptomic profiles. *Acta Neuropathol Commun*. **2016** Feb 29;4:20.
- HUANG WS, METCALF CA, SUNDARAMOORTHY R, WANG Y, ZOU D, THOMAS RM, ZHU X, CAI L, WEN D, LIU S, ROMERO J, QI J, CHEN I, BANDA G, LENTINI SP, DAS S, XU Q, KEATS J, WANG F, WARDWELL S, NING Y, SNODGRASS JT, BROUDY MI, RUSSIAN K, ZHOU T, COMMODORE L, NARASIMHAN NI, MOHEMMAD QK, IULIUCCI J, RIVERA VM, DALGARNO DC, SAWYER TK, CLACKSON T,

- SHAKESPEARE WC. "Discovery of 3-[2-(imidazo[1,2-b]pyridazin-3-yl)ethynyl]-4-methyl-N-{4-[(4-methylpiperazin-1-yl)methyl]-3-(trifluoromethyl)phenyl}benzamide (AP24534), a potent, orally active pan-inhibitor of breakpoint cluster region-abelson (BCR-ABL) kinase including the T315I gatekeeper mutant". *J. Med. Chem.* **2010**. 53 (12): 4701–19
- Hübner JM, Kool M, Pfister SM, Pajtler KW. Epidemiology, molecular classification and WHO grading of ependymoma. *J Neurosurg Sci.* **2018** Feb; 62(1):46-50.
 - INGRID E WERTZ AND VISHVA M DIXIT, Signaling to NF-kappaB: regulation by ubiquitination, *Cold Spring Harb Perspect Biol.* **2010** Mar; 2(3):a003350.
 - JACKSON, ROBERT C., ET AL. "Modelling of the cancer cell cycle as a tool for rational drug development: A systems pharmacology approach to cyclotherapy." *PLoS Computational Biology*, vol. 13, no. 5, **2017**, p. e1005529.
 - JONES DT, JÄGER N, KOOL M, ZICHER T, HUTTER B, SULTAN M, ET AL. "Dissecting the genomic complexity underlying medulloblastoma". *Nature.* **2012**. 488 (7409): 100–5.
 - JIAPAER S, FURUTA T, TANAKA S, KITABAYASHI T, NAKADA M. Potential Strategies Overcoming the Temozolomide Resistance for Glioblastoma. *Neurol Med Chir (Tokyo).* **2018** Oct 15;58(10):405-421.
 - JIMENEZ-PASCUAL A, SIEBZEHRUBL FA. Fibroblast Growth Factor Receptor Functions in Glioblastoma. *Cells.* 2019 Jul 13;8(7):715.
 - JURATLI TAREQ A. PAMELA S. JONES, NANCY WANG, MEGHA SUBRAMANIAN, SIMON J. B. AYLWIN, YAZMIN ODIA, MS ELHAM ROSTAMI, OLAFUR GUDJONSSON, BRIAN L. SHAW DANIEL P. CAHILL, EVANTHIA GALANIS, FRED G. BARKER, SANDRO SANTAGATA, PRISCILLA K. BRASTIANOS, Targeted treatment of papillary craniopharyngiomas harboring BRAF V600E mutations, *Cancer*, Volume125, Issue17, September 1, **2019**, 2910-2914

- JUREK PM, ZABŁOCKI K, WAŚKO U, MAZUREK MP, OTLEWSKI J, JELEŃ F. Anti-FGFR1 aptamer-tagged superparamagnetic conjugates for anticancer hyperthermia therapy. *Int J Nanomedicine*. **2017**;12:2941-2950. Published 2017 Apr 11
- KAITLYN KASEMODEL AND KATARZYNA ROBERTS. Metal-Based Chemotherapy Drugs. *Proc. Okla. Acad. Sci.* 99: pp 106 - 113 (**2019**).
- KAN M, WANG F, XU J, CRABB JW, HOU J, MCKEEHAN WL. An essential heparin-binding domain in the fibroblast growth factor receptor kinase. *Science*. **1993**; 259(5103):1918–1921
- KARNTHALER-BENBAKKA C., GROZA D., K. KRYEZIU, V. PICHLER, A. ROLLER, W. BERGER, P. HEFFETER, C.R. KOWOI, *Angew. Chem. Int. Ed.* **2014**, 53, 12930 -12935
- KATARZYNA WADOWSKA ET AL, Genetic Markers in Lung Cancer Diagnosis: A Review, *International journal of molecular sciences*, **2020**.
- KATOH, M. FGFR inhibitors: effects on cancer cells, tumor microenvironment and whole-body homeostasis. *Int. J. Mol. Med.* 38, 3–15 (**2016**).
- KENTARO INAMURA, Lung Cancer: Understanding Its Molecular Pathology and the 2015 WHO Classification, *Front. Oncol.*, 28 August **2017**.
- KHALIL, A. A.; ABDEL HAMIDE, S. G.; AL-OBAID, A. M.; ELSUBBAGH, H. I. *Arch Pharm* **2003**, 336, 95.
- Khan RA, de Almeida A, Al-Farhan K, Alsalmeh A, Casini A, Ghazzali M, Reedijk J. Transition-metal norharmane compounds as possible cytotoxic agents: New insights based on a coordination chemistry perspective. *J Inorg Biochem*. **2016** Dec;165:128-135.
- KHAN, R., USMAN, M., DHIVYA, R. ET AL. Heteroleptic Copper(I) Complexes of “Scorpionate” Bis-pyrazolyl Carboxylate Ligand with Auxiliary Phosphine as Potential Anticancer Agents: An Insight into Cytotoxic Mode. *Sci Rep* **7**, 45229 (**2017**).
- KNIGHT JAMES AND DE JESUS ORLANDO, Pilocytic Astrocytoma, *StatPearls*, **2020**.

- KIM JINKUK, IN-HEE LEE, HEE JIN CHO, JEONGWU LEE, PETER J. PARK, DO-HYUN NAM. Spatiotemporal Evolution of the Primary Glioblastoma Genome. *Cancer Cell*. 28, 318–328 September 14, **2015**.
- KLEINBERG LAWRENCE, Polifeprosan 20, 3.85% carmustine slow release wafer in malignant glioma: patient selection and perspectives on a low-burden therapy. *Patient Prefer Adherence*. **2016** Nov 24;10:2397-2406.
- KLIGERMAN S, WHITE C. Epidemiology of lung cancer in women: risk factors, survival, and screening. *AJR Am J Roentgenol* **2011**;196:287-95
- KOWOL CR, HEFFETER P, MIKLOS W, ET AL. Mechanisms underlying reductant-induced reactive oxygen species formation by anticancer copper(II) compounds. *J Biol Inorg Chem*. **2012**;17(3):409-423.
- KUMAR V, ABBAS AK, ASTER JC (**2013**). "12". *Robbins Basic Pathology* (9th ed.). Elsevier Saunders. p. 505
- LABBE, S. & THIELE, D. J. PIPES, and wiring: the regulation of copper uptake and distribution in yeast. *Trends Microbiol*. **7**, 500–505 (**1999**).
- LADDHA SS, WADODKAR SG, MEGHAL SK, ARKIVOC. (2006);11:1-20.; HU S, XIE G, ZHANG DX, DAVIS C, LONG W, HU Y, ET AL., *Bioorg Med Chem Lett*. (2012);22: 6401–6305; Kh. Atia AJ, Al-Mufrgeiy SS., *American J Chem*. (**2012**);2:150-156.
- LAMBERT AW, PATTABIRAMAN DR, WEINBERG RA. Emerging Biological Principles of Metastasis. *Cell*. **2017**;168(4):670-691.
- LANG L, TENG Y. Fibroblast Growth Factor Receptor 4 Targeting in Cancer: New Insights into Mechanisms and Therapeutic Strategies. *Cells*. **2019**;8(1):31. Published 2019 Jan 9.
- LAZAREVIĆ T, RILAK A, BUGARČIĆ ŽD. Platinum, palladium, gold and ruthenium complexes as anticancer agents: Current clinical uses, cytotoxicity studies and future perspectives. *Eur J Med Chem*. **2017** Dec 15;142:8-31.
- LEHMAN, J.M., M.E. GWIN, AND P .P . Massion, Immunotherapy and Targeted Therapy for Small Cell Lung Cancer: There Is Hope. *Curr Oncol Rep*, **2017**. 19(7): p. 49

- LEMMON, M. A. & SCHLESSINGER, J. **2010**. Cell signaling by receptor tyrosine kinases. *Cell*, 141, 1117-34.
- LEMJABBAR-ALAOUI H, HASSAN OU, YANG YW, BUCHANAN P. Lung cancer: Biology and treatment options. *Biochim Biophys Acta*. **2015**;1856(2): 189-210.
- LEONARDO G FERREIRA, RICARDO N DOS SANTOS, GLAUCIUS OLIVA, ADRIANO D ANDRICOPULO, Molecular docking and structure-based drug design strategies, *Molecules*. **2015** Jul 22;20(7):13384-421.
- LE RHUN EMILIE, MATTHIAS PREUSSER, PATRICK ROTH PATRICK WEN, GUIDO REIFENBERGER, MICHAEL WELLER. Molecular targeted therapy of glioblastoma. *NEW DRUGS*. **2019**. 80, 101896.
- LEWIS RA (**2011**). "Chapter 4: Developing Molecular Modeling Programs: The Use and Limitations of Physical Models." In Gramatica P, Livingstone DJ, Davis AM (eds.). *Drug Design Strategies: Quantitative Approaches*. RSC Drug Discovery. Royal Society of Chemistry. Pp. 88–107
- Li X. The FGF metabolic axis. *Front Med*. **2019**;13(5):511-530.
- LI, X., WANG, C., XIAO, J., MCKEEHAN, W. L. & WANG, F. Fibroblast growth factors, old kids on the new block. *Semin Cell Dev Biol*, **2016**,53, 155-67.
- Lipinski, C.A.; Lombardo, F.; Dominy, B.W.; Feeney, P.J. Experimental and computational approaches to estimate solubility and permeability in drug discovery and development settings. *Adv. Drug Deliv. Rev.* **2012**, 64, 4–17
- LISSOWSKA J, FORETOVA L, DABEK J, ET AL. Family history and lung cancer risk: international multicentre case-control study in Eastern and Central Europe and meta-analyses. *Cancer Causes Control*. **2010**;21:1091-104.
- LIU, Y.; ZHANG, Y.; ZHONG, H.; JIANG, Y.; LI, Z.; ZENG, G.; CHEN, M.; SHAO, B.; LIU, Z.; LIU, Y. Application of molecular docking for the degradation of organic pollutants in the environmental remediation: A review. *Chemosphere*. **2018**, 203, 139–150.
- LOOMIS, D., GROSSE, Y., LAUBY-SECRETAN, B., EL GHISSASSI, F., BOUVARD, V., BENBRAHIM-TALLAA, L., GUHA, N., BAAN, R.,

- MATTOCK, H., STRAIF, K. & INTERNATIONAL AGENCY FOR RESEARCH ON CANCER MONOGRAPH WORKING GROUP, I. **2013**. The carcinogenicity of outdoor air pollution. *Lancet Oncol*, 14, 1262-3.
- LOUIS DN, OHGAKI H, WIESTLER OD, CAVENEE WK, BURGER PC, JOUVET A, SCHEITHAUER BW, KLEIHUES P. The 2007 WHO classification of tumours of the central nervous system. *Acta Neuropathol*. **2007** Aug;114(2):97-109.
 - LU, J., LIU, X., ZHENG, J. *et al*. Lin28A promotes IRF6-regulated aerobic glycolysis in glioma cells by stabilizing SNHG14. *Cell Death Dis* 11, 447 (**2020**).
 - LUZIA LEIROS SENA FERNANDES RIBEIRO DANTAS ET AL, In Vivo and In Vitro Toxicity Evaluation of Hydroethanolic Extract of *Kalanchoe brasiliensis* (Crassulaceae) Leaves, *Journal of Toxicology*, **2018**.
 - MALCHERS, F., DIETLEIN, F., SCHOTTLE, J., LU, X., NOGOVA, L., ALBUS, K., FERNANDEZ-CUESTA, L., HEUCKMANN, J. M., GAUTSCHI, O., DIEBOLD, J., PLENKER, D., GARDIZI, M., SCHEFFLER, M., BOS, M., SEIDEL, D., LEENDERS, F., RICHTERS, A., PEIFER, M., FLORIN, A., MAINKAR, P. S., KARRE, N., CHANDRASEKHAR, S., GEORGE, J., SILLING, S., RAUH, D., ZANDER, T., ULLRICH, R. T., REINHARDT, H. C., RINGEISEN, F., BUTTNER, R., HEUKAMP, L. C., WOLF, J. & THOMAS, R. K. Cell-autonomous and non-cell-autonomous mechanisms of transformation by amplified FGFR1 in lung cancer. *Cancer Discov*. **2014**. 4, 246-57.
 - MALINA A, MILLS JR, PELLETIER J. Emerging therapeutics targeting mRNA translation. *Cold Spring Harb Perspect Biol*. **2012**;4(4):a012377. Published 2012 Apr 1.
 - MALVEZZI M, CARIOLI G, BERTUCCIO P, ET AL. European cancer mortality predictions for the year 2017, with focus on lung cancer. *Ann Oncol* **2017**;28:1117-23.
 - MARK A. LEMMON AND JOSEPH SCHLESSINGER, Cell signaling by receptor-tyrosine kinases, *Cell*. **2010**; 141(7): 1117–1134

- MASARU KATOH, Fibroblast growth factor receptors as treatment targets in clinical oncology, *Nature Reviews Clinical Oncology* volume 16, pages105–122(2019).
- MELIN, B.S.; BARNHOLTZ-SLOAN, J.S.; WRENSCH, M.R.; JOHANSEN, C.; IL'YASOVA, D.; KINNERSLEY, B.; OSTROM, Q.T.; LABRECHE, K.; CHEN, Y.; ARMSTRONG, G.; ET AL. Genome-wide association study of glioma subtypes identifies specific differences in genetic susceptibility to glioblastoma and non-glioblastoma tumors. *Nat. Genet.* **2017**, *49*, 789.
- MENG, X.Y.; ZHANG, H.X.; MEZEI, M.; CUI, M. Molecular docking: A powerful approach for structure-based drug discovery. *Curr. Comput. Aided Drug Des.* **2011**, *7*, 146–157.
- ZAVALA-VEGA S, PALMA-LARA I, ORTEGA-SOTO E, TREJO-SOLIS C, DE ARELLANO IT, UCHARIMA-CORONA LE, GARCIA-CHACÓN G, OCHOA SA, XICOHTENCATL-CORTES J, CRUZ-CÓRDOVA A, LUNA-PINEDA VM, JIMÉNEZ-HERNÁNDEZ E, VÁZQUEZ-MERAZ E, MEJÍA-ARANGURÉ JM, GUZMÁN-BUCIO S, REMBAO-BOJORQUEZ D, SÁNCHEZ-GÓMEZ C, SALAZAR-GARCIA M, ARELLANO-GALINDO J. Role of Epstein-Barr Virus in Glioblastoma. *Crit Rev Oncog.* 2019;24(4): 307-338.
- MESSERSCHMIDT JL, PRENDERGAST GC, MESSERSCHMIDT GL. How Cancers Escape Immune Destruction and Mechanisms of Action for the New Significantly Active Immune Therapies: Helping Nonimmunologists Decipher Recent Advances. *Oncologist.* **2016**;21(2):233-243.
- MONTEMURRO NICOLA, Glioblastoma Multiforme and Genetic Mutations: The Issue Is Not Over Yet. An Overview of the Current Literatur. *J Neurol Surg A Cent Eur Neurosurg.* **2020** Jan;81(1):64-70.
- MULTHOFF G, MOLLS M, RADONS J. Chronic inflammation in cancer development. *Front Immunol.* **2012**;2:98.
- MYONG NH. Loss of E-cadherin and Acquisition of Vimentin in Epithelial-Mesenchymal Transition are Noble Indicators of Uterine Cervix Cancer Progression. *Korean J Pathol.* **2012**;46(4):341-348.

- NAGAR AA, RATHI LG, CHUGH N, PISE VJ, BENDALE A., *Der Pharm Chem.* **2010**, 2: 37- 43.
- N.H. CAMPBELL, N.H.A. KARIM, G.N. PARKINSON, M. GUNARATNAM, V. PETRUCCI, A.K. TODD, R. VILAR, S. NEIDLE, *J. Med. Chem.* **2011**, 55, 209-222
- National Cancer Institute at the National Institute of Health, Targeted Therapy to Treat Cancer. **2018**.
- National Cancer Institute at the National Institute of Health. *Hormone Therapy to Treat Cancer.* **2020**; Available from:<https://www.cancer.gov/about-cancer/treatment/types/hormone-therapy>
- Nicholas A. Butowski, MD, 2015 Epidemiology and diagnosis of brain tumors
- NICHOLAS BRADY, POLLY CHUNTOVA, LINDSEY K. BADE, AND KATHRYN L. SCHWERTFEGER, The FGF/FGFR axis as a therapeutic target in breast cancer, *Expert Rev Endocrinol Metab.* **2013** July ; 8(4): 391–402
- NOWAK J, SEIDEL C, BERG F, PIETSCH T, FRIEDRICH C, VON HOFF K, RUTKOWSKI S, WARMUTH-METZ M. MRI characteristics of ependymoblastoma: results from 22 centrally reviewed cases. *AJNR Am J Neuroradiol.* **2014** Oct;35(10):1996-2001.
- O’Hare, T. et al. AP24534, a pan-BCR-ABL inhibitor for chronic myeloid leukemia, potently inhibits the T315I mutant and overcomes mutation-based resistance. *Cancer Cell* 16, 401–412 (**2009**).
- OHGAKI H, KLEIHUES P. Epidemiology and etiology of gliomas. *Acta Neuropathol.* **2005** Jan;109(1):93-108.
- ONOI K, CHIHARA Y, UCHINO J, SHIMAMOTO T, MORIMOTO Y, IWASAKU M, KANEKO Y, YAMADA T, TAKAYAMA K. Immune Checkpoint Inhibitors for Lung Cancer Treatment: A Review. *J Clin Med.* 2020 May 6;9(5):1362.
- OKAZAKI I, ISHIKAWA S, ANDO W, ET AL. Lung Adenocarcinoma in Never Smokers: Problems of Primary Prevention from Aspects of Susceptible Genes and Carcinogens. *Anticancer Res.* **2016**;36:6207-24.

- ORNITZ DM, ITOH N. Fibroblast growth factors. *Genome Biol.* **2001**; 2(3)
- OSTROM QT, GITTLEMAN H, LIAO P, VECCHIONE-KOVAL T, WOLINSKY Y, KRUCHKO C, BARNHOLTZ-SLOAN JS. CBTRUS Statistical Report: Primary brain and other central nervous system tumors diagnosed in the United States in 2010-2014. *Neuro Oncol.* **2017** Nov 6;19(suppl_5):v1-v88.
- OSTROM QT, LUC BAUCHET, FAITH G DAVIS, ISABELLE DELTOUR, JAMES L FISHER, CHELSEA EASTMAN LANGER, MELIKE PEKMEZCI, JUDITH A SCHWARTZBAUM, MICHELLE C TURNER, KYLE M WALSH, MARGARET R WRENSCH, JILL S BARNHOLTZ-SLOAN, Response to “The epidemiology of glioma in adults: a ‘state of the science’ review”, *Neuro-oncology*, **2015**, 17,4, 624-626.
- OWA T, YOSHINO H, YOSHIMATSU K, NAGASU T. Cell cycle regulation in the G1 phase: a promising target for the development of new chemotherapeutic anticancer agents. *Curr Med Chem.* **2001** Oct;8(12): 1487-503.
- OZDEMIR-KAYNAK ELIF, QUTUB AMINA A., YESIL-CELIK TAS OZLEM, Advances in Glioblastoma Multiforme Treatment: New Models for Nanoparticle Therapy, *Front. Physiol.*, 19 March **2018**; 9,170
- P. R. MARSHAM, J. M. WARDLEWORTH, F. T. BOYLE, L. F. HENNEQUIN, R. KIMBELL, M. BROWN, A. L. JACKMAN. Design and synthesis of potent non-polyglutamatable quinazolinone antifolate thymidylate synthase inhibitors. *J Med Chem.* **1999**;42:3809
- P. SKEHAN, ET AL., R. STORENG, D. SCUDIERO, A. MONKS, J. MCMAHON, D. VISTICA, J.T.WARREN, H. BOKESCH, S. KENNEY, M.R. BOYD, *J. Natl. Cancer Inst.* 82 (**1990**) 1107–1112.
- P.K. PAIK, R. SHEN, D. FERRY, ET AL. A phase 1b open-label multicenter study of AZD4547 in patients with advanced squamous cell lung cancers: preliminary antitumor activity and pharmacodynamic data. *J Clin Oncol*, 32 (suppl 5) (**2014**), p. 8035.

- PANDEY R, CAFLISCH L, LODI A, BRENNER AJ, TIZIANI S. Metabolomic signature of brain cancer. *Mol Carcinog.* **2017** Nov; 56(11):2355-2371.
- PAPAC RJ. Spontaneous regression of cancer: Possible mechanisms. *In Vivo.* **1998**;12:571–578
- PAPAC RJ. Spontaneous regression of cancer. *Cancer Treat Rev.* **1996**;22:395–423
- PARIKH KA, VENABLE GT, ORR BA, CHOUDHRI AF, BOOP FA, GAJJAR AJ, KLIMO P JR. Pineoblastoma-The Experience at St. Jude Children's Research Hospital. *Neurosurgery.* **2017** Jul 1;81(1):120-128.
- PATEL JD. Lung cancer in women. *J Clin Oncol* **2005**; 23: 3212-8
- PATEL ANOOP P., JAMES L FISHER, EMMA NICHOLS, FOAD ABD-ALLAH, JEMAL ABDELA, AHMED ABDELALIM, HAFTOM NIGUSE ABRAHA, DOMINIC AGIUS, FARES ALAHDAB, TAHIYA ALAM, CHRISTINE A ALLEN, NAHLA HAMED ANBER, ASHISH AWASTHI, HAMID BADALI, ABATE BEKELE BELACHEW, ALI BIJANI, TONE BJØRGE, FÉLIX CARVALHO, FERRÁN CATALÁ-LÓPEZ, JEE-YOUNG J CHOI, AHMAD DARYANI, MEAZA GIRMA DEGEFA, GEBRE TEKLEMARIAM DEMOZ, HUYEN PHUC DO, MANISHA DUBEY, EDUARDA FERNANDES, IRINA FILIP, KYLE J FOREMAN, ABADI KAHSU GEBRE, YILMA CHISHA DEA GERAMO, NIMA HAFEZINEJAD, SAMER HAMIDI, JAMES D HARVEY, HAMID YIMAM HASSEN, SIMON I HAY, SEYED SINA NAGHIBI IRVANI, MIHAJLO JAKOVLJEVIC, RAVI PRAKASH JHA, AMIR KASAEIAN, IBRAHIM A KHALIL, EJAZ AHMAD KHAN, YOUNG-HO KHANG, YUN JIN KIM, GETNET MENGISTU, KARZAN ABDULMUHSIN MOHAMMAD, ALI H MOKDAD, GABRIELE NAGEL, MOHSEN NAGHAVI, GURUDATTA NAIK, HUONG LAN THI NGUYEN, LONG HOANG NGUYEN, TRANG HUYEN NGUYEN, MOLLY R NIXON, ANDREW T OLAGUNJU, DAVID M PEREIRA, GABRIEL DAVID PINILLA-MONSALVE, HOSSEIN POUSTCHI, MOSTAFA QORBANI, AMIR RADFAR, ROBERT C REINER, GHOLAMREZA ROSHANDEL, HOSEIN SAFARI, SAEID SAFIRI,

ABDALLAH M SAMY, SHAHABEDDIN SARVI, MASOOD ALI SHAIKH, MEHDI SHARIF, RAJESH SHARMA, SARA SHEIKHBAHA EI, REZA SHIRKOOHI, JASVINDER A SINGH, MARI SMITH, RAFAEL TABARÉS-SEISDEDOS, BACH XUAN TRAN, KHANH BAO TRAN, IRFAN ULLAH, ELISABETE WEIDERPASS, KIDU GIDEY WELDEGWERGS, EBRAHIM M YIMER, VESNA ZADNIK, ZOUBIDA ZAIDI, RICHARD G ELLENBOGEN, THEO VOS, VALERY L FEIGIN, CHRISTOPHER JL MURRAY, CHRISTINA FITZMAURICE, JAMES L FISHER, EMMA NICHOLS, FOAD ABD-ALLAH, JEMAL ABDELA, AHMED ABDELALIM, HAFTOM NIGUSE ABRAHA, DOMINIC AGIUS, FARES ALAHDAB, TAHIYA ALAM, CHRISTINE A ALLEN, NAHLA HAMED ANBER, ASHISH AWASTHI, HAMID BADALI, ABATE BEKELE BELACHEW, ALI BIJANI, TONE BJØRGE, FÉLIX CARVALHO, FERRÁN CATALÁ-LÓPEZ, JEE-YOUNG J CHOI, AHMAD DARYANI, MEAZA GIRMA DEGEFA, GEBRE TEKLEMARIAM DEMOZ, HUYEN PHUC DO, MANISHA DUBEY, EDUARDA FERNANDES, IRINA FILIP, KYLE J FOREMAN, ABADI KAHSU GEBRE, YILMA CHISHA DEA GERAMO, NIMA HAFEZI-NEJAD, SAMER HAMIDI, JAMES D HARVEY, HAMID YIMAM HASSEN, SIMON I HAY, SEYED SINA NAGHIBI IRVANI, MIHAJLO JAKOVLJEVIC, RAVI PRAKASH JHA, AMIR KASAEIAN, IBRAHIM A KHALIL, EJAZ AHMAD KHAN, YOUNG-HO KHANG, YUN JIN KIM, GETNET MENGISTU, KARZAN ABDULMUHSIN MOHAMMAD, ALI H MOKDAD, GABRIELE NAGEL, MOHSEN NAGHAVI, GURUDATTA NAIK, HUONG LAN THI NGUYEN, LONG HOANG NGUYEN, TRANG HUYEN NGUYEN, MOLLY R NIXON, ANDREW T OLAGUNJU, DAVID M PEREIRA, GABRIEL DAVID PINILLA-MONSALVE, HOSSEIN POUSTCHI, MOSTAFA QORBANI, AMIR RADFAR, ROBERT C REINER, GHOLAMREZA ROSHANDEL, HOSEIN SAFARI, SAEID SAFIRI, ABDALLAH M SAMY, SHAHABEDDIN SARVI, MASOOD ALI SHAIKH, MEHDI SHARIF, RAJESH SHARMA, SARA SHEIKHBAHA EI, REZA SHIRKOOHI, JASVINDER A SINGH, MARI SMITH, RAFAEL TABARÉS-

SEISDEDOS, BACH XUAN TRAN, KHANH BAO TRAN, IRFAN ULLAH, ELISABETE WEIDERPASS, KIDU GIDEY WELDEGWERGS, EBRAHIM M YIMER, VESNA ZADNIK, ZOUBIDA ZAIDI, RICHARD G ELLENBOGEN, THEO VOS, VALERY L FEIGIN, CHRISTOPHER JL MURRAY, CHRISTINA FITZMAURICE. Global, regional, and national burden of brain and other CNS cancer, 1990–2016: a systematic analysis for the Global Burden of Disease Study 2016, *The Lancet Neurology*, **2019**, 18 (4), 376-393.

- PEIFER, M., FERNANDEZ-CUESTA, L., SOS, M. L., GEORGE, J., SEIDEL, D., KASPER, L. H., PLENKER, D., LEENDERS, F., SUN, R., ZANDER, T., MENON, R., KOKER, M., DAHMEN, I., MULLER, C., DI CERBO, V., SCHILDHAUS, H. U., ALTMULLER, J., BAESSMANN, I., BECKER, C., DE WILDE, B., VANDESOMPELE, J., BOHM, D., ANSEN, S., GABLER, F., WILKENING, I., HEYNCK, S., HEUCKMANN, J. M., LU, X., CARTER, S. L., CIBULSKIS, K., BANERJI, S., GETZ, G., PARK, K. S., RAUH, D., GRUTTER, C., FISCHER, M., PASQUALUCCI, L., WRIGHT, G., WAINER, Z., RUSSELL, P., PETERSEN, I., CHEN, Y., STOELBEN, E., LUDWIG, C., SCHNABEL, P., HOFFMANN, H., MULEY, T., BROCKMANN, M., ENGEL-RIEDEL, W., MUSCARELLA, L. A., FAZIO, V. M., GROEN, H., TIMENS, W., SIETSMA, H., THUNNISSEN, E., SMIT, E., HEIDEMAN, D. A., SNIJDERS, P. J., CAPPUZZO, F., LIGORIO, C., DAMIANI, S., FIELD, J., SOLBERG, S., BRUSTUGUN, O. T., LUND-IVERSEN, M., SANGER, J., CLEMENT, J. H., SOLTERMANN, A., MOCH, H., WEDER, W., SOLOMON, B., SORIA, J. C., VALIDIRE, P., BESSE, B., BRAMBILLA, E., BRAMBILLA, C., LANTUEJOUL, S., LORIMIER, P., SCHNEIDER, P. M., HALLEK, M., PAO, W., MEYERSON, M., SAGE, J., SHENDURE, J., SCHNEIDER, R., BUTTNER, R., WOLF, J., NURNBERG, P., PERNER, S., HEUKAMP, L. C., BRINDLE, P. K., HAAS, S. & THOMAS, R. K. **2012**. Integrative genome analyses identify key somatic driver mutations of small-cell lung cancer. *Nat Genet*, 44, 1104-10.

- PIETANZA, M.C. AND M. LADANYI, Bringing the genomic landscape of small- cell lung cancer into focus. *Nat Genet*, **2012**. 44(10): p. 1074-5.
- POLAMARASETTY APAROY, KAKULARAM KUMAR REDDY, PALLU REDDANNA, Structure and Ligand Based Drug Design Strategies in the Development of Novel 5- LOX Inhibitors, *Current Medicinal Chemistry*, **2012**, 19, 3763-3778.
- POMERLEAU, C. S., POMERLEAU, O. F., SNEDECOR, S. M. & MEHRINGER, A. M. **2004**. Defining a never-smoker: results from the nonsmokers survey. *Addict Behav*, 29, 1149-54.
- PORTA, R., BOREA, R., COELHO, A., KHAN, S., ARAUJO, A., RECLUSA, P., FRANCHINA, T., VAN DER STEEN, N., VAN DAM, P., FERRI, J., SIRERA, R., NAING, A., HONG, D. & ROLFO, C. FGFR a promising druggable target in cancer: Molecular biology and new drugs. *Crit Rev Oncol Hematol*, **2017**, 113, 256-267.
- POWERS, C. J., MCLESKEY, S. W. & WELLSTEIN, A. Fibroblast growth factors, their receptors and signaling. *Endocr Relat Cancer*, **2000**, 7, 165-97.
- QUIGLEY MR, MAROON JC. The relationship between survival and the extent of the resection in patients with supratentorial malignant gliomas. *Neurosurgery*. **1991** Sep;29(3):385-8; discussion 388-9.
- RAASCHOU-NIELSEN, O., SORENSEN, M., KETZEL, M., HERTEL, O., LOFT, S., TJONNELAND, A., OVERVAD, K. & ANDERSEN, Z. J. **2013**. Long-term exposure to traffic-related air pollution and diabetes-associated mortality: a cohort study. *Diabetologia*, 56, 36-46.
- RIEGER AM, NELSON KL, KONOWALCHUK JD, BARREDA DR. Modified annexin V/propidium iodide apoptosis assay for accurate assessment of cell death. *J Vis Exp*. **2011**;(50):2597.
- RISBRIDGER GP, DAVIS ID, BIRRELL SN, TILLEY WD. Breast and prostate cancer: more similar than different. *Nat Rev Cancer*. **2010** Mar;10(3): 205-12.

- ROSKOSKI, R. JR. Classification of small molecule protein kinase inhibitors based upon the structures of their drug-enzyme complexes. *Pharmacol. Res.* **103**, 26–48 (2016).
- ROUSSEL MF, HATTEN ME (2011). *Cerebellum development and medulloblastoma*. Current Topics in Developmental Biology. 94. pp. 235–82.
- RUIZ-CEJA, K. A. & CHIRINO, Y. I. 2017. Current FDA-approved treatments for non- small cell lung cancer and potential biomarkers for its detection. *Biomed Pharmacother*; **90**, 24-37.
- SAADEH S. M., “Synthesis, characterization and biological properties of Co(II), Ni(II), Cu(II) and Zn(II) complexes with an SNO functionalized ligand,” *Arabian Journal of Chemistry*, vol. 6, no. 2, pp. 191–196, **2013**.
- SABARI, J.K., ET AL., Unravelling the biology of SCLC: implications for therapy. *Nat Rev Clin Oncol*, **2017**. 14(9): p. 549-561
- SALCMAN M. (2003) Surgical Therapy and Problems in the Treatment of Private Malignant Gliomas. In: Petrovich Z., Brady L.W., Apuzzo M.L.J., Bamberg M. (eds) Combined Modality Therapy of Central Nervous System Tumors. Medical Radiology (Radiation Oncology). Springer, Berlin, Heidelberg.
- SALGA MS, ALI HM, ABDULLA MA, ABDELWAHAB SI. Acute oral toxicity evaluations of some zinc(II) complexes derived from 1-(2-Salicylaldiminoethyl)piperazine schiff bases in rats. *Int J Mol Sci.* **2012**;13(2):1393–1404.
- SANA RAOOF ET AL, Targeting FGFR overcomes EMT-mediated resistance in EGFR mutant non-small cell lung cancer, *Oncogene*, **2019** Sep;38(37): 6399-6413
- SANTINI C., M. PELLEI, V. GANDIN, M. PORCHIA, F. TISATO, C. MARZANO, *Chem. Rev.* **2014**, 114, 815-862;
- SARKAR A, PAITAL AR, KHAN RA, ARJMAND F, BERTOLASI V, MATHONIERE C, CLÉRAC R, RAY D. Ligand dependent self-assembly of hydroxido-bridged dicopper units templated by sodium ion. *Dalton Trans.* **2013** Sep 14;42(34):12495-506.

- SCHRAMM K., ISKAR M., STATZ B., JAGER N., HAAG D., SLABICKI M., PFISTER S.M., ZAPATKA M., GRONYCH J., JONES D.T.W., et al. DECIPHER pooled shRNA library screen identifies PP2A and FGFR signaling as potential therapeutic targets for DIPGs. *Neuro Oncol.* **2019**
- SEO, A. N., JIN, Y., LEE, H. J., SUN, P. L., KIM, H., JHEON, S., KIM, K., LEE, C. T. & CHUNG, J. H. **2014**. FGFR1 amplification is associated with poor prognosis and smoking in non-small-cell lung cancer. *Virchows Arch*, 465, 547-58.
- SÉHÉDIC D., CIKANKOWITZ A., HINDRÉ F., DAVODEAU F., GARCION E. (**2015**). Nanomedicine to overcome radioresistance in glioblastoma stem-like cells and surviving clones. *Trends Pharmacol. Sci.* 36, 236–252.
- SEVELDA F, MAYR L, KUBISTA B, LÖTSCH D, VAN SCHOONHOVEN S, WINDHAGER R, PIRKER C, MICKSCHE M, BERGER W. EGFR is not a major driver for osteosarcoma cell growth in vitro but contributes to starvation and chemotherapy resistance. *J Exp Clin Cancer Res.* 2015 Nov 2;34:134.
- SINGH J, CHUAQUI CE, BORIACK-SJODIN PA, LEE WC, PONTZ T, CORBLEY MJ, CHEUNG HK, ARDUINI RM, MEAD JN, NEWMAN MN, PAPADATOS JL, BOWES S, JOSIAH S, LING LE (Dec **2003**). "Successful shape-based virtual screening: the discovery of a potent inhibitor of the type I TGFbeta receptor kinase (TbetaRI)". *Bioorganic & Medicinal Chemistry Letters.* 13 (24): 4355–9.
- SOGNIER MA, HITTELMAN WN. Mitomycin-induced chromatid breaks in HeLa cells: a consequence of incomplete DNA replication. *Cancer Res.* **1986** Aug;46(8):4032-40.
- SPIEGELBERG L, HOUBEN R, NIEMANS R, ET AL. Hypoxia-activated prodrugs and (lack of) clinical progress: The need for hypoxia-based biomarker patient selection in phase III clinical trials. *Clin Transl Radiat Oncol.* **2019**;15:62-69.
- STANCULEANU DL, DANIELA Z, LAZESCU A, BUNGHEZ R, ANGHEL R. Development of new immunotherapy treatments in different cancer types. *J Med Life.* **2016**;9(3):240-248

- Statistics adapted from the American Cancer Society's publication, Cancer Facts & Figures 2020, the ACS website (January 2020), the CBTRUS Statistical Report: Primary Brain and Other Central Nervous System Tumors Diagnosed in the United States in 2012-2016 (January 2020), and the National Cancer Institute website (January 2020).
- SUBRAMANIYAM RAJALAKSHMI, AAFREEN FATHIMA, JONNALAGADDA RAGHAVA RAO AND BALACHANDRAN UNNI NAIR, Antibacterial activity of copper(ii) complexes against Staphylococcus aureus, *RSC Advances*, **2014**, 4, 32004-32012.
- SUN, X., GUO, W., SHEN, J. K., MANKIN, H. J., HORNICEK, F. J. & DUAN, Z. 2015. Rhabdomyosarcoma: Advances in Molecular and Cellular Biology. *Sarcoma*, **2015**, 232010.
- TABASSUM, S., AHMAD, A., KHAN, R. A., HUSSAIN, Z., SRIVASTAV, S., SRIKRISHNA, S. & ARJMAND, F. Chiral Heterobimetallic Complexes Targeting Human DNA-Topoisomerase I α . *Dalton Trans.* 42, 16749–16761 (**2013**).
- TALMADGE, J. E. & FIDLER, I. J. AACR centennial series: the biology of cancer metastasis: historical perspective. *Cancer Res.* **2010**. 70, 5649-69.
- TANNER, Y. & GROSE, R. P. **2016**. Dysregulated FGF signalling in neoplastic disorders. *Semin Cell Dev Biol*, 53, 126-35.
- TAYLOR OLIVIA G., BRZOWSKI JOSHUA S., SKELDING KATHRYN A. Glioblastoma Multiforme: An Overview of Emerging Therapeutic Targets. *Frontiers in Oncology*. **2019**, 9 (963).
- TEJASWI KANDERI AND VIKAS GUPTA. Glioblastoma Multiforme. *StatPearls*. **2020**.
- TERENCE A., LÖTSCH D., VAN SCHOONHOVEN S., ROLLER A., C.R. KOWOL, W. BERGER, B.K. KEPPLER, G. BARONE, Another step toward DNA selective targeting: NiII and CuII complexes of a Schiff base ligand able to bind gene promoter G-quadruplexes, *Dalton Trans.* **2016**, 45, 7758-7767

- TISATO, F., MARZANO, C., PORCHIA, M., PELLEI, M. & SANTINI, C. Copper in diseases and treatments, and copper-based anticancer strategies. *Med. Res. Rev.* 30, 708–749 (2010).
- TISEO, M., GELSOMINO, F., ALFIERI, R., CAVAZZONI, A., BOZZETTI, C., DE GIORGI, A. M., PETRONINI, P. G. & ARDIZZONI, A. FGFR as potential target in the treatment of squamous non small cell lung cancer. *Cancer Treat Rev*, 2015. 41, 527-39.
- TJames E. Talmadge and Isaiah J. Fidler, The Biology of Cancer Metastasis: Historical Perspective, *AACR Centennial Series*, July 7, 2010.
- TORRE LA, BRAY F, SIEGEL RL, FERLAY J, LORTET-TIEULENT J AND JEMAL A. Global cancer statistics, 2012. *CA Cancer J Clin*; 2015.
- TORRES PHM, SODERO ACR, JOFILY P, SILVA-JR FP. Key Topics in Molecular Docking for Drug Design. *Int J Mol Sci*. 2019;20(18):4574.
- TOUAT, M., ILEANA, E., POSTEL-VINAY, S., ANDRE, F. & SORIA, J. C. 2015. Targeting FGFR Signaling in Cancer. *Clin Cancer Res*, 21, 2684-94.
- TRAVIS, W. D., BRAMBILLA, E., NICHOLSON, A. G., YATABE, Y., AUSTIN, J. H., BEASLEY, M. B., CHIRIEAC, L. R., DACIC, S., DUHIG, E., FLIEDER, D. B., GEISINGER, K., HIRSCH, F. R., ISHIKAWA, Y., KERR, K. M., NOGUCHI, M., PELOSI, G., POWELL, C. A., TSAO, M. S., WISTUBA, I. & PANEL, W. H. O. The 2015 World Health Organization Classification of Lung Tumors: Impact of Genetic, Clinical and Radiologic Advances Since the 2004 Classification. *J Thorac Oncol*, 2015. 10, 1243-60.
- TSAO, A. S., SCAGLIOTTI, G. V., BUNN, P. A., JR., CARBONE, D. P., WARREN, G. W., BAI, C., DE KONING, H. J., YOUSAF-KHAN, A. U., MCWILLIAMS, A., TSAO, M. S., ADUSUMILLI, P. S., RAMI-PORTA, R., ASAMURA, H., VAN SCHIL, P. E., DARLING, G. E., RAMALINGAM, S. S., GOMEZ, D. R., ROSENZWEIG, K. E., ZIMMERMANN, S., PETERS, S., IGNATIUS OU, S. H., REUNGWETWATTANA, T., JANNE, P. A., MOK, T. S., WAKELEE, H. A., PIRKER, R., MAZIERES, J., BRAHMER, J. R., ZHOU, Y., HERBST, R. S., PAPANIKOLAOU, V. A., REDMAN, M. W., WYNES, M. W., GANDARA, D. R., KELLY, R. J.,

- HIRSCH, F. R. & PASS, H. I. 2016. Scientific Advances in Lung Cancer **2015**. *J Thorac Oncol*, 11, 613-38.
- TUCKER, J. A. ET AL. Structural insights into FGFR kinase isoform selectivity: diverse binding modes of AZD4547 and ponatinib in complex with FGFR1 and FGFR4. *Structure* 22, 1764–1774 (2014).
 - TURNER, N. & GROSE, R. **2010**. Fibroblast growth factor signalling: from development to cancer. *Nat Rev Cancer*, 10, 116-29.
 - UENO, K OHTAWA, K MITSUI, Y KODERA, M HIROTO, A MATSUSHIMA, Y INADA AND H NISHIMURA, Cell cycle arrest and apoptosis of leukemia cells induced by L-asparaginase, Ueno, K Ohtawa, K Mitsui, Y Koder, M Hiroto, A Matsushima, Y Inada and H Nishimura, *Leukemia* (1997) 11, 1858–186
 - USMAN, M., ZAKI, M., KHAN, R. A., ALSALME, A., AHMAD, M. & TABASSUM, S. Coumarin centered copper(II) complex with appended-imidazole as cancer chemotherapeutic agents against lung cancer: molecular insight via DFT-based vibrational analysis. *RSC Adv.* 7, 36056–3607 (2017).
 - UZBEKOV R. E. Analysis of the Cell Cycle and a Method Employing Synchronized Cells for Study of Protein Expression at Various Stages of the Cell Cycle, *Biochemistry*, Vol. 69, No. 5, **2004**, pp. 485496.
 - VOJTEK M, MARQUES MPM, FERREIRA IMPLVO, MOTA-FILIFE H, DINIZ C. Anticancer activity of palladium-based complexes against triple-negative breast cancer. *Drug Discov Today*. **2019** Apr; 24(4):1044-1058.
 - WADA CHIEKI, AKIRA KURATA , RYUICHI HIROSE, YOSHIKI TAZAKI, SHINICHI KAN, YOSHIHIRO ISHIHARA AND TORU KAMEYA, Primary leptomeningeal ependymoblastoma, *Journal of Neurosurgery*, **1986**, 64 (6).
 - WEENINK B, FRENCH PJ, SILLEVIS SMITT PAE, DEBETS R, GEURTS M. Immunotherapy in Glioblastoma: Current Shortcomings and Future Perspectives. *Cancers (Basel)*. **2020** Mar 22;12(3):751.
 - WEINBERG, R.A., *The biology of cancer*. Second edition. ed. **2014**, New York: Garland Science, Taylor & Francis Group. xx, 876, A 6, G 30, I 28 pages.

- WEISS, J., ET AL., Frequent and focal FGFR1 amplification associates with therapeutically tractable FGFR1 dependency in squamous cell lung cancer. *Sci Transl Med*, **2010**. **2**(62): p. 62ra93
- WERTZ, I. E. & DIXIT, V. M. Regulation of death receptor signaling by the ubiquitin system. *Cell Death Differ*. **2010**. **17**, 14-24.
- Wesseling P, van den Bent M, Perry A. Oligodendroglioma: pathology, molecular mechanisms and markers. *Acta Neuropathol*. **2015** Jun;129(6): 809-27.
- WIEDEMANN, M. & TRUEB, B. Characterization of a novel protein (FGFRL1) from human cartilage related to FGF receptors. *Genomics* **69**, 275–279 (**2000**).
- WILSON, G.L.; LILL, M.A. Integrating structure-based and ligand-based approaches for computational drug design. *Future Med. Chem*. **2011**, **3**, 735–750
- *World Cancer Report 2014*. World Health Organization. **2014**. pp. Chapter 1.1.
- World Health Organization, **2015**
- World Health Organization, World health statistics 2018: monitoring health for the SDGs, sustainable development goals. World Health Organization, **2018**
- WU, Y. M., SU, F., KALYANA-SUNDARAM, S., KHAZANOV, N., ATEEQ, B., CAO, X., LONIGRO, R. J., VATS, P., WANG, R., LIN, S. F., CHENG, A. J., KUNJU, L. P., SIDDIQUI, J., TOMLINS, S. A., WYNGAARD, P., SADIS, S., ROYCHOWDHURY, S., HUSSAIN, M. H., FENG, F. Y., ZALUPSKI, M. M., TALPAZ, M., PIENTA, K. J., RHODES, D. R., ROBINSON, D. R. & CHINNAIYAN, A. M. Identification of targetable FGFR gene fusions in diverse cancers. *Cancer Discov*, **2013**. **3**, 636-47.
- XIAO Y, CHEN DI, ZHANG X, CUI Q, FAN Y, BI C, DOU QP. Molecular study on copper-mediated tumor proteasome inhibition and cell death. *Int J Oncol*. **2010** Jul;37(1):81-87.
- XIE, Y., SU, N., YANG, J. ET AL. FGF/FGFR signaling in health and disease. *Sig Transduct Target Ther* **5**, 181 (**2020**).

- YAFANG HU ET AL, 90-kDa Ribosomal S6 Kinase Is a Direct Target for the Nuclear Fibroblast Growth Factor Receptor 1 (FGFR1) ROLE IN FGFR1 SIGNALING. *The Journal of Biological Chemistry*. July **2004**. 279, 29325-29335
- YAN L, ROSEN N, ARTEAGA C. Targeted cancer therapies. *Chin J Cancer*. **2011**;30(1):1-4
- YAN YK, MELCHART M, HABTEMARIAM A, SADLER PJ. Organometallic chemistry, biology and medicine: ruthenium arene anticancer complexes. *Chemical Communications*. **2005**;38:4764-4776.
- YANGLI XIE, NAN SU, JING YANG, QIAOYAN TAN, SHUO HUANG, MIN JIN, ZHENHONG NI, BIN ZHANG, DALI ZHANG, FENGTAO LUO, HANGANG CHEN, XIANDING SUN, JIAN Q. Feng2, Huabing Qi and Lin Chen, FGF/FGFR signaling in health and disease, *Signal Transduction and Targeted Therapy* (**2020**)5:181.
- YAZMIN ODIA, Gangliocytomas and Gangliogliomas: Review of Clinical, Pathologic and Genetic Features. *Clin Oncol*. **2016**; 1: 1017.
- YOULDEN DR, CRAMB SM, BAADE PD. The International Epidemiology of Lung Cancer: geographical distribution and secular trends. *J Thorac Oncol* **2008**;3:819-31.
- ZANG X. 2018 Nobel Prize in medicine awarded to cancer immunotherapy: Immune checkpoint blockade - A personal account. *Genes Dis*. **2018** Oct 18;5(4):302-303.
- ZENG Y, MA J, ZHAN Y, XU X, ZENG Q, LIANG J, CHEN X. Hypoxia-activated prodrugs and redox-responsive nanocarriers. *Int J Nanomedicine*. **2018**;13:6551-6574
- ZHANG, H. AND J. CHEN, Current status and future directions of cancer immunotherapy. *J Cancer*, **2018**. **9**(10): p. 1773-1781
- ZHOU J, TAO D, XU Q, GAO Z, TANG D. Expression of E-cadherin and vimentin in oral squamous cell carcinoma. *Int J Clin Exp Pathol*. **2015**;8(3): 3150-3154.

- ZHOU SF, ZHONG WZ. Drug Design and Discovery: Principles and Applications. *Molecules*. **2017**;22(2):279.

Curriculum Vitae

Mery La Franca

Personal details

Date and Place of Birth: 19.01.1992, Tbilisi
(Georgia)

Citizenship: Italian

E-mail: merylafranca92@gmail.com



Education

November 2020 - Now: Specializing in Hospital Pharmacy (University of Messina, Italy)

November 2017 - October 2020: PhD Student in Molecular and Bimolecular Sciences, University of Palermo, in co-tutorship with the Medical University of Vienna.

November 2017 — October 2018 and June 2020 — October 2020: Chemical and Pharmaceutical Biological Sciences and Technologies, University of Palermo.

Supervised by Prof. Giampaolo Barone.

Main occupation: design and synthesis of new anti cancer drugs, FGFR inhibitors.

November 2018 — June 2020: Institute of Cancer Research of Medical University of Vienna.

Supervised by Univ. Prof. Dr. Mag. Walter Berger.

Main occupation: *in vitro* and *in vivo* evaluation of new anti cancer drugs, FGFR inhibitors.

December 2017: Qualification examination for the profession of Pharmacist, Second Session of 2017, Palermo (Italy).

September 2012 — October 2017: Master's Degree in Pharmacy, Class LM-13, Class of Master Degrees in Pharmacy and Industrial Pharmacy, reporting the vote of *110/110 with honors* (University of Palermo).

Experimental thesis in Pharmaceutical Chemistry (CHIM/08) with a dissertation entitled "*Synthesis and antiproliferative activity of new 4-quinazolinone derivatives*". Promotor: Dr. Maria Valeria Raimondi.

Experience

2019 - Cotutor of experimental thesis , University of Palermo:

- Identification of new ligands of the FGFR4, design and synthesis of a drug discovery library of 4-quinazolinones. Master Degree in Pharmaceutical Chemistry and Technology
- Design and synthesis of multitarget compounds with quinazolinone structure potential inhibitors of dihydrofolate reductase and tubulin. Master Degree in Pharmacy and Industrial Pharmacy

September 2016 — June 2017: Collaborator at the Hospital Pharmacy Unit at A.R.N.A.S Hospital "Civico" , Palermo.

Practical-Professional curricular internship

List of publications

- Raimondi M.V; Randazzo O.; **La Franca M.**; Barone G.; Vignoni E.; Rossi D.; Collina S. DHFR Inhibitors: Reading the Past for Discovering Novel Anticancer Agents. MDPI, *Molecules* 2019, 24(6), 1140; <https://doi.org/10.3390/molecules24061140>.
- Raimondi, M.V., Listro, R., Cusimano, M.G., **La Franca, M.**, Faddetta, T., Gallo, G., Schillaci, D., Collina, S., Leonchiks, A., Barone, G., Pyrrolomycins as antimicrobial agents. Microwave-assisted organic synthesis and insights into their antimicrobial

mechanism of action, *Bioorganic & Medicinal Chemistry* (2019), Volume 27, Issue 5, 1 March 2019, Pages 721-728 doi: <https://doi.org/10.1016/j.bmc.2019.01.010>.

In preparation

- **Mery La Franca et al.**
“Design, synthesis and biological evaluation of new hypoxia activated Cu(II) transition complex, FGFR inhibitor”.
- **Mery La Franca et al.**
“Design, synthesis and biological evaluation of new quinazolin-4(3H)one, FGFR inhibitor”.
- **Mery La Franca et al.**
“ SAR studies of new quinazolin-4(3H)ones against NSCLS and SCLC”.
- **Mery La Franca*** and Lisa Gabler*.
“ FGFR5 in cancer past and future”
- Lisa Gabler, Carola Nadine Jaunecker, Sonja Katz, Sushilla van Schoonhoven, Bernhard Englinger, Christine Pirker, Thomas Mohr, Petra Vician, Mirjana Stojanovic, Valentin Woitzuck, Dominik Kirchhofer, **Mery La Franca**, Johannes Gojo, Bettina Grasl-Kraupp, Brigitte Marian, Michael Grusch, Sabine Spiegl-Kreinecker, Daniela Lötsch, Walter Berger.
“ Fibroblast growth factor receptor 4 supports aggressiveness of a GBM subset by regulating integrin-mediated cell adhesion and survival”
- Marlene Mathuber, Michael Gutmann, **Mery La Franca**, Petra Vician, Anna Laemmerer, Patrick Moser, Bernhard K. Keppler, Walter Berger*and Christian R. Kowol* “Development of a ponatinib-based cobalt(III) prodrug system”

Conference abstracts and poster presentations

- Raimondi, M.V., Listro, R., Cusimano, M.G., **La Franca, M.**, Faddetta, T., Gallo, G., Schillaci, D., Collina, S., Leonchiks, A., Barone, G. Novel Sortase A inhibitors to counteract Gram-positive bacterial biofilms. Presented at the 2nd Molecules Medicinal Chemistry Symposium (MMCS): Facing Novel Challenges in Drug Discovery, Barcelona, Spain, 15–17 May 2019
- **La Franca, M.**; Spatola, R.; Barone, G.; Raimondi, M.V.; Progettazione e sintesi di nuovi complessi metallici potenziali inibitori dell'FGFR4. Atti del Congresso della Società Chimica Italiana - Congresso Congiunto delle Sezioni Sicilia e Calabria 2019 (pp.). Palermo.
- **La Franca, M.**; Raimondi, M.V.; Barone, G., Design of copper(II) complexes as potential anticancer prodrugs. Italian-Spanish-Portuguese Joint Meeting in Medicinal Chemistry, MedChemSicily2018
- **La Franca, M.**; Randazzo, O.; Plescia, F.; Maggio, B.; Daidone, G.; Raffa, D.; Li Petri, G.; Listro, R.; Ribaudò, A.; Barone, G.; Raimondi, M.V., Progettazione e sintesi di nuovi derivati 4-chinazolinonici potenziali inibitori della diidrofolato reduttasi. Atti del Congresso della Società Chimica Italiana - Congresso Congiunto delle Sezioni Sicilia e Calabria 2018 (pp.62-62). Catania.
- Ribaudò, A.; Cusimano, M.G.; Plescia, F.; Maggio, B.; Daidone, G.; Raffa, D.; **La Franca, M.**; Li Petri, G.; Randazzo, O.; Listro, R.; Barone, G.; Schillaci, D.; Raimondi, M.V.; Sintesi e valutazione biologica di nuovi nitroderivati analoghi della pirrolomicina D attivi su *Pseudomonas aeruginosa*. Atti del Congresso della Società Chimica Italiana - Congresso Congiunto delle Sezioni Sicilia e Calabria 2018 (pp.61-61). Catania.
- Listro, R.; Cusimano, M.G.; Plescia, F.; Maggio, B.; Daidone, G.; Raffa, D.; **La Franca, M.**; Li Petri, G.; Ribaudò, A.; Randazzo, O.; Barone, G.; Schillaci, D.; Raimondi, M.V.; Pirrolomicine che inibiscono la Sortasi A nelle infezioni sostenute da batteri Gram-positivi. Atti del Congresso della Società Chimica Italiana - Congresso Congiunto delle Sezioni

Sicilia e Calabria 2018 (pp.63-63). Catania.

- Randazzo, O.; Li Petri, G.; Plescia, F.; Maggio, B.; Daidone, G.; Raffa, D.; **La Franca, M.**; Listro, R.; Ribaudò, A.; Barone, G.; Raimondi, M.V.; Sintesi di un isostero del 3,5-dimetil-6-fenil-8-(trifluorometil)- 5,6-diidropirazolo [3,4-f] [1,2,3,5] tetrazepin-4(3H)-one (CF₃-TZP) con potenziale attività biologica. Atti del Congresso della Società Chimica Italiana - Congresso Congiunto delle Sezioni Sicilia e Calabria 2018 (pp.60-60). Catania.

Acknowledgements

Doing this PhD has been one of the most formative and unforgettable experiences of my life. In addition to the many scientific knowledge acquired, it allowed me to have an unparalleled life experience.

The two years spent in Vienna allowed me to enrich myself culturally, personally and intellectually. I've met many people who have always supported me such as my Neapolitan friend Nunzia Matrone, my Romanian friend Patricia Triplea and my Serbian friend Mirja Petrovic, who will remain friends for life.

This doctoral thesis was born from a great personal and intellectual commitment of the people who supported and helped me in the last three years of work. This work would not exist without Dr. Maria Valeria Raimondi who personally supported the work, and she believed in my potential since the experimental thesis of the master. I thank my Italian tutor Prof. Giampaolo Barone who believed in this work by providing me with the tools to develop the project. This work would never have had light without my Austrian tutor Prof. Walter Berger, whom I sincerely thank, also for the enormous intellectual and personal debt contracted with him beyond the boundaries of this work.

I couldn't have done this job without my Viennese colleagues, who were a big and beautiful Austrian family. Thanks to Lisa Gabler (my pasta al fourno), my best partner, who has always helped me, teaching me many things (besides German), always making me have fun. Thank you for your empathy Mirja Stojanovic, even if we never understood each other in words (because we didn't speak the same language) you were the person who always understood me first of all. Thanks Dominik Kirchofer (my Domiii), who helped me every day at every moment without ever saying no, as well as for the many drinks together. Thanks to Hemma Schüffl and Sonja Hager, my work roommates, who never hesitated to help me whenever I needed it and for the many daily laughs together. Thanks to Alessia Stefanelli, the first person who introduced me to the city, culture and work.

Thanks to Petra Vician, who patiently taught me to work with animals. I also thank Alessio Terenzi, a very rational person, both for personal and work support. I also thank Anna Lämmerer, Carola Jaunecker, Christine Pirker, Daniela Lötsch-Gojo, Gerard Zeitler, Monika Caban (especially for Soplica), Petra Heffeter, Thomas Mohr and the Austrian chemists Christian Kowol and Marlene Mathuber.